Spectroscopic Studies of Ionic, Rydberg and Ion-Pair States of Small Molecules

by

Shiliang Wang

Doctor of Philosophy

The University of Edinburgh

1999

Declaration

I hereby declare that this thesis has been composed by myself, and the work presented in it is my own, except where due acknowledgement is given, and was carried out at the University of Edinburgh except where indicated.

Shiliang Wang

25 October 1999

Date

道可道，非常道。名可名，非常名。
無名天地之始。有名萬物之母。

老子道德 上篇
第一章

The Tao that can be told of
Is not the Absolute Tao;
The Names that can be given
Are not the Absolute Names.

The Nameless is the origin of Heaven and Earth;
The Named is the Mother of All Things.

Lao-tzu, Chapter 1, *Tao Te Ching*.

To my beloved wife, Aili.

Acknowledgements

I feel my language is so limited to express my gratitude to my supervisor Professor Robert Donovan, who offered me the Ph.D position with a studentship and has been giving me constant guidance, invaluable advice and tremendous support during my study. I think one could not expect a better supervisor than him. I would also like to thank my the other supervisor Dr. Kenneth Lawley for his continued direction in the theoretical aspect and the stimulating discussions we had on explaining experimental observation, which have been proved very beneficial to my work. Now, I would like to highlight my special thanks to Dr. Trevor Ridley. His extensive experience regarding experimental matters and expert skills in data analyses have been extremely helpful. He has also given me enormous support in many aspects, including English language, during my writing up, and proof read my whole thesis very patiently and attentively, which are extremely appreciated. I am also very grateful to Mr. Robert Maier for his technical assistance. The great administrative helps from Margaret Stewart and Annette Roper are also very appreciated.

I would like to thank all other members in our group including Neil Macleod, Pat O'Keeffe, John Hennessy, Alistair Nelson, Sandy Flexen, and Marc de Vries, who have been made my time of studying very enjoyable.

The spectroscopic studies using the unique VUV source produced by laser induced plasmas (presented in Chapter 9) were carried out in Rutherford Appleton Laboratory(RAL). I would like to take this opportunity to thank all the members of the X-ray group in RAL, Dr. Ric Allott, Dr. Edmond Turcu, Dr. Nic Lisi, Mr. Nick Spencer and Mr. Waseem Shaikh. I am also very grateful to Dr. Ken Ledingham, and Mr. Tom McCanny of Glasgow University for their support and assistance during the work in RAL.

Special thanks go to my wife, Aili, who has been always there for me.

Finally, I would like to take this opportunity to thank Edinburgh University for the financial support and CVCP for the receipt of an ORS award.

Abstract

The ionic, Rydberg and ion-pair states of a number of small molecules have been studied using a variety of spectroscopic techniques. These techniques used were resonance enhanced multiphoton ionisation (REMPI) spectroscopy, zero electron kinetic energy pulse-field ionisation (ZEKE-PFI) photoelectron spectroscopy and zero ion kinetic energy pulse-field dissociation (ZIKE-PFD) spectroscopy.

Firstly, a detailed study of the higher Rydberg states of C_6H_6 and C_6D_6 was performed using mass-resolved polarisation-dependent (2+1) REMPI spectroscopy. Three long series of gerade Rydberg states (two *nd* and possibly one *ng*) converging on the first ionisation energy, previously observed up to n=8, were extended up to n=30. By scanning the two-photon energy up to the ionisation limit, coherent two-photon ZEKE-PFI spectra of the ionic states of benzene-h_6 and -d_6 were obtained for the first time. The vibrational structure in the ZEKE spectrum is essentially the same as in the (2+1) REMPI spectra of Rydberg states but different from the (1+1′) ZEKE spectrum reported previously. Substitution effects and the influence of lowering the symmetry on the Rydberg states were also investigated by comparing studies of C_6H_5F, C_6H_5Cl, *p*-$C_6H_4F_2$ and *o*-$C_6H_4F_2$ molecules.

Second, the Rydberg and ionic states of CF_3I have been studied using both REMPI and zero kinetic energy pulse-field ionisation (ZEKE-PFI) photoelectron spectroscopy. The ground state of the ion was characterised using coherent two-photon (one-colour) ZEKE-PFI spectroscopy. The 6*p* Rydberg states were studied using two-photon REMPI spectroscopy with linear and circular polarised light. The strongest members with Ω=2 were identified and used as resonant intermediates in two-colour (2+1′) ZEKE-PFI experiments, which allowed the unambiguous assignment of the majority of the vibrational structure of the intermediate states.

Third, multiphoton pathways to the lowest cluster of ion-pair states of ICl and I_2, at energies close to the dissociation limit, are presented. These very high vibrational levels are detected in the anion (Cl^- and I^-) or cation (I^+) channel by

pulsed field ionisation. Using a variable time delay before field ionisation, ion pair states up to 50 cm^{-1} below the dissociation limit are observed to survive for at least 2 μs, indicating a stabilisation process analogous to that operating in high Rydberg electronic states. The analogy between these stabilised ion-pair states and ZEKE (zero electron kinetic energy) states suggests calling them ZIKE (zero ion kinetic energy) states. The atomic ion yield signal is highly structured both above and below the free ion threshold, indicating the role of doorway states which are coupled to the dense ion-pair vibrational manifold near dissociation. This coupling appears to be very efficient and competes successfully with radiative decay and further up-pumping that would result in ionisation. One difference with ZEKE spectroscopy is that these initially prepared states have to undergo both an electronic transition as well as a large angular momentum change, in order to be stabilised.

Fourth, molecular photofragment spectroscopy has been used to obtain new insight into the ultraviolet photodissociation of ozone. The formation of $O_2(b^1\Sigma_g^+)$ following absorption in the Huggins band (335–352 nm) of O_3 has been observed for the first time. The nascent $O_2(b^1\Sigma_g^+)$ photofragment was detected using two-colour resonance enhanced multiphoton ionisation (REMPI), with the $3s\sigma_g{}^1\Pi_g$ Rydberg state as the resonant intermediate state.

Finally, a new VUV generation technique (laser induced plasma), which may be used for spectroscopic studies, has been characterised. Some preliminary results using this new VUV generation source for single photon ionisation and ion-pair formation studies of polyatomic molecules (CH_3Br and CH_3I) have been obtained. In addition, high resolution ion-pair formation from CH_3Br using coherent VUV laser radiation generated by four wave mixing has been recorded in both CH_3^+ and Br^- channels.

Contents

Chapter 1 Introduction 1

1.1 Rydberg states and resonance enhanced multiphoton ionisation (REMPI) spectroscopy 3

1.1.1 Rydberg states 3

1.1.2 REMPI spectroscopy 4

1.2 High Rydberg states, ionic states and zero electron kinetic energy pulsed field ionisation (ZEKE-PFI) photoelectron spectroscopy 7

1.2.1 Ionic states and photoionisation 7

1.2.2 D.C. field ionisation of high Rydberg states 8

1.2.3 Pulse field ionisation of high Rydberg states 10

1.2.4 ZEKE-PFI photoelectron spectroscopy 12

1.3 Ion-pair states and the spectroscopy of near-dissociation vibrational levels of an ion-pair state 16

1.3.1 Ion-pair states 16

1.3.2 Photoion-pair formation 17

1.3.3 D.C. field-induced ion-pair formation from high vibrational ion-pair states 18

1.3.4 Pulse field dissociation of near dissociation vibrational levels of an ion-pair state 19

1.4 References 22

Chapter 2 Experimental 25

2.1 Introduction 25

2.2 The REMPI apparatus 25

2.2.1 Laser system 25

2.2.2 The REMPI spectrometer 27

2.3 The ZEKE apparatus 30

2.3.1 Laser system 30

2.3.2 The ZEKE Spectrometer 32

2.4 ZIKE-PFD experiments 35
2.4.1 Laser system 35
2.4.2 Arrangements for pulse field experiments 35
2.5 VUV radiation from a laser induced plasma 37
2.5.1 The laser plasma source 37
2.5.2 The VUV radiation and detection electronics 39
2.5.3 Higher resolution output 41
2.6 Resonantly enhanced four-wave-difference-frequency (FWDF) mixing 41
2.7 Reference 44

Chapter 3 Higher Rydberg States of C_6H_6, C_6D_6, C_6H_5F, C_6H_5Cl, *p*-$C_6H_4F_2$ and *o*-$C_6H_4F_2$ Studied by Two-photon Resonance Ionisation Spectroscopy 45

3.1 Introduction 45
3.2 Experimental 48
3.3 Results and discussions 49
3.3.1 Benzene (C_6H_6 and C_6D_6) 49
3.3.2 Fluorobenzene (C_6H_5F) 62
3.3.3 Chlorobenzene (C_6H_5Cl) 68
3.3.4 *p*-Difluorobenzene ($C_6H_4F_2$) 72
3.3.5 *o*-Difluorobenzene ($C_6H_4F_2$) 75
3.4 Conclusion 79
3.5 References 80

Chapter 4 Coherent Two-Photon ZEKE-PFI Spectra of Benzene and Substituted Benzenes 82

4.1 Introduction 82
4.2 Experimental 83
4.3 Results and discussions 83
4.3.1 Benzene-h_6 and -d_6 83
4.3.2 Chlorobenzene 88

4.3.3 *o*-Difluorobenzene.....91
4.3.4 *p*-Difluorobenzene.....93
4.4 Conclusion.....94
4.5 References.....94
Chapter 5 Ionic and Rydberg States of CF_3I Studied by High Resolution Photoelectron (ZEKE-PFI) and Resonance Enhanced Multiphoton Ionisation Spectroscopy (REMPI).....96
5.1 Introduction.....96
5.2 Experimental.....97
5.3 Results.....98
5.3.1 Coherent Two-Photon ZEKE-PFI Spectrum of CF_3I^+.....98
5.3.2 Resonance-Enhanced Multiphoton Ionisation Spectra of CF_3I.....101
5.3.3 (2+1′) ZEKE-PFI spectra using the 6p Rydberg states as resonant intermediates.....106
5.4 Discussion.....111
5.4.1 The Electronic Structure of the 6p cluster of Rydberg States.....111
5.4.2 Interpretation of the spectra.....112
5.5 Conclusion.....113
5.6 References.....113
Chapter 6 The Spectroscopy of Near-Dissociation Ion-Pair States of ICl.....116
6.1 Introduction.....116
6.2 Experimental.....118
6.3 Results.....119
6.3.1 Three-photon, two-colour dissociative ion-pair formation via the $E0^+(\upsilon = 24)$ intermediate state.....122
6.3.2 Ion-pair formation using three-colour multiphoton excitation via $\upsilon = 2$ of the B state.....126

6.3.3 The ZIKE-PFD spectrum of ICl 130
6.4 Discussion 135
6.5 Conclusions 137
6.6 References 138
Chapter 7 The Spectroscopy of Near-Dissociation Ion-Pair States of I_2 139
7.1 Introduction 139
7.2 Experimental 140
7.3 Results 141
7.3.1 Ion-pair formation using two-colour three-photon excitation 141
7.3.2 Effect of jet-cooling 142
7.3.3 High resolution study of the 17890 cm^{-1} band 146
7.3.4 Ion-pair formation using three-colour multiphoton excitation 148
7.3.5 The ZIKE-PFD spectrum of I_2 151
7.4 Discussion 159
7.5 Conclusion 164
7.6 References 165
Chapter 8 Photodissociation of Ozone between 335 and 352 nm to give $O_2(b\ ^1\Sigma_g^+) + O(^3P_J)$ 166
8.1 Introduction 166
8.2 Experimental 167
8.3 Results and Discussion 168
8.3.1 Use of the O_2 ($d3s\sigma_g\ ^1\Pi_g$) state as a resonant intermediate in identifying the photolysis products. 168
8.3.2 Photolysis of ozone by Huggins band excitation 171
8.4 Conclusion 176
8.5 References 176
Chapter 9 Photoionisation and Photoion-Pair Formation Studies using VUV Radiation Generated by

Laser Produced Plasmas and Four Wave Difference Frequency Mixing 178

9.1 Introduction 178

9.2 Experimental 179

9.3 Results and discussions 180

9.3.1 Characterisation of VUV radiation from laser-produced plasmas .. 180

9.3.2 Improvement of spectral resolution and application to photoionisation of NO 182

9.3.3 Application to ion-pair formation survey studies 186

9.3.4 Ion-pair formation from CH_3Br using four-wave-frequency-difference mixing (FWFD) 188

9.4 Conclusion 192

9.5 References 193

Appendix 195

A.1 List of acronyms 195

A.2 University regulations 196

A.2.1 Courses attended 196

A.2.2 Conferences attended 196

A.3 List of publications 197

List of Figures

Figure 1-1: Potential energy diagram of I_2 showing different types of states: (a) ground valence state ($X0_g^+$), (b) excited valence state ($B0_u^+$), (c) ion-pair states ($E0_g^+$ and $D0_u^+$) and (d) Rydberg state [243, $^2\Pi_{3/2}]nl$ of the neutral molecule. The ground state of the I_2 cation is also shown (e).....2

Figure 1-2: (2+1) REMPI process: two-photons absorbed to excite the molecule to a Rydberg state and another photon to ionise the molecule.....5

Figure 1-3: The potential (solid line) experienced by a Rydberg electron due to the ionic core (Coulomb potential) and the potential (dashed line) experienced by a Rydberg electron with the application of an electric field.....9

Figure 1-4: Two colour (1+1′) ZEKE-PFI: The first photon excites the molecule to an intermediate state, the second photon further excites the molecule to very high (n≥150) Rydberg states, then the molecule is ionised by using a delayed, pulsed electric field.....13

Figure 1-5: TIPPS process: One-photon is absorbed to excite the molecule to very high vibrational (v≥10000) ion-pair states, the molecule is then dissociated using a delayed pulsed electric field.....19

Figure 1-6: ZIKE-PFD process: Three-photons are sequentially absorbed to excite the molecule to very high vibrational (v≥10000) ion-pair states, and the molecule is then dissociated using a delayed pulsed electric field.....21

Figure 2-1: A schematic diagram of the laser system used for one-colour (2+1) REMPI experiments (solid part) and two-colour experiments (plus dotted part).....26

Figure 2-2: A schematic diagram of the REMPI spectrometer.....28

Figure 2-3: A schematic diagram of the laser system used for two-colour ZEKE-PFI experiments. 31

Figure 2-4: A schematic diagram of the ZEKE spectrometer. 33

Figure 2-5: A schematic diagram of the laser arrangement for three-colour triple-resonance enhanced multiphoton ion-pair formation experiments 36

Figure 2-6: Negative HV pulse output from the bipolar fast high voltage transistor switch. when connecting –HV input to –2 kV and +HV to (a) earth; (b) a negative bias voltage (-Δ); (c) a positive bias voltage(Δ) 38

Figure 2-7: Negative high voltage pulse when connecting the –HV of the switch to -2016 V and the +HV to earth measured by using a HV probe on a LeCroy oscilloscope. 38

Figure 2-8: A schematic diagram of the experimental set-up used for characterisation of VUV radiation from laser induced plasmas 40

Figure 2-9: A schematic diagram of the experimental setup for photoionisation and photoion-pair study using VUV radiation from laser-induced plasma 42

Figure 2-10: A schematic diagram of the experimental arrangement for VUV generation using FWFD and one-photon ion-pair formation study of CH_3Br. 43

Figure 3-1: The linearly polarised two-photon spectrum of C_6H_6 in the 67000-70000 cm^{-1} region. The insert shows a high resolution scan of the strong peak under linear and circular polarisation 50

Figure 3-2: The linearly and circularly polarised two-photon spectra of C_6H_6 in the 67000-74400 cm^{-1} region recorded in the C_2^+ mass channel. 52

Figure 3-3: The linearly and circularly polarised two-photon spectra of C_6H_6 in the 73000-74600 cm^{-1} region. The peaks marked with * are atomic carbon resonances. 53

Figure 3-4: The linearly and circularly polarised two-photon spectra of C_6D_6 in the 72200-73600 cm^{-1} region recorded in C_2^+ mass channel. 55

Figure 3-5: The linearly and circularly polarised two-photon spectra of C_6D_6 in the 73000-74600 cm^{-1} region recorded in the C_2^+ mass channel. ...56

Figure3-6: The πe_{1g} degenerate HOMO orbitals of benzene. For convenience, the upper one (a) will be denoted as b_1 type and the lower one (b) as a_2 type orbital. (D_{6h}).....60

Figure3-7: The schematic diagrams of the overlap (a) between the Rydberg orbitals d_{xz} and benzene HOMO orbital $\pi e_{1g}(b_1)$, (b) between the Rydberg orbitals d_{z^2} and benzene HOMO orbital $\pi e_{1g}(b_1)$ and (c) between the Rydberg orbitals d_{xy} and benzene HOMO orbital $\pi e_{1g}(b_1)$. Note that d_{xz} is mainly located in the xz plane with its lobes about ±45° to the xy plane while d_{z^2} mainly surrounds the z axis and out of the molecular plane (xy) with small lobes in the molecule plane with opposite ("–") phase. The d_{xy}, however, mainly lies in the molecular plane. 61

Figure 3-8: The linearly and circularly polarised two-photon spectra of C_6H_5F in the 66500-69500 cm^{-1} region in the C^+ mass channel. 63

Figure 3-9: The linearly and circularly polarised two-photon spectra of C_6H_5F in the 69000-74000 cm^{-1} region recorded in the C_2^+ mass channel. ...64

Figure 3-10: The linearly and circularly polarised two-photon spectrum of C_6H_5Cl in the 65000-70000 cm^{-1} region in the C^+ mass channel.....69

Figure 3-11: The linearly and circularly polarised two-photon spectrum of C_6H_5Cl in the 68000-74000 cm^{-1} region in the C_2^+ mass channel. 70

Figure 3-12: The linearly polarised two-photon spectra of *p*-$C_6H_4F_2$ in the 69000-73000 cm^{-1} region composed of several consecutive scans recorded in the CF^+ mass channel.....73

Figure 3-13: The linearly polarised two-photon spectrum of *o*-$C_6H_4F_2$ in the 62400-64200 cm^{-1} region in the parent ion mass channel. 76

Figure 3-14: The linearly polarised two-photon spectra of *o*-$C_6H_4F_2$ in the 68000-73000 cm^{-1} region composed of several consecutive scans in the CF^+ mass channel. 78

Figure 4-1: (a) Coherent two-photon ZEKE spectrum of benzene-h_6 at 150 torr pressure of benzene-h_6 vapour/argon mixture. The feature marked by * is caused by an accidental resonance (see text). (b) Coherent two-photon ZEKE spectrum of benzene-d_6 at 230 torr pressure of benzene-d_6 vapour/argon mixture. Both spectra are normalised to the square of the simultaneously recorded laser power. 84

Figure 4-2: Coherent two-photon ZEKE spectrum of benzene-h_6 at 430 torr of benzene vapour/helium mixture. The spectrum is normalised to the square of the simultaneously recorded laser power..... 87

Figure 4-3: Coherent two-photon ZEKE spectra of C_6H_6 at different (total) pressures with different carrier gases (a) Ar: upper trace 225 torr and lower trace 150 torr. (b)He: Upper trace 180 torr and lower trace 120 torr. All spectra in this figure are normalised to the square of the simultaneously recorded laser power. 89

Figure 4-4: Coherent two-photon ZEKE spectrum of chlorobenzene (lower trace) together with (1+1) REMPI spectrum (upper trace) recorded in parent mass channel. 90

Figure 4-5: Coherent two-photon ZEKE spectrum of *o*-difluorobenzene (lower trace) together with the (1+1)REMPI spectrum recorded in the parent mass channel (upper trace). 92

Figure 4-6: Coherent two-photon ZEKE spectrum of *p*-difluorobenzene (lower trace) together with the (1+1)REMPI spectrum recorded in the parent mass channel (upper trace). 93

Figure 5-1: The coherent two-photon one-colour ZEKE-PFI spectrum of CF_3I^+ ($^2E_{3/2}$). (* indicates an atomic iodine line). 99

Figure 5-2: The (2+1) REMPI spectrum of CF_3I in the region 65300-68100 cm^{-1}. The assignments shown are for three states with Ω=0, 1 & 2. 102

Figure 5-3: (2+1)REMPI spectra of CF_3I using linearly (LP) and circularly (CP) polarised light. 104

Figure 5-4: (3+1)REMPI spectra of CF_3I using linearly (LP) and circularly (CP) polarised light. 105

Figure 5-5: The (2+1′) ZEKE-PFI spectra of CF_3I^+ ($^2E_{3/2}$) via various members (0_0^0, 3_0^1, 3_0^2,3_0^3 and 6_0^3) of the [$^2E_{3/2}$]6p;2 Rydberg state. (* indicates an atomic iodine line). 107

Figure 5-6: (2+1′) ZEKE-PFI of CF_3I^+ ($^2E_{3/2}$) via various members (5_0^1, $5_0^1 3_0^1$, $5_0^1 3_0^2$ and $5_0^1 3_0^3$) of the [$^2E_{3/2}$]6p;2 Rydberg state. 108

Figure 6-1: Potential curves of $I^{35}Cl$ and the excitation schemes used in this work. The potential for the B state is constructed by the same method described in ref.10. The E and f states are constructed using the turning points from ref.15 and ref.17. The f' state was obtained by simply shifting the f potential up by the difference in their term energies. The Rydberg states were constructed using Morse potentials. Excitation schemes: (a) *via* the continuum of B state; (b) *via* bound level υ =2 of B state. 120

Figure 6-2: Double-resonance (bound-free-bound) REMPI spectrum of ICl. The E state is excited *via* the continuum of the B state. The $E0^+$ vibrational progressions of $I^{35}Cl$ and $I^{37}Cl$ are marked by ladders. .. 121

Figure 6-3: Ion-pair formation spectra from $I^{35}Cl$ following multiphoton excitation under DC field conditions. The molecule was excited from the ground state $X(0^+)$ to $E(0^+)$ (υ=24, low J) *via* the continuum of the B state by two-photon bound-free-bound transitions. Another tuneable photon from the second laser was scanned around the ion-pair formation threshold. The field-free and field-induced thresholds are marked on the spectra. a) I^+: the signal above the field-induced threshold mainly comes from an ion-pair formation process at the three photon level, while the signal below the field-induced threshold is due to dissociative

ionisation of ICl at the four-photon level; b) $^{35}Cl^-$: shows onset at the field-induced ion-pair threshold. 123

Figure 6-4: (1+1+1')+1 or 1' REMPI spectra of $I^{35}Cl$ recorded in the region 69600-71600 cm^{-1} (I^+ channel). The calculated vibrational levels of the $[\Pi_{3/2}]5d:0$ and $[\Pi_{3/2}]6p:0$ Rydberg states are marked in the spectrum by ladders. The insert is a higher resolution scan around 70500 cm^{-1}. 124

Figure 6-5: (a) (1+1')+1' REMPI spectrum enhanced by accidental resonance recorded by exciting $I^{35}Cl$ using a visible photon (ν_1) and a frequency doubled photon($\nu_2=2\nu_1$) in a one-laser experiment, collecting I^+. This spectrum is identical to that recorded in the $I^{35}Cl^+$ mass channel. The spectrum is plotted against the one-photon energy. (b) Simulation of the band contour of for the B←X (2,0) transition of $I^{35}Cl$..... 127

Figure 6-6: Ion-pair formation spectra of $I^{35}Cl$ following multiphoton excitation under DC field conditions. The molecule was excited from the ground state $X0^+$ to f $'0^+$ (υ=12, J=21), via B(υ =2, J=20), by one visible photon and one frequency-doubled UV photon from the first laser. Another tuneable photon from the second laser was then scanned around the ion-pair formation threshold. The field-free and field-induced threshold are marked on the spectra. (a) I^+: the signal above the field-lowered threshold comes from an ion-pair formation process at the three photon level while that below the field-lowered threshold comes from dissociative ionisation of $I^{35}Cl$ at the four-photon level. The background signal comes from two colour excitation from the first laser only. (b) $^{35}Cl^-$: onset of the field-lowered ion-pair threshold. The total energy is $\nu_1+\nu_2+\nu_3$ plus the rotational energy of the ground state..... 129

Figure 6-7: Time-of-flight mass spectrum of $^{35}Cl^-$ at four different excitation energies using a delayed pulsed-field (Delay time 1.4 μs, pulse field strength 1250 V/cm). a) Excitation energy 72506 cm^{-1}; b) Excitation energy 72519 cm^{-1}; c) Excitation energy 72520 cm^{-1}; (d) Excitation energy 72939 cm^{-1}. All excitation energies are relative to υ=0, J=0 of ground state of ICl. The excitation scheme is the same as in figure 6-6. 131

Figure 6-8: Time-of-flight spectra of $^{35}Cl^-$ at an excitation energy of 72519 cm^{-1} with different time delay of the pulsed field (pulsed field strength 1250 V/cm). Delay times: (a) 1.03 μs , (b) 1.43 μs , (c) 1.615 μs , (d) 1.73 μs and (e) 1.83 μs. The excitation scheme is the same as in figure 6-6. 133

Figure 6-9: (a) ZIKE-PFD spectrum of $I^{35}Cl$ recorded in the $^{35}Cl^-$ channel with the boxcar gated on the fast arrival peak as shown in figure 6-7b (pulsed field 1250 V/cm at a delay time of 1.4 μs). The excitation scheme is the same as in figure 6-6: (b) Replot of the spectrum in figure 6-6b for comparison. 134

Figure 7-1: The one-laser two-colour excitation scheme. 142

Figure 7-2: Ion-pair formation spectra using multiphoton excitation (ν_1+ ν_2+ ν_1: with ν_2=2 ν_1) enhanced by accidental resonance (a) I^+, (b)I^-. 143

Figure 7-3: Cooling effect of carrier gases (He and Ar) on the REMPI spectra of I_2 recorded in the I^+ mass channel, (a)Total pressure I_2/He 100 torr; (b) total pressure I_2/He 500 torr; (c)total pressure I_2/Ar 300 torr. 144

Figure 7-4: (a) Higher resolution scan of the 17890 cm^{-1} band in fig.7-2a; (b) LIF spectrum recorded simultaneously with (a) but in a static cell; (c) simulation of the band contour of (20,0) band of I_2 (B←X). 147

Figure 7-5: (a) and (b) Ion-pair formation spectra of I_2 using three-colour multiphoton excitation (ν_1+ ν_2 + ν_3: with ν_2=2 ν_1). One visible photon ν_1 pumps the molecule from the ground state X(υ =0,

J=13) to the B state (υ =20, J=12). A frequency doubled photon ν_2 (=2 ν_1) subsequently excites the molecule to the E (υ =168, J=13) state by accidental resonance. Then another tunable photon ν_3 (from the second laser) is scanned through the ion-pair threshold region. The field-free and field-induced thresholds are marked with downward arrows on the spectra. The features marked by * and upwards arrows are explained in the text. Total energy is relative to υ =0, J=0 in the ground state. (a) I^+ and (b) I^-. (c) LIF spectrum of B←X transitions of I_2 by absorption of ν_3 in a static cell recorded simultaneously with (a) when scanning ν_3. The LIF spectrum is plotted on the same total energy scale as in (a) and (b) for direct visual comparison of the band head positions and for the dips in the I^+ spectrum in (a). 149

Figure 7-6: Effect of a small dc field, applied prior to the high voltage extraction pulse, on the time-of-flight spectra of I^+ (produced by ion-pair formation). Extraction pulse +1.25 kV/cm and time delay 3.485 μs. (a)zero external dc field: green-total energy at 72048 cm^{-1} (below threshold); red-total energy at 72068 cm^{-1} (above threshold); (b) Total energy at 72068 cm^{-1}: red-zero external dc field; blue-external dc field 125 mV/cm. 152

Figure 7-7: Time-of-flight spectra of I^- formation. The time delay of the extraction pulse after laser firing is 3.485 μs. (a) TOF spectra with excitation energy 72055.6 cm^{-1}, which is between the field-free threshold and the field-lowered threshold, with four different dc bias fields: 0.0, +6.25,-6.25 and -9.38 V/cm. (b)TOF spectra with excitation energy 72068 cm^{-1}, which is above field-free threshold, with dc=0.0 and +6.25V. The calculated initial kinetic energies of the ions are marked by arrows. 154

Figure 7-8: A time-of-flight spectrum of I^+ produced following ion-pair formation at a total energy of 72048 cm^{-1}, which is between the

field-free and field lowered thresholds, (extraction pulse 1.25kV/cm and time delay 3.485 μs). The dc bias field is 15.63 V/cm. The calculated initial kinetic energy of the ions is marked by arrows..... 155

Figure7-9: ZIKE spectra observed with different dc bias fields. The excitation scheme is the same as in fig.7-5a, (extraction pulse 1.25 kV/cm and time delay 3.485 μs). The feature marked by * is due to electronic interference caused by a strong prompt ion signal at small dc field (1.56 V/cm). 157

Figure 7-10: Comparison of I^+ spectra recorded using constant field extraction and pulse field extraction (385 ns delay). (a) Upper trace: constant field; lower trace: pulse field at 385 ns delay after laser firing. (b) Intensities measured at five different total energies below zero-field threshold marked by arrows in (a), normalised to the intensity at -10.6 cm^{-1}, (+) DC; (x) 385ns delay; (o) ratio of intensities with delayed pulse field to that with constant field extraction..... 158

Figure 7-11: Small dc field induced "prompt" ion-pair formation spectra of I_2 recorded in I^+ channel with different dc bias fields, (extraction pulse 1.25 kV/cm and time delay 3.485 μs). 160

Figure 7-12: Extrapolation to determine the zero-field ion-pair formation threshold. The red edges of a series of spectra taken at different dc bias fields are plotted as a function of the square root of the dc field, (extraction pulse 1.25 kV/cm and time delay 3.485 μs)..... 160

Figure 7-13: Several potential energy curves of I_2. The $D(0_u^+)$ curve is constructed using the parameters given by Tellinghuisen[13]. The $E0_g^+$ curve is made using its known turning points[12]. The potential curves of the Rydberg states are constructed assuming a Morse potential. 161

Figure 8-1: (2+1) REMPI spectra of the photofragments produced from photolysis of O_3: (a) and (b) are the (2,2) and (2,3) bands

respectively of the $d3s\sigma_g\ ^1\Pi_g \leftarrow\leftarrow O_2(a^1\Delta_g)$ transition recorded by probing the molecular photofragments produced in the 254 nm (Hartley band) photolysis. The spectrum in (c) is the (2,0) band of the $d3s\sigma_g\ ^1\Pi_g \leftarrow\leftarrow O_2(b\ ^1\Sigma_g^+)$ transition recorded by probing the molecular photofragment produced in the 340nm (Huggins band) photolysis. The REMPI scheme in (a) and (b) are the result of a combination of (2′+1) and (2′+1′) processes whereas the spectrum in (c) is produced *via* a combination of ((1+1′)+1) and ((1+1′)+1′) processes. The features labelled with asterisks are those due to transitions from the depleted odd J levels of $O_2(a\ ^1\Delta_g)$. These features are completely absent in the $O_2(b\ ^1\Sigma_g^+)$ band due to nuclear spin restrictions. 169

Figure 8-2: The Photofragment Excitation (PHOFEX) spectrum of O_3 recorded by probing the production of O ($^3P_0$) with λ_{probe} = 226.23 nm while scanning the photolysis laser in the 335 - 345 nm region (full scheme shown in the insert). 171

Figure 8-3: (a) The one-colour REMPI excitation spectrum of ozone recorded by photolysing ozone between 349.7 nm and 351.8 nm and detecting the O_2 fragments formed by (2 + 1) REMPI with the same laser. (b) The (2′ + 1′) spectrum of the (2,0) band of the $d3s\sigma_g\ ^1\Pi_g \leftarrow\leftarrow O_2(b\ ^1\Sigma_g^+)$ transition recorded by 340 nm photolysis of ozone followed by probing the O_2 fragments formed between 349.7 nm and 351.8 nm. 175

Figure 9-1: Single-photon ionisation spectra of (a) nitric oxide (5.0×10^{-1} torr) ,(b) toluene (1.0×10^{-1} torr),(c) acetone (1.1×10^{-1} torr), (d) benzene (1.1×10^{-1} torr) and (e) xylene (1.0×10^{-1} torr) using VUV radiation from laser-produced plasmas. 1/4 meter spectrograph was used. 181

Figure 9-2: VUV radiation intensity from a laser-produced plasma measured using a PMT after a MgF_2 window 183

Figure 9-3: VUV radiation intensity from a laser-produced plasma measured using a photodiode without a MgF_2 window. 183

Figure 9-4: VUV single-photon ionisation spectrum of NO which shows a sharp step function at the ionisation threshold upon which is superimposed vibrational levels of the NO^+ ground state. 184

Figure 9-5: Comparison between the one-photon photoionisation spectra of nitric oxide using (a) synchrotron radiation (adapted from ref.8) and (b) VUV radiation from laser-induced plasma (reproduced from figure 9-4). 185

Figure 9-6: VUV single-photon excitation function of CH_3Br which shows ion-pair formation below the ionisation threshold and ionisation of the parent molecule above the ionisation threshold. 187

Figure 9-7: VUV single-photon excitation function of CH_3I which shows ion-pair formation below the ionisation threshold and ionisation of the parent molecule above ionisation threshold 189

Figure 9-8: Excitation functions of ion-pair formation recorded in CH_3^+ and $^{81}Br^-$ mass channels 190

Figure 9-9: Excitation functions of ion-pair formation of CH_3Br recorded in CH_3^+ mass channel. Positions of Rydberg states observed in absorption spectroscopy (ref. 9) are labelled in the figure. Dotted line are VUV power curves using Rhodamine 700, Rhodamine 101, Rhodamine B and Rhodamine 6G to provide the visible photons. No signal was observed in the region of 131.5-132 nm in which strong absorption was observed corresponding to $[^2\Pi_{3/2}]6p$. 191

List of Tables

Table 1-1: Properties of high Rydberg states and their n dependence. 4

Table 3-1: Transition energies and quantum defects of the origin bands of C_6H_6 .. 54

Table 3-2: Transition energies and quantum defects of the origin bands of C_6D_6 .. 57

Table 3-3: Transition energies and quantum defects of the origin bands of C_6H_5F. 66

Table 3-4: Symmetry species and selection rules of transition from ground states ($^1A_1$) to Rydberg states for monosubstituted benzene. 67

Table 3-5: Transition energies and quantum defects of the origin bands of C_6H_5Cl. 71

Table 3-6: Transition energies and quantum defects of the origin bands of p-$C_6H_4F_2$ 74

Table 3-7: Transition energies and quantum defects of the origin bands of o-$C_6H_4F_2$ 77

Table 4-1: Vibrational frequencies (cm^{-1}) of benzene-h_6 and -d_6. (those in parentheses are for -d_6) 85

Table 4-2: Vibrational frequencies (cm^{-1}) of o-difluorobenzene. 92

Table 5-1: Peak positions for the $\tilde{X}\,^2E_{3/2}$ state of CF_3I^+ obtained by ZEKE-PFI. 100

Table 5-2: Peak positions and assignments for the [$^2E_{3/2}$] 6p Rydberg states of CF_3I. 103

Table 5-3: Vibrational frequencies (in cm^{-1}) for several states of CF_3I and CF_3I^+. 110

Table 7-1: The frequencies of B←X, E←X, and f←X transitions. The values in green colour indicate when the B state and E state come into accidental resonance. 145

Table 9-1: Ionisation potentials of nitric oxide, acetone, toluene, xylene and benzene measured by single-photon ionisation using VUV radiation from laser-produced plasmas. 180

Table 9-2: Comparison between Peaks observed in ion-pair production

spectrum using VUV radiation from laser-produced plasma and Rydberg states of CH_3Br. The state with a prime has an excited state ionic core while the others have a ground state ionic core. 186

Chapter 1

Introduction

Electronically excited molecular states can be classified into three main types: i.e. valence states, ion-pair states and Rydberg states. As an example, figure 1-1 shows the potential energy curves of the three different types of electronic states of I_2. The valence states (figure 1-1b) arise from different arrangements of electrons within the outer valence shell of a molecule. The dissociation normally leads to two ground state or low lying excited neutral fragments. Rydberg states (figure 1-1d) result from the promotion of an electron from the outermost molecular orbital into an orbital which lies to higher energy and has a higher quantum number. Thus they correlate with an exited fragment (i.e. a Rydberg excited atomic fragment) and a ground state fragment. The ion-pair states (figure 1-1c) dissociate to form a pair of oppositely charged ions rather than two-neutral fragments. Molecular ionic states (figure1-1e), on the other hand, are the rovibronic states of the ionic core left when the molecule is ionised, corresponding to the complete removal of an electron.

In this thesis, the spectroscopy and the interaction of high lying excited electronic states of several small molecules have been studied in the vacuum ultraviolet (VUV) region from 8-11 eV (65000-91000 cm^{-1}). Several spectroscopic techniques have been applied following both single photon and multiphoton excitation schemes. This chapter includes descriptions of the molecular states studied and the theoretical background to the spectroscopic techniques.

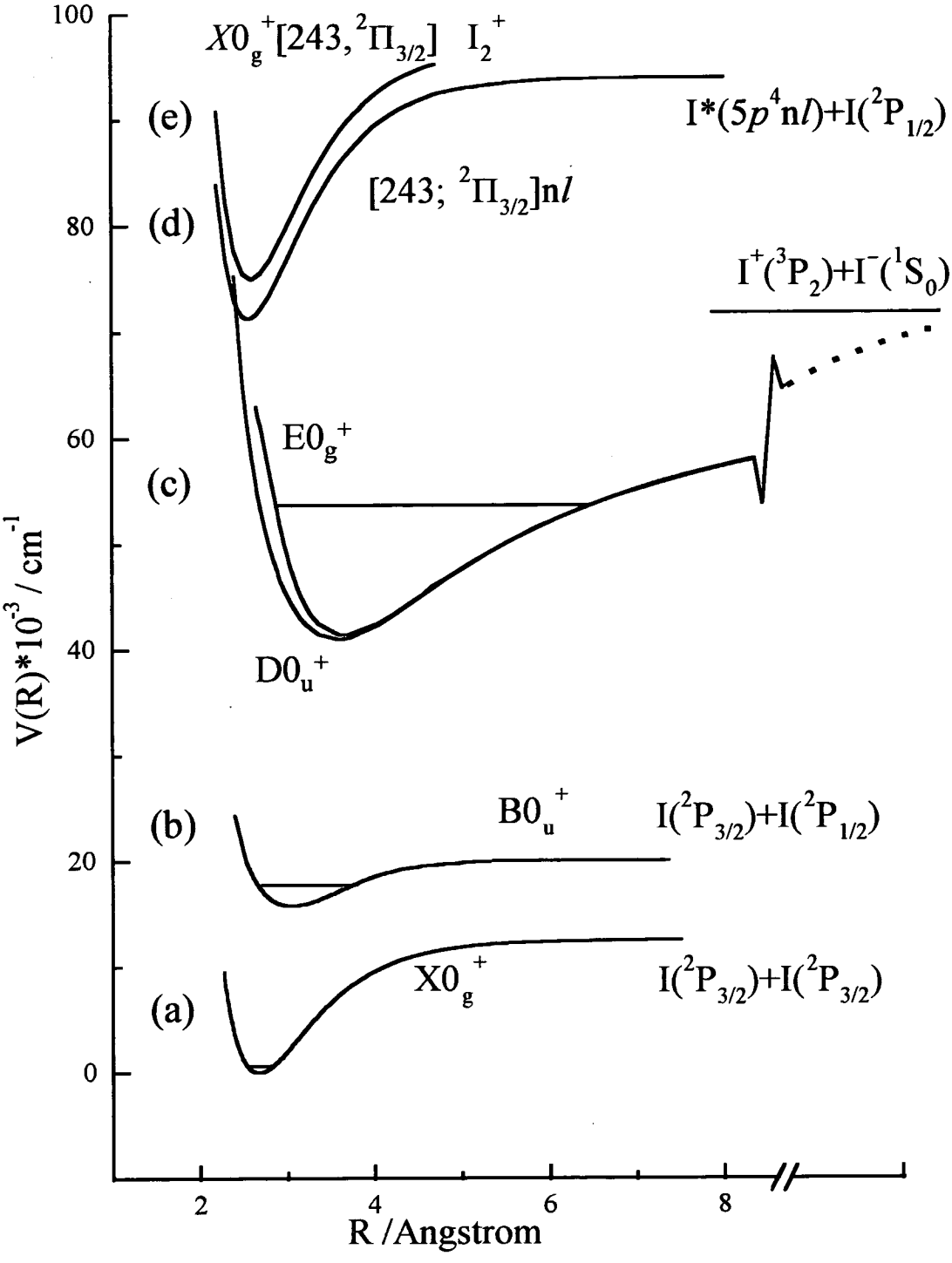

Figure 1-1: Potential energy diagram of I_2 showing different types of states: (a) ground valence state ($X0_g^+$), (b) excited valence state ($B0_u^+$), (c) ion-pair states ($E0_g^+$ and $D0_u^+$) and (d) Rydberg state [243, $^2\Pi_{3/2}$]n*l* of the neutral molecule. The ground state of the I_2 cation is also shown (e).

1.1 Rydberg states and resonance enhanced multiphoton ionisation (REMPI) spectroscopy

1.1.1 Rydberg states

Molecular Rydberg states may be considered in terms of a positive ion core (consisting of the nuclei and all the valence electrons) with a nonbonding Rydberg electron in a large, spatially diffuse orbital. As in many-electron atoms, the molecular Rydberg states can be arranged in series, each of which is characterised by a particular value of quantum defect, and each of which converges to the ionisation limit appropriate to its ion core. For any one Rydberg state, its term value, T_n, its quantum defect, δ, and the ionisation energy, IE, will be related via the following modified form of the Rydberg formula[1-2]:

$$T_n = IE - \frac{R}{(n-\delta)^2} \qquad (1.1)$$

$$R = \frac{\mu}{m_e} R_\infty \qquad (1.2)$$

where R_∞ is Rydberg constant (109737 cm^{-1}), m_e is the electron mass, μ is the reduced mass of the molecule system and R is the mass corrected value of the Rydberg constant. The magnitude of δ provides an indication of the extent to which the wavefunction of the Rydberg electron penetrates into the core region. For a given n, δ for different l values decreases in the order $s>p>d$ where an s orbital radial wavefunction has a non-zero amplitude at the nucleus and therefore penetrates more into the core than the other orbitals which have nodes there. The typical values for benzene[2-3], for example, are $\delta(ns)\sim0.77$, $\delta(np)\sim0.5$, while for $\delta(nd)\sim 0$. Such qualitative ideas have proven very useful in interpreting the patterns of excited states observed in many families of polyatomic molecules, though, in some circumstances, modifications due to configuration interaction (i.e. mixing between zero-order states sharing a common symmetry species but arising from different electronic configurations) can complicate such simple expectations.

Most properties of Rydberg states vary rapidly with the principal quantum number n, typically as an integer power of n. The classical radius of the electron orbit, the period of the orbital motion, the binding energy and the energy spacing between adjacent Rydberg states scale as n^2, n^3, n^{-2} and n^{-3}, respectively. Representative values[4] for these properties at selected values of n are summarised in table 1-1.

Table 1-1: Properties of high Rydberg states and their n dependence.

Property	n dependence[a]	n=10	n=100	n=1000
Mean radius	$a_0 n^2$	5.3 nm	0.53 μm	53 μm
Period of electron motion	$\tau_0 n^3$	0.15 ps	0.15 ns	0.15 μs
Binding energy	Rn^{-2}	1100 cm^{-1}	11 cm^{-1}	0.1 cm^{-1}
Spacing between adjacent levels	$2Rn^{-3}$	200 cm^{-1}	0.2 cm^{-1}	$2x10^{-4}$ cm^{-1}

[a] a_0 is the Bohr radius (0.053 nm). $\tau_0=1/\nu_0$, ν_0 is the Bohr orbit frequency ($6.6x10^{15}$ Hz).

1.1.2 REMPI spectroscopy

REMPI spectroscopy has been widely used for the study of Rydberg states of gaseous molecular species. There are many variants of this technique. Here, one of the simplest (and most practical) types of REMPI scheme will be demonstrated. For more information on this technique and its other chemical applications, the reader is referred to a recent review article[5] and reference therein. A schematic diagram is shown in figure 1-2. The common notation to describe a REMPI scheme is to specify a process using the number of photons needed to reach the intermediate state, plus the number needed to ionise the intermediate state. In the particular example shown in figure 1-2, the molecular species of interest needs to absorb two photons to reach a Rydberg state and then absorbs another in order for it to be ionised, thus can be denoted as (2+1) REMPI. The REMPI spectrum obtained by measuring the ion yield (or the yield of the accompanying photoelectrons) as a function of excitation wavelength will provide a signature of

the two-photon transition in the neutral molecule; analysis will furnish information about the Rydberg state. For a Rydberg state to appear in the REMPI spectrum, the transition moment between the ground state and the Rydberg state must be nonzero.

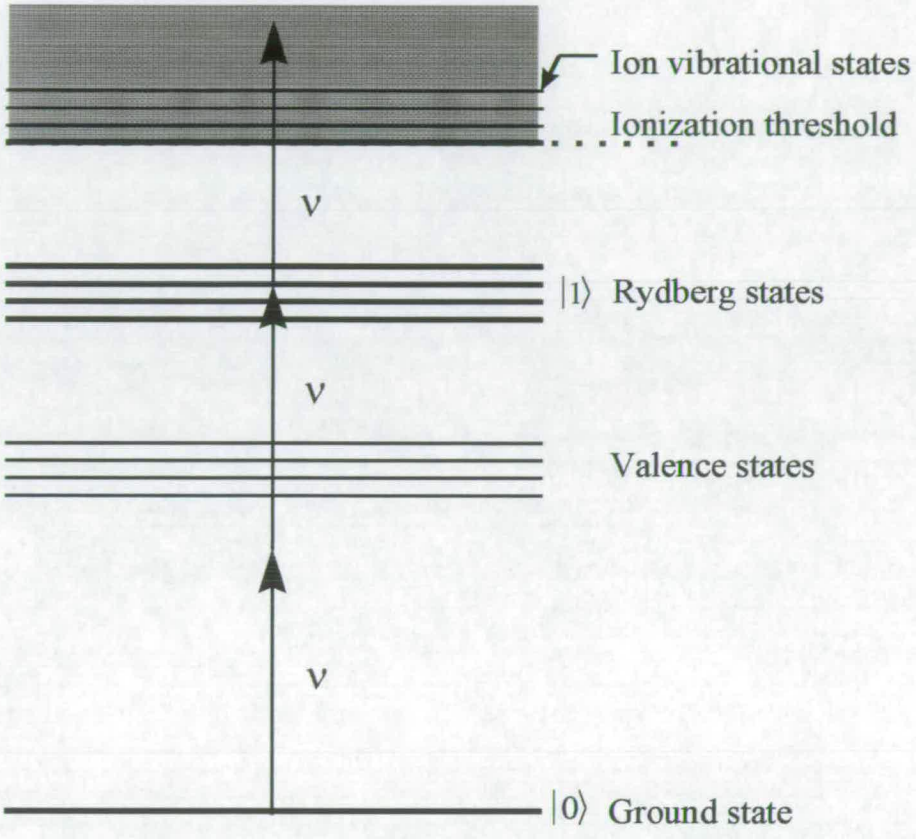

$$M \xrightarrow{2h\nu} M^* \xrightarrow{h\nu} M^+ + e^-$$

Figure 1-2: (2+1) REMPI process: two-photons absorbed to excite the molecule to a Rydberg state and another photon to ionise the molecule.

One advantage of REMPI is that multiphoton excitations can provide a means of populating excited states via transitions forbidden in traditional one-photon absorption spectroscopy. The two photon excitation scheme, for example, has been used to characterise the gerade Rydberg states of benzene, which were otherwise absent in one-photon absorption spectroscopy (see chapter 3).

Sensitivity to the polarisation of the laser radiation is another important advantage of REMPI over one-photon absorption. For example, a two-photon transition involving a change in symmetry species is predicted to have a polarisation ratio Ω (defined as the ratio of signals for circular to linear polarisation) of 1.5. If the transition does not involve a change in symmetry, the ratio is expected to be $\Omega<1.5$[45, 47-48].

The other advantage of REMPI is that using visible or ultraviolet photons can often provide one ready means of populating an excited state lying at energies that, in one-photon absorption, would fall in the technically more demanding vacuum ultraviolet spectral region. Although multiphoton excitation cross-sections are much smaller than one photon absorption cross sections, this can be compensated for by using high light intensities. For most spectroscopic applications, the necessary high light intensities needed for REMPI can be achieved by focusing the output of common (nanosecond pulse duration) tunable dye lasers. This points to another potential benefit of multiphoton excitation method. The interaction is concentrated in a localised volume, the focal volume, thus rendering the technique ideally matched for use with supersonic molecular beams.

The sequential absorption of more than one photon, through real intermediate states at the one-photon level, is another means for examining electronically excited states which can not be accessed using vertical excitation schemes. The usefulness of the sequential multiphoton excitation is well recognised in molecular spectroscopy. One example of the use of sequential multiphoton excitation is Optical-Optical Double Resonance (OODR) spectroscopy. Here, the first photon is resonant with a vibrational level of a bound excited state which has a good Franck-Condon overlap with the ground state. A second photon is then absorbed which can populate vibrational levels in a rovibronic state which is not in the Franck-Condon window of the ground state. A variant of the OODR technique involves either a repulsive intermediate state or the continuum (repulsive limb) of a bound state. It is then called bound-free-bound excitation. Here, the Franck-Condon window of the electronic ground state is much extended through bond-stretching following the absorption of the first photon. An example for both

schemes can be found in Chapter 6 (figure 6-1a and b). Both of these techniques have been widely used to characterise lower vibrational levels of the ion-pair states of the diatomic halogens and interhalogens[6-10].

1.2 High Rydberg states, ionic states and zero electron kinetic energy pulsed field ionisation (ZEKE-PFI) photoelectron spectroscopy

1.2.1 Ionic states and photoionisation

The term photoionisation implies the production of a positive ion-electron pair on the interaction of sufficiently energetic photons (≥ionisation limit) with gaseous atoms or molecules[11]. The ionic states are simply the quantum states of the resulting atomic or molecular ion.

Ionic states are most commonly studied by photoelectron spectroscopy. In conventional photoelectron spectroscopy (PES)[12], a fixed frequency light source irradiates molecules at a photon energy well above their ionisation threshold (by several eV). The resulting photoelectrons are then energy analysed. Electrons are emitted at different energies, as the resulting ion can be left in different rovibronic states (an ion left with a high amount of vibrational energy, say, will emit a slower photoelectron, simply due to conservation of energy). Thus the ionic energy levels can be determined by the energy spacings of the peaks in the photoelectron spectrum.

In threshold photoelectron spectroscopy (TPS)[13], the light source is now scanned, and a filter is set up to detect only very slow photoelectrons. By monitoring this slow-electron signal as the photon energy is scanned over the different ionisation thresholds, the ion energy levels may also be determined. However, with the threshold technique, the ionic energy levels are determined from the (scanned) photon energy, rather than from the generally more difficult electron kinetic energy analysis. There are other advantages to the threshold technique. It is

easier to optimise a high-throughput, high-resolution detection of threshold electrons, compared with conventional photoelectron spectroscopy.

1.2.2 D.C. field ionisation of high Rydberg states

It is well documented in atomic physics that an electric field can distort the potential in which an electron moves so that photoionisation is possible at lower photon energies (excitation to Rydberg states) than the ionisation limit[14]. This process is usually referred to as field ionisation.

For the field ionisation in a constant electric field, the simplest description is the classic model. In the presence of a homogeneous electric field, the long-range potential† of a hydrogenic atom is given by

$$V(r) = -\frac{e}{4\pi\varepsilon_0 r} - Fz \qquad (1.3)$$

in real units, where r is the electron-core distance, z is the component of r along the external field and F is the field strength. Along z axis (x=y=0, r=z), the potential $V(z)$ have

$$V(z) = -\frac{e}{4\pi\varepsilon_0 z} - Fz \qquad (1.4)$$

This potential, as shown in figure 1-3, has a saddle point (a local maximum) in the direction of the electric field. The position of this saddle point can be obtained by differentiating the Eq.1.4,

$$\frac{dV(z)}{dz} = \frac{e}{4\pi\varepsilon_0 z^2} - F = 0 \qquad (1.5)$$

$$\text{thus } z_{sp} = \sqrt{\frac{e}{4\pi\varepsilon_0 F}} \qquad (1.6)$$

This corresponds to the saddle point occurring at an energy,

$$E_{sp} = eV(z_{sp}) = -2\sqrt{\frac{e^3 F}{4\pi\varepsilon_0}} \qquad (1.7)$$

---

† It is important to note that in the direction perpendicular to the field direction (z=0), we still have $V(r) = -\frac{e}{4\pi\varepsilon_0 r}$ thus no saddle point is present in this direction.

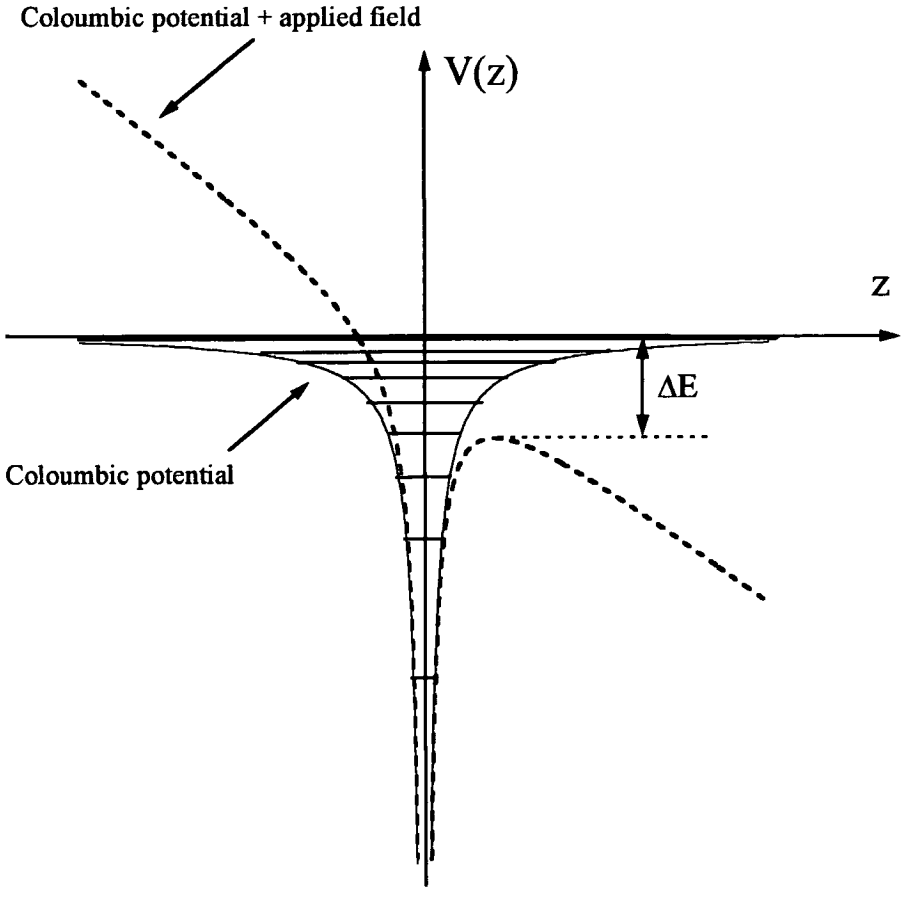

Figure 1-3: The potential (solid line) experienced by a Rydberg electron due to the ionic core (Coulomb potential) and the potential (dashed line) experienced by a Rydberg electron with the application of an electric field.

below the asymptotic field free ionisation limit. Substituting all constants in Eq.1.7 and rewriting it in cm^{-1} units, one obtains,

$$E_{sp} = -6.12\sqrt{F} \qquad (1.8)$$

where E_{sp} is given in cm^{-1} and F in V/cm. Classically ionisation of a Rydberg electron in a specific orbital will occur if the applied field is large enough to lower the saddle point below the electron binding energy resulting in a sharp ionisation threshold that is shifted from the field free value by the amount given by Eq.1.8.

For molecules and non-hydrogenic atoms, the size of a Rydberg state with a high value of principal quantum number n is so large compared to that of the positively charged ion core that the latter, regardless of its structure, appears as a point charge to the distant electron. The electron-core interaction is dominated by the Coulomb attraction thus Eq.1.8 should also apply to molecules and non-hydrogenic atoms.

The classic saddle point model has been demonstrated very successful by a number of studies[15-17], especially most recent one by Merkt et al.[18], to predict the lowering of the ionisation energy induced by a constant electric field for atoms and molecules.

1.2.3 Pulse field ionisation of high Rydberg states

The ionisation behaviour of Rydberg states in a pulsed field is far more complex. For simplicity, the hydrogenic atom, which is a good approximation for molecular high Rydberg states, will be used as a model for discussion.

As soon as an electric-field is applied, the n^2 electronic degeneracy of hydrogenic Rydberg states is partially removed. More specifically, spherical symmetry is lost, l ceases to be a good quantum number as the electric field mixes different l states. At low electric fields, the interaction between the hydrogenic atom and the electric field can be dealt with as a perturbation on the hydrogenic Hamiltonian in the Schrödinger equation. The perturbation leads to a linear splitting of the degenerate zero-field states (linear Stark effect) fanning out into a "manifold" for each m_l, which remains a good quantum number. They are given in atomic units to first order by[19-20],

$$E = -\frac{1}{2n^2} + \frac{3}{2}F(n_1 - n_2)n \qquad (1.9)$$

where n_1 and n_2 are non-negative integers labelling different members of the manifold, constrained by the relationship $n_1+n_2+|m_l|+1=n$. For $m_l=0$, the extreme "blue-shifted" state of the manifold has $n_1-n_2=n-1$, while the extreme "red-shifted" state has $n_1-n_2=-n+1$. The energy separation between these extreme states of the manifold increases with n.

As the electric-field is increased from zero, blue-shifted members originating from one value of n will approach the red-shifted states of high n. This gives rise to "avoided-crossings", as the field strength is increased, two quantum states approach one another in energy, then recede. An atom in one state may "jump" to another if this crossing is approached rapidly (diabatic). If the crossing is approached slowly (adiabatic) the atom is more likely to stay in the same state.

The two extreme cases of the diabatic and adiabatic field ionisation correspond to very different ionisation behaviour. Ionisation of a population of Rydberg states distributed equally among all Stark states of a given n will occur over a wide range of field strengths if the ionisation is diabatic. The reddest (n_1-n_2= $-n+1\approx -n$) state with m=0, having electron density peaked along the z axis and located in the vicinity ("downhill") of the saddle point[14, 21], ionises first, as soon as the field reach a critical value (F_c) that the energy curve crosses the saddle point energy, i.e. when

$$-\frac{1}{2n^2}-\frac{3}{2}F_c nn = E_{sp} \qquad (1.10)$$

In atomic unit, Eq.1.8 can be rewritten as

$$E_{sp} = -2\sqrt{F_c} \qquad (1.11)$$

Combining Eq.1.10 and 1.11, one gets

$$F_c = \frac{1}{9n^4} \qquad (1.12)$$

As the binding energy of the Rydberg states with zero-field is $E = -\frac{1}{2n^2}$, Eq.1.12 can be rewritten as

$$E = -4.59\sqrt{F_c} \qquad (1.13)$$

E in cm^{-1}, F_c in V/cm.

The bluest state, on the other hand, having electron density peaked in the z axis but on the opposite side ("uphill") far away from the lower barrier, ionises last although its energy level is lifted to above the saddle point. Empirically, it is observed that the bluest state ionises at approximately twice the field strength as the reddest[21]. Thus,

$$E = -3.06\sqrt{F_c} \qquad (1.14)$$

E in cm^{-1}, F_c in V/cm.

If the field is applied slowly enough, such that all avoided crossings are traversed adiabatically, field ionisation occurs when the saddle-point energy equals the initial Rydberg state binding energy[19], thus the same rule as for the classical saddle-point model (Eq.1.8.) will hold for adiabatic ionisation.

Adiabatic field ionisation has its origin in the deviation of the electronic potential from a pure Coulomb potential at short range[21]. It is therefore an important mechanism only for Rydberg states that can penetrate into the ion core region. It is of negligible significance for high m_l states.

It is almost impossible to predict which field ionisation mechanism will apply to individual pulsed field ionisation experiments. A very recent experiment made by Merkt et al[18] on Ar atoms shows evidence that no simple rules can be given to describe the shift in the ionisation potential induced by the pulsed field. They observed that the field ionisation occurs predominately adiabatically at n=27 with slew rates of 2.2×10^{10} $Vcm^{-1}s^{-1}$, but predominately diabatically at n=69 with slew rates of 3.6×10^{8} $Vcm^{-1}s^{-1}$.

1.2.4 ZEKE-PFI photoelectron spectroscopy

A new form of photoelectron spectroscopy, which relies on the pulsed-field ionisation of high molecular Rydberg states, has emerged in the last few years[21-25]. This technique is now generally referred to as zero electron kinetic energy pulse field ionisation(ZEKE-PFI) photoelectron spectroscopy. Since firstly reported by Müller-Dethlefs, Schlag and their co-workers[26], it has rapidly become an important tool for determining spectroscopic properties of ions and ionisation energies of molecules. This new technique typically offers one or more orders of magnitude improvement in energy resolution over conventional photoelectron spectroscopy.

The principle of the method is illustrated in figure 1-4 by one of the most practised variants for aromatic molecules. In the particular double-resonant variant shown, one laser is used to excite the molecule from its ground state to an excited

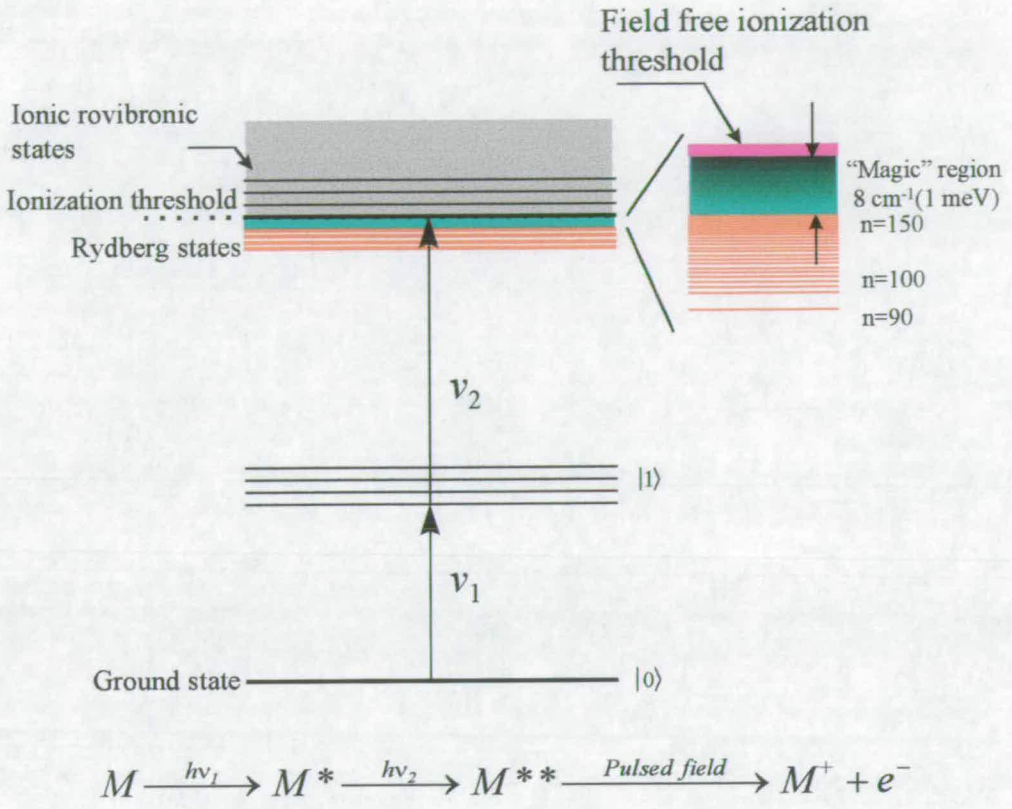

Figure 1-4: Two colour (1+1′) ZEKE-PFI: The first photon excites the molecule to an intermediate state, the second photon further excites the molecule to very high (n≥150) Rydberg states, then the molecule is ionised by using a delayed, pulsed electric field.

state (as an intermediate state). A second laser pulse is then used to further excite the molecule to a range of unresolved high Rydberg states (n≥150) in the region just below one of the energetic thresholds of the allowed quantum states of the ion on which those Rydberg states converge. Any energetic electrons (formed via an autoionisation process, for example) will quickly recoil from the interaction region. Then after a delay time ranging typically from several hundreds of nanoseconds to several microseconds, the ZEKE electrons can be detected by the field ionisation of the prepared Rydberg states by application of a pulsed electric field, which act as an extraction field as well. A ZEKE-PFI spectrum is obtained by measuring the multiphoton (or one-photon, if tunable vacuum ultraviolet radiation is available) excitation spectrum for forming photoelectrons with zero kinetic energy; precise energy eigenvalues are obtained because the spectral resolution is determined,

ultimately, by the bandwidth of the exciting laser. It was discovered by Reiser et al[27] that those high Rydberg states just below (a few wavenumbers) the ionisation threshold have unexpectedly long lifetimes (up to some ten microseconds) which are in completely disagreement with the simple n^3 scaling law. It is expected that these Rydberg states should only survive for 0.2-10 ns based on the n^3 scaling law (table 1-1).

The origin of the long lifetime of the ZEKE Rydberg states is still under heavy discussion, and different models have been invoked. There were initially two possible explanations for the increased lifetime of the Rydberg states: stabilisation of the Rydberg electrons by interactions with the rotating molecular core[28] and stabilisation of the electrons by interactions with stray electric fields and collisions with ions[29]. The latter one, which was first proposed by Chupka, developed by Bixon and Jortner[30] and confirmed experimentally by Vrakking and Lee[31-32] , has now been commonly accepted as the main mechanism responsible for the lifetime lengthening of high Rydberg states. In ZEKE-PFI spectroscopy[29], the high n Rydberg states initially populated by photoexcitation are low l states due to the strict dipole allowed selection rule of $\Delta l=\pm 1$. The low l states are relatively penetrating compared to the high l states and the lifetimes should follow the n^3 scaling law. However, by interacting with the stray fields and surrounding ions (and perhaps neutrals), these short lived, high n, low l Rydberg states involve into high n high l and m_l states. High l, m_l Rydberg states will experience a centrifugal potential on top of the Coulomb potential. The centrifugal potential barrier prevents Rydberg electrons having high l, m_l from interacting with the core anymore. A Rydberg electron in a high n, high l and m_l orbital is said to be non-penetrating and is considered in semiclassical terms as moving in a circular orbit. Non-penetrating orbitals are therefore extremely insensitive to decay processes such as autoionisation and predissociation.

The l, m_l mixing is only significant for Rydberg states having high n ($\geq$150) just below threshold due to their high densities[25]. For lower Rydberg states, however, the Rydberg electron still collides with the core, leading to intramolecular relaxation and particularly to predissociation into neutral products. This accounts

for the surprising observation that the bandwidths in ZEKE spectroscopy are generally not larger than 5-10 cm^{-1}, even when the height of the ionisation pulsed field is increased, since the lower Rydberg states have decayed in the waiting period (typically several microseconds) before the ionisation pulsed field is applied.

Under experimental conditions typical for ZEKE spectroscopy (electric field slew rates of 0.01-10 V/(cm·ns), principal quantum numbers $n>>100$), ionisation is expected to be predominantly diabatic[29]. Additional circumstances further enhance the probability of observing diabatic field ionisation[21]. Firstly, in molecular systems the penetrating low m_l Rydberg states that are most likely to undergo adiabatic field ionisation are precisely the states that are subject to a rapid decay by either autoionisation or predissociation. These states are unlikely to survive the delay time of several hundreds of nanoseconds separating photoexcitation and the pulsed ionising electric field in the ZEKE experiments. This delay time can thus be viewed as a filter that only leaves behind nonpenetrating, diabatically ionising states[33]. Secondly, as just described above, high Rydberg states are very sensitive to their environment and are likely to undergo an l, m_l mixing process as a consequence of interaction with neighbouring charged particles, or of interaction of the Rydberg system with an inhomogeneous electric field. These processes tend to reduce the penetrating character of the prepared states and favour diabatic field ionisation.

As pointed out first by Chupka[29], the field correction of the line position in the ZEKE spectra can be approximated as

$$\Delta E = -4\sqrt{F} \qquad (1.15)$$

E in cm^{-1}, F in V/cm. This has been commonly accepted and used by ZEKE spectroscopists to characterise the low-frequency onset of the lines observed in ZEKE-PFI spectra, and subsequently to determine the ionisation thresholds.

An important variant of the ZEKE-PFI technique was introduced by Zhu and Johnson[34] in 1991. They demonstrated that it was possible to selectively detect the ions, instead of the electrons, arising from field ionisation, by mass analysed threshold ionisation (MATI). This is more difficult, since discrimination against the prompt ions is more difficult than for prompt electrons because of their mass difference. In typical experiments, this may be accomplished by the introduction of a

small pre-pulsed electric field in the waiting period between photoexcitation and pulsed field ionisation (by a larger field). If the photon energy is scanned and the ions originating from field-ionisation are detected, the resulting spectra are equivalent to the ZEKE-PFI spectrum, but MATI clearly offers additional information about mass. This technique is advantageous when working with cluster or radical sources[25], as illustrated by the MATI spectrum of C_6H_6·Ar van der Waals complexes recorded by Krause and Neusser[46].

1.3 Ion-pair states and the spectroscopy of near-dissociation vibrational levels of an ion-pair state

1.3.1 Ion-pair states

The simplest definition of an ion-pair state[35] of a neutral diatomic molecule AB, for example, is one in which bond-breaking leads to the production of a pair of oppositely charged ions, A^++B^-, rather than two neutral fragments (figure1-1c). Because of electronic configurations, where at least one electron occupies an anti-bonding orbital, and the effect of the long-range Coulombic attraction between the ions, ion-pair states displays an unusual combination of properties. These states have long equilibrium bond lengths, R_e, small equilibrium vibrational frequencies, ω_e and large dissociation energies D_e.

Since ion-pair states correlate with the atomic ions A^++B^-, the asymptotic form of the potential energy curve V(R) is dominated by the Coulombic potential (1/R), in which R is the internuclear distance. As a consequence, the ion-pair state supports an infinite number of vibrational levels which converge to the dissociation limit. The correspondence between Rydberg state energy level spacings and ion-pair state vibrational energy level spacings has been noted previously by Asaro and Dalgarno[36] and Pan and Mies[37]. Similar to a Rydberg series converging to an

ionisation limit, the term values of these near dissociation vibrational levels could be expressed as[37]:

$$T_\upsilon = IE_{A^+ + B^-} - \frac{R}{(\upsilon - \delta)^2} \qquad \upsilon > 2000 \qquad (1.16)$$

$$R = \frac{1}{m_e}\frac{M_A^+ M_B^-}{M_A^+ + M_B^-} R_\infty \qquad (1.17)$$

Where υ is the vibrational quantum number and IE_{A^+, B^-} is the ion-pair formation threshold to which the vibrational levels converge. M_A^+ is the mass of the cation, and M_B^- is the mass of the anion. R_∞ is the Rydberg constant and R is the mass corrected Rydberg constant of the diatomic molecule.

1.3.2 Photoion-pair formation

In some cases, when sufficiently energetic photons interact with gaseous molecules, ion formation can arise from a quite different process — the formation of a positive ion-negative ion pair rather than a positive ion-electron pair as in photoionisation. For a diatomic molecule AB, for example,

$$AB + h\nu \longrightarrow A^+ + B^- \qquad (1.18)$$

This is commonly referred to as "photoion-pair formation". This process has been studied in some (~50) molecules and has been summarised in the extensive review by Berkowitz[11].

Photoion-pair formation normally involves photoexcitation to an electronically excited state, with subsequent evolution to a pair of ions. A number of experimental studies revealed that the initially excited states are of Rydberg character. For instance, the photoion-pair production spectrum of Cl_2 recorded by Berkowitz et al[38] showed a wealth of structure, which was assigned to vibrational levels of four Rydberg states. The vibrational intensity distribution within a Rydberg member does not depart substantially from the expected Franck-Condon distribution in absorption. More recently, the high resolution photoion-pair formation of I_2 and ICl have been studied by Donovan et al[39] using VUV laser radiation. They demonstrated that in the threshold region the photoion-pair

formation spectrum recorded in both positive and negative ion channels essentially reproduces the one-photon absorption spectrum for both molecules.

Direct excitation from the ground state to the ion-pair continuum seems to be rare or very weak. An exception is reported by Dehmer and Chupka[40]. They recorded a high resolution yield spectrum of O_2 photoion-pair formation in the vicinity of the energetic threshold. Steplike structure was readily apparent in the spectrum, and the energy differences between the half-rise positions of adjacent steps are equal to the rotational spacings in the ground state of O_2. They claimed that this indicated that, at threshold, ion-pairs were formed by direct dissociation. The relative intensities of the steps correspond to within about 20% to the theoretical Boltzmann distribution (78 °K). They thought that this gave additional evidence in support of a direct dissociation mechanism. They interpreted that the observation of direct dissociation with considerable intensity was caused by strong interaction between a Rydberg state and an ion-pair state resulting in an avoided crossing.

1.3.3 D.C. field-induced ion-pair formation from high vibrational ion-pair states

Since the lowering of the ionisation threshold described by Eq.1.7 is a purely electrostatic effect, independent of electron mass or reduced mass, one would expect that similar considerations apply to ion-pair formation. This was first confirmed experimentally by Pratt and co-workers[41] in 1992 who observed the lowering of the ion-pair formation threshold of H_2 under a DC field. Molecular hydrogen was excited from its ground electronic state to $\upsilon = 6$ of the $E,F\Sigma_g^+$ state by pumping Q(J=0) using two photons. A third tunable photon was then used to excite to the ion-pair threshold. Scanning this final photon energy, and monitoring H^- from ion-pair production, the energetic threshold for ion-pair formation was observed. By varying the DC field in the photoexcitation region, this threshold moves. The plot of the threshold energies as a function of the square root of the electric-fields shows that all experimental points fall on a perfect straight line, with a slope of 5.9±0.1 $cm^{-1}/(V/cm)^{1/2}$. By pumping Q(J=1), a slope of 5.7±0.1

$cm^{-1}/(V/cm)^{1/2}$ was obtained. Both values are very close to the expected value of 6.1 $cm^{-1}/(V/cm)^{1/2}$ from Eq.1.8.

1.3.4 Pulse field dissociation of near dissociation vibrational levels of an ion-pair state

A new technique, threshold ion-pair production spectroscopy (TIPPS), was developed by Martin and Hepburn[42-44] in 1997. The principle of this method is shown in figure 1-5. In TIPPS, as in MATI, dissociation of molecules into pair of

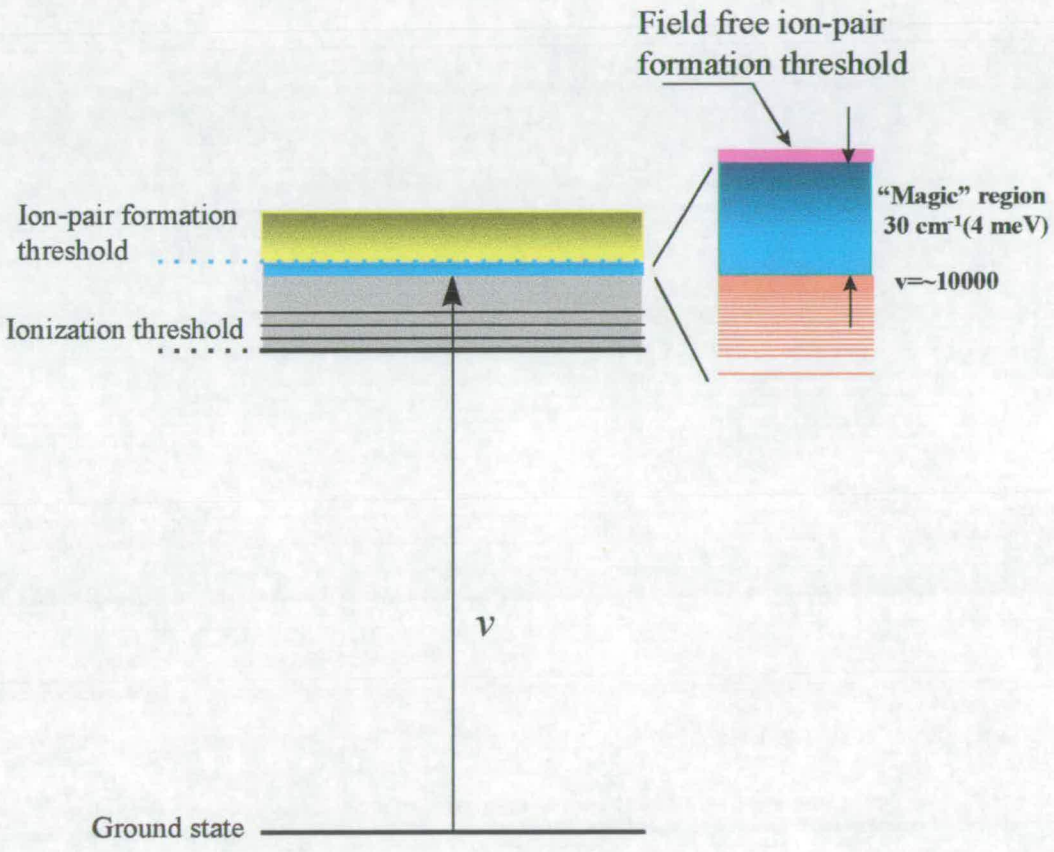

$$AB \xrightarrow{h\nu} AB^{*} \xrightarrow{\text{Pulsed field}} A^{+} + B^{-}$$

Figure 1-5: TIPPS process: One-photon is absorbed to excite the molecule to very high vibrational (v≥10000) ion-pair states, the molecule is then dissociated using a delayed pulsed electric field.

ions is achieved in three distinct steps. The molecule is first photoexcited into high vibrational levels of an ion-pair state using a VUV laser. Then a pre-pulsed electric field is applied after photoexcitation (200-300 ns delay) to discriminate against the prompt ions, pushing them out of the field of view. Finally a second pulsed field is applied at a delay of about 4 μs to dissociate the high υ ion-pair states. By scanning the VUV photon energy and collecting the ion signal due to this second pulse, the TIPPS spectrum is recorded.

It is expected that, analogous to the initially prepared high n low l Rydberg states in ZEKE and MATI experiments, the initially excited high υ low J ion-pair states which are susceptible to decay (which can happen very quickly) may be stabilised by external perturbations. Inhomogeneous electric fields (possibly due to surrounding ions), mix the J and M_J quantum number, allowing an initially excited low J state to evolve to a higher J, M_J state. The centrifugal barrier would then prevent the positive and negative ions from interacting thus making them long lived. The stabilisation effect due to surrounding ions was demonstrated by an experiment by Martin[44]. Two TIPPS spectra of HCl were recorded with VUV fluences that differ by a factor of 6. Varying the VUV fluence changes the ion density and thus the external perturbation. The signal on the red side (lower υ) of the TIPPS peak was enhanced with higher ion density thus indicating better stabilisation for lower υ ion-pair states which compete with autoionisation and predissociation.

The discrimination field, besides pushing away the prompt ions, also has the effect of depleting the highest υ ion-pair states. By recording spectra with several different discrimination fields, and observing the shifts in the blue edges of these peaks, the field-free dissociation threshold was extrapolated. This technique has been successfully applied to HF, HCI and O_2 molecules[42-44].

Measurement of an energetic threshold IE_{A^+, B^-} for splitting a diatomic molecule AB into a pair of ions, allows determination of the dissociation energy of the molecule $D_0(AB)$, if the electron affinity (EA(B)) and ionisation potential IE(A) of the fragments are known:

$$D_0(AB) = IE_{A^+, B^-} - IE(A) + EA(B) \qquad (1.19)$$

Almost all atomic ionisation potentials are known to accuracy better than 1 cm^{-1}, as are many electron affinities. Using this method, Martin and Hepburn[43] have got significantly improved neutral dissociation energy $D_0(HCl)$ over literature value. It seems promising that this technique could also be used for the determination of neutral dissociation energy of polyatomic molecules.

Alternatively, if the bond energy of a polyatomic molecule is better known, by measuring the ion-pair dissociation energy IE_{A^+, B^-}, the ionisation energy of the radicals could be determined.

There is no restriction in extending this technique to multiphoton excitation (figure 1-6). It is expected that compared to the single photon excitation used by

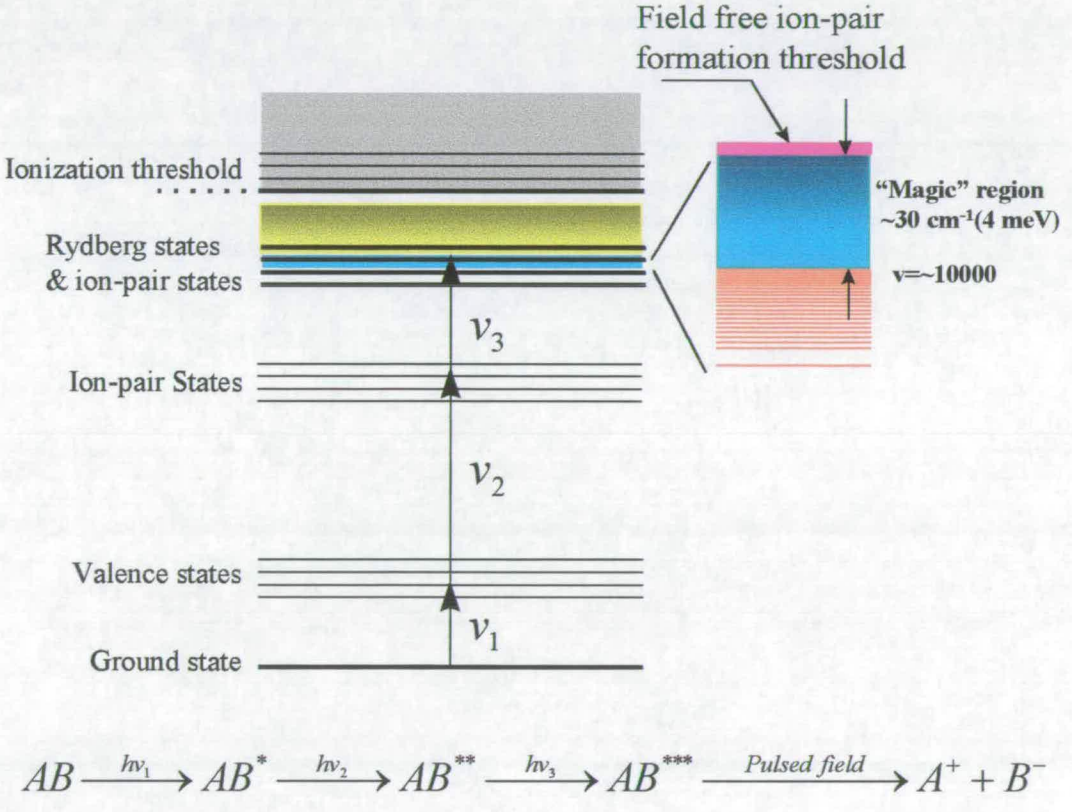

Figure 1-6: ZIKE-PFD process: Three-photons are sequentially absorbed to excite the molecule to very high vibrational (v≥10000) ion-pair states, and the molecule is then dissociated using a delayed pulsed electric field.

Martin and Hepburn, multiphoton excitation offers the opportunity of (i) widening the Franck-Condon window, (ii) accessing a wider range of electronic states that can act as doorway states to the final ion-pair states and (iii) avoiding the need to generate VUV photons and is thus less demanding. In this thesis, analogous to ZEKE-PFI, we will refer to this method as zero ion kinetic energy - pulse field dissociation (ZIKE-PFD) photoion-pair formation spectroscopy.

1.4 Reference

1. A.B.F. Duncan, *Rydberg Series in Atoms and Molecules*, New York, Academic, 1971.
2. M.B. Robin, *Higher Excited States of Polyatomic Molecules*, Vols. 1, 2, 3. New York, Academic, 1974.
3. R.L. Whetten, S.G. Grubb, C.E., Otis, A.C. Albrecht, and E.R. Grant, *J. Chem. Phys.* 1985, **82**, 1115.
4. R. Signorell and F. Merkt, in *The Role of Rydberg States in Spectroscopy and Photochemistry*, editor C. Sandorfy, Kluwer Academic Publishers, 1999, 479.
5. M.N.R. Ashfold and J.D. Howe, *Annu. Rev. Phys. Chem.* 1994, **45**, 57.
6. R.J. Donovan, T. Ridley, K.P. Lawley and P. Wilson, *Chem. Phys. Lett.* 1992, **196**, 173.
7. R.J. Donovan, J.G. Goode, K.P. Lawley, T. Ridley, and A.J. Yencha, *J. Phys. Chem.* 1994, **98**, 2236.
8. Z. Min, T. Ridley, K.P. Lawley and R.J. Donovan, *J. Photochem. Photobiol. Part A: Chem.* 1996, **100**, 9.
9. P.J. Jewsbury, T. Ridley, K.P. Lawley and R.J. Donovan, *J. Mol. Spectrosc.* 1993, **157**, 33.
10. R.J. Donovan, K.P. Lawley, Z. Min, T. Ridley and A.J. Yarwood, *Chem. Phys. Lett.* 1994, **226**, 525.
11. J. Berkowitz, in *VUV and Soft X-ray Photoionization*, Edited by U. Becker and D.A. Shirley. Plenum Press, New York, 1996, 263.

12. D.W. Turner, *Molecular photoelectron spectroscopy*, Wiley-Interscience, New York, 1970.

13. T. Baer and P.-M. Guyon, in *High Resolution* Laser *Photoionisation and Photoelectron Studies*, Edited by I. Powis, T. Baer and C.-Y. Ng, Chichester, Wiley, 1995.

14. R.F. Stebbings and F.B. Dunning, *Rydberg States of Atoms and Molecules*, Cambridge University Press, London, 1983.

15. M.A. Duncan, T.G. Dietz and R.E. Smalley, *J. Chem. Phys.* 1981, **75**, 2118.

16. S.T. Pratt, J.L. Dehmer and P.M. Dehmer, *J. Chem. Phys.* 1989, **90**, 2201.

17. E.D. Poliakoff, J.L. Dehmer, A.C. Parr and G.E. Leroi, *Chem. Phys. Lett.* 1984, **111**, 128.

18. F. Merkt, A. Osterwalder, R. Seiler, R. Signorell, H. Palm, H. Schmutz and R. Gunzinger, *J. Phys. B: At. Mol. Opt. Phys.* 1998, **31**, 1705.

19. T.F. Gallagher, *Rydberg atoms*, Cambridge University Press, London, 1994.

20. H.A. Bethe and E.E. Salpeter, *Quantum Mechanics of One- and Two-Electron Atoms*, Springer-Verlag, Berlin, 1957.

21. F. Merkt, *Annu. Rev. Phys. Chem.* 1997, **48**, 675.

22. K. Müller-Dethlefs and E.W. Schlag, *Annu. Rev. Phys. Chem.* 1991, **42**, 109.

23. I. Powis, T. Baer and C.-Y. Ng, eds. *High Resolution Laser Photoionisation and Photoelectron Studies*, Chichester, Wiley, 1995.

24. K. Müller-Dethlefs, E.W. Schlag, E. Grant, K. Wang and V. Mckoy, *Adv. Chem. Phys.* 1995, **90**, 1.

25. K. Müller-Dethlefs and E.W. Schlag, *Angew. Chem. Int. Ed.* 1998, **37**, 1346.

26. K. Müller-Dethlefs, M. Sander and E.W. Schlag, *Chem. Phys. Lett.* 1984, **112**, 291.

27. G. Reiser, W. Habenicht, K. Müller-Dethlefs and E.W. Schlag, *Chem. Phys. Lett.* 1998, **152**, 119.

28. D. Bahatt and U. Even, R. D. Levine, *J. Chem. Phys.* 1993, **98**, 1744.

29. W.A. Chupka, *J. Chem. Phys.* 1993, 98, 4520; *ibid.* 1993, **99**, 5800.

30. J. Jorter and M. Bixon, *J. Chem. Phys.* 1995, **102**, 5636.

31. M. J. J. Vrakking, Y. T. Lee, *J. Chem. Phys.* 1995, **102**, 8818; *ibid.* 1995, **102**, 8833;

32. M. J. J. Vrakking, *J. Chem. Phys.* 1996, **105**, 7336.

33. F. Merkt, *Phys. Rev. Lett.* 1996, **76**,3526.

34. L. Zhu and P. Johnson, *J. Chem. Phys.* 1991, **94**, 5769.

35. K.P. Lawley and R.J. Donovan, *J. Chem. Soc., Faraday Trans.* 1993, **89**, 1885.

36. C. Asaro and A. Dalgarno, *Chem. Phys. Lett.* 1963, **39**, 1872.

37. S. Pan and F.H. Mies, *J. Chem. Phys.* 1988, **89**, 3096.

38. J. Berkowitz, C.A. Mayhew and B. Ruscic, *Chem. Phys.*, 1988, **123**, 317.

39. R.J. Donovan, A.C. Flexen, K.P. Lawley and T. Ridley, to be published.

40. P.M. Dehmer and W.A. Chupka, *J. Chem. Phys.* 1975, **62**, 4525.

41. S.T. Pratt, E.F. McCormack, J.L. Dehmer and P.M. Dehmer, *Phys. Rev. Lett.* 1992, **68,** 584.

42. J.D.D. Martin and J.W. Hepburn, *Phys. Rev. Lett.*, **79**, 3154(1977).

43. J.D.D. Martin and J.W. Hepburn, *J. Chem. Phys.*, **109**, 8139(1998).

44. J.D.D. Martin, PhD thesis, University of Waterloo, 1998.

45. M.A.C. Nascimento, *Chem. Phys.* 1983, **74**, 51.

46. H. Krause and H.J. Neusser, *J. Chem. Phys.* 1992, **97**, 5923.

47. W.M. McClain and R.A. Harris, in *Excited States*, edited by E.C. Lim, Academic press, New York, 1977.

48. F. Metz, W.E. Howard, L. Wunsch, H.J. Neusser and E.W. Schlag, *Proc. R. Soc. London* 1978 **A363**, 381.

Chapter 2

Experimental

2.1 Introduction

A variety of spectroscopic techniques were used in this thesis and two separate experimental arrangements were used for the work. The REMPI apparatus consisted of an excimer pumped dye laser system, a molecular beam (unskimmed) and a time-of-flight spectrometer (without magnetic shielding). Most of the REMPI experiments and all of the ZIKE-PFD were performed on this machine. The ZEKE apparatus consisted of an Nd:YAG pumped dye laser system, a molecular beam (skimmed) and a time-of-flight spectrometer (with magnetic shielding). All ZEKE-PFI experiments were performed on this machine. This chapter also includes a description of two ways in which VUV radiation was generated, namely, from a laser induced plasma and from four-wave frequency-difference mixing in Kr.

2.2 The REMPI apparatus

2.2.1 Laser system

A schematic diagram of the laser system used for one-colour (2+1) REMPI experiments (solid part) and two-colour experiments (plus dotted part) is shown in figure 2-1. A XeCl excimer laser (Lambda Physik EMG 201 MSC) was used to pump two tunable dye lasers (Lambda Physik FL2002 and FL3002). The excimer laser produced intense (~400 mJ/pulse) ultraviolet (308 nm) short pulses (~25 ns). The typical operating repetition rate in our experiments was ~5 Hz. It could be used directly to pump all laser dyes from ultraviolet to visible (330-760 nm). For two-colour experiments, the excimer laser beam was split into two, using a 50/50 or 75/25 beam splitter as required, so as to pump two dye lasers simultaneously. These two dye lasers had a resolution of ~0.2 cm^{-1}.

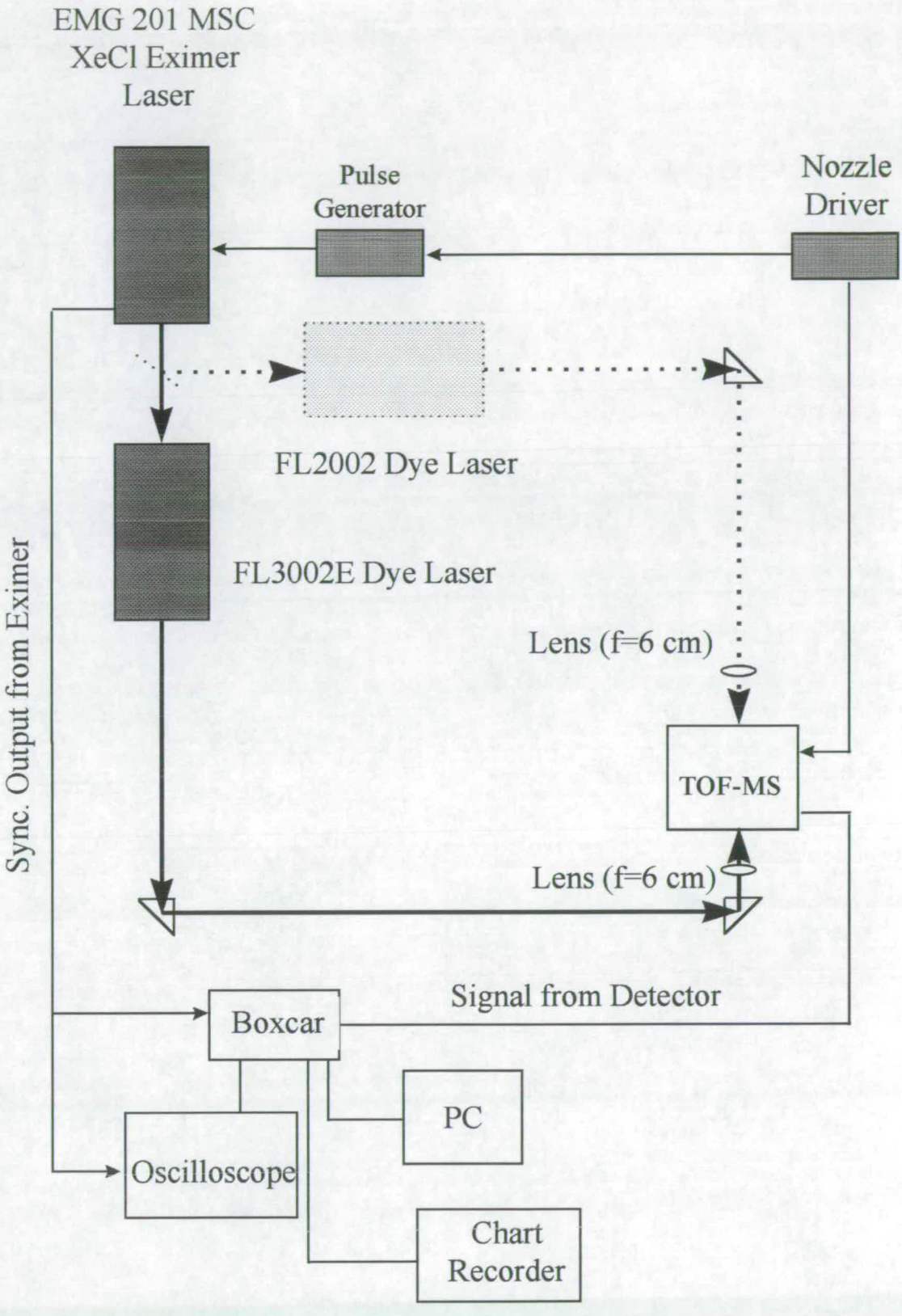

Figure 2-1: A schematic diagram of the laser system used for one-colour (2+1) REMPI experiments (solid part) and two-colour experiments (plus dotted part)

Radiation below 330 nm was achieved by frequency doubling of the output from the dye lasers using a series of KD*P (KH_2PO_4) and BBO (Beta-Barium Borate) crystals. The K*DP crystals could be used to produce laser light in the wavelength range of 265-335 nm from the fundamental output (530-670 nm) of the dye laser. The BBO Type I crystal could be used to produce 220-315 nm radiation while the BBO type II can be used to produce even shorter wavelengths (205-222 nm). The frequency doubled light was separated from the fundamental by using a Pellin Broca prismatic beam separator. Alternatively, the dye fundamental output, if it is >500 nm, could be removed after the doubling crystals using a colour filter (UG5). The laser beam(s) was focused into the ionisation chamber using a 6 cm focal length lens. The linearly and circularly polarised light were produced by a Soleil Babinet polariser.

2.2.2 The REMPI spectrometer

A schematic diagram of the REMPI spectrometer which consisted of a vacuum system, a molecular beam and a time-of-flight mass spectrometer is shown in figure 2-2. The vacuum system consisted of two differentially pumped vacuum chambers. The ionisation chamber, which contained a pulsed nozzle and ion extraction optics, was pumped by a diffusion pump with a liquid nitrogen trap backed by a Maruyama Type 150 rotary pump. The smaller chamber, which housed the time-of-flight tube and the microchannel plate detector, was pumped independently using a turbomolecular pump (Turbotronik NT150/360) backed by a Maruyama 150 rotary pump. The molecular beam was generated by pulsing a carrier gas and sample through a nozzle (General Valve, 250 μm diameter orifice), into the ionisation region of a linear time-of-flight mass spectrometer. The typical repetition of the pulsed nozzle was ~5Hz with a pulse duration of ~180-300 μs. The pressure in both chambers were monitored using Pirani and Penning gauges (Edwards). Under operating conditions the pressure in the ionisation chamber could reach 8×10^{-6} torr whereas the pressure in the time-of-flight chamber was $\leq 2 \times 10^{-6}$ torr.

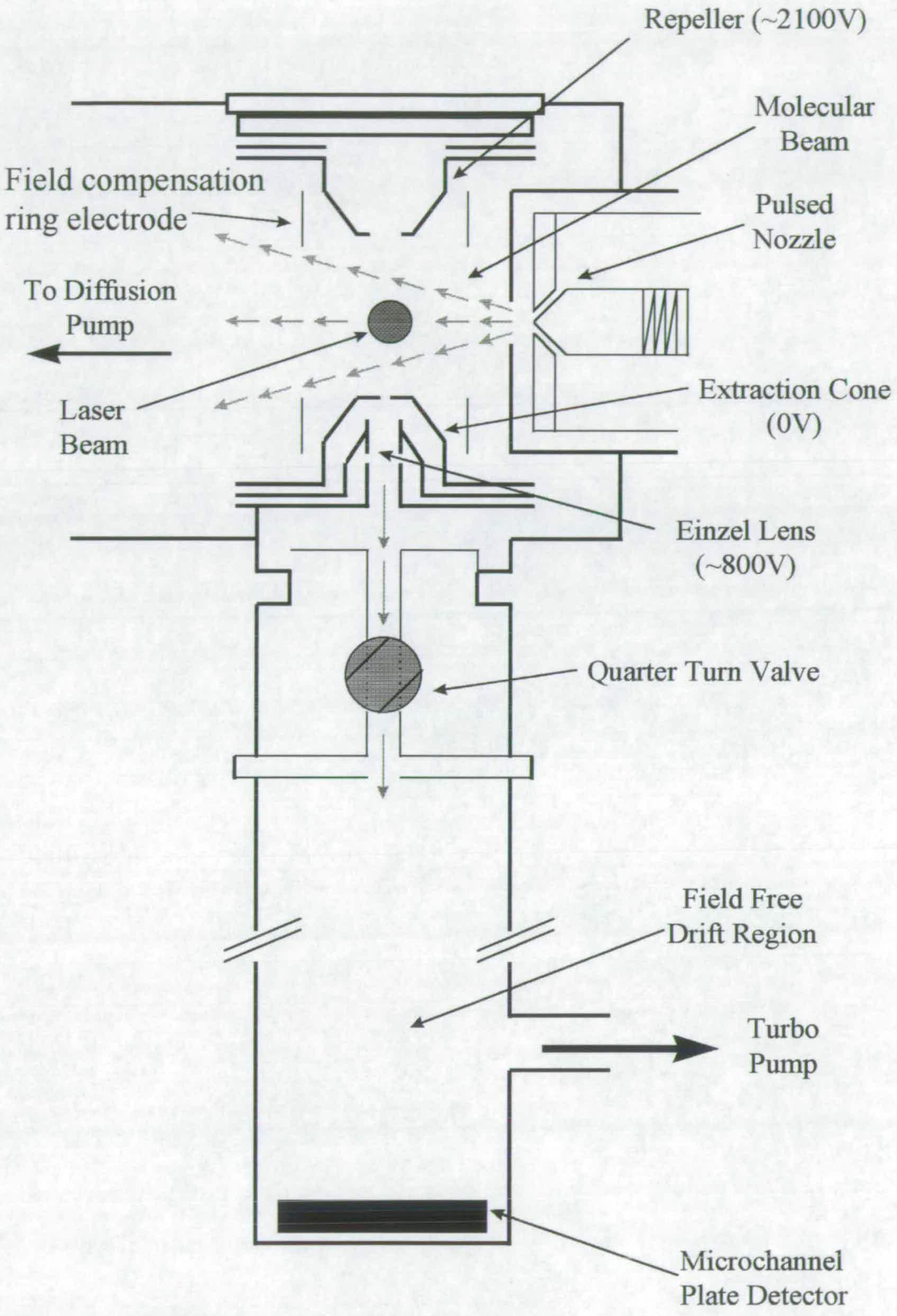

Figure 2-2: A schematic diagram of the REMPI spectrometer

The ion extraction optics consisted of two conical electrodes with flat bottoms which were opposite to each other. Two ring electrodes applied with appropriate voltages were used to compensate for the inhomogeneousity of the electric fields in the interaction region. The lower electrode was held at earth and this defines the start of the time-of-flight mass spectrometer (~52 cm). For REMPI experiments, 2.1 kV was applied to the upper electrode. The two electrodes were separated by 1.6 cm such that the molecular beam and laser beams intersected perpendicularly midway between these two electrodes. The ions were extracted and accelerated perpendicularly to these two beams down to the flight tube and then collimated by an Einzel lens immediately following the extraction optics. Typically, 700-900 V was applied to the Einzel lens.

After travelling down the flight tube, the ions hit the front of the microchannel plate detector and produce secondary electrons, being multiplied by the dual multichannel plates (MCP). A maximum of 5 kV was applied to the resistant distributor circuit for the MCP. The maximum voltage applied to each plate was thus about 1 kV. The multiplied electron signal was collected by an anode, and generates a voltage across a 50 Ω resistor. This unamplified signal was monitored using a digital oscilloscope (LeCroy 9344C) and processed using a Stanford Research Systems SRS250 boxcar integrator. The resulting spectra were recorded on a PC and a chart recorder.

The timing of the experiment was controlled by the nozzle driver. The output pulse from the nozzle driver triggered a Farnell pulse generator. The excimer laser was then triggered externally by the output from Farnell. The synchronous output from the excimer was used to trigger the oscilloscope and boxcar integrators. The overlap between the gas pulse and laser pulse was adjusted by varying the time delay of the trigger pulse for the excimer laser from the Farnell pulse generator.

2.3 The ZEKE apparatus

2.3.1 Laser system

A schematic diagram of the laser system used for two-colour ZEKE-PFI experiments (for example, (2+1′) ZEKE-PFI of CF_3I) is shown in figure 2-3. A Q-switched Nd:YAG laser was used to pump two tunable dye lasers (Quanta Ray PDL-2 and PDL-3). The Nd:YAG laser (Spectra Physics, DCR2A) was Q-switched to produce short (≈ 8 ns), intense (≈ 1000 mJ/pulse) pulses in the near-infrared (λ_{YAG} = 1.064 μm) with a repetition rate of 10 Hz. This radiation was frequency doubled in a non-linear crystal to produce the second harmonic ($\lambda_{YAG}/2$ = 532 nm) light. The 532 nm light could be used to pump a dye laser and/or sum-mixed with the residual infra-red to generate the third harmonic ($\lambda_{YAG}/3$ = 355 nm). Laser dyes suitable for operation below 542 nm had to be pumped with the 355 nm light. However, at wavelengths greater than 542 nm, pumping with 532 nm was normally used, since it was usually more efficient than pumping with 355 nm radiation. For two-colour experiments, the 532 nm light was split into two beams using a beam splitter (75/25 or 50/50) to pump both of the dye lasers. In some two colour experiments, both 532 and 355 nm light were needed, each pumping one dye laser, respectively. The PDL-2 dye laser had a resolution of ~0.5 cm^{-1} whereas the PDL-3 dye laser had a resolution of ~0.1 cm^{-1}.

The frequency doubling of the output from the dye lasers was achieved using either KD*P or BBO crystals. The KD*P crystals were mounted within a wavelength extender module (Quanta-Ray WEX) which allowed automatic tracking of the crystal that produced the dye second harmonic while the dye laser scanned over its wavelength range. The dye lasers were scanned using a home built stepper module which was triggered by the data collection software installed on a PC. The BBO crystal was in a home built mount and the dye second harmonic was manually tracked by monitoring a small part(~5%) of the ultraviolet out using a photodiode

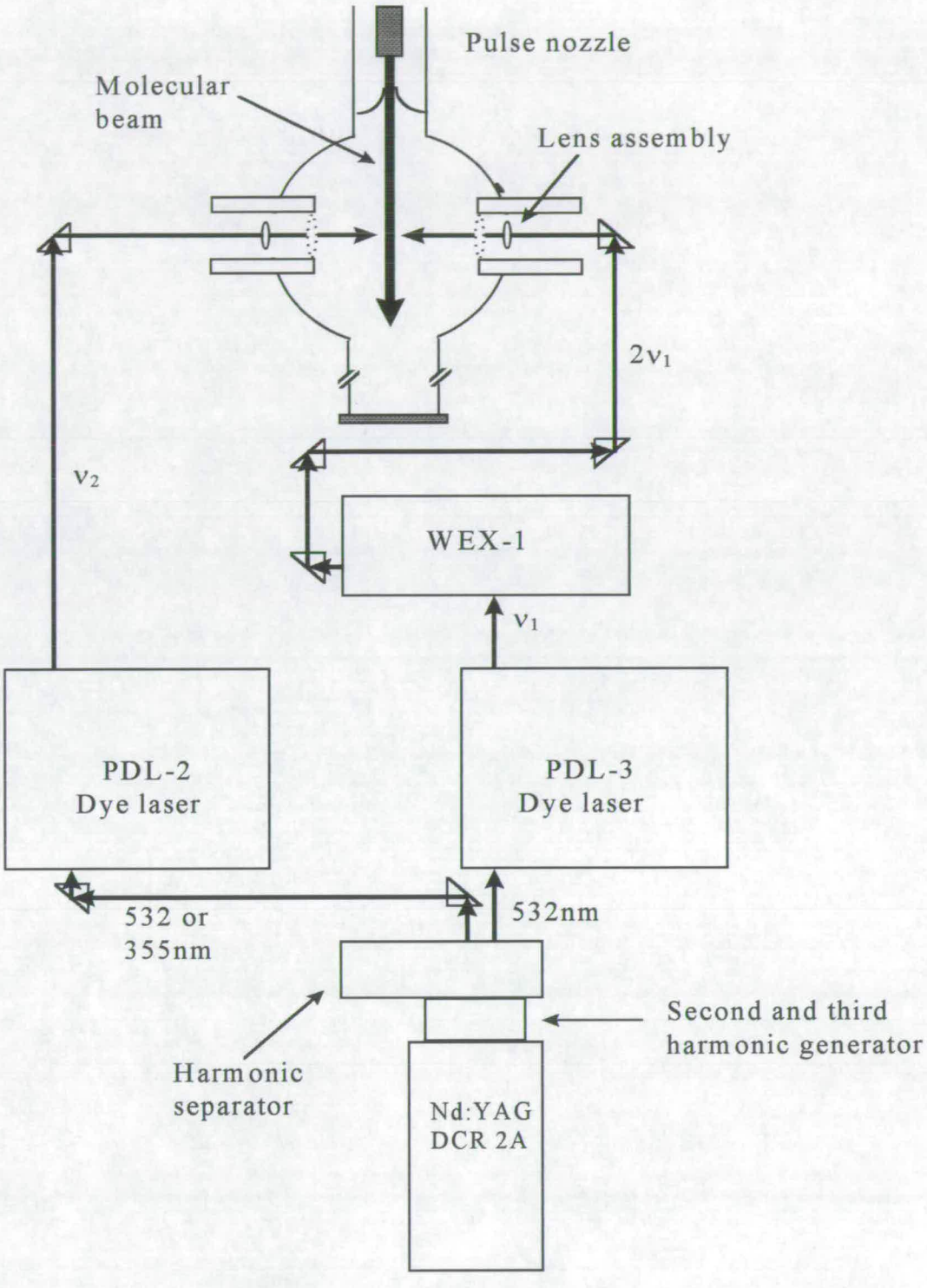

Figure 2-3: A schematic diagram of the laser system used for two-colour ZEKE-PFI experiments

and a oscilloscope. Colour filters were used to remove the dye fundamental output after the doubling crystals for the red and green dyes whereas a Pellin Broca prismatic beam separator was used to separate the fundamental and the second harmonic of the blue and near ultraviolet dyes. The linearly and circularly polarised light were also produced by a Soleil Babinet polariser. For REMPI and ZEKE-PFI experiments for CF_3I, the counter-propagating laser beams were focused into the interaction region in the vacuum chamber by two lenses which also formed the entrance windows, one of them has the appropriate focal length (~8 cm) for ultraviolet light and the other for visible. In order to have the flexibility to manipulate the focusing conditions, the system was modified. Two plain quartz windows were installed and the lenses were controlled by an X-Y-Z three-dimensional translator outside the vacuum chamber. This was used for coherent two-photon ZEKE-PFI experiments of benzenes and the (2+1) REMPI experiments of *p*- and *o*-difluorobenzenes.

2.3.2 The ZEKE Spectrometer

A schematic diagram of the ZEKE spectrometer which consisted of a vacuum system, a molecular beam and a time-of-flight mass spectrometer is shown in figure 2-4. The vacuum system consisted of two differentially pumped vacuum chambers. The main chamber, which contained a time-of-flight spectrometer, was pumped by a Balzers TPU 510S turbomolecular pump (500 ls^{-1}) backed by a Maruyama CP-80 rotary pump. The smaller chamber, which housed the pulsed nozzle, was pumped independently using an Edwards 160-700 Diffusion pump (700 ls^{-1}) with a liquid nitrogen trap. The diffusion pump was backed by an Edwards ED200 rotary pump.

The molecular beam was generated by pulsing a carrier gas and sample through a nozzle (General Valve, aperture 300 μm). The supersonic expansion jet was skimmed using a Beam Dynamics skimmer (diameter 0.49 mm) which was positioned ~4 cm from the aperture of the nozzle to produce a narrowed collimated molecular beam. The alignment of the nozzle and the skimmer was achieved by

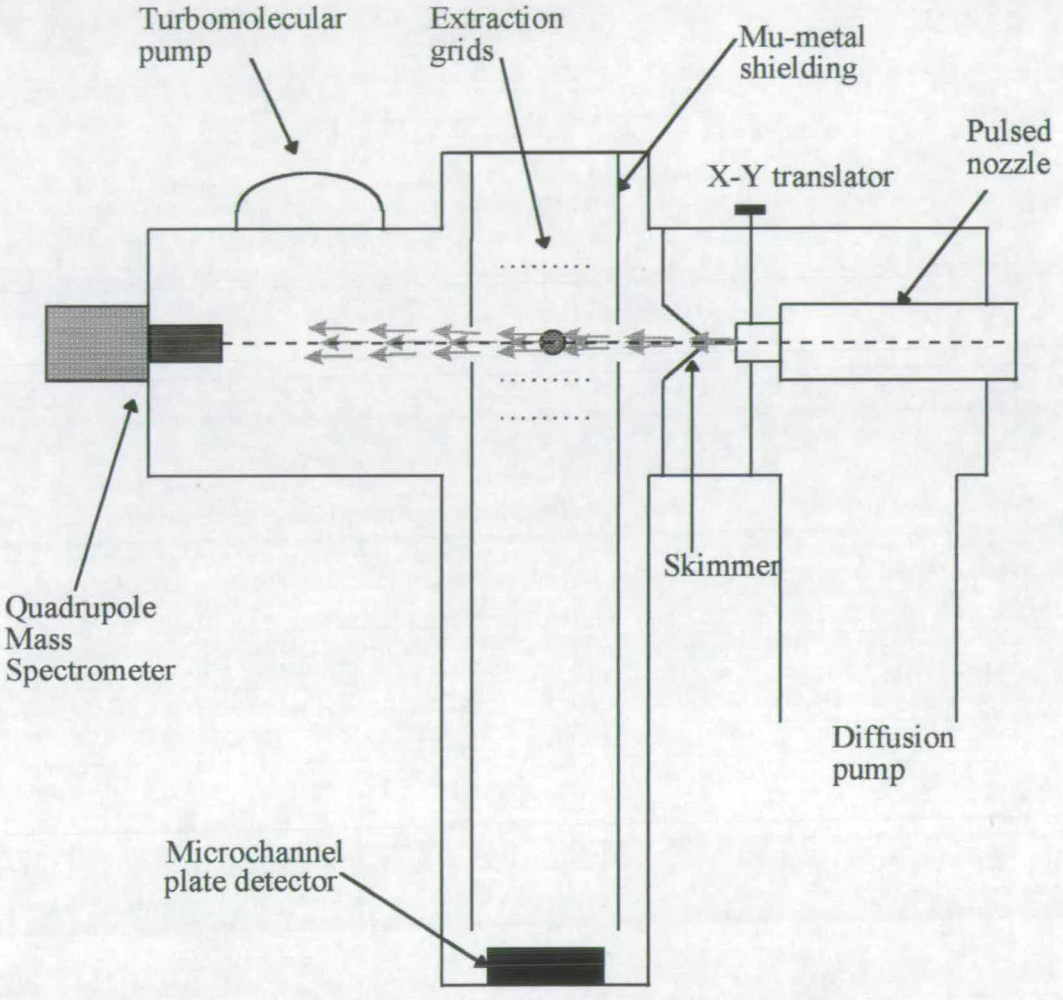

Figure2-4: A schematic diagram of the ZEKE spectrometer

varying the nozzle position with an X-Y translator and monitoring the molecular beam on an inline VG SX200quadruple mass spectrometer. The repetition rate of the pulsed valve was 10 Hz with a pulse duration of 300 μs. Under operating conditions the pressure in the expansion chamber could reach 5×10^{-6} torr whereas the pressure in the main chamber only reached 4×10^{-7} torr (from a pressure of 2.3 $\times 10^{-7}$ torr with the pulsed expansion being switched off). The pressure in both chambers was monitored using Pirani and Penning gauges (Edwards).

The time-of-flight mass spectrometer, including the ion/electron collection optics, a free-drift flight tube and a dual microchannel plate (Galileo) detector, was enclosed in a single layer of 2 mm thick mu-metal magnetic shielding. The ion/electron collection optics consisted of three parallel copper mesh grids. The bottom grid was held at earth and this defined the start of the field-free drift region (40 cm) for the time-of-flight spectrometer. The top and middle grids were separated by 3 cm such that the molecular beam and the laser beams intersected perpendicularly midway between these two grids. The ions or electrons were extracted perpendicularly down the flight tube to the detector. For ZEKE-PFI experiments, the pulsed field, which was used to ionise the high *n* Rydberg states and to send the ZEKE electrons to the detector, was applied to the top grid. The pulsed field applied to the top plate was supplied by a home built, variable output, pulsed voltage unit with an output range of 0.6 V to 21 V. The small pulse field, which was used for discrimination of fast electrons (non-zero kinetic energy electrons), was applied to the middle grids. This was supplied by a Farnell pulse generator with a range of 30 mV to 10 V. The spectrometer could also operate on the ion detection mode, for REMPI and ion-pair formation experiments. In this case, 2.5 kV was applied to the top grid to extract the ions and the middle grid was simply grounded.

After travelling down the flight tube, the electrons (ZEKE) or ions (REMPI) hit the front of the microchannel plate detector and produced secondary electrons, being multiplied by the dual multichannel plates. The multiplied electron signal was collected by an anode, and generated a voltage across a 50 Ω resistor. This unamplified signal was monitored using a digital oscilloscope (LeCroy 9310) and

processed using a Stanford Research Systems SRS250 boxcar integrator. The resulting spectra were recorded on a PC and a chart recorder.

The timing of the experiment was controlled by the Q-switch output of the Nd:YAG laser which was used to trigger the oscilloscope, a four-channel EG&G digital delay pulse generator and boxcar integrators. The timing of the pulsed jet and the pulsed electric fields was then determined by the output from the EG&G digital delay pulse generator. The overlap between the gas pulse and laser pulse was adjusted by varying the time delay of the trigger pulse for the nozzle from the (EG&G) pulse generator.

2.4 ZIKE-PFD experiments

All ZIKE-PFD experiments in this thesis were performed on the REMPI apparatus therefore only additional details concerning ZIKE-PFD experiments will be given in this section.

2.4.1 Laser system

A schematic diagram of laser arrangements for three-colour triple-resonance enhanced multiphoton ion-pair formation experiments is shown in figure 2-5. The same laser system as described in section 2.2.1 was used. In order to achieve three colours using two dye lasers, Coumarin 153 dye was used in the FL3002 dye laser to produce visible photons which were then frequency doubled. No beam separator was used and thus both the visible light and the frequency doubled beam were overlapped and introduced into the chamber. The other dye laser, FL2002, provides the third photon.

2.4.2 Arrangements for pulse field experiments

The excimer laser was also triggered by the nozzle driver via the Farnell pulse generator. In order to eliminate the instability of the TOF signal due to the jitter of the excimer laser synchronous output, a photodiode signal was used to

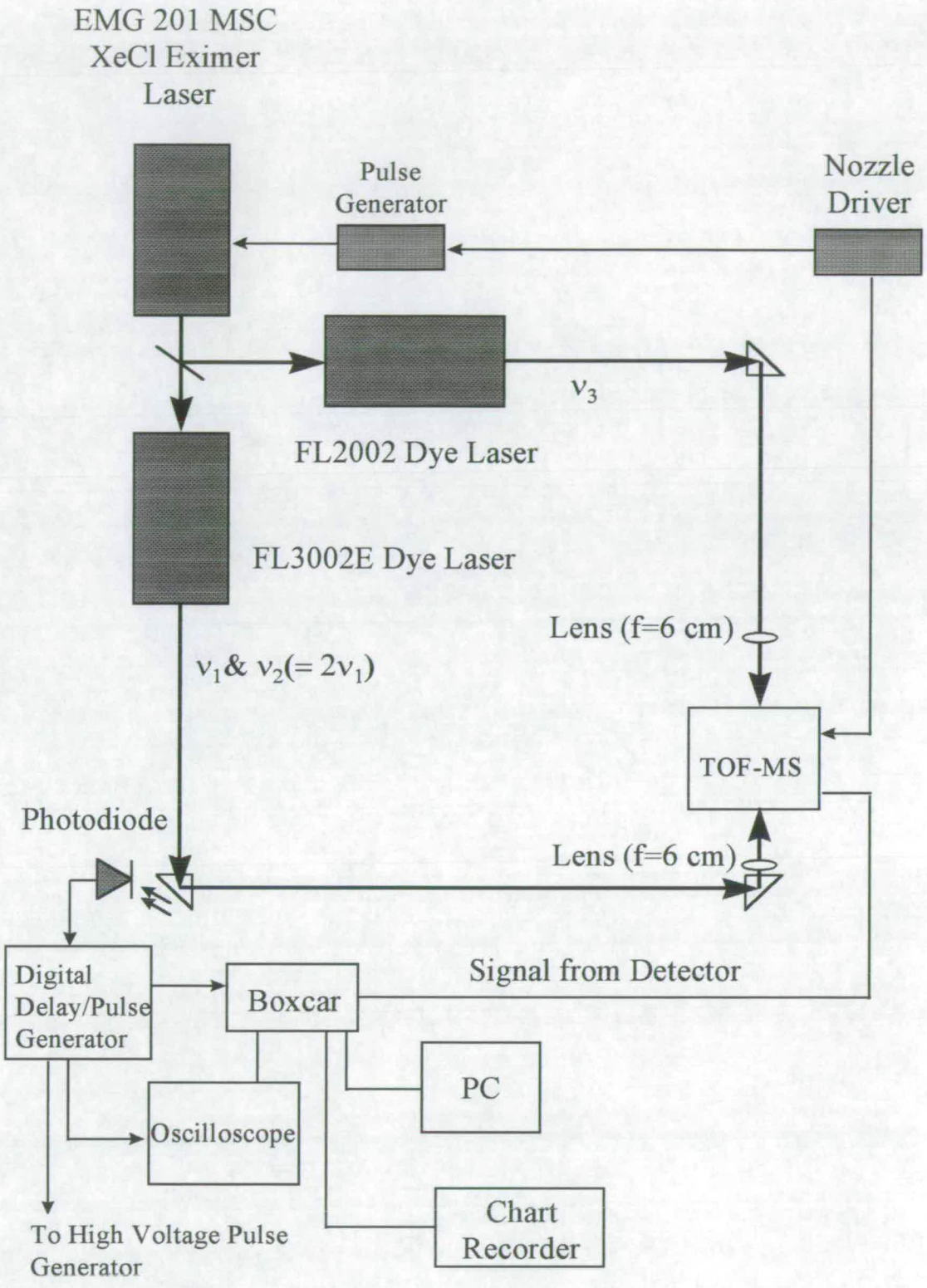

Figure 2-5: A schematic diagram of the laser arrangement for three-colour triple-resonance enhanced multiphoton ion-pair formation experiments

trigger the oscilloscope, a four-channel digital delay/pulse generator (Stanford Research System) and the boxcar integrators. The timing of the pulsed electric fields was then determined by the output from the digital delay/pulse generator. For ZIKE-PFD experiments, the pulsed field, which was used to dissociate the high υ ion-pair states and to send the ZIKE ions to the detector, was applied to the upper electrode. The pulsed field applied to the top plate was supplied by a bipolar fast high voltage transistor switch (GHTS60A, Behlke Electronic), with variable output up to 6 kV. This bipolar switch could provide positive or negative high voltage pulses. The high voltage pulse can be floated on a given (bias) voltage which was very useful for ZIKE experiments. For negative ion collection, a negative high voltage pulse was needed. Figure 2-6 illustrates the negative HV pulse output obtained from the bipolar fast high voltage transistor switch, when connecting –HV input to –2 kV and +HV to earth, or a negative bias voltage ($-\Delta$), or a positive bias voltage(Δ), respectively. The small bias voltage was used to move the prompt ions before the high voltage pulse. For positive ion detection, a positive HV pulse output was obtained from the bipolar fast high voltage transistor switch, by connecting +HV input to +2 kV and –HV to earth, or a positive bias voltage (Δ), or a negative bias voltage($-\Delta$), respectively. Figure 2-7 shows an example of the high voltage pulse when connecting the –HV of the switch to –2 kV and the +HV to earth, which was measured using a high voltage probe on a LeCroy oscilloscope (9344C).

2.5 VUV radiation from a laser induced plasma

2.5.1 The laser plasma source

The plasma was generated (in Rutherford-Appleton laboratory (RAL)) by interaction of an 8-pulse train picosecond (7ps) excimer laser system with a copper target. The high repetition rate picosecond KrF laser system has been described in detail elsewhere and only a brief outline will be given here[1]. A Spectra Physics-375 synchronously pumped mode locked dye laser operating at 82 MHz produced a 7 ps

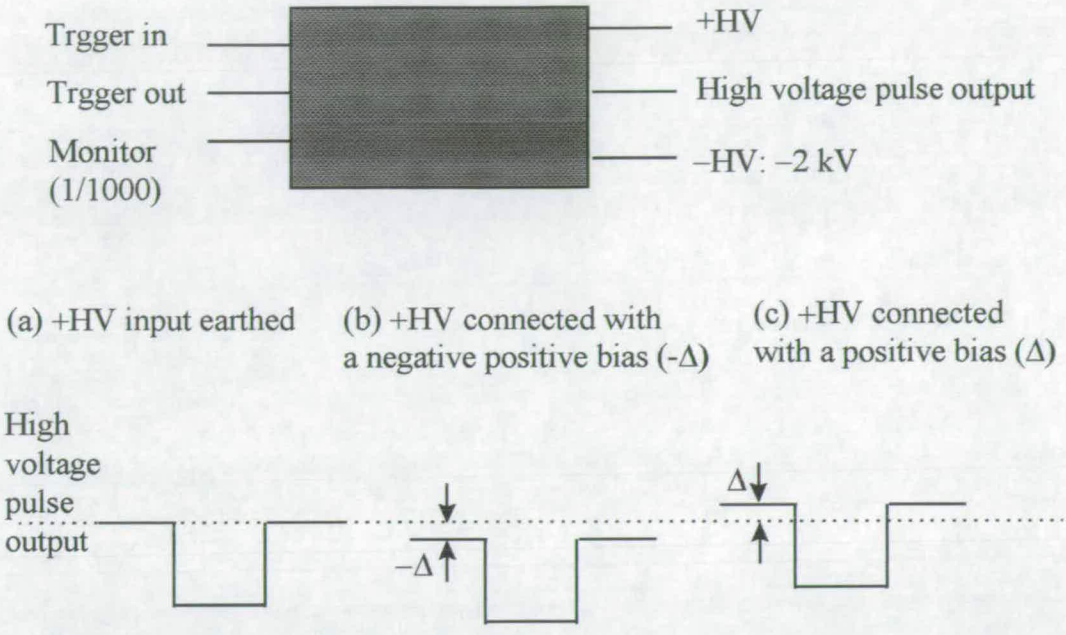

Figure 2-6: Negative HV pulse output from the bipolar fast high voltage transistor switch. when connecting –HV input to –2 kV and +HV to (a) earth; (b) a negative bias voltage (-Δ); (c) a positive bias voltage(Δ).

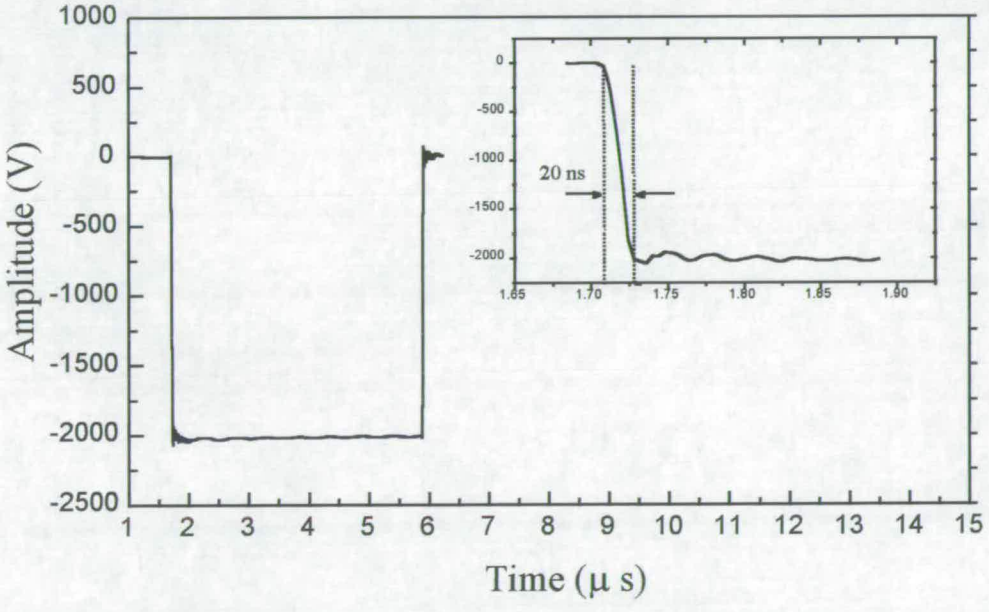

Figure 2-7: Negative high voltage pulse when connecting the –HV of the switch to -2016 V and the +HV to earth measured by using a HV probe on a LeCroy oscilloscope..

pulse at 746 nm which was then converted to the third harmonic at 248 nm. This laser pulse passed through a multiplexer to form an 8-pulse train of picosecond pulses separated by 1.85ns. This pulse train was then amplified by a double pass in a KrF excimer laser operating at 248 nm, each train having an average energy of 120 mJ (15x8 mJ). The high power density on the target resulted in a plasma temperature at $>10^6$ K and a plasma particle density of about 1×10^{22} cm^{-3}. The combination of a high temperature and a high particle density resulted in an extremely bright continuum emission.

2.5.2 The VUV radiation and detection electronics

A schematic diagram of the experimental set-up used for characterisation of VUV radiation is shown in figure 2-8. The 248 nm laser beam was focused on the continuously moving copper tape target located in the vacuum chamber. The spot diameter on the tape target was estimated about to be 25 μm. The VUV radiation formed from the laser plasmas was collected and focused by a multichannel plate to the entrance slit of a 1/4 meter spectrograph, with a 600 lines/mm concave grating. The radiation was then introduced into the parallel-plates ionisation chamber through which the gaseous molecules to be studied were flowed. The ionisation chamber was separated from the spectrograph by a MgF_2 window. The two plates were 23x140 mm in size with an separation of 25 mm. One of the plate was earthed. The other one was connected to a charge-sensitive preamplifier with a capacitive feedback through a 1-pF capacitor. The signal from the preamplifier was a fast risetime voltage step with an exponential return to the baseline with a time constant of 100 μs. The voltage was given by $\frac{Q}{C}$, where Q is the charge produced by the photoionisation or/and ion-pair formation and C is the capacity of the feedback capacitor (1-pF). Thus if all photons were absorbed by the gas filled in the ionisation chamber, the photon number of the VUV radiation could be obtained. The signal was measured using a LeCroy oscilloscope (9310) and averaged for 100 laser shots for each (VUV) wavelength (by tuning the grating of the spectrograph).

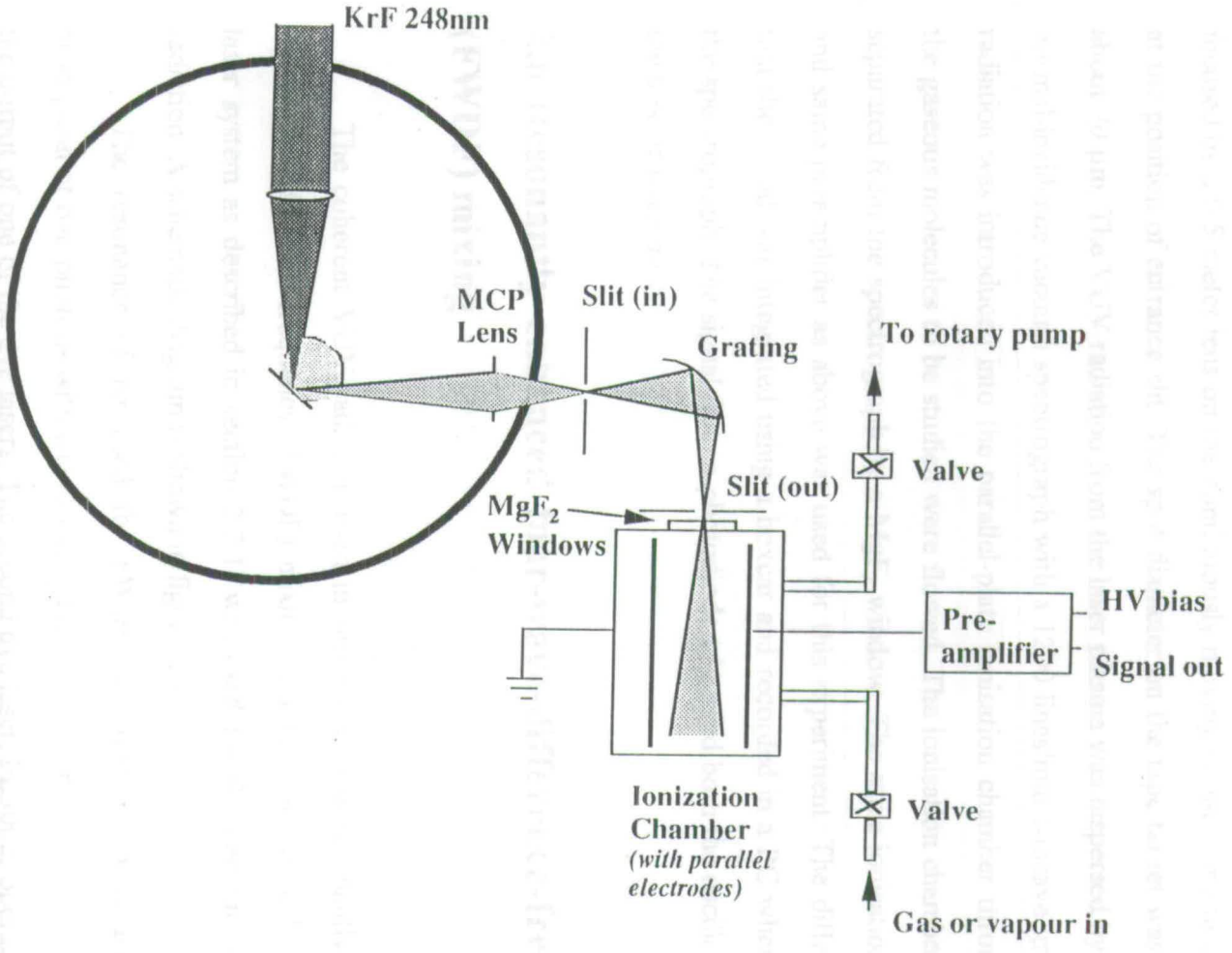

Figure 2-8:A schematic diagram of the experimental set-up used for characterisation of VUV radiation from laser induced plasmas

2.5.3 Higher resolution output

A 1-meter spectrograph with a 1200 lines/mm concave grating was used to improve the spectral resolution. A schematic diagram of the experimental set-up to improve the spectral resolution is shown in figure 2-9. The laser system for the plasma generation was the same as above. The 248 nm laser beam was passed through a 1-meter normal-incidence vacuum spectrograph via an end window and focused by a 0.5 meter lens on the continuously moving copper tape target located at the position of entrance slit. The spot diameter on the tape target was estimated about 70 μm. The VUV radiation from the laser plasma was dispersed by a 1-meter normal-incidence vacuum spectrograph with a 1200 lines/mm concave grating. The radiation was introduced into the parallel-plate ionisation chamber through which the gaseous molecules to be studied were flowed. The ionisation chamber was also separated from the spectrograph by a MgF_2 window. The same ionisation chamber and same preamplifier as above was used for this experiment. The difference was that the signal was integrated using a boxcar and recorded in a PC when scanning the spectrograph. The signal from a photodiode triggered both the oscilloscope and the boxcar integrator.

2.6 Resonantly enhanced four-wave-difference-frequency (FWDF) mixing

The coherent VUV radiation used in this thesis was resonantly enhanced four-wave-difference-frequency (FWDF) mixing in a krypton gas cell. The same laser system as described in section 2.2.1, was used for the generation of VUV radiation. A schematic diagram is shown in figure 2-10.

The resonance of Kr used for FWDF at 94094cm^{-1} was accessed by absorption of two photons with wavelength of λ_1=212.55 nm by frequency doubling the output of one of the dye lasers. The second dye laser, FL3002, operating with a range of dyes in the visible frequency range, provided the third photon (ν_3). The VUV photon energy produced by FWFD was then decided by $\nu_{VUV}=2\nu_1-\nu_3$. Two

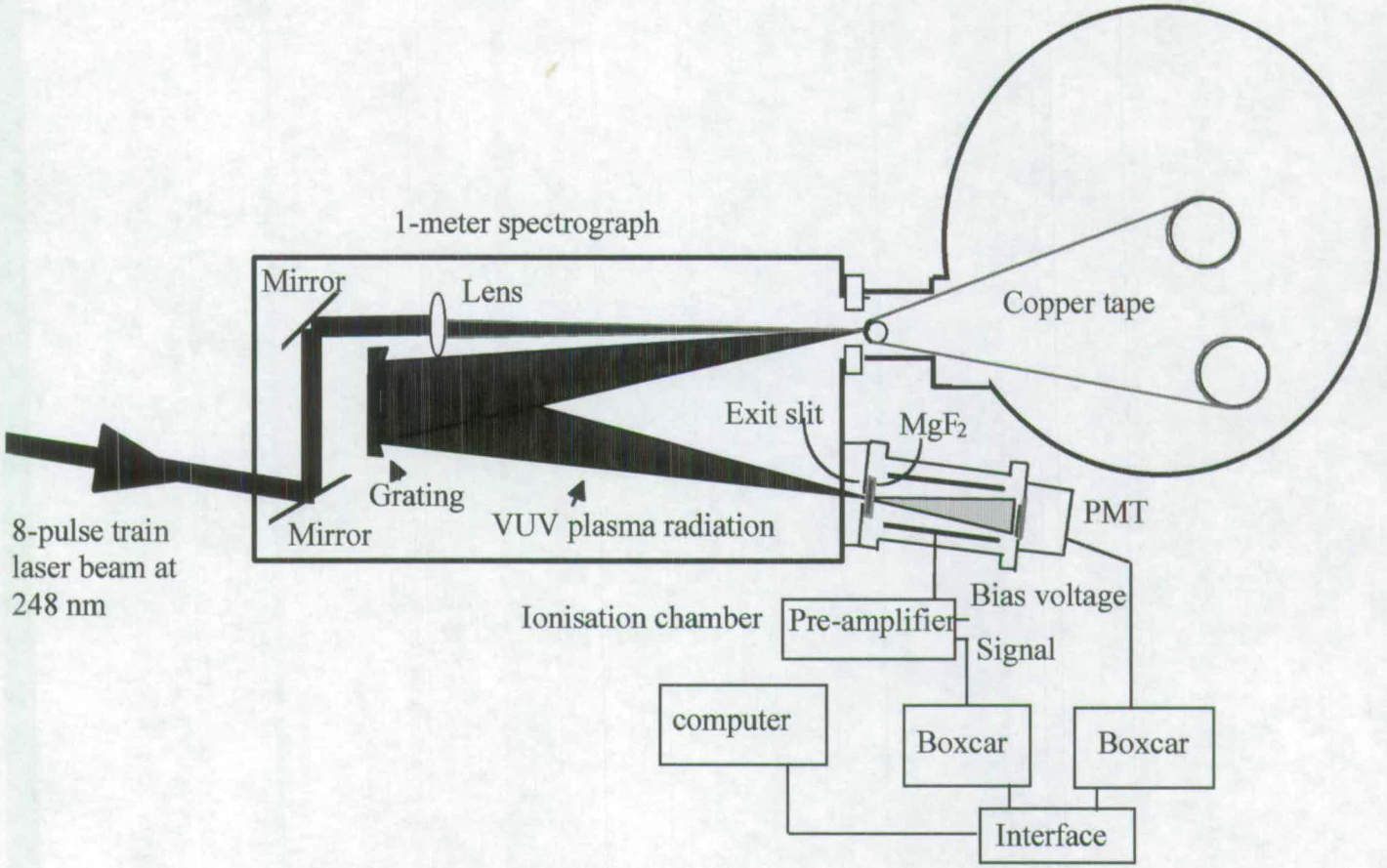

Figure 2-9: A schematic diagram of the experimental set-up for photoionisation and photoion-pair study using VUV radiation from laser-induced plasma.

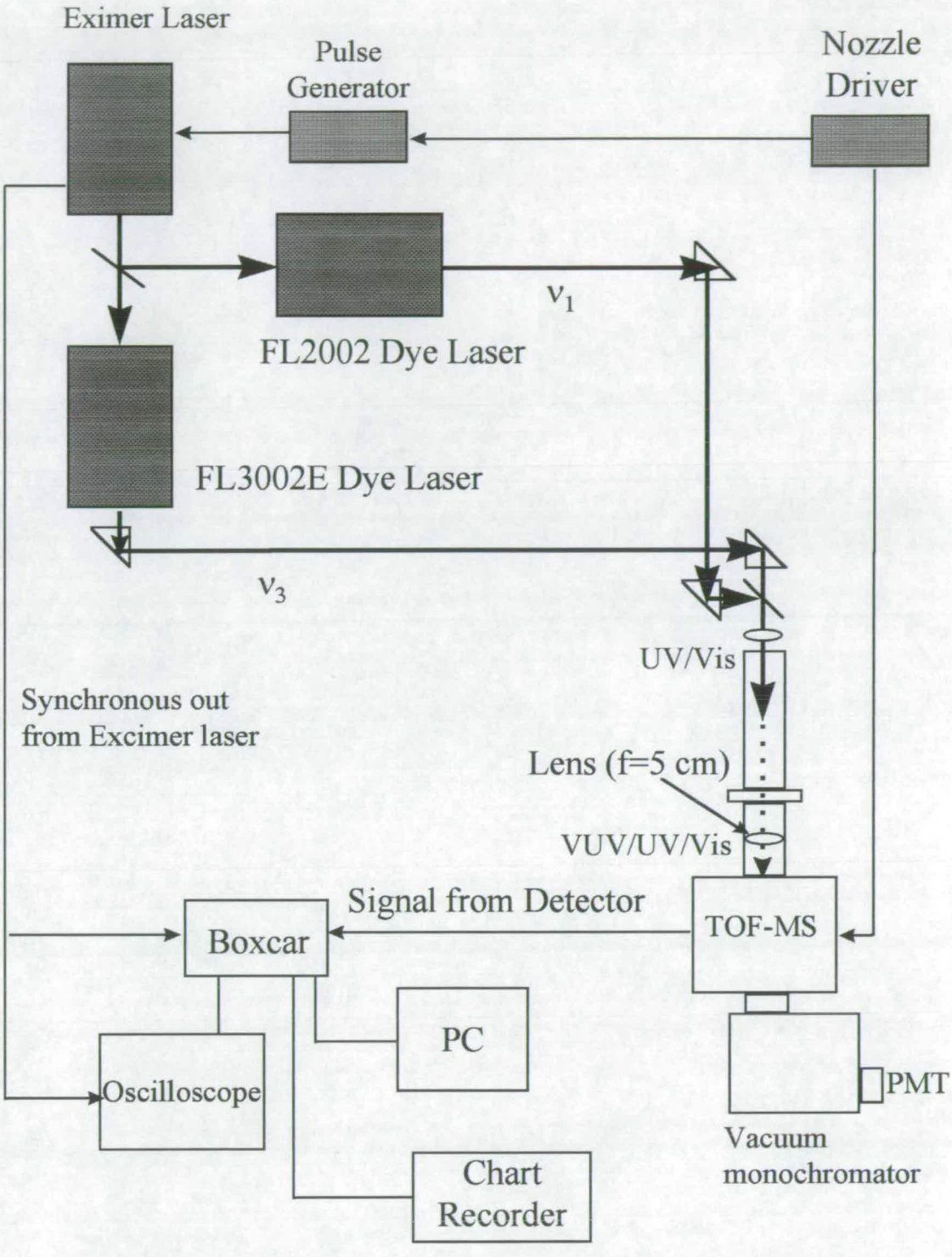

Figure 2-10: A schematic diagram of the experimental arrangement for VUV generation using FWFD and one-photon ion-pair formation study of CH_3Br.

beams were collimated and focused roughly in the centre of the Kr gas cell with a 20 cm focal-length lens. The Kr gas cell was 40 cm in length, 2.5 cm in diameter and filled with about 20 torr Kr. A quartz window was sealed to the entrance end of the cell and, at the exit, a MgF_2 window was sealed to separate the gas cell and a shorter glass cell which coupled to the REMPI apparatus (see section 2.2.2). The VUV beam generated was thus then focused to the interaction region by a translatable 1-cm diameter and 5-cm focal-length LiF lens which was adjusted by a small magnet outside the short glass cell. The VUV power was monitored after it had passed through the ionisation chamber of the REMPI mass spectrometer by a solar blind photomultiplier (Hamamatsu R1459) detector in conjunction with a 1/4 meter spectrograph (Acton Research Corporation, VM-502). The data acquisition arrangement was the same as for the REMPI experiments, except changing the polarity of all voltages of the ion optics and MCP detector when monitoring negative ions.

2.7 Reference

1. I.C.E.Turcu, I.N.Ross, P.Trenda, C.W.Wharton, R.A.Meldrum, H.Daido, M.S.Schultz, P.Fluck, A.G.Michette, A.P.Juna, J.R.Maldonado, H.Shields, G.J.Tallents, L.Dwivedi, J.Krishnan, D.L.Stevens, T.J.Jenner, D.Batani, and H.Goodson, *Proc.SPIE* 1994, **2015**, 243.

Chapter 3

Higher Rydberg States of C_6H_6, C_6D_6, C_6H_5F, C_6H_5Cl, *p*-$C_6H_4F_2$ and *o*-$C_6H_4F_2$ Studied by Two-photon Resonance Ionisation Spectroscopy

3.1 Introduction

The Rydberg states of benzene, one of the most widely investigated polyatomic molecules, continue to attract particular interest because of the molecule's high symmetry. The initial work was done by Price and Wood[1] and later by Wilkinson[2] with higher resolution using VUV one-photon absorption. They found a Rydberg series with quantum defect of δ=0.46, n=3-8, and three series of δ=0.16, 0.11 and 0.05, n=4-7, converging on the first ionisation limit. The former was assigned to an *p* series and the latter three with near-zero quantum defects were attributed either to an *f* or *d* series. The (3+1) REMPI spectrum recorded by Johnson[3] was virtually identical to the one-photon absorption spectrum. In addition, a 3*s* Rydberg state with its origin at 51085 cm^{-1} was also identified in his (2+1) REMPI experiment[3]. Grant and co-workers[4] repeated the (3+1) REMPI experiment in a jet-cooled molecular beam and extended the *p* series of δ=0.46 up to n=13 and one of the *f* series with δ=0.05 up to n=14. They obtained the ionisation energy of 74573±2.0 cm^{-1} for benzene-h_6 and 74592.5±1.2 cm^{-1} for benzene-d_6 by extrapolating the *f* series. In their (2+1) REMPI experiments performed later[5], they found five low, n=3-8, gerade Rydberg series in benzene-h_6 and -d_6 with quantum defects of δ= -0.11, 0.05, 0.02, 0.06 and 0.77 converging on ionisation limits at 74573 (-h_6) and 74592.5 cm^{-1} (-d_6), respectively. In their (4+1) REMPI

experiments[6], the same five series plus an extra series (n=4-7) with δ=0.24 were observed. The δ=0.77 states were assigned to an *ns* Rydberg series[5]. They assigned the series having δ=0.24 as that in which the molecule has an electron in the nd_2 Rydberg orbital (subsequently abbreviated to an nd_2 series) as this is the only one which exhibits a polarisation ratio of 4.5 signifying pure rank four activity[6]. The series with δ=-0.11 was assigned as an nd_1 series according to its two-photon polarisation behaviour. Of the three remaining Rydberg series (δ=0.05, 0.02 and 0.06), that having δ=0.05 was thought to be an nd_0 series because the other two series start, empirically, at n=5. The participation of $g(l=4)$ orbitals is thus indicated as the lowest members of two of the Rydberg series are at the n=5 level. Nevertheless, the higher Rydberg states of these series, lying closer to the ionisation limit, were not observed because of the spectral congestion and resonance interference with strong hot bands associated with transitions to the first excited singlet state $S_1(^1B_{2u})$, at the one-photon level.

Very recently, Neusser and co-workers[7] reported a double resonance (i.e., (1+1′) via single rotational lines of $S_1 6^1$ vibronic level) study of high Rydberg states (n=48-110) of benzene-h_6 and -d_6 using two Fourier-transform limited nanosecond laser pulses. They identified 20 Rydberg series in benzene-h_6 and 64 series in benzene-d_6 converging on different rotational levels of the ionic core. The rotationless ionisation energies of 74556.58±0.05 (-h_6) and 74583.50±0.05 cm^{-1} (-d_6) were obtained, respectively. These are the most accurate values for the ionisation energies and differ from the values[8] obtained in recent ZEKE experiments lying about 0.5 cm^{-1} lower. All observed series showed low quantum defects below 0.01.

The Rydberg states of monohalogenated benzenes, however, have not been studied very thoroughly. Price and co-workers[9] found two Rydberg series of fluorobenzene with quantum defects of 0.49 and 0.03 in the one-photon far ultraviolet absorption spectrum. They found a slight difference between the limits of convergence of the two series. A later study by Gilbert and Shandorfy[10] recorded the VUV spectrum of fluorobenzene with a resolution superior to that of the early study and found both series (n=3-8) converge to 9.20 eV (~74200 cm^{-1}). The two

series with quantum defects of 0.49 an 0.03 were assigned by the above authors to *np* and *nd* Rydberg states, respectively, which appear to be the analogues of similar series of benzene observed by Wilkinson[2]. No *ns* Rydberg series converging on the first IE of fluorobenzene has ever been observed in one-photon VUV absorption spectroscopy though, in contrast to benzene, it is a fully allowed transition.

The first and only observation of *s* type Rydberg states of fluorobenzene was reported by Goodman and co-workers[11] using (2+1) REMPI spectroscopy which showed a vibrationally resolved 3*s* state with its origin at 50914 cm^{-1}. In a later study[12], the same group observed the n=4 and possibly n=5 member of the *d* series of fluorobenzene with resolved vibrational structure using (3+1) REMPI. The origins they reported are slightly lower (10-60 cm^{-1}) than that by one-photon absorption which was explained as possibly being different symmetry components. They also claimed to observe 3*p* (with origin at 55568 cm^{-1}) and 5*p* states.

For chlorobenzene, the high Rydberg states are even less well investigated. The one-photon VUV absorption spectrum of jet-cooled chlorobenzene obtained by Ichimura et al[13] using synchrotron radiation showed some fragmentary structure in the Rydberg region. No assignments, however, have ever been made. Asselin et al[14] observed three Rydberg states 3*d*, 4*p* and 4*d* with origins at 60300(δ=0.081), 64690(δ=0.405) and 66390(δ=−0.022) cm^{-1} using double resonance multiphoton ionisation photoelectron spectroscopy via the S_1 state.

The high Rydberg states of the difluorobenzenes are also poorly understood. Gilbert and Sandorfy[15] observed one Rydberg series with quantum defect of δ=0.07 (n=4-10) and another with δ=0.52 (n=4-7) for *p*-difluorobenzene in the one-photon absorption spectrum. They also observed one Rydberg series of δ=0.03 (n=3-7) and another with δ= 0.46 (n=4-10) for *o*-difluorobenzene[15]. Fujii et al[16] investigated the Rydberg states of jet-cooled *p*-difluorobenzene using (1+1′) REMPI via the S_1 state. They observed four series of δ= 0.016, 0.041, -0.09 and -0.01 with n=8-14 via the origin of the S_1 state and one series of δ=0.081 with n=15-30 via $S_1 5^1$. All of them converge on the first IE. No REMPI study on the Rydberg states of *o*-difluorobenzene has ever been reported.

In this work a detailed study of the higher Rydberg states of C_6H_6 and C_6D_6 using mass-resolved (2+1) REMPI will be presented. The goal of this study is to investigate the higher Rydberg states of benzene in the energy region which Grant and co-workers[5] were unable to access and below the energy region studied by Neusser and co-workers[7]. A comparison study for C_6H_5F, C_6H_5Cl, *p*-$C_6H_4F_2$ and *o*-$C_6H_4F_2$ was also performed.

3.2 Experimental

The molecular beam was generated by pulsing a mixture of benzene, fluorobenzene or chlorobenzene, *p*-difluorobenzene and *o*-difluorobenzene at their vapour pressures with He or Ar through a General Valve nozzle. The REMPI spectra of benzene, fluorobenzene and chlorobenzene were recorded on the REMPI apparatus. Coumarin 153, Coumarin 307, Rhodamine B, Rhodamine 6G, and Rhodamine 101 dyes were used. The laser pulse energy delivered in each laser pulse after frequency doubling was 2-5 mJ. This provided a very high power density (~10^{10}-10^{11} W/cm^2) in the interaction region with the molecular beam. At high power intensities the dominant fragments were C^+ and C_2^+. The fragmentation, following the two-photon absorption to the Rydberg states, probably occurs by absorption of one or more additional photons to the repulsive ionic states. For simplicity, however, all spectra recorded in the present work will be denoted as (2+1) REMPI spectra. The C^+ and C_2^+ signal intensity were so strong that reduced voltages of ~4kV (normally 5 kV) for the MCP detector and 110 V (normally 2 kV) for the extraction plate were used. Correspondingly the lens voltage was reduced to zero. Circular polarisation was achieved by passing the beam through a Soleil Babinet prism.

The REMPI spectra of *p*-difluorobenzene and *o*-difluorobenzene were recorded on the ZEKE apparatus. Rhodamine 110, Rhodamine 6G, Rhodamine B, Rhodamine 6G/Rhodamine B mixture, Rhodamine 101, and Rhodamine 101/DCM mixture dyes were used. The laser pulse energy delivered in each laser pulse after

frequency doubling was 100-200 μJ, providing power densities about 10^8-10^9 W/cm^2.

All spectra, except where indicated, were recorded in the C^+ and C_2^+ mass channels and all spectra presented here were normalised to the square of the simultaneously recorded laser power. Calibration was made by simultaneously recording the REMPI spectrum and the laser induced fluorescence (LIF) spectrum of I_2 in a static cell. At ~73000 cm^{-1} region, the calibration was accurate to ±0.5 cm^{-1}. The widths of the bands in the spectrum further reduced the accuracy to ±1 cm^{-1}. Only benzene-h_6 and -d_6 were fully calibrated, the rest are accurate to ±5 cm^{-1}.

3.3 Results and discussions

3.3.1. Benzene (C_6H_6 and C_6D_6)

The mass resolved (2+1) REMPI spectra of jet-cooled C_6H_6 and C_6D_6 were recorded using both linearly and circularly polarised light in the energy region from 60000 cm^{-1} to the first IE (~74600 cm^{-1}). In the low energy region up to 73000 cm^{-1}, studied by Grant and co-workers[5] by collecting all ions rather than using C^+ and C_2^+, our spectra reproduce theirs. For reference, a detailed two-photon REMPI spectrum of benzene-h_6 recorded in the C^+ mass channel in the 4*d* region is shown in figure 3-1. The quantum defects δ of the Rydberg series were determined by the Rydberg formula, using the ionisation energy values of 74556.58±0.05 (-h_6) and 74583.50±0.05 cm^{-1} (-d_6), respectively.

It can be seen that the strongest feature in spectrum figure 3-1 is the origin of n=4 at 68080 cm^{-1} with a quantum defect of -0.12 (denoted as nR_g(-0.11), for the convenience of comparison with Grant and co-worker's work[5], their labels will be used for the Rydberg series of benzene observed in the present work). The polarisation study shows that it is a totally symmetric (A_{1g}) state. Built upon the origin are the weaker vibrational levels 6_0^1 and 1_0^1 which have about 1/3 of the intensity of the origin. This relatively weak vibrational activity makes the origin of higher Rydberg states easy to resolve and identify. Because this origin is weaker in

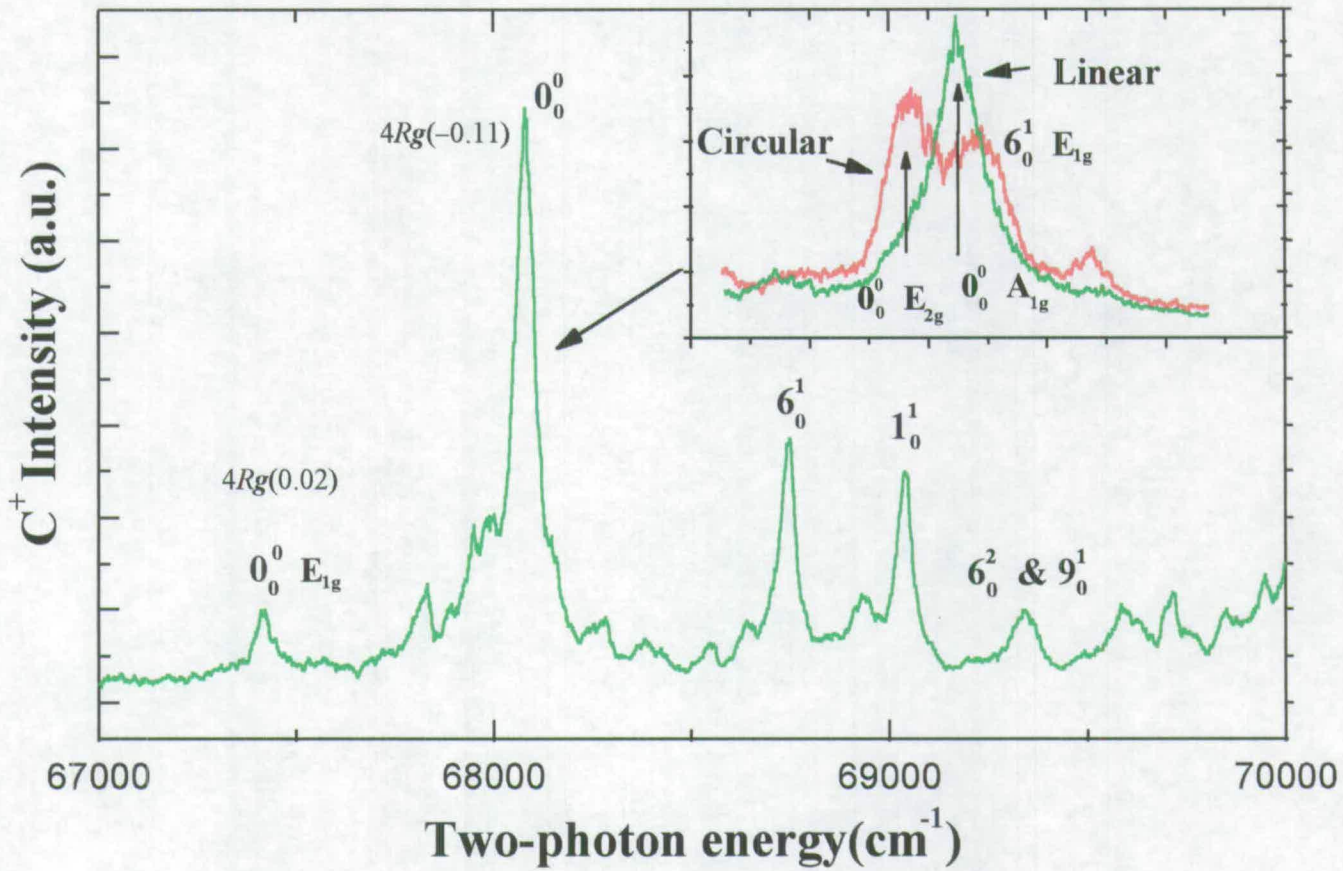

Figure 3-1: The linearly polarised two-photon spectrum of C_6H_6 in the 67000-70000 cm^{-1} region. The insert shows a high resolution scan of the strong peak under linear and circular polarisation.

the spectrum recorded with circularly polarised light a second underlying origin can be observed at 68051 cm^{-1} which corresponds to an E_{2g} origin (see the insert of figure 3-1). Further to the red of the A_{1g} origin there is another origin at 67411 cm^{-1} with E (E_{1g}) symmetry which has a quantum defect of 0.08 ($nR_g(0.05)$).

Figure 3-2 presents the Rydberg series from n=4-16 of C_6H_6 recorded in the C_2^+ mass channel with linearly and circularly polarised light. The linear spectrum consists of a series of sharp distinct features with an average quantum defect of -0.15 which is obviously the extension of the strong *d* Rydberg series, $nR_g(-0.11)$, observed strongly at the n=4 level. The circular spectrum consists of the extension of the two very closely spaced Rydberg series (with quantum defects of 0.04 and 0.00) whose low members can be resolved but merge as n increase. The Rydberg series with the smallest quantum defect δ=0.00 ($nR_g(0.02)$) starts at n=5. A very weak series having quantum defect δ=0.77 ($nR_g(0.77)$)is also observed and its quantum defect suggests that it belongs to the *s* Rydberg series.

Figure 3-3 presents the Rydberg series from n=9-30 of C_6H_6 recorded in the C^+ mass channel with linearly and circularly polarised light. Again, it can be seen that the features appearing in the spectrum are quite regular which suggests that no significant interaction between these Rydberg states and valence states occur in this region. All of the same features are observed in the equivalent spectrum of C_6D_6 as shown in figure 3-4 and 3-5. The transition energies of all electronic origins of C_6H_6 and C_6D_6 observed in this region are tabulated in tables 3-1 and 3-2.

The isotope shift of the ground state benzene cation is 27 cm^{-1}, calculated using the updated lowest vibrationless and rotationless ionisation potential 74556.57 cm^{-1} for C_6H_6 and 74583.51 cm^{-1} for C_6D_6 obtained by Neusser and co-workers[7]. The observed isotope shifts between all three corresponding Rydberg series of C_6H_6 and C_6D_6 are 27 $\pm$ 5 cm^{-1}, in good agreement with the above value. In comparison, it is found that the values are between 11-73 cm^{-1} for lower members (n=3-7) observed by Grant and co-workers[5], who claimed that this might partially reflect the interaction between Rydberg series and valence states in this lower energy region.

EDINBURGH UNIV. LIBRARY

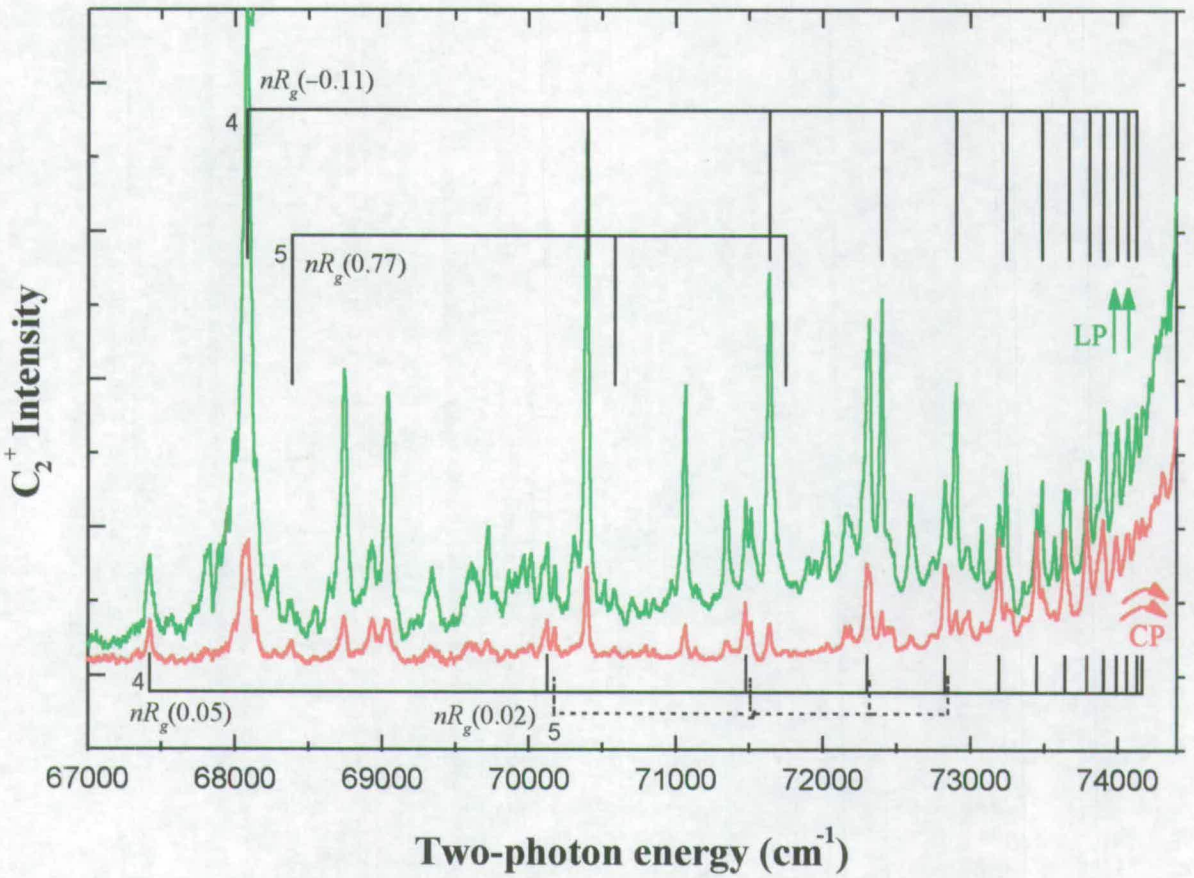

Figure 3-2: The linearly and circularly polarised two-photon spectra of C_6H_6 in the 67000-74400 cm^{-1} region recorded in the C_2^+ mass channel.

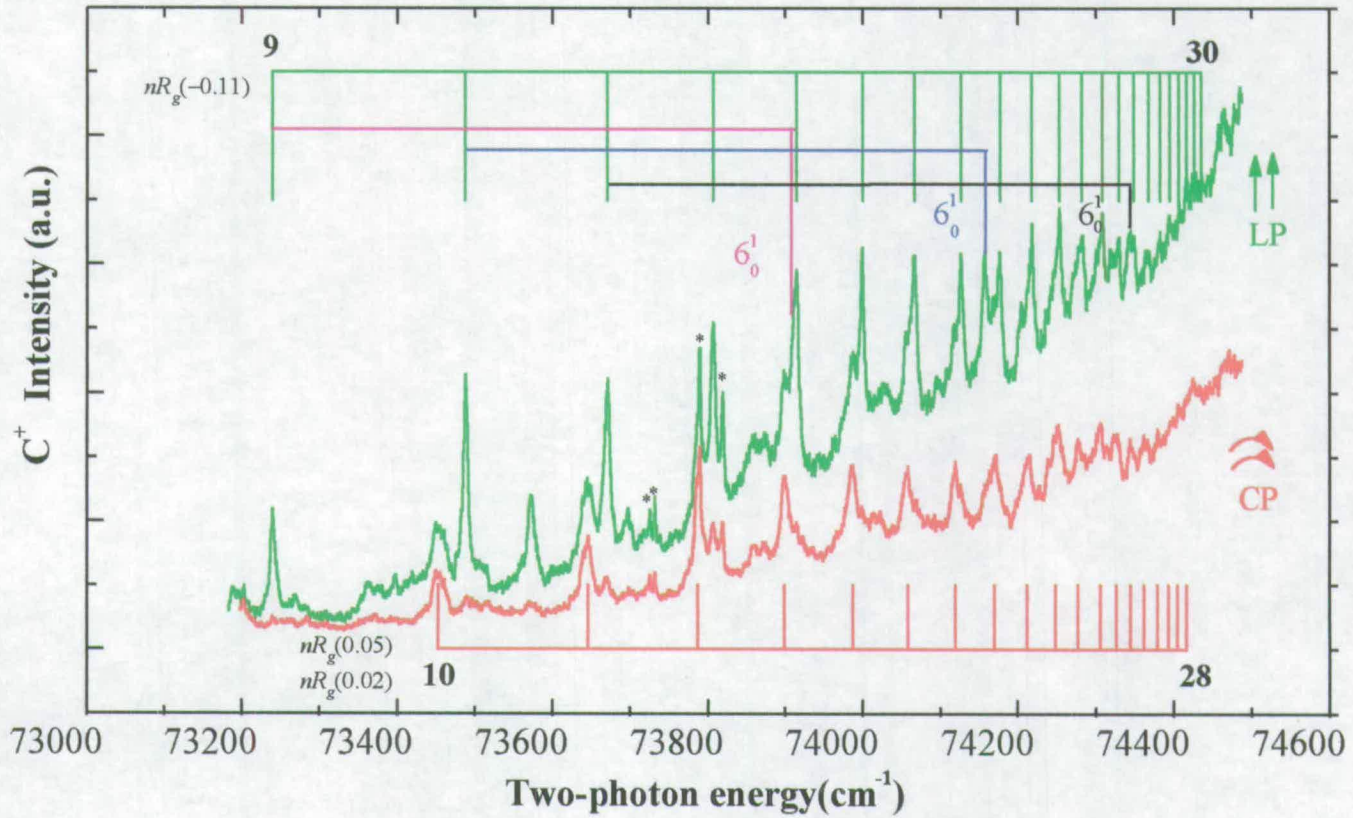

Figure 3-3: The linearly and circularly polarised two-photon spectra of C_6H_6 in the 73000-74600 cm^{-1} region. The peaks marked with * are atomic carbon resonances.

Table 3-1: Transition energies and quantum defects[a] of the origin bands of C_6H_6

	nd_1 (–0.11)		nd_0 (0.05)		ng (0.02)	
n	ν_{00}	δ	ν_{00}	δ	ν_{00}	δ
3	*62968*	*-0.075*	*60775*	*0.180*		
4	*68072*	*-0.108*	*67409*	*0.088*		
5	*70389*	*-0.115*	*70106*	*0.047*	*70160*	*0.017*
6	*71630*	*-0.103*	*71469*	*0.059*	*71507*	*0.022*
7	*72403*	*-0.110*	*72301*	*0.058*	*72317*	*0.024*
7	72403	-0.138	72295	0.045	72313	0.006
8	72897	-0.130	72822	0.062	72834	0.018
9	73238	-0.123	73190	0.047	73200	0.005
10	73488	-0.133	73449	0.049	73460	-0.005
11	73673	-0.143	73640	0.051	73646	0.021
12	73811	-0.134	73785	0.033	73793	0.012
13	73920	-0.131	73899	0.02		
14	74008	-0.138	73987	0.02		
15	74079	-0.158	74058	-0.02		
16	74136	-0.161	74119	-0.01		
17	74183	-0.146	74170	0.01		
18	74224	-0.164	74212	0.00		
19	74258	-0.16	74248	-0.01		
20	74287	-0.16	74277	0.03		
21	74311	-0.16	74306	-0.07		
22	74333	-0.16	74326	0.01		
23	74352	-0.15	74345	0.09		
24	74369	-0.19	74363	0.05		
25	74384	-0.19	74379	-0.01		
26	74396	-0.13	74394	-0.09		
27	74408	-0.19	74405	-0.08		
28	74418	-0.16	74417	-0.17		
29	74428	-0.15				
30	74436	-0.19				

[a]Values given in italics are from ref.5

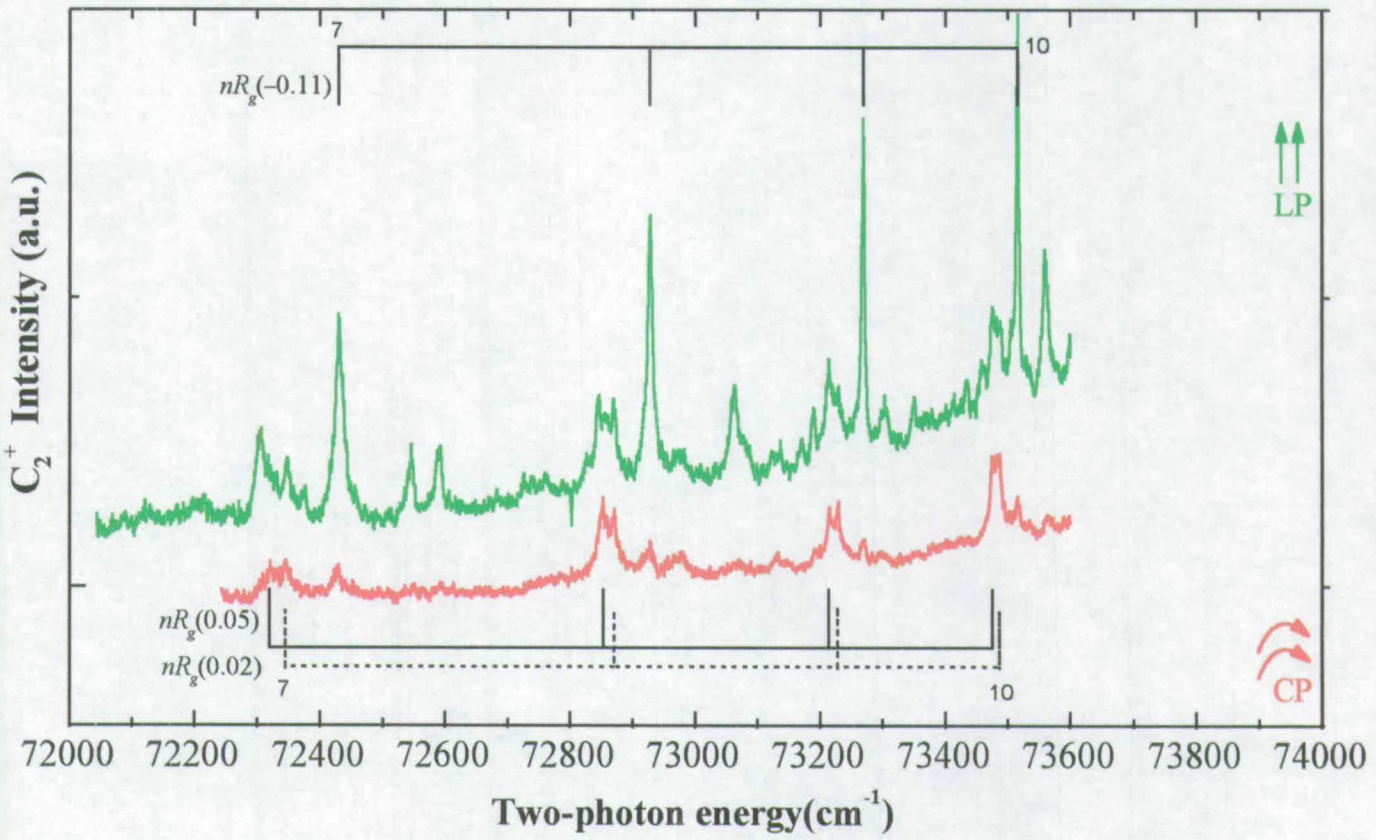

Figure 3-4: The linearly and circularly polarised two-photon spectra of C_6D_6 in the 72200-73600 cm^{-1} region recorded in C_2^+ mass channel.

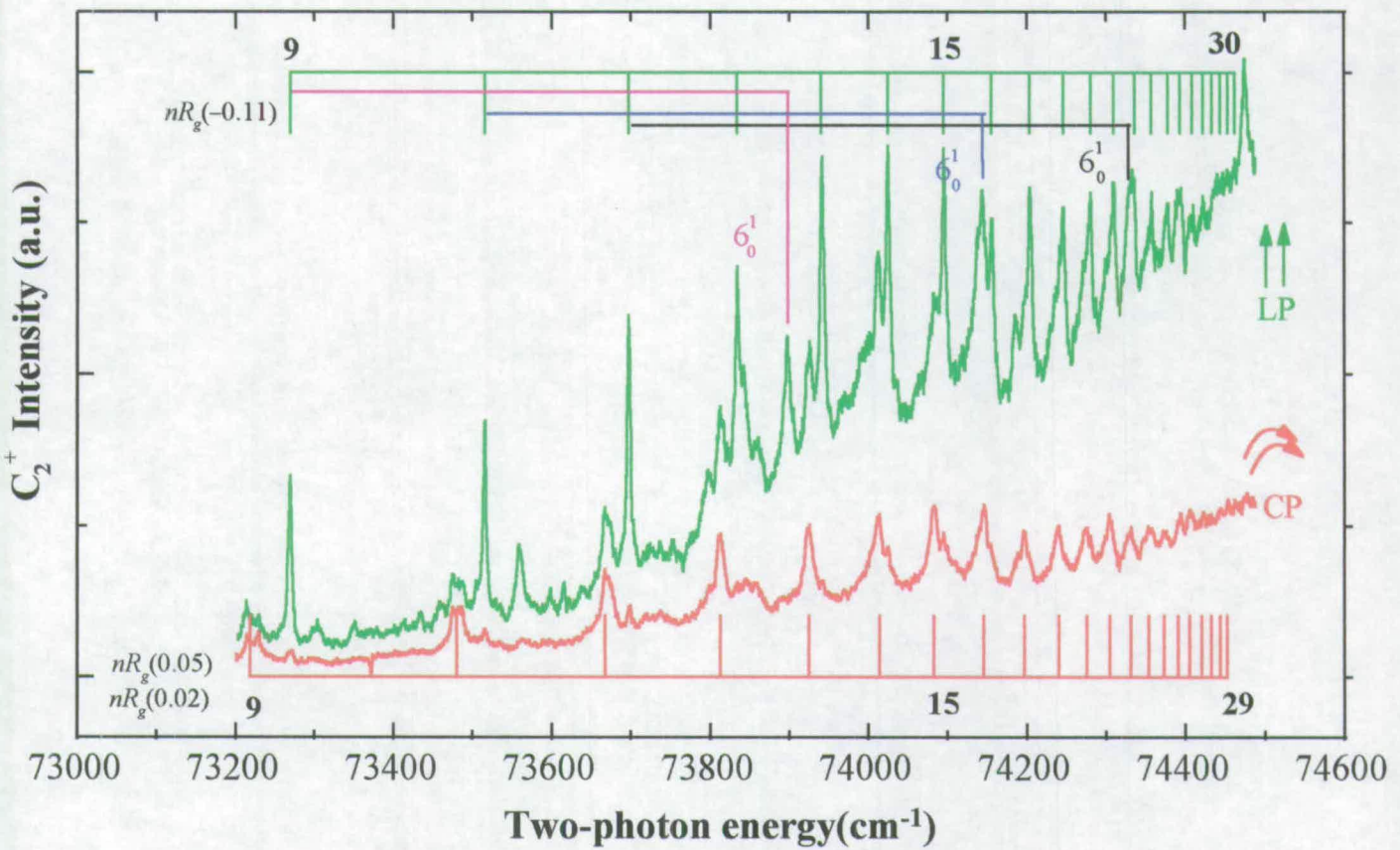

Figure 3-5: The linearly and circularly polarised two-photon spectra of C_6D_6 in the 73000-74600 cm^{-1} region recorded in the C_2^+ mass channel.

Table 3-2: Transition energies and quantum defects[a] of the origin bands of C_6D_6

	nd_1 (−0.11)		nd_0 (0.05)		ng (0.02)	
n	ν_{00}	δ	ν_{00}	δ	ν_{00}	δ
3	*63020*	-0.079				
4	*68121*	-0.117	*67420*	*0.089*		
5	*70414*	-0.124	*70135*	*0.039*	*70187*	*0.008*
6	*71674*	-0.122	*71499*	*0.045*	*71535*	*0.011*
7			*72319*	*0.049*	*72345*	*0.015*
8	*72937*	-0.104	*72854*	*0.054*	*72870*	*0.017*
7	72430	-0.138	72313	0.048	72339	0.007
8	72924	-0.131	72849	0.046	72867	0.005
9	73268	-0.131	73212	0.055	73227	0.007
10	73515	-0.134	73474	0.053	73485	0.005
11	73699	-0.138	73668	0.050	73676	0.002
12	73839	-0.140	73816	0.043	73819	0.023
13	73950	-0.161	73932	-0.018	73935	-0.003
14	74036	-0.157	74025	-0.02		
15	74105	-0.139	74093	0.05		
16	74164	-0.173	74154	0.00		
17	74210	-0.147	74204	-0.01		
18	74252	-0.19	74246	-0.04		
19	74285	-0.18	74280	-0.01		
20	74314	-0.18	74309	0.01		
21	74339	-0.18	74334	0.02		
22	74360	-0.18	74357	-0.02		
23	74381	-0.26	74376	-0.01		
24	74395	-0.14	74393	0.03		
25	74411	-0.21	74407	0.04		
26	74424	-0.21				
27	74431	0.21				
28	74446	-0.20				
29	74454	-0.11				
30	74463	-0.11				

[a]Values given in italics are from ref.5.

It is important to stress that the spectra shown in figures 3-2, 3-3, 3-4 and 3-5 were obtained under fully focused conditions. With a lower laser power density, only heavily congested spectra were observed which were dominated by the hot bands and sequence bands from the ground state to the first excited singlet state $S_1(^1B_{2u})$ at the one-photon level instead of the sharp Rydberg series.

In total, three extended Rydberg series have been observed in the (2+1) REMPI spectrum of benzene. The strongest series $nR_g(-0.11)$ can be resolved up to n=30. The two weaker series, $nR_g(0.05)$ and $nR_g(0.02)$, which dominate under circularly polarised light and merge into one feature from n=12, can be observed up to n=28. All three Rydberg series of benzenes ($-h_6$ and $-d_6$) converge very nicely to the first ionisation limit. In addition, the isotope shift seems very regular in this energy region. This suggests that no significant interaction between the Rydberg series and valence states occurs in this region.

All the δ values are near zero thus they could be assigned to *nd* Rydberg states. However, above n=5, the possible observation of *g* series can not be ruled out because *g* Rydberg series are also fully allowed in a two-photon transition from the ground state though it is expected to be weak due to poor *g* orbital overlap with the benzene π orbital system.

In the molecular Rydberg states of benzene, the one-electron atomic *d* orbital is split by the molecular core central field of D_{6h} into three components: $d_0(d_{z^2})(a_{1g})$, $d_1(d_{xz}, d_{yz})(e_{1g})$ and $d_2(d_{x^2-y^2}, d_{xy})(e_{2g})$[†]. Further interaction with the degenerate ion core, $^2E_{1g}$, produces the molecular symmetry states E_{1g}; E_{2g}, A_{1g} and A_{2g}; E_{1g}, B_{1g} and B_{2g}[‡], respectively. Of these, E_{1g}, A_{1g} and E_{2g} are two-photon allowed. Therefore only four *d* series, $d_0(E_{1g})$, $d_1(A_{1g})$, $d_1(E_{2g})$, and $d_2(E_{1g})$, can be observed by two-photon REMPI. From the polarisation study, the strongest series $nR_g(-0.11)$ under linear polarisation which almost disappears under circular polarisation can be assigned straightforwardly to $d_1(A_{1g})$ while the Rydberg series just on the red side of this series (figure 3-1 insert) which is very weak and can only be identified with circular polarisation has been assigned to $d_1(E_{2g})$. Another

[†] The low case symmetry symbols denote the symmetry of Rydberg (atomic) orbitals.
[‡] The high case symmetry symbol denote the symmetry of molecular symmetry species.

Rydberg series which has a quantum defect of 0.24 and exhibits a polarisation ratio of 4.5 signifying pure rank four activity in a four-photon transition has been assigned unambiguously to $d_2(E_{1g})$ by Grant and co-workers[6]. Thus, of the d Rydberg series, only $d_0(E_{1g})$ remains unassigned. It seems likely that of the remaining two Rydberg series observed which dominate under circularly polarisation light, the Rydberg series $nR_g(0.05)$ most likely corresponds to $d_0(E_{1g})$ as the other one starts at n=5. All of the other molecules (substituted benzenes) studied in this work also show a Rydberg series which starts at n=5. This encourages us to assign this remaining Rydberg series ($nR_g(0.02)$) which has the smallest quantum defect to a g Rydberg series with more confidence. This is consistent with the fact that the higher l orbital has less probability of penetrating the core and thus has a smaller quantum defect.

The dominant intensity of the d_1 Rydberg series under linear polarisation can be explained by the Rydberg orbital overlap with the benzene π orbital system. Figure 3-6 shows a schematic diagram of the πe_{1g} orbitals of the benzene ground state. The two-photon transition corresponds to excitation of an electron from one of the two benzene πe_{1g} orbitals (denoted as b_1 and a_2) which have equal energy (i.e. degenerate) to one of the Rydberg d orbitals. Among those d orbitals, it is clearly seen, as shown in figure 3-7, that the best overlap occurs between d_{xz} and $\pi e_{1g}(b_1)$ (fig3-7a) or between d_{yz} and $\pi e_{1g}(a_2)$. Next is between d_{z^2} and πe_{1g} (figure 3-7b). The worst overlap occurs between d_{xy} or $d_{x^2-y^2}$ and benzene πe_{1g} system (figure 3-7c) because d_{xy} and $d_{x^2-y^2}$ predominately lie in the molecular plane (nodal plane) of the benzene πe_{1g} orbital. Thus the $\pi e_{1g} \rightarrow d_1$ (d_{xz}, d_{xz}) excitation will dominate in the linearly two-photon transition spectrum while the $\pi e_{1g} \rightarrow d_2$ (d_{xy}, $d_{x^2-y^2}$) should always be the weakest. It is noticed experimentally that in the four-photon spectrum $\pi e_{1g} \rightarrow d_2$ is also hardly seen under linear polarisation[6]. Under circular polarisation, though it is a rank four transition which has the highest polarisation ratio (the ratio between the signal intensities under circularly polarisation and linearly polarisation light) of 4.5, and is seen with medium intensity in the spectrum.

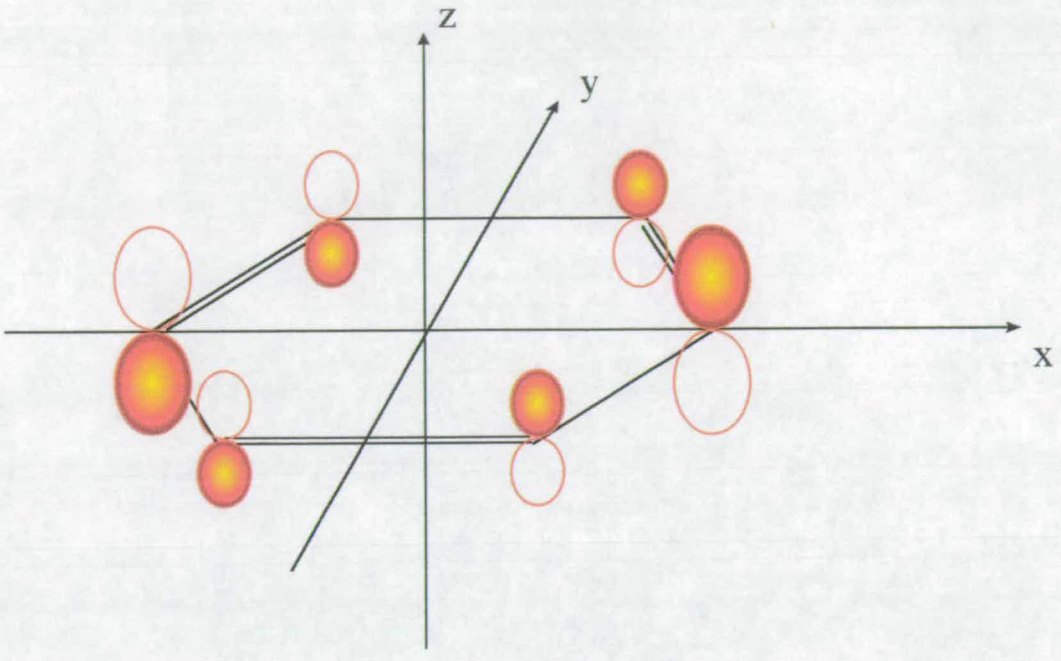

(a)

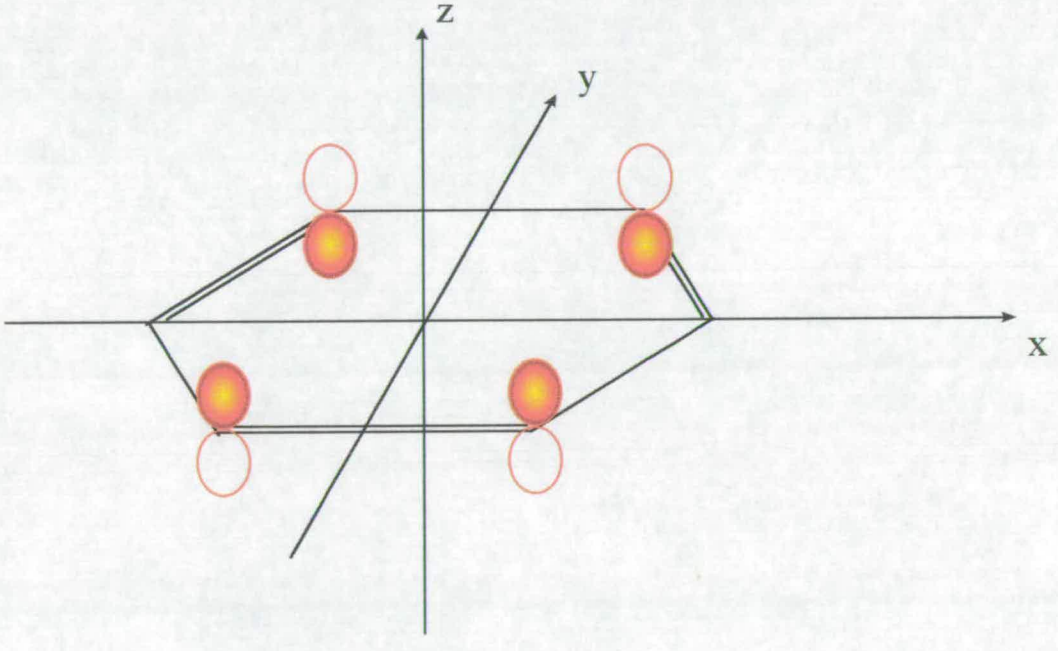

(b)

Figure3-6: The πe_{1g} degenerate HOMO orbitals of benzene. For convenience, the upper one (a) will be denoted as b_1 type and the lower one (b) as a_2 type orbital. (D_{6h})

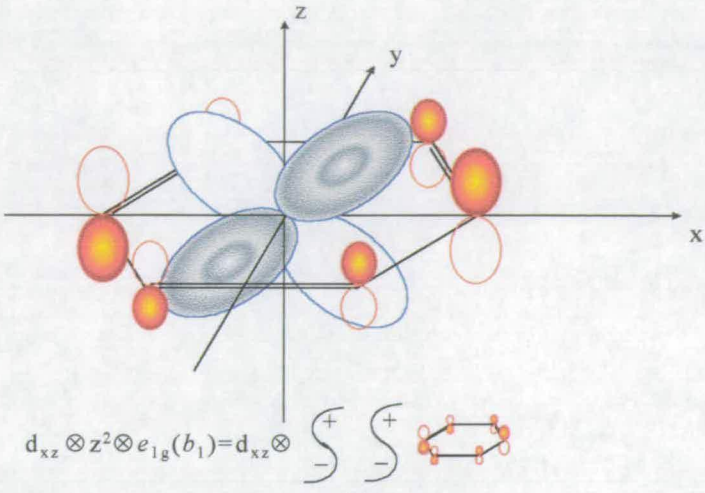

(a)

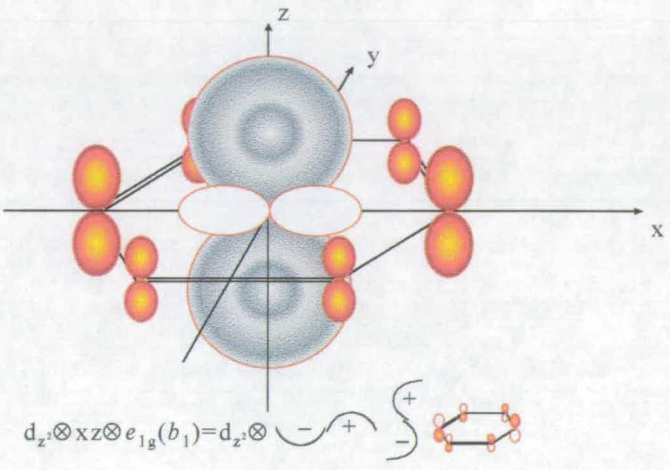

(b)

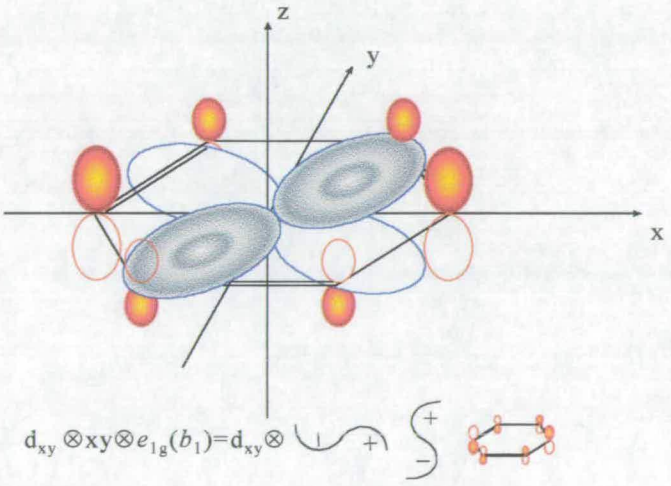

(c)

Figure 3-7: The schematic diagrams of the overlap (a) between the Rydberg orbitals d_{xz} and benzene HOMO orbital $\pi e_{1g}(b_1)$, (b) between the Rydberg orbitals d_{z^2} and benzene HOMO orbital $\pi e_{1g}(b_1)$ and (c) between the Rydberg orbitals d_{xy} and benzene HOMO orbital $\pi e_{1g}(b_1)$. Note that d_{xz} is mainly located in the xz plane with its lobes about ±45° to the xy plane while d_{z^2} mainly surrounds the z axis and out of the molecular plane (xy) with small lobes in the molecule plane with opposite ("–") phase. The d_{xy}, however, mainly lies in the molecular plane.

The vibrational structure of the Rydberg REMPI spectrum of benzene has the same appearance as that of the photoelectron spectrum[19-20] suggesting that no significant change in geometry occurs between the Rydberg state in benzene and ionic benzene (ground state cation). The major vibrational activity of benzene is one quanta of ν_6 and ν_1. As pointed out previously by Grant and co-workers[5], 6_0^1 has the same polarisation behaviour as its origin in the nd_1 Rydberg series and therefore appears to have the same symmetry, A_{1g}. This is due to Jahn-Teller distortion of benzene on the e_{2g} potential surface. The relatively weak vibrational activity makes the origin of higher Rydberg states easy to resolve and recognise.

3.3.2 Fluorobenzene (C_6H_5F)

The two-photon REMPI spectrum of fluorobenzene in the region 66000-69500 cm^{-1} is shown in figure 3-8. No significant features were observed in the lower energy region (n=3). The main features appearing in figure 3-8 are very similar to those in figure 3-1 and correspond to 4d Rydberg states based on the ground state of the ion. The strong sharp feature at 67828 cm^{-1} has almost the same quantum defect (-0.14) as the A_{1g} origin of benzene and the small feature at 67331 cm^{-1} has almost zero quantum defect (0.03) as does the E_{1g} origin of benzene. (The quantum defects are calculated using the ionisation energy of 74230±5 cm^{-1} measured using MATI by Lembach and Brutschy[17]). An interesting difference is the prominent intensity of the $6a_0^1$ transition compared with the spectrum of benzene (figure 3-1). One of the possible reasons for this is that in C_{2v} symmetry the 6a mode is a totally symmetric vibration and thus is fully allowed while in the case of benzene ν_6 can only gain intensity by Jahn-Teller distortion.

The frequencies of the totally symmetric modes of the strongest A_1 component at n=4 are (in cm^{-1}): ν_{6a} (506), ν_{7a} (1188), ν_{8a} (1606) and ν_{9a} (1168). The peak at 68825 cm^{-1}, 996 cm^{-1} from the origin at 67829 cm^{-1} could correspond to $6a_0^2$ or 1_0^1 and the peak at 69330 cm^{-1} could be assigned as $6a_0^3$ or $1_0^1 6a_0^1$.

As in benzene, another near-zero quantum defect (0.00) series seems to start at n=5 (69848 cm^{-1}) as shown in figure 3-9 and it can be seen more clearly under

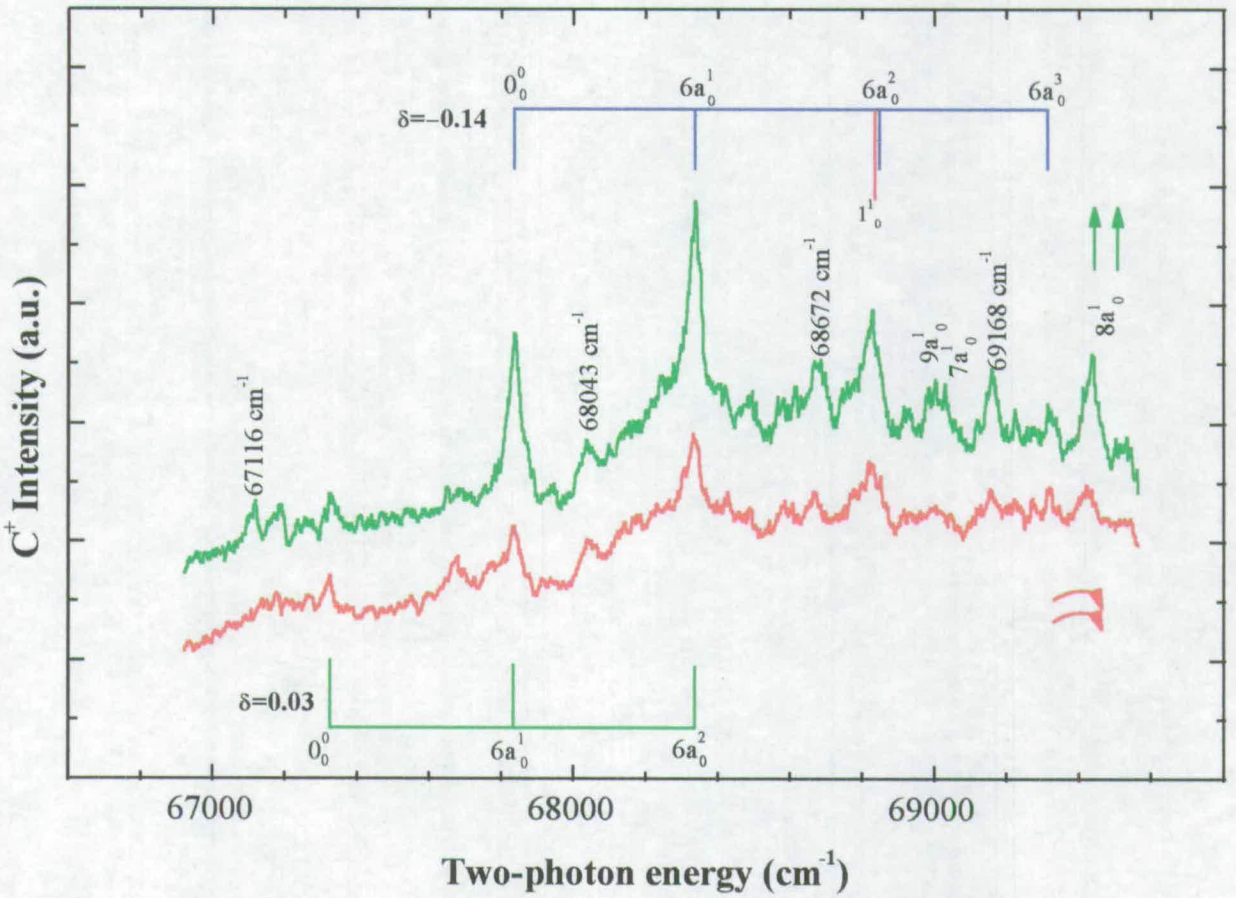

Figure 3-8: The linearly and circularly polarised two-photon spectra of C_6H_5F in the 66500-69500 cm^{-1} region in the C^+ mass channel.

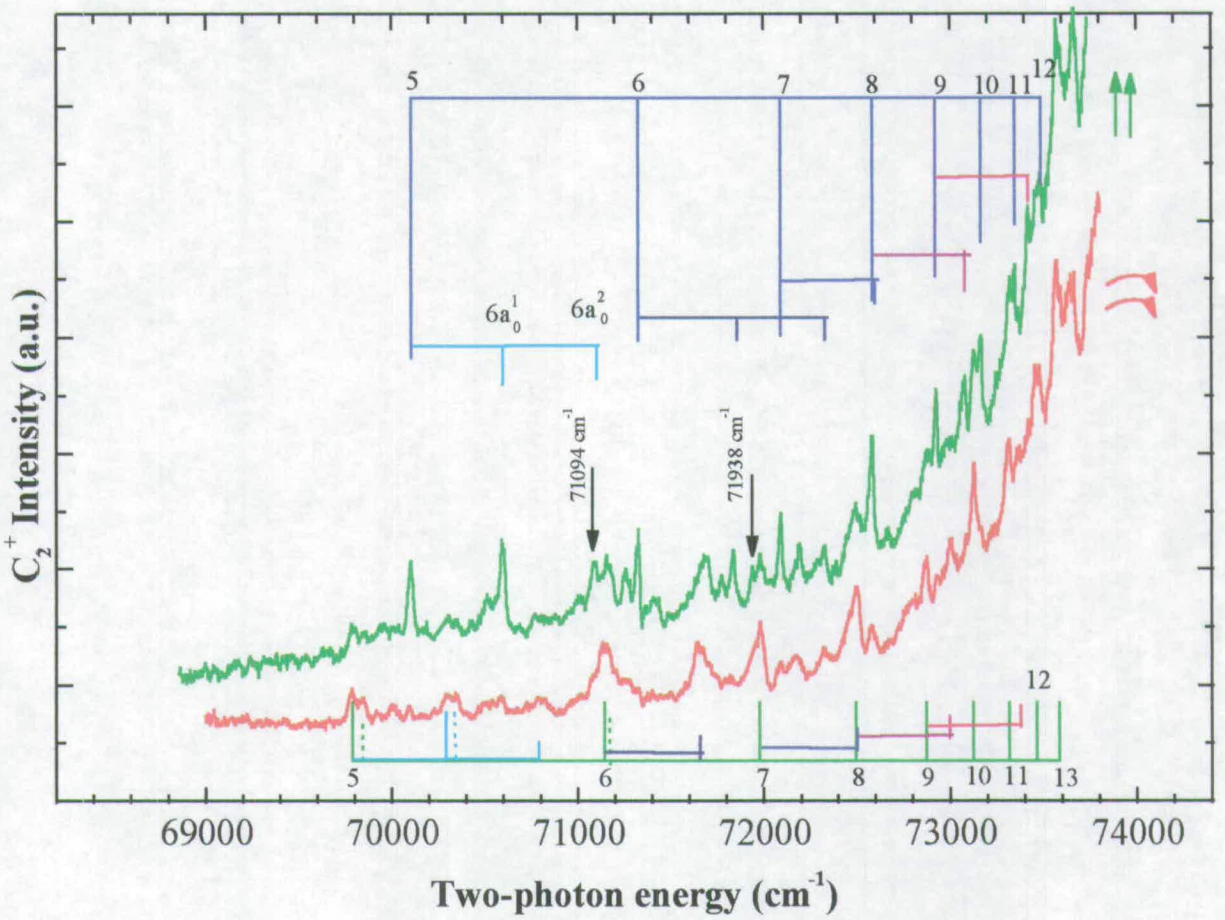

Figure 3-9: The linearly and circularly polarised two-photon spectra of C_6H_5F in the 69000-74000 cm^{-1} region recorded in the C_2^+ mass channel.

circular polarisation. It can not be ruled out, however, that one of the weak features (67100-67300 cm^{-1}) might correspond to its lower member. The feature at 68043 cm^{-1} possibly corresponds to the n=5 member of the *ns* Rydberg series converging on the first IE. Its quantum defect of 0.79 supports this possible assignment. However, no higher member of such a series with a reasonable intensity has been observed. The features at 68672 and 69168 cm^{-1} could not be assigned to any symmetric vibration built on the observed A_1 origin and possibly correspond to a 5*p* origin with a quantum defect of 0.56 and one quanta of ν_{6a} built on it.

By close examination of figure 3-8 it can be seen that another weak feature at 67116 cm^{-1} shows similar polarisation behaviour as the strongest *d* series having a quantum defect δ= -0.14 and thus also has A_1 symmetry. This could be a Rydberg origin having a quantum defect of δ=0.08. The features appearing at 71094 cm^{-1} and 71928 cm^{-1} could be the higher members of this series (n=6 and 7). The absence of its member at n=5 may be due to interference from a strong signal of a carbon atomic resonance in that region. This might suggest that another weak totally symmetric Rydberg series appears in the two-photon REMPI spectra of fluorobenzene. Its quantum defect suggests that it could be an *f* (A_1) Rydberg series.

As can be seen in figure 3-9, the Rydberg series can only be resolved up to n=13 due to the increased activity of mode 6a, with a resultant increase in spectral congestion. The transition energies of all electronic origins of C_6H_5F observed in this work are tabulated in table 3-3.

For mono-substituted benzenes, the double degeneracy of the $^2E_{1g}$ core of the benzene cation is expected to be removed by the presence of the substituent. One of the former e_{1g} orbitals has its maximum electron density (b_1 type) while the other has a node (a_2 type). The HOMO of mono-substituted benzene is the b_1 orbital. Such a loss of degeneracy should allow more Rydberg series to be observed. Two-photon transitions from the HOMO ($^1A_1$) πb_1 to *ns*(1), *np*(3), *nd*(5), *nf* (7) (the number in the brackets is the number of the symmetry species) states are all allowed and thus more Rydberg series are expected to be observed.

Table 3-3: Transition energies and quantum defects of the origin bands of C_6H_5F

	nd_{xz}(-0.14)		nd(0.03)		ng (0.00)		nf(0.08)	
n	ν_{00}	δ	ν_{00}	δ	ν_{00}	δ	ν_{00}	δ
4	67835	-0.142	67338	0.010			67116	0.073
5	70100	-0.154	69786	0.031	69848	-0.004		
6	71326	-0.147	71134	0.047	71161	0.020	71094	0.085
7	72088	-0.157	71977	0.021			71938	0.081
8	72580	-0.155	72494	0.050				
9	72919	-0.149	72868	0.023				
10	73164	-0.146	73120	0.057				
11	73345	-0.135	73314	0.055				
12	73484	-0.128	73463	0.049				
13			73580	0.007				

The number of Rydberg series of fluorobenzene observed in this work, however, is essentially the same as benzene. The relative intensity and quantum defects of these series of the two molecule are also very similar. This indicates that there is very little influence of substituent (F) on the electron excitation from the benzene π orbital to Rydberg states converging to first IE of fluorobenzene. Therefore the state having quantum defect of 0.79 can be assigned to an *s* Rydberg state and those three series having near zero quantum defects (δ= -0.14, 0.03 and 0.00) should still be assigned to *nd* series and/or *ng* series. In C_{2v} symmetry, five *d* Rydberg electron orbitals d_{z^2}, d_{xz}, d_{yz}, $d_{x^2-y^2}$ and d_{xy} (the z-axis is selected in the C–F bond direction, lying in the plane of benzene ring rather than perpendicular to the benzene ring as in the case of benzene, the x-axis is perpendicular to the molecular plane and the y-axis lies in the molecular plane and perpendicular to the C–F bond) couple to the ground state ion core B_1 to produce the molecular symmetry states B_1, A_1, A_2, B_1 and B_2, respectively. All these five series are two-photon allowed. The strong series under linear polarisation which is reduced in intensity most under circular polarisation can be definitely assigned to $nd_{xz}(A_1)$. The other two series with near-zero quantum defects which dominate under circular polarisation could be assigned to $nd_{z^2}(B_1)$, $nd_{yz}(A_2)$, $nd_{x^2-y^2}(B_1)$ or $nd_{xy}(B_2)$. No definite assignments for

these two series could be made based on the present evidence. However, from the comparison to benzene, it is very unlikely that any one of the remaining two series belong to $nd_{z^2}(B_1)$ or $nd_{yz}(A_2)$ because both lie in the molecular plane and thus have the worst overlap with the πb_1 orbital as in benzene. The Rydberg series having δ=0.00 starts at n=5, and by the same argument, this series could be assigned to a g series.

From table 3-4, it can be seen that two f series have A_1 symmetry. The extra weak series observed for fluorobenzene having quantum defect of 0.08 and an A_1

Table 3-4: Symmetry species[a] and selection rules[b] of transition from ground states ($^1A_1$) to Rydberg states for monosubstituted benzene.

	Molecular[c] electronic term(C_{2v})
ns	$B_1(1,2)$
np_x	$A_1(1,2^*)$
np_y	$A_2(2)$
np_z	$B_1(1,2)$
nd_{z^2}	$B_1(1,2)$
nd_{yz}	$A_2(2)$
nd_{xz}	$A_1(1,2^*)$
nd_{xy}	$B_2(1,2)$
$nd_{x^2-y^2}$	$B_1(1,2)$
$nf_{z(5z^2-3r^2)}$	$B_1(1,2)$
$nf_{x(5z^2-3r^2)}$	$A_1(1,2^*)$
$nf_{y(5z^2-3r^2)}$	$A_2(2)$
$nf_{z(x^2-y^2)}$	$B_1(1,2)$
nf_{xyz}	$B_2(1,2)$
$nf_{x(x^2-3y^2)}$	$A_1(1,2^*)$
$nf_{y(y^2-3x^2)}$	$A_2(2)$

[a]Coordinate system used has the z-axis along the C-F bond and x-axis perpendicular to the molecular plane. [b]Selection rules (in parentheses) are indicated as follows: 1 means transition from ground state allowed in one-photon; 2 means allowed in two-photon; asterisk indicates two-photon polarisation ratio Ω<1. [c]Core symmetry: $(a_1)^2(a_2)^2\ b_1$ B_1 (monosubstituted benzene)

symmetry could possibly be one of the two *f* series. Only one member could possibly be assigned to a *p* Rydberg state thus it is concluded that no strong *p* series is observed, though it is two-photon fully allowed.

3.3.3 Chlorobenzene (C_6H_5Cl)

The two-photon REMPI spectra of chlorobenzene in the region 65000-70000 cm^{-1} and 68800-73400 cm^{-1} are shown in figures 3-10 and 3-11, respectively. No significant features were observed in the lower energy region (n=3). Comparing to benzene and fluorobenzene, the spectra of chlorobenzene shown in figure 3-10 seem much more complicated. Firstly, three Rydberg series having quantum defects of δ=0.22, 0.10, 0.06 appear in the n=4 and n=5 region with an extra origin with δ=0.02 appearing in the n=5 region. (The quantum defects are calculated using the ionisation energy of 73170±5 cm^{-1} measured using ZEKE by Wright et al[18]). The series with δ=0.06 is the strongest and the series with δ=0.10 disappears from n=6. Secondly, the intensities of all features decrease when changing the polarisation of the laser radiation from linear to circular in which the two series with δ=0.10 and 0.06 decrease slightly more. Thirdly, the peaks seem quite broad in the n=4–5 region.

The intensity pattern of the vibrational states of the strongest series is similar to that of fluorobenzene which shows strong ν_{6a} activity. The clearly resolved totally symmetric mode of the strongest Rydberg series of chlorobenzene in n=4 is ν_{6a} with frequency of 424 cm^{-1}. Other vibrations are difficult to identify due to the broad width of the features in the spectrum. The feature centred at 67129 cm^{-1} with frequency of 1166 cm^{-1} is possibly one quanta of ν_{9a} or ν_{7a} or a combination of the two built on the origin of 4*d*(0.06) considering the corresponding frequencies of these two vibrations of the cation are 1200 and 1147 cm^{-1}. Those peaks at 67594 and 68018 cm^{-1} are 6a progressions built on ν_{7a} or ν_{9a} at 67129 cm^{-1}. The peak at 68288 cm^{-1} corresponds to $7a_0^2$ or $9a_0^2$ (with energy 2284 cm^{-1}).

As can be seen in figure 3-11, the strongest Rydberg series can only be resolved up to n=16 due to the increased activity of mode 6a, with a resultant

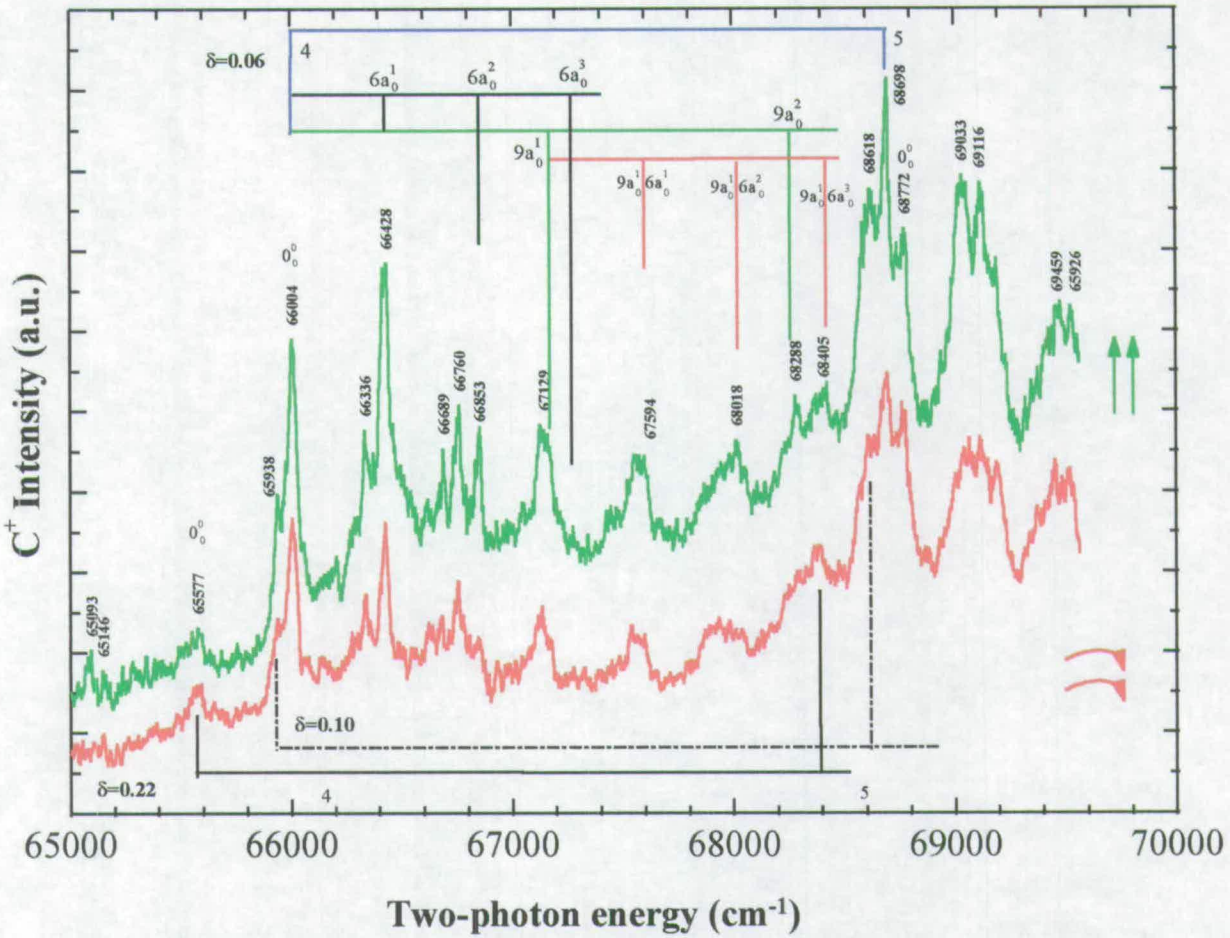

Figure 3-10: The linearly and circularly polarised two-photon spectrum of C_6H_5Cl in the 65000-70000 cm^{-1} region in the C^+ mass channel.

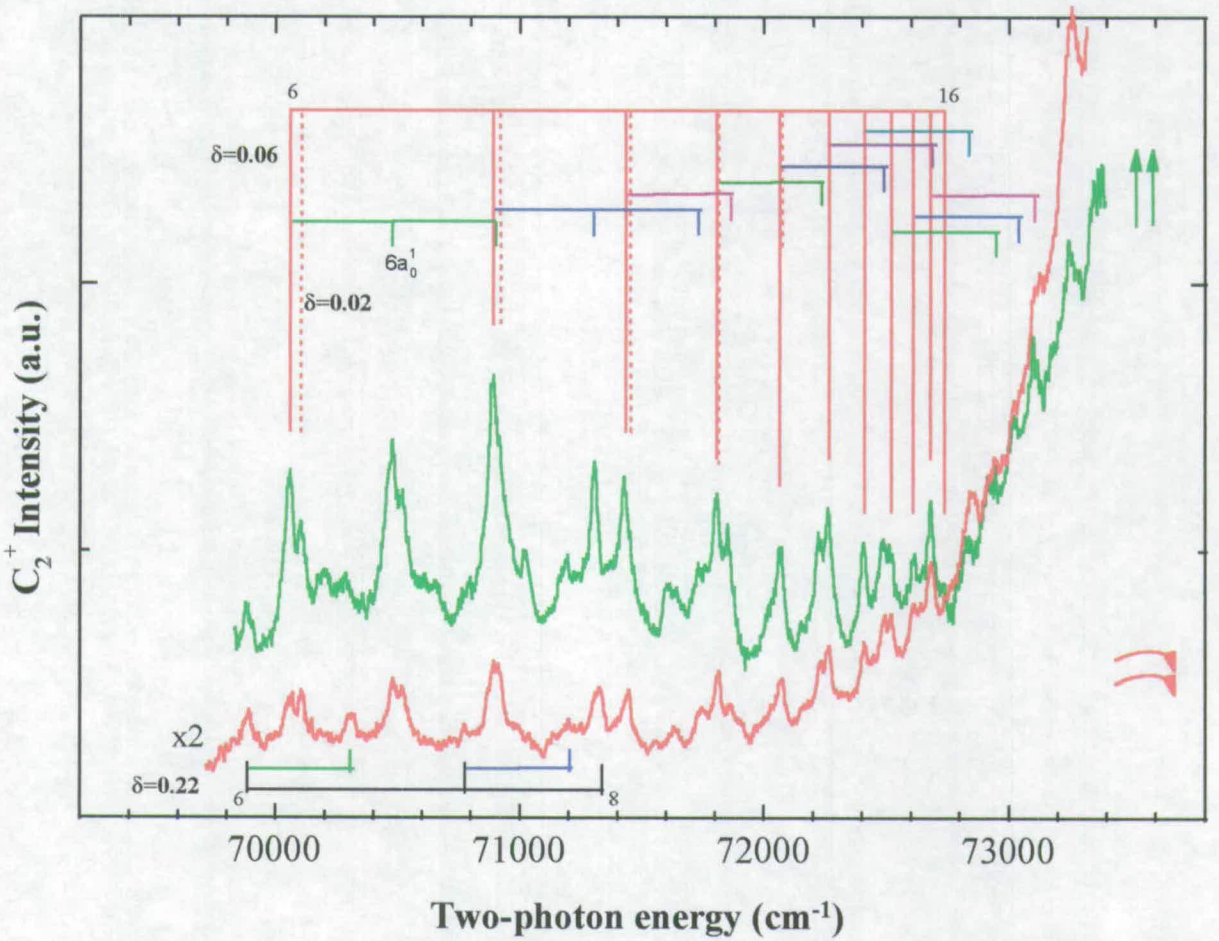

Figure 3-11: The linearly and circularly polarised two-photon spectrum of C_6H_5Cl in the 68000-74000 cm^{-1} region in the C_2^+ mass channel.

increase in spectral congestion. The transition energies of all electronic origins of C_6H_5Cl observed in this work are tabulated in table 3-5.

Table 3-5: Transition energies and quantum defects of the origin bands of C_6H_5Cl

	nd_{xz} (0.06)		nf(0.10)?		ng (0.02)		nd (0.22)	
n	ν_{00}	δ	ν_{00}	δ	ν_{00}	δ	ν_{00}	δ
4	66004	0.087	65938	0.100			65577	0.200
5	68698	0.047	68618	0.090	68772	0.005	68392	0.208
6	70060	0.060			70102	0.020	69892	0.215
7	70892	0.059			70913	0.028	70771	0.236
8	71425	0.069			71446	0.022	71346	0.244
9	71806	0.031						
10	72064	0.038						
11	72260	0.015						
12	72405	0.024						
13	72516	0.046						
14	72613	-0.036						
15	72680	0.035						
16	72738	0.062						

With a heavier substituent, the REMPI spectra of the Rydberg series of chlorobenzene seems somewhat different from those of benzene and fluorobenzene. In total, three strong series (δ=0.10, 0.06 and 0.02) have been observed in linear polarisation light. The first two start at n=4 and merge into one from n=6 while the third starts at n=5. All of them reduce in intensity in circular polarised light indicating that they are symmetric (A_1) Rydberg states. Their near-zero quantum defects rule out the assignment of p series. It is possible that one of them is an *nd*, one of them is an *nf* and the other one is an *ng* series. The strongest one (δ=0.06) is very possibly an *nd* because that $nd_{xz}(A_1)$ orbital has better orbital overlap with the HOMO orbital than the other two. The one with δ=0.02 starting at n=5 might be an *ng* series. The remaining one could be an *nf* series. It is not feasible to give an assignment for the weak series with quantum defect of δ=0.22 at this stage.

It is noticed that the polarisation ratios are not as small as in benzene and fluorobenzene. This is possibly due to some underlying, unresolvable series presented in the spectrum of chlorobenzene which may also explain the broadening of features appeared in the spectrum.

Asselin et al[14] observed three Rydberg origins at 60300, 64690 and 66390 cm^{-1} having quantum defects of 0.081, 0.405 and -0.022 using double resonance multiphoton ionisation photoelectron spectroscopy (DR-MPI-PES) via the S_1 state. These three origins were tentatively assigned as 3*d*, 4*p* and 4*d* Rydberg states. The 4*p* Rydberg state exhibited rich vibrational structure while the 3*d* and 4*d* showed much less vibrational activity. No polarisation study was been done in their experiments. By excitation from vibration levels of different symmetry, however, they claimed that the 3*d* Rydberg orbital which they observed had a_2 symmetry which corresponds to an overall B_2 symmetry for the Rydberg state. As for 4*d*, its quantum defect is almost the same as one of the Rydberg series (δ=0.06) that we observed which has A_1 symmetry. However, Asselin et al[14] precluded the possibility for A_1 symmetry for this Rydberg state though they claimed that it was difficult to determine the symmetry because of the scarce spectral data they obtained. Thus it appears that the states which are selectively populated in resonant two-photon transitions are different from these accessed in a non-resonant pathway.

3.3.4 *p*-Difluorobenzene ($C_6H_4F_2$)

The two-photon REMPI spectrum of *p*-difluorobenzene has been recorded in the region 69000-73200 cm^{-1} and is shown in figure 3-12. Again, Rydberg series similar to those in benzene were observed. Three series having near zero quantum defects δ=0.04, -0.12 and -0.13 were well resolved at n=5-6, the latter two merge into one when n>6. Another series having δ=0.75 also appeared in the spectrum (n=6-8). This can be assigned to an *s* Rydberg series quite straightforwardly. Comparing to other series, the intensities of the two series having δ=-0.12 and -0.13 seem to be reduced more when varying the polarisation from linear to circular. This suggests that these two series might have A_{1g} symmetry. This is not conclusive, however, due to the much lower laser power density (Nd:YAG laser system) used

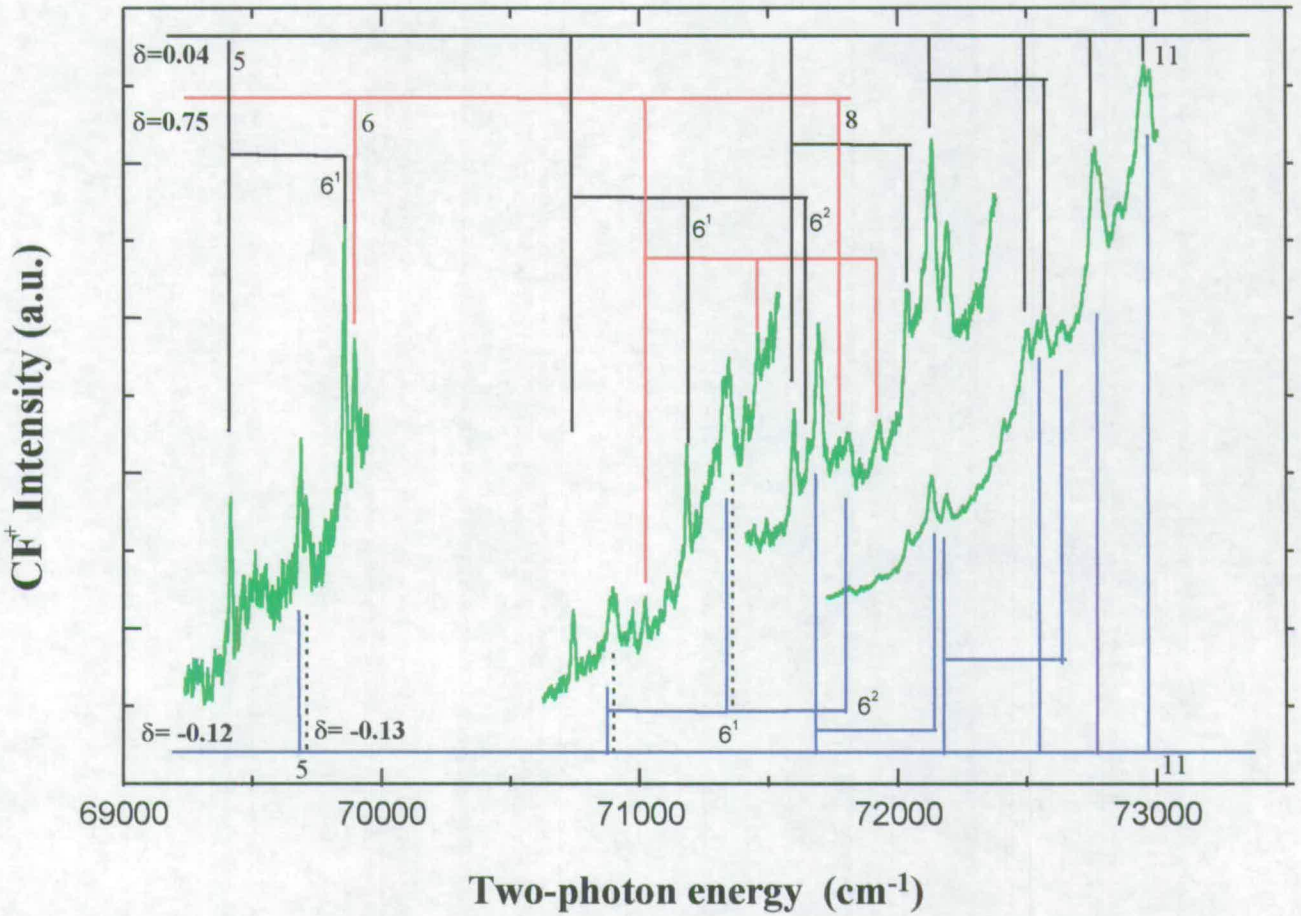

Figure 3-12: The linearly polarised two-photon spectra of *p*-$C_6H_4F_2$ in the 69000-73000 cm^{-1} region composed of several consecutive scans recorded in the CF^+ mass channel

here which resulted in overall weak signals. Further experiments need to be done using higher laser power densities as for benzene. The transition energies of all electronic origins of *p*-difluorobenzene observed in this work are tabulated in table 3-6.

Table 3-6: Transition energies and quantum defects of the origin bands of *p*-$C_6H_4F_2$

	nd_{xz} (-0.012)		*ng* (-0.13)?		*nd* (0.04)		*ns* (0.75)	
n	ν_{00}	δ	ν_{00}	δ	ν_{00}	δ	ν_{00}	δ
5	69690	-0.120	69709	-0.135	69417	0.04		
6	70926	-0.100	70942	-0.121	70776	0.05	69898	0.75
7	71693	-0.098			71600	0.05	71057	0.76
8	72190	-0.080			72131	0.06	71776	0.76
9	72542	-0.087			72502	0.05		
10	72782	-0.040			72765	0.04		
11	72975	-0.067			72953	0.07		

In the molecular Rydberg states of *p*-difluorobenzene which has a lower symmetry (D_{2h}) than benzene, an atomic *d* orbital is split by the molecular core field of D_{2h} into five components. They are $d_{z^2}(a_{1g})$, $d_{xz}(b_{2g})$, $d_{yz}(b_{3g})$, $d_{x^2-y^2}(a_{1g})$ and $d_{xy}(b_{1g})$. On the other hand, we have only one $s(a_{1g})$ orbital even under the core field. Coupling with the ion-core B_{2g} produces the molecular symmetry states B_{2g}, A_{1g}, B_{1g}, B_{2g} and B_{3g}. Excitation of the electron from the HOMO πb_{2g} to these Rydberg orbitals are all allowed in a two-photon transition. Experimentally, however, the same number of Rydberg series was observed as in benzene. In the absorption spectrum, Gilbert and Sandorfy[15] failed to observe any structure belonging to an *s* series though it becomes allowed in one-photon absorption under the lower symmetry. From the preliminary polarisation study, the Rydberg series of δ=-0.12 can be assigned to $d_{xz}(A_{1g})$, which is the only one of the five *d* series having the same symmetry as the ground state. The other series having a quantum defect of -0.13 which lies just on the blue side of the $d_{xz}(A_{1g})$ series and shows the same

polarisation behaviour as $d_{xz}(A_{1g})$ indicates that it might also be a totally symmetric state. Thus it seems that this series does not belong to any of the other *d* series. Considering this series starts at n=5 and also appears at n=6 with the same vibrational structure as $6d_{xz}(A_{1g})$ then merges into one with the $d_{xz}(A_{1g})$ series at higher energies, it strongly suggest that this is a *g* Rydberg series. The surprising point here is that this *g* series has such a large quantum defect and appears with such strong intensity in our spectra especially at n=6, which is almost as strong as $6d_{xz}(A_{1g})$.

The assignment of the series with quantum defect of 0.04 is difficult based on the present evidence. It is noted that the intensity of the δ=0.04 series is similar to or stronger than the $d_{xz}(A_{1g})$ series which is reverse compared with benzene and mono-substitute benzenes.

Unlike our results which show less series than expected, Fujii et al[16] observed more series than expected by (1+1′) REMPI via the S_1 state. Via the origin of the S_1 state, they found four Rydberg series of quantum defect δ =0.016, 0.041, -0.09(0.91) and -0.01(0.99). The S_1 state can be described in molecular orbital language as the state arising from the excitation of an electron in the HOMO πb_{2g} to the LOMO πa_u. Therefore the electronic state of S_1 state is B_{2u}. Assuming that the electronic transition from the S_1 state to the Rydberg state occurs by excitation of an electron in the a_u molecular orbital to the *s* or *d* orbitals mentioned above, only three of them, i.e., $d_{xz}(b_{2g})$, $d_{yz}(b_{3g})$, and $d_{xy}(b_{1g})$, are allowed under the molecular symmetry of D_{2h}. Fujii et al[16] explained that more series were observed than expected was possibly due to the lowering of the D_{2h} symmetry of *p*-difluorobenzene to C_{2h}. No attempt was made to involve a *g* series to explain their observation.

3.3.5 *o*-Difluorobenzene ($C_6H_4F_2$)

The two-photon REMPI spectrum of *o*-difluorobenzene has been recorded in the region 62400-73000 cm^{-1}. Unlike other substituted benzenes, the lowest energy two-photon resonant system corresponding to 3*d* region can be observed, as shown in figure 3-13. Only one Rydberg origin having δ=-0.07 with its vibrations

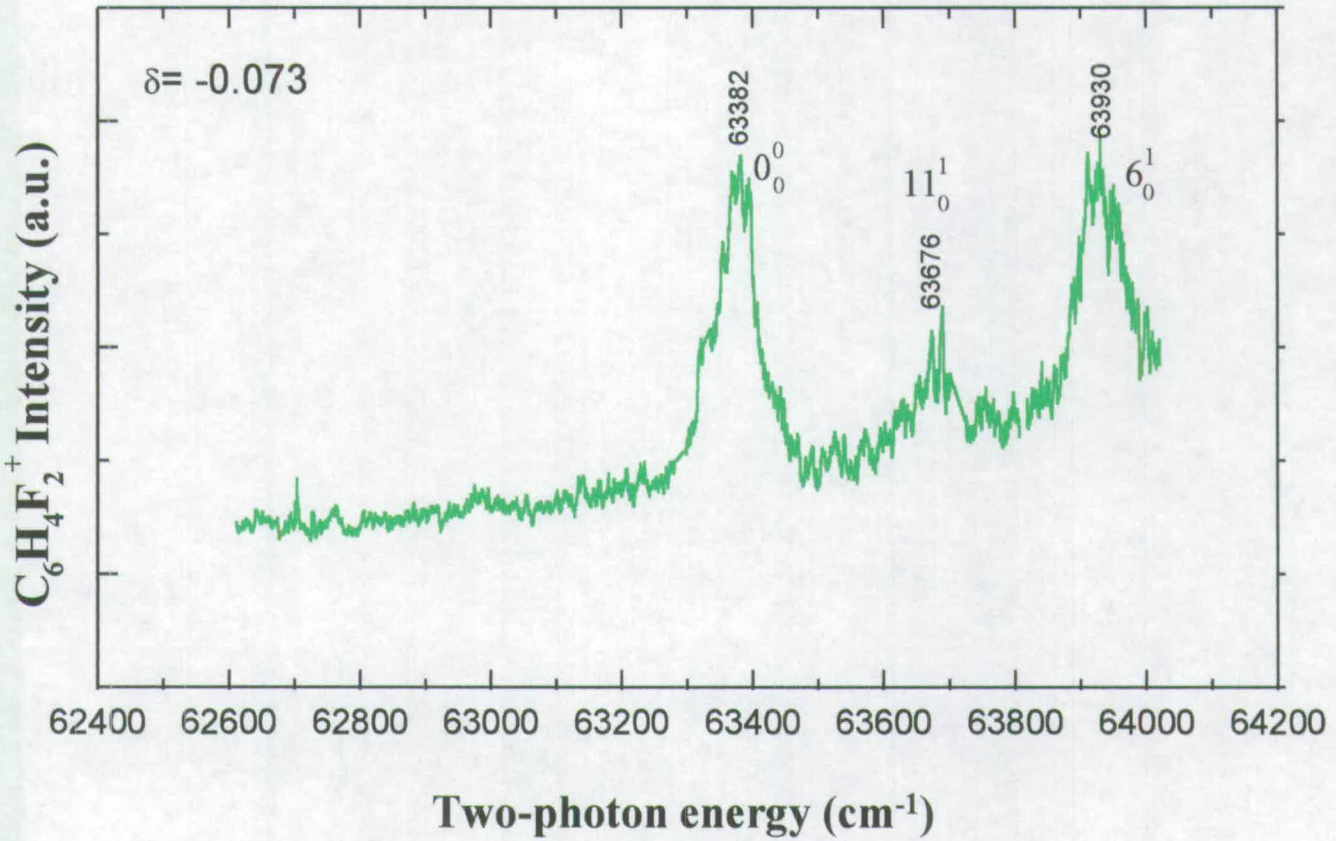

Figure 3-13: The linearly polarised two-photon spectrum of *o*-$C_6H_4F_2$ in the 62400-64200 cm^{-1} region in the parent ion mass channel.

ν_6 and ν_{11} was observed in this region. (The quantum defects in this section were calculated using the new ionisation energy, 75007±5 cm^{-1}, obtained by ZEKE study in the next chapter).

To higher energy, the spectrum is dominated by two strong series having quantum defects of 0.02 and -0.13 (n=4-7) as shown in figure 3-14. It is believed that the origin with δ = -0.13 belongs to the same series with δ = -0.07 at n=3 as shown in figure 3-13. From the preliminary polarisation study, it is found that this series has A_1 symmetry. In contrast to other molecules, no *s* series was observed at all.

Besides the two origins having the same quantum defects as those observed in the 4*d* region another two new weak origins start to appear, again, at n=5. One having a quantum defect of 0.04 appears just on the red side of the 5*d*(0.02) origin and the other having a quantum defect of -0.15 on the blue side of the 5*d*(-0.13). The origin of δ=-0.15 has the same polarisation behaviour as that of 5*d*(–0.13) thus is also an A_1 state. Similar to *p*-difluorobenzene, the relative intensities of δ=0.02 and δ=-0.13 are reversed compared to the equivalent series in benzene and monofluorobenzene. The transition energies of all electronic origins of *o*- difluorobenzene observed in this work are tabulated in table 3-7.

Table 3-7: Transition energies and quantum defects of the origin bands of *o*-$C_6H_4F_2$

	nd (-0.13)		*ng* (-0.15)?		*nd* (0.02)		*nf* (0.04)?	
n	ν_{00}	δ	ν_{00}	δ	ν_{00}	δ	ν_{00}	δ
3	63382	-0.07						
4	68531	-0.13			68099	0.01		
5	70834	-0.13	70876	-0.16	70580	0.02	70537	0.04
6	72090	-0.14			71921	0.03	71890	0.06
7	72851	-0.14			72758	0.01		

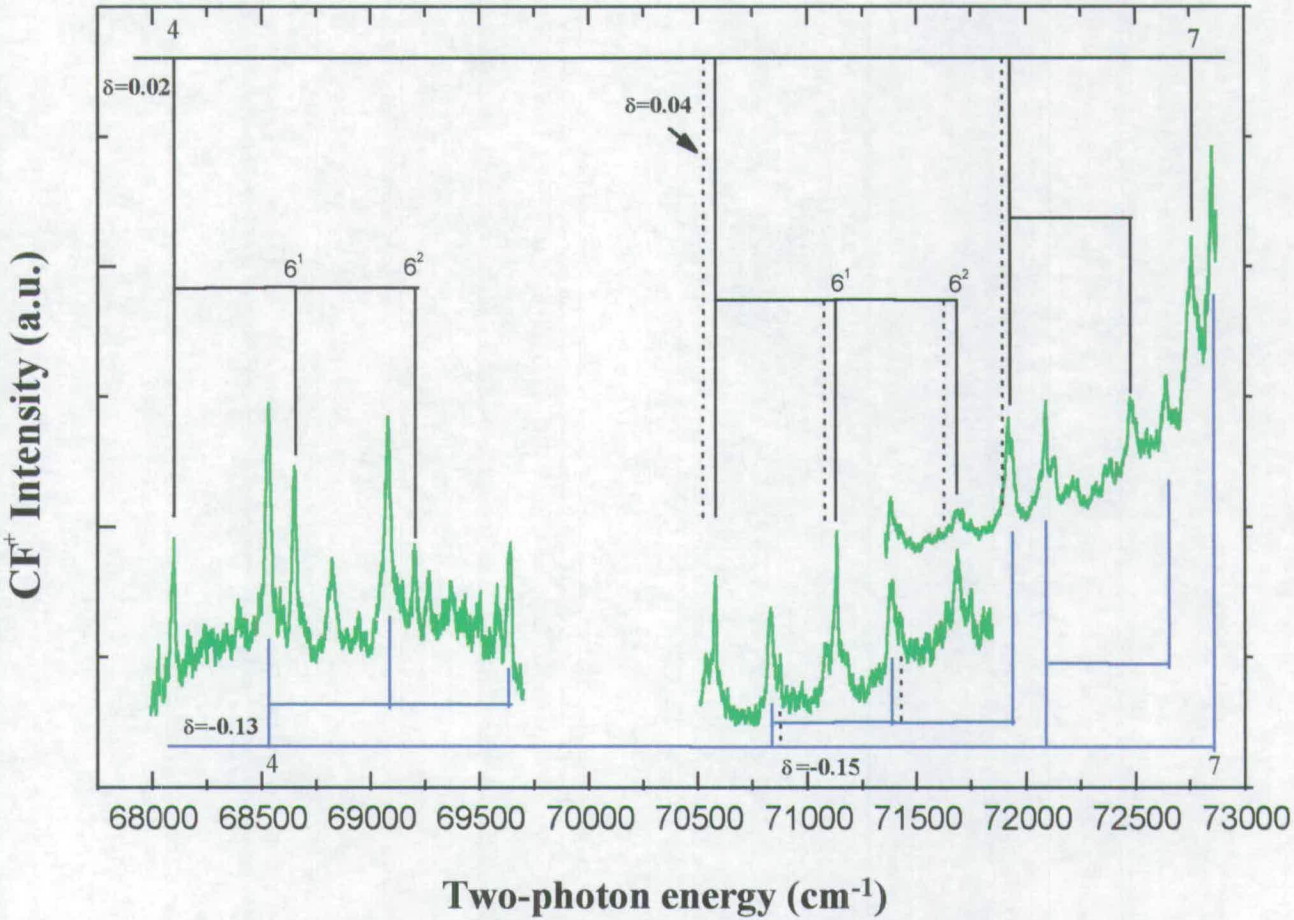

Figure 3-14: The linearly polarised two-photon spectra of *o*-$C_6H_4F_2$ in the 68000-73000 cm^{-1} region composed of several consecutive scans in the CF^+ mass channel

Similar to mono-substitute benzenes, two-photon transitions from the HOMO ($^1A_1$) πb_1 to *ns*(1), *np*(3), *nd*(5) and *nf* (7) (the number in the bracket is the number of the symmetry species) states are all allowed for *o*-difluorobenzene under the molecular C_{2v} symmetry and thus more Rydberg series are expected to be observed. However, Rydberg series having similar quantum defects of δ=-0.13, -0.15, 0.02 as *p*-difluorobenzene, except for the absence of the *s* series, δ=0.75, were observed for *o*-difluorobenzene. A new Rydberg state, δ=0.04, appeared at n=5. The uncertainty here is that both series of δ=-0.15 and δ=0.04 can only be resolved at n=5, though their vibrational structure can also be seen. Thus it is difficult to give a definite assignment for these two states. Considering there is no corresponding series observed in *p*-difluorobenzene, one possible assignment for δ=0.04 state is a *f* state because it is fully allowed in *o*-difluorobenzene.

3.4 Conclusion

The (2+1) REMPI spectra of benzene-h_6 and -d_6 has been considerably extended by REMPI studies using the fragment channels C^+ or C_2^+. In total three extended Rydberg series have been observed in the (2+1) REMPI spectra of both molecules. The strongest series nR_g(-0.11) can be resolved up to n=30. The two weaker series nR_g(0.05) and nR_g(0.02), which dominate under circularly polarised light and merge into one from n=12, can be observed up to n=28. The dominant intensity of the nR_g(-0.11) series in linearly polarised light is qualitatively explained by the orbital overlap between the atomic Rydberg *d* orbitals and the HOMO orbital.

The (2+1) REMPI spectrum of C_6H_5F recorded in the C^+ or C_2^+ mass channels is very similar to benzene-h_6 and -d_6. Although the lowered symmetry permits *p* and *f* series to be excited, in addition to *ns*, *nd*, and *ng* series, the only additional features are very weak and possibly correspond to an *f* (A_1) series. With a heavier substituent, the REMPI spectra of chlorobenzene became more complicated, especially in n=4-5 region.

Two strong series (n=5-11) are observed with quantum defects of -0.12 and 0.04 together with weaker ones (n=6-8) and (n=5-6) with quantum defects of 0.75 and -0.13 for p-$C_6H_4F_2$. Because of the lower signal to noise ratio in the spectrum it was not possible to determine conclusive polarisation effects. With lower symmetry for o-$C_6H_4F_2$, similar two strong Rydberg series with quantum defects of -0.13 (n=3-7) and 0.02 (n=4-7) are observed together with weaker ones (n=5) and (n=5-6) with quantum defects of 0.04 and -0.15 were observed.

3.5 References

1. W.C. Price and R.W. Wood, *J. Chem. Phys.* 1935, **3**, 439.
2. P.G. Wilkinson, *Can. J. Phys.* 1956, **34**, 596.
3. P.M. Johnson, *J. Chem. Phys.* 1976, **64**, 4143.
4. S.G. Grubb, R.L. Whetten, C.E. Otis, A.C. Albrecht and E.R. Grant, *Chem. Phys. Lett.* 1984, **108**, 420.
5. R.L. Whetten, S.G. Grubb, C.E. Otis, A.C. Albrecht and E.R. Grant, *J. Chem. Phys.* 1985, **82**, 1115.
6. S.G. Grubb, C.E. Otis, R.L. Whetten, E.R. Grant and A.C. Albrecht, *J. Chem. Phys.* 1985, **82**, 1135.
7. R.G. Neuhauser, K. Siglow and H.J. Neusser, *J. Chem. Phys.* 1997, **106**, 896.
8. I. Fischer, R. Lindner and K. Müller-Dethlefs, *J. Chem. Soc. Faraday Trans.* 1994, **90**, 2425.
9. Hammond, V.J., Price, W.C., Teegan, J.P. and Walsh, A.D., *Faraday Disc. Soc.* 1950, **9**, 53.
10. R. Gilbert and C. Sandorfy, *Chem. Phys. Lett.* 1971, **9**, 121.
11. K. Krogh-Jespersen, R.P. Rava and L. Goodman, *Chem. Phys. Lett.* 1979, **64**, 413.
12. K. Krogh-Jespersen, R.P. Rava and L. Goodman, *Chem. Phys.* 1979, **47**, 321.
13. T. Ichimura, A. Hiraya and K. Shobatake, UVSOR 618, *Activity Report* (March, 1991).

14. P. Asselin, F. Piuzzi, J.Le Calve, M. Mons and I. Dimicoli, *Chem. Phys.* 1994, **181**, 271.

15. R. Gilbert and C. Sandorfy, *Chem. Phys. Lett.* 1974, **27**, 457.

16. M. Fujii, T. Kakinuma, N. Mikami and M. Ito, *Chem. Phys. Lett.* 1986, **127**, 297.

17. G. Lembach and B. Brutschy, *J. Phys. Chem.* 1996, **100**, 19758.

18. T. Wright, S. I. Panov and T.A. Miller, *J. Chem. Phys.* 1995, **102**, 4793.

19. A.W. Potts, W.C. Price, D.G. Streets and T.A. Williams, *Faraday, Disc. Chem. Soc.* 1972, **54**, 168.

20. L. Asbrink, E. Lindholm and O. Edqvist, *Chem. Phys. Lett.* 1970, **5**, 609.

Chapter 4

Coherent Two-Photon ZEKE-PFI Spectra of Benzene and Substituted Benzenes

4.1 Introduction

Since its development in Munich in 1984 by Muller-Dethlefs, Schlag and co-workers[1], the ZEKE-PFI photoelectron spectroscopic technique has been used widely to measure the adiabatic ionisation energies and to study the vibrational structure in the molecular cation[2-4]. As a prototype polyatomic molecule, benzene has been studied extensively using this technique[5-7]. Most studies have concentrated on using a selected resonant vibronic state as a step to the ionisation threshold, allowing a change from the ground state Franck-Condon factor[5-7]. This gives information on both the intermediate and ionic states. In particular, the so-called "$\Delta\upsilon$=0" propensity rule is found to be reasonably applicable for vibrations in cases where the changes in geometry between the resonant intermediate state and the cation are small.

Rather than using an intermediate state (S_1) as most other studies did, in this work, as a continuing study of the Rydberg states presented in Chapter 3, the two-photon energy was simply scanned up to the unresolved higher Rydberg states lying just below the ionisation threshold. These Rydberg states have been demonstrated to be long lived in the presence of small stray fields caused by the surrounding ions. With a delay of a few μs, all prompt photoelectrons will leave the ionisation region under a small external discrimination electric field. With the subsequent application of a pulsed electric field, the long-lived Rydberg molecules will be ionised and give rise to "ZEKE" electrons. By detecting these ZEKE electrons, the coherent two-photon ZEKE spectra of benzene were obtained. A comparison study of C_6H_5Cl, *p*-$C_6H_4F_2$ and *o*-$C_6H_4F_2$ was also performed.

4.2 Experimental

The ZEKE-PFI experiments presented in this section were performed on the ZEKE apparatus described in chapter 2. The dye laser PDL-3 was pumped by the third harmonic (355 nm) of the Q-switched Nd:YAG laser. Coumarin 540 and Coumarin 500/540 mixture dyes were used. This light was then doubled using a KD*P crystal (C3) to allow two-photon excitation to the ionisation limits of benzene, chlorobenzene and difluorobenzene between 73000 and 76000 cm^{-1}.

In the ZEKE-PFI experiments the pulsed electric fields were arranged as follows. The voltage pulse on the top plate was between 2 and 4 V/cm, applied at approximately 1.4 to 3 μs after the laser excitation. The pulse on the bottom plate was between 0.3 and 1.1 V/cm applied between 300 ns and 900 ns after the laser excitation. A mixture of benzene, or chlorobenzene or difluorobenzene at its vapour pressure and He or Ar, was introduced into the chamber through the General Valve pulsed nozzle with a stagnation pressure of between 100 and 500 Torr. The laser power was measured using a photodiode and integrated by a Stanford Research SR250 boxcar and stored on a PC.

4.3 Results and discussions

4.3.1 Benzene-h_6 and -d_6

The coherent two-photon one colour ZEKE-PFI photoelectron spectrum of the ionic ground states of benzene-h_6 and benzene-d_6 ($\tilde{X}\,^2E_{1g}$) is shown in figure 4-1. It is similar to conventional H (Lα) (121.5 nm) PES observed by Price and co-workers[8] which was dominated by the origin, and vibrational assignments are readily made. The peak positions with assignments are shown in table 4-1.

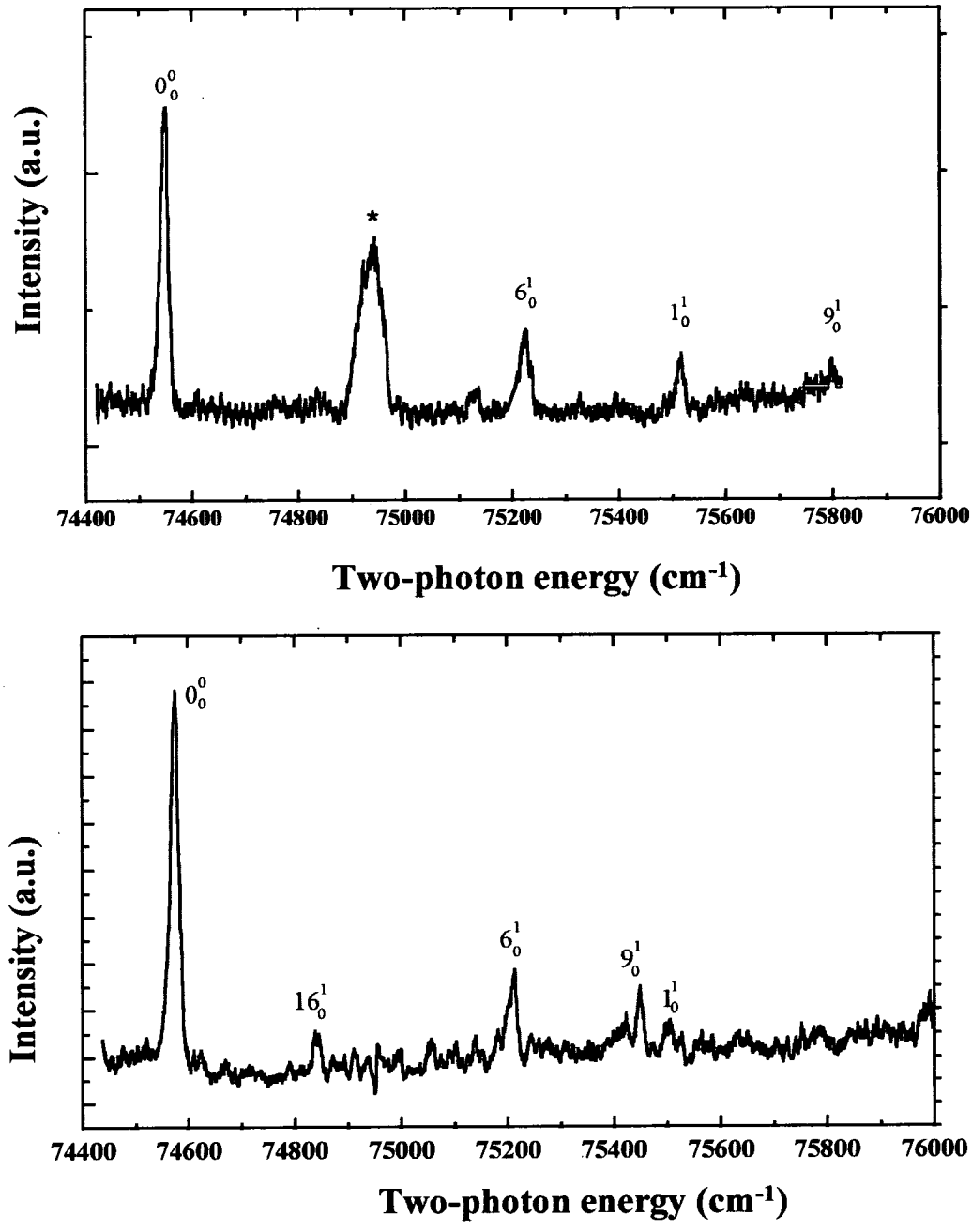

Figure 4-1: (a) Coherent two-photon ZEKE spectrum of benzene-h_6 at 150 torr pressure of benzene-h_6 vapour/argon mixture. The feature marked by * is caused by an accidental resonance (see text). (b) Coherent two-photon ZEKE spectrum of benzene-d_6 at 230 torr pressure of benzene-d_6 vapour/argon mixture. Both spectra are normalised to the square of the simultaneously recorded laser power.

Table 4-1: Vibrational frequencies (cm^{-1}) of benzene-h_6 and -d_6. (those in parentheses are for -d_6)

	ν_6	ν_1	ν_9
Ion[a]	675(638)±5	967(928)±5	1247(875)±5
Ion[b]	674	967	1228
Rydberg[c] (n=3-7)	670-682 (619-632)	955-968 (913-928)	1233-1270 (865-874)
S_0[d]	608(580)	993(946)	1178(869)
S_1[d]	552(498)	923(879)	1154

[a]This work.

[b]Ref.7.

[c]Ref.10.

[d]Ref.15, 16 and 17.

The peak width in the PFI spectrum is about 15 cm^{-1}, slightly larger than the value of 9 cm^{-1} in the (1+1′) MATI spectrum via S_1 6^1 as an intermediate state observed by Krause and Neusser[7]. The broad width could be due to the same reason suggested by Krause and Neusser[7] which was thought to be caused by the rotational states involved. The other possibility could be the power broadening under our experimental conditions. The first peak can be assigned to the adiabatic transition to the origin of the ion. Taking into account the field correction (about 5 cm^{-1}), the adiabatic ionisation energies of C_6H_6 and C_6D_6 of IE=74555±5 cm^{-1} and 74582±5 cm^{-1} are obtained. The IE value of C_6H_6 is in good agreement with recent values obtained with (1+1′) ZEKE (74555.0±0.4 cm^{-1})[5] and (1+1′) MATI (74555.5±0.5 cm^{-1})[7].

In the spectrum of C_6H_6 the strong origin is followed by the strongest of the subsidiary peaks with a frequency of 675 cm^{-1} and then by the second strongest of these with 967 cm^{-1}. Both show similar H mass dependence as corresponding vibrational frequencies of Rydberg states[5]. The former can be assigned as the Jahn-Teller active mode, ν_6, and the latter to the ring breathing mode, ν_1. The peak

appearing in benzene-h_6 spectrum at 1247 cm^{-1} might correspond to the peak at 1220 cm^{-1} in the conventional PES spectrum by Price and co-workers[8]. The corresponding peak seems to disappear in the spectrum of benzene-d_6 because it is H mass dependent. They claimed it moved to a point in between ν_6 and ν_1. However, due to the low resolution in the conventional PES, they could not distinguish it clearly from the rest in their spectrum though they claimed they could see the effect on the rotational contour of these bands. The PFI spectrum shown in figure 4-1b, clearly shows a peak at 875 cm^{-1} which is located between ν_6 and ν_1. This gives an unambiguous assignment of the ν_9 which is H mass dependent.

In comparison with the REMPI spectrum recorded in the C^+ or $C_6H_6^+$ channel, it is found that the strong broad feature centred at 388 cm^{-1} marked by * in figure 4-1a comes from the hot band 6_1^0 of the one-photon accidental resonance $S_1 \leftarrow S_0$. The strong increase in the ion production captures some low energy electrons in the cloud. A similar effect has been observed in the ZEKE-PFI spectrum of I_2 by Cockett et al[9]. These electrons are extracted by the delayed field pulse and appear at the same time-of-flight as ZEKE electrons. Besides, accidentally hitting a ZEKE excitation 1_0^1 after absorption of the second photon could also make a contribution to the signal intensity. This is illustrated by the spectrum shown in figure 4-2 recorded with higher backing pressure. The broad peak is now split into two narrower peaks located at 364 and 388 cm^{-1}. Their relative intensities to the origin peak are dramatically reduced. This confirms that they come from hot bands. The energy of 364 cm^{-1} plus the frequency of ν_6 (608 cm^{-1}) of the ground state gives 972 cm^{-1}, equivalent to one quanta of ν_1 in the ion. Thus this peak can be attributed to the accidentally hitting a ZEKE state (ν_1) together with a near-resonance at the one-photon level. The second of the two peaks at 388 cm^{-1} corresponds to the true $S_1 \leftarrow S_0$ 6_1^0 absorption and a near-resonance at the two-photon level.

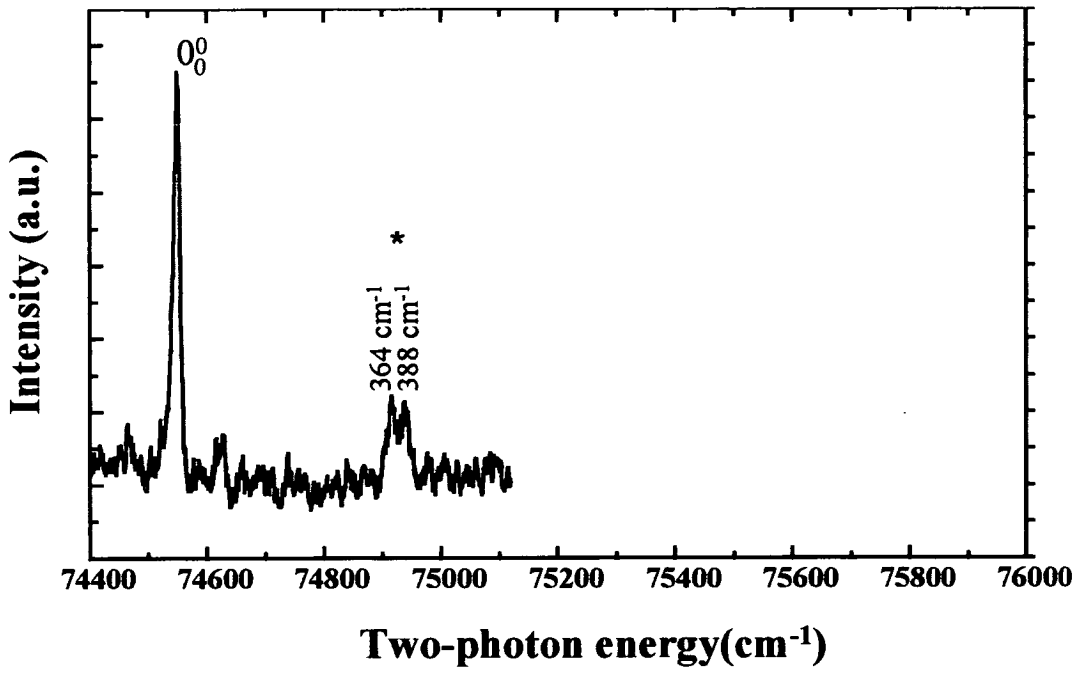

Figure 4-2: Coherent two-photon ZEKE spectrum of benzene-h_6 at 430 torr of benzene vapour/helium mixture. The spectrum is normalised to the square of the simultaneously recorded laser power.

It is noticed that a strong doublet feature (343 and 363 cm^{-1}) appearing in the (1+1′) MATI spectrum via $S_1 6^1$ obtained by Krause and Neusser[7], is at a similar position as the doublet feature in figure 4-2. They assigned this feature as the doublet of $6^1(\pm 3/2)$ and interpreted the splitting as due to the quadratic dynamic Jahn-Teller effect. No splitting of $6^1(\pm 1/2)$ was observed in their MATI spectrum[7]. Although one of the features (364 cm^{-1}) of the doublet in our spectrum (figure 4-2) appears at the same position as the higher component of $6^1(\pm 3/2)$ doublet in their spectrum, they are not the same. Firstly, as pointed out before by Whetten et al[10], the direct coherent two-photon transition from the vibrationless ground state to $6^1(\pm 3/2)$ of the ground state cation is not allowed. Thus it is not expected to see the $6^1(\pm 3/2)$ peak in a coherent two-photon ZEKE-PFI spectrum. Secondly, the cooling effect indicates that the doublet in our ZEKE spectrum does not originate from a cold band. Thirdly, no obvious corresponding peak is observed for C_6D_6.

A systematic investigation of the cooling effect on the ZEKE-PFI spectrum of C_6H_6 by varying the backing pressures was also carried out. Figure 4-3a shows the results with argon as the carrier gas while figure 4-3b shows the spectra with helium. Both illustrate that the intensities of all cold bands 0_0^0, 6_0^1 and 1_0^1 increase with higher backing pressure while that of the broad peak originating from the hot band (vibrational and rotational hot) decreases. By increasing the backing pressure, the internal temperature is cooled down. The number of neutral molecules at the vibrationless and rotationless ground state increases thus all peaks due to cold bands become stronger.

4.3.2 Chlorobenzene

The coherent two-photon ZEKE-PFI spectrum of the ground state of the chlorobenzene cation is shown in figure 4-4. The first strong peak at 73165 cm^{-1} can be assigned as the origin. Thus the field-corrected adiabatic ionisation energy is 73170±5 cm^{-1}, in good agreement with the result of Wright et al[11] (73170±5 cm^{-1}).

The next intense peak appears at 421 cm^{-1} above the 0_0^0. In comparison with the (1+1′) ZEKE-PFI spectrum via S_1 (Wright et al)[11], this feature can be assigned to $6a^1$. Other features appear at 700, 798, 842, 937 and 966 cm^{-1}. It is expected that only vibrations of a_1 symmetry (or even overtones of non-a_1 vibrations) will be excited in the cation (since the ground state has a_1 symmetry). As the known fundamental frequency for ν_{16a} is 348 cm^{-1} in (1+1′) ZEKE-PFI[11], one possible assignment for the 700 cm^{-1} feature is $16a_0^2$. The other possibility is 12_0^1, as the frequency of ν_{12} is 717 cm^{-1} in the (1+1′) ZEKE-PFI spectrum[11]. Similarly, the 798 cm^{-1} feature could be assigned to $16b_0^2$ or $10a_0^1$. The feature at 966 cm^{-1} could be ν_1 and the small shoulder on its blue side could be ν_{18a}.

The feature at 937 cm^{-1} does not appear to be assignable to any fundamental frequency or combination band. In comparison with the (1+1) REMPI spectrum recorded under the same conditions and shown in the upper trace of figure 4-4, it

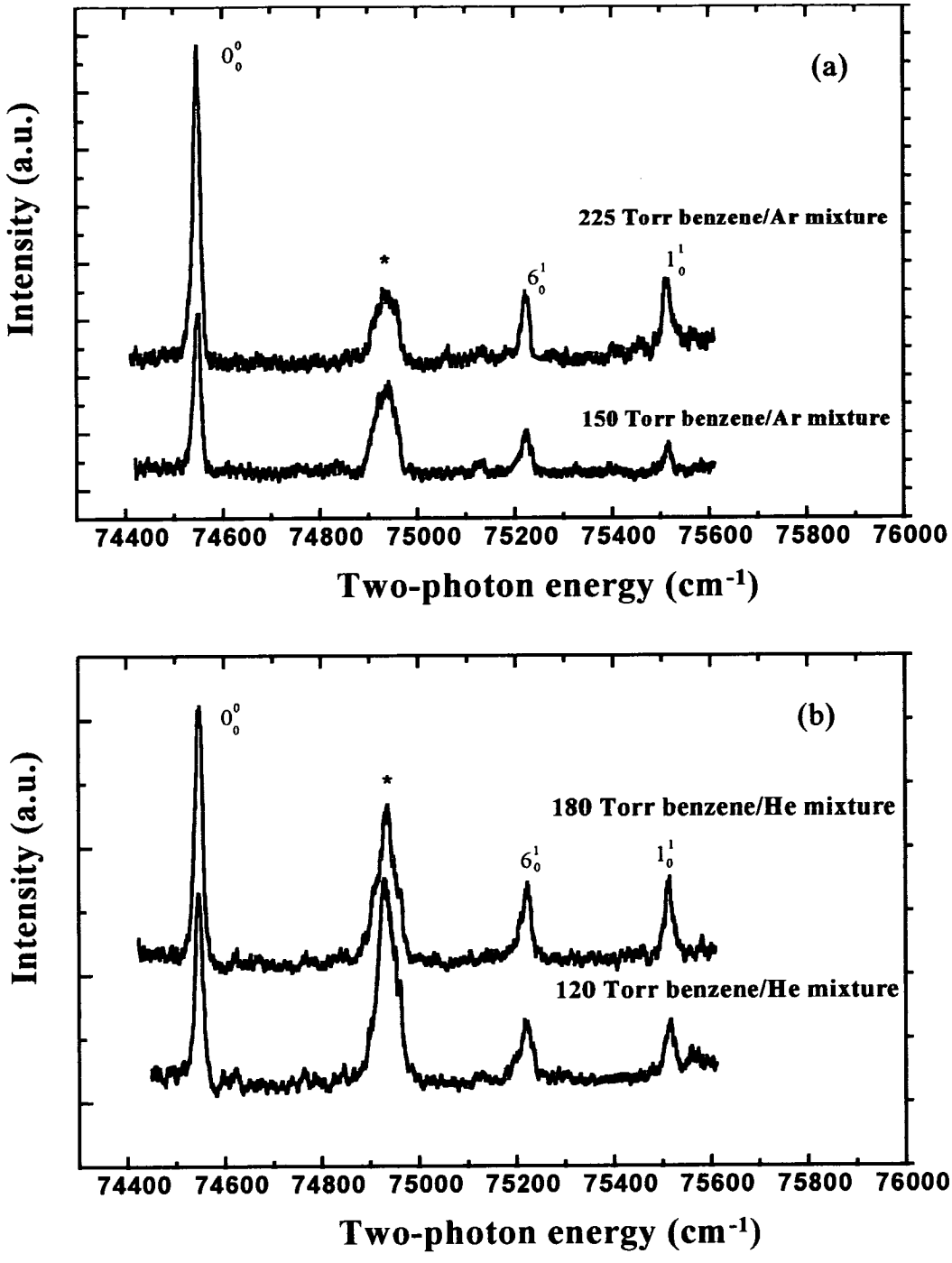

Figure 4-3: Coherent two-photon ZEKE spectra of C_6H_6 at different (total) pressures with different carrier gases (a) Ar: upper trace 225 torr and lower trace 150 torr. (b)He: Upper trace 180 torr and lower trace 120 torr. All spectra in this figure are normalised to the square of the simultaneously recorded laser power.

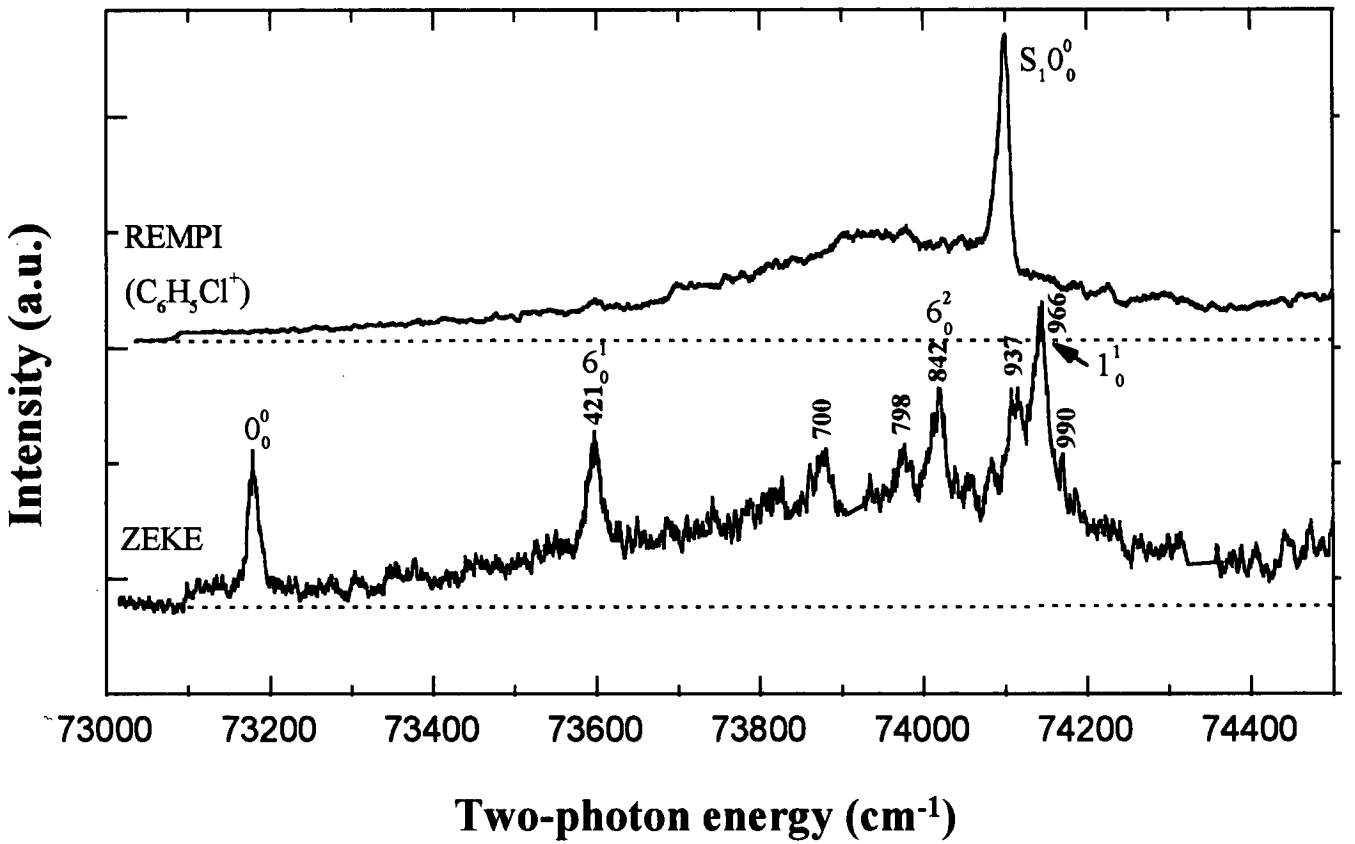

Figure 4-4: Coherent two-photon ZEKE spectrum of chlorobenzene (lower trace) together with (1+1) REMPI spectrum (upper trace) recorded in parent mass channel.

can be seen that this could be due to strong increase of ion production caused by one-photon accidental resonance $S_1 \leftarrow S_0\ 0_0^0$.

The vibrational structure of the cation appearing in the ZEKE-PFI spectrum is essentially the same as the coherent two-photon REMPI spectrum of the Rydberg states presented in Chapter 3. However, one difference is that ν_1 is hardly seen in the REMPI spectrum while it is the strongest feature in the ZEKE spectrum. The feature corresponding to $6a^2$ is also stronger than that in the REMPI spectrum. It is noticed that both features, especially ν_1, are very close to the strong accidental resonance at the one-photon level ($6a^2$ 45 cm^{-1} to the red and ν_1 18 cm^{-1} to the blue of $S_1 \leftarrow S_0\ 0_0^0$). Thus, the increasing of the intensity of these two peaks might be due to near-resonant enhancement at the one-photon level. Similar phenomenon is observed for *o*-difluorobenzene and *p*-difluorobenzene which will be shown later.

4.3.3 *o*-Difluorobenzene

No ZEKE-PFI spectrum of *o*-difluorobenzene has previously been reported. Figure 4-5 shows the coherent two-photon ZEKE-PFI spectrum of *o*-difluorobenzene. The first lowest energy feature appearing at 75002 cm^{-1} corresponds to the adiabatic ionisation energy. The field-corrected adiabatic ionisation energy is thus 75007±5 cm^{-1}, which is in good agreement with the photoelectron spectrum[12] (9.30 eV≈75000 cm^{-1}). Strong features appearing at 554 and 752 cm^{-1} above the origin can be assigned to ν_{6a} and ν_1, respectively. The comparison of the frequencies of ν_{6a} and ν_1 of the cation with those of the neutral molecule is shown in table 4-2. Caution must be taken when comparing the intensities of $6a_0^1$ and 1_0^1 with that of the origin because the former two might be (near-resonant) enhanced at the one-photon level. The weak features at 1108, 1149 and 1196 cm^{-1} could be assigned to the first overtone of 6a and the fundamental frequencies of 9a and 7a, respectively.

Again, the strongest feature at ~75650 cm^{-1} in this spectrum is a false ZEKE peak caused by the photoelectrons having very low kinetic energies trapped by the ion cloud. Unlike in benzene, the one-photon $S_1 \leftarrow S_0$ transition 0_0^0 band is fully

allowed in *o*-difluorobenzene and is extremely strong. The two-photon energy exceeds the ionisation energy by only 650 cm^{-1}, therefore the photoelectrons produced have very low kinetic energy and thus are easily trapped.

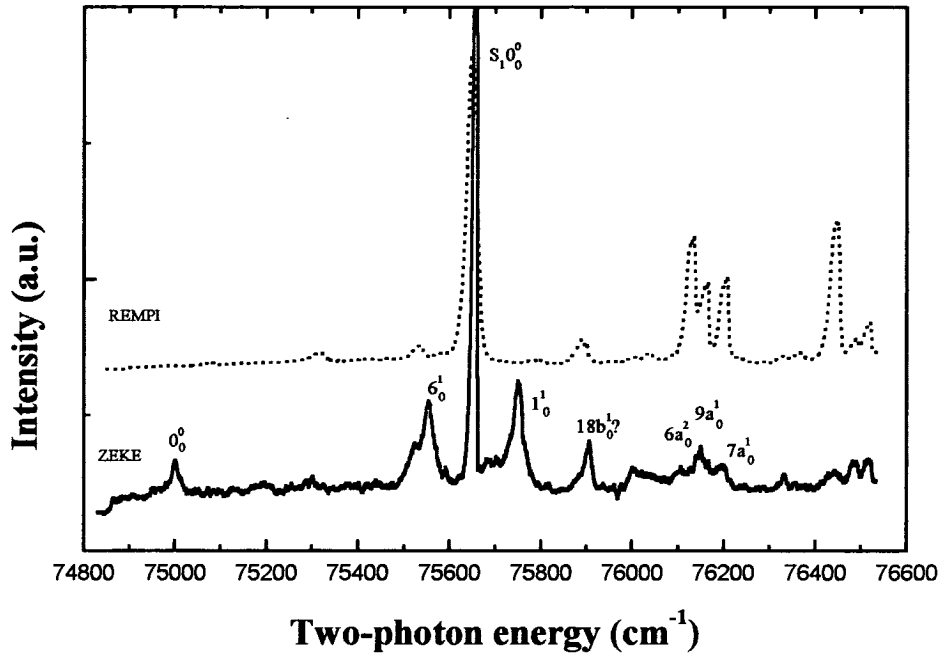

Figure 4-5: Coherent two-photon ZEKE spectrum of *o*-difluorobenzene (lower trace) together with the (1+1)REMPI spectrum recorded in the parent mass channel (upper trace).

Table 4-2: Vibrational frequencies (cm^{-1}) of *o*-difluorobenzene.

	ν_{6a}	ν_1
Ion[a]	554±5	752±5
Rydberg[b] (n=4-6)	545-555	
S_0[c]	568	762
S_1[d]	485	721

[a]This work. [b]Chapter 3 of this thesis. [c]Ref.13. [d]Ref.14.

4.3.4 *p*-Difluorobenzene

Figure 4-6 shows the coherent two-photon ZEKE spectrum of *p*-difluorobenzene. Unlike other substituted-benzenes, the S_1 state of *p*-difluorobenzene is located slightly less than (~100 cm^{-1}) halfway between the ground state of the neutral S_0 and the ground state of the cation. As a result, most of these features appearing in the spectrum are possibly caused by accidentally hitting a ZEKE excitation together with the intermediate resonance or from Coulomb effects due to resonances in S_1 state at the one-photon level. Thus the full assignments for these features in this spectrum are not possible. On the other hand, however, no significant false ZEKE signal caused by the strong one-photon resonance corresponding to $S_1 \leftarrow S_0$ 0_0^0 (~73650 cm^{-1}) is observed because a further two photons are needed to ionise the S_1 0^0 level and therefore the photoelectrons have large kinetic energies and can thus easily escape.

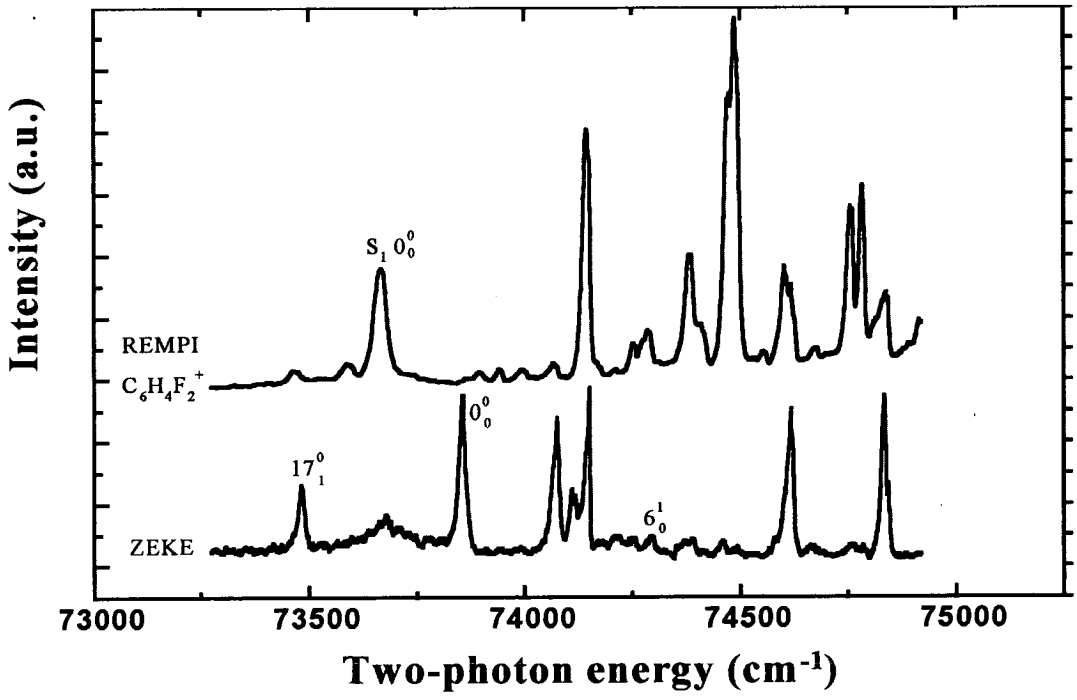

Figure 4-6: Coherent two-photon ZEKE spectrum of *p*-difluorobenzene (lower trace) together with the (1+1)REMPI spectrum recorded in the parent mass channel (upper trace).

The field dependence of the strong feature appearing at 73866 cm^{-1} indicates that it is a true ZEKE peak. The field corrected energy for this ZEKE peak is

73871±5 cm^{-1}, which is in good agreement with the adiabatic ionisation energy (73872±3 cm^{-1}) measured by Rieger et al[18] using (1+1′) ZEKE-PFI via S_1 6^1 state. Considering that the frequency of ν_{17} of the ground state S_0 of the neutral molecule is 374 cm^{-1}, the feature at -374 cm^{-1} below the origin can be assigned to 17_1^0 ZEKE peak straightforwardly.

4.4 Conclusion

By scanning the two-photon energy up to the ionisation limit, coherent two-photon ZEKE-PFI spectra of the ionic states of benzene-h_6 and -d_6 have been obtained for the first time. The vibrational structure in the ZEKE spectrum is essentially the same as in the coherent two-photon REMPI spectra of the Rydberg states but different from the (1+1′) ZEKE and (1+1′) MATI spectra reported previously.

The same technique has been applied to substituted benzenes: C_6H_5Cl, *o*-$C_6H_4F_2$ and *p*-$C_6H_4F_2$. The adiabatic ionisation energies of C_6H_5Cl and *p*-$C_6H_4F_2$ are in good agreement with previously reported values. The accurate adiabatic ionisation energy of *o*-$C_6H_4F_2$ is determined for the first time.

Among these three substitute molecules, the vibrational structure in the ZEKE spectrum of C_6H_5Cl is less influenced by the intermediate resonance in S_1 and is similar to that in the coherent two-photon REMPI spectra of Rydberg states. In the case of *p*-$C_6H_4F_2$, on the other hand, the vibrational structure in the ZEKE spectrum is heavily congested by the one-photon resonance, only the origin can be clearly identified.

4.5 References

1. K. Müller-Dethlefs, M. Sander and E.W. Schlag, *Chem. Phys. Lett.* 1984, **112**, 291.
2. K. Müller-Dethlefs and E.W. Schlag, *Annu. Rev. Phys. Chem.* 1991, **42**, 109.

3. I. Powis, T. Baer and C.-Y. Ng, eds. *High Resolution Laser Photoionisation and Photoelectron Studies*, Chichester, Wiley, 1995.

4. K. Müller-Dethlefs and E.W. Schlag, *Angew. Chem. Int. Ed.* 1998, **37**, 1346.

5. L.A. Chester, M. Sander, K. Müller-Dethlefs and E.W. Schlag, *J. Chem. Phys.* 1987, **86**, 4737.

6. R. Lindner, H. Sekiya, B. Beyl and K. Müller-Dethlefs, *Angew. Chem. Int. Ed. Engl.* 1993, **32**, 603.

7. H. Krause and H.J. Neusser, *J. Chem. Phys.* 1992, **97**, 5923.

8. A.W. Potts, W.C. Price, D.G. Streets and T.A. Williams, *Faraday, Disc. Chem. Soc.*, 1972, **54**, 168.

9. M.C.R. Cockett, J.G. Goode, K.P. Lawley and R.J. Donovan, *J. Chem. Phys.* 1995, **102**, 5226.

10. R.L. Whetten, K-J. Fu and E.R. Grant, *J. Chem. Phys.* 1983, **79**, 2626.

11. T. Wright, S. I. Panov and T.A. Miller, *J. Chem. Phys.* 1995, **102**, 4793.

12. R. Gilbert and C. Sandorfy, *Chem. Phys. Lett.* 1974, **27**, 457.

13. G. Varsanyi, *Assignments for Vibrational Spectra of Seven Hundred Benzene Derivatives*, Wiley, New York, 1974.

14. A.K. Swinn and S.H. Kable, *J. Mol. Spectrosc.* 1998, **191**, 49.

15. J.H. Callomon, T.M. Dunn and I.M. Mills, *Philos. Trans. R. Soc. London. Ser.* A. 1966, 259, 499.

16. G.H. Atkinson and C.S. Parmenter, *J. Mol. Spectrosc.* 1978, **73**, 20.

17. F.M. Garforth and C.K. Ingold, *J. Chem. Soc.* 1948, 433.

18. D. Rieger, G. Reiser, K. Müller-Dethlefs and E.W. Schlag, *J. Phys. Chem.* 1992, **96**. 12.

Chapter 5

Ionic and Rydberg States of CF_3I Studied by High Resolution Photoelectron (ZEKE-PFI) and Resonance-Enhanced Multiphoton-Ionisation (REMPI) Spectroscopy

5.1 Introduction

The Rydberg states of CF_3I were first studied by Sutcliffe & Walsh[1] who recorded the vacuum-ultraviolet (VUV) absorption spectrum and reported an *ns* Rydberg series converging on the ground state of CF_3I^+ ($\tilde{X}\,^2E_{3/2}$). This allowed the determination of the first ionisation energy as 83984 cm^{-1} (10.41 eV). Further VUV absorption work by Herzberg[2] demonstrated the involvement of the Jahn-Teller effect in the $[^2E_{3/2}]6s$ states. Taatjes et al[3]. later reported the (2+1) REMPI spectrum for the same region in conjunction with polarisation measurements. The observed transitions consisted of intense origin bands with considerably weaker vibrational structure. To higher energy Waits et al.[4], using (2+1) REMPI, observed a Rydberg state at around 66000 cm^{-1} which has no one photon analogue. This was ascribed to a *6p* Rydberg state based on the ground state ionic core ($\tilde{X}\,^2E_{3/2}$). No assignment of the extensive vibronic structure was made but it was clear that the structure differed considerably from that of the *6p* states of methyl iodide[5]. No sign of the corresponding upper spin-orbit states (two-photon energy ~ 71000 cm^{-1}) was seen due to the dominance of one-photon absorption to a repulsive state, leading to dissociation, in the same region.

CF_3I^+ has been the subject of a number of photoelectron studies[6-9]. The He(I) photoelectron spectrum (PES) was investigated by Cvitas et al.[8] with vibrational resolution (~80 cm^{-1}). Both spin-orbit components of the ground ionic

state ($\tilde{X}\,^2E_{3/2}$ and $\tilde{X}\,^2E_{1/2}$) showed relatively long progressions (up to three quanta) in two vibrational modes of 1000 and 240 cm^{-1}, corresponding to modes ν_1 (symmetric C-F stretch) and ν_3 (symmetric C-I stretch). This is in contrast to the He(I) photoelectron (PES) spectrum of CH_3I where very short vibrational progressions with dominant origin bands were observed[10]. The vertical ionisation energy (IE) for the ground ionic state of CF_3I ($\tilde{X}\,^2E_{3/2}$) was found to be 84280 cm^{-1} (10.45 eV) in relatively good agreement with that found by Sutcliffe & Walsh[1] although the adiabatic IE was estimated to be around 83100 cm^{-1} (10.30 eV).

The Rydberg[5,11-13] and ionic states[10,14-17] of the unfluorinated analogue CH_3I have been extensively studied. Several groups[5,11,12] have reported that the Rydberg spectra consist of intense origin bands with little vibrational structure. However photoelectron spectra (using both ZEKE-PFI[14-16], and time-of-flight methods[17]), obtained via the repulsive $\tilde{A}$ state, show extended vibrational structure (particularly in ν_3, the carbon-iodine stretch) due to bond stretching in the intermediate state at the one-photon level. A similar effect was observed by Min et al[13] in a two-colour REMPI study of the Rydberg states of CH_3I using a repulsive intermediate state.

In this chapter, the high resolution ZEKE-PFI[18] photoelectron spectrum of CF_3I obtained via coherent two-photon (one-colour) excitation, and also by using the $[^2E_{3/2}]6p$ Rydberg states as resonant intermediates in a two-colour process will be presented. The *6p* Rydberg states of CF_3I have also been studied using both two- and three-photon excitation techniques in combination with polarisation measurements. This approach has allowed the unambiguous assignment of the majority of the vibronic structure of the *6p* Rydberg states.

5.2 Experimental

All (one- and two-colour) ZEKE-PFI experiments and (2+1) REMPI of the $[^2E_{3/2}]6p$ manifold of the Rydberg states of CF_3I were performed using the ZEKE apparatus. The details of this apparatus have been described in chapter 2, thus only additional details will be given here. With the ZEKE apparatus, a mixture of CF_3I

(Fluorochem, 50-200 Torr) and Helium (200-400 Torr) was expanded through a pulsed nozzle and then skimmed to produce a cooled, collimated molecular beam. For one-colour coherent two-photon ZEKE-PFI experiments, laser dyes Coumarin 460 and 480, and a mixture (50/50) of them, were used in the dye laser (PDL-2) pumped by the third harmonic (355 nm) of an Nd:YAG laser to provide the required fundamental wavelengths. The fundamental output was then frequency doubled using a BBO crystal. The frequency doubled radiation was separated from the dye fundamental by a Pellin Broca prismatic beam separator. The tracking of the BBO crystal was manually controlled when monitoring the power of a small part of the frequency doubled light using a photodiode and a oscilloscope. For one-colour (2+1)REMPI experiments, laser dye R640 and a dye mixture of R590 with R610, were used in a PDL-3 dye laser. This was pumped by 532 nm radiation from the Nd:YAG laser to provide the required fundamental wavelengths which were then frequency doubled using a K*DP crystal. For two-colour ZEKE-PFI experiments, different combinations (both dye lasers pumped by 532 nm light or one by 532 nm and the other by 355 nm) of the laser pumping arrangements were used depending on the wavelengths required. Calibration of dye fundamentals was made using the optogalvanic lines from a neon lamp. Circular and linear polarised light was produced using a Soleil Babinet polariser.

5.3 Results

5.3.1 Coherent Two-Photon ZEKE-PFI Spectrum of CF_3I^+

Figure 5-1 illustrates the coherent two-photon one-colour ZEKE-PFI photoelectron spectrum of CF_3I in the range 83300-87200 cm^{-1}, showing the lower spin-orbit component of the ionic ground state ($\tilde{X}\,^2E_{3/2}$). It is similar to the conventional He(I) PES[8] in that it is dominated by the symmetric vibrational modes ν_1 (973 cm^{-1}), ν_2 (735 cm^{-1}) and ν_3 (205 cm^{-1}) and their combinations. Vibrational assignments are readily made by reference to previous work on the He(I) photoelectron spectrum[8] and the known neutral ground state frequencies[20]. The

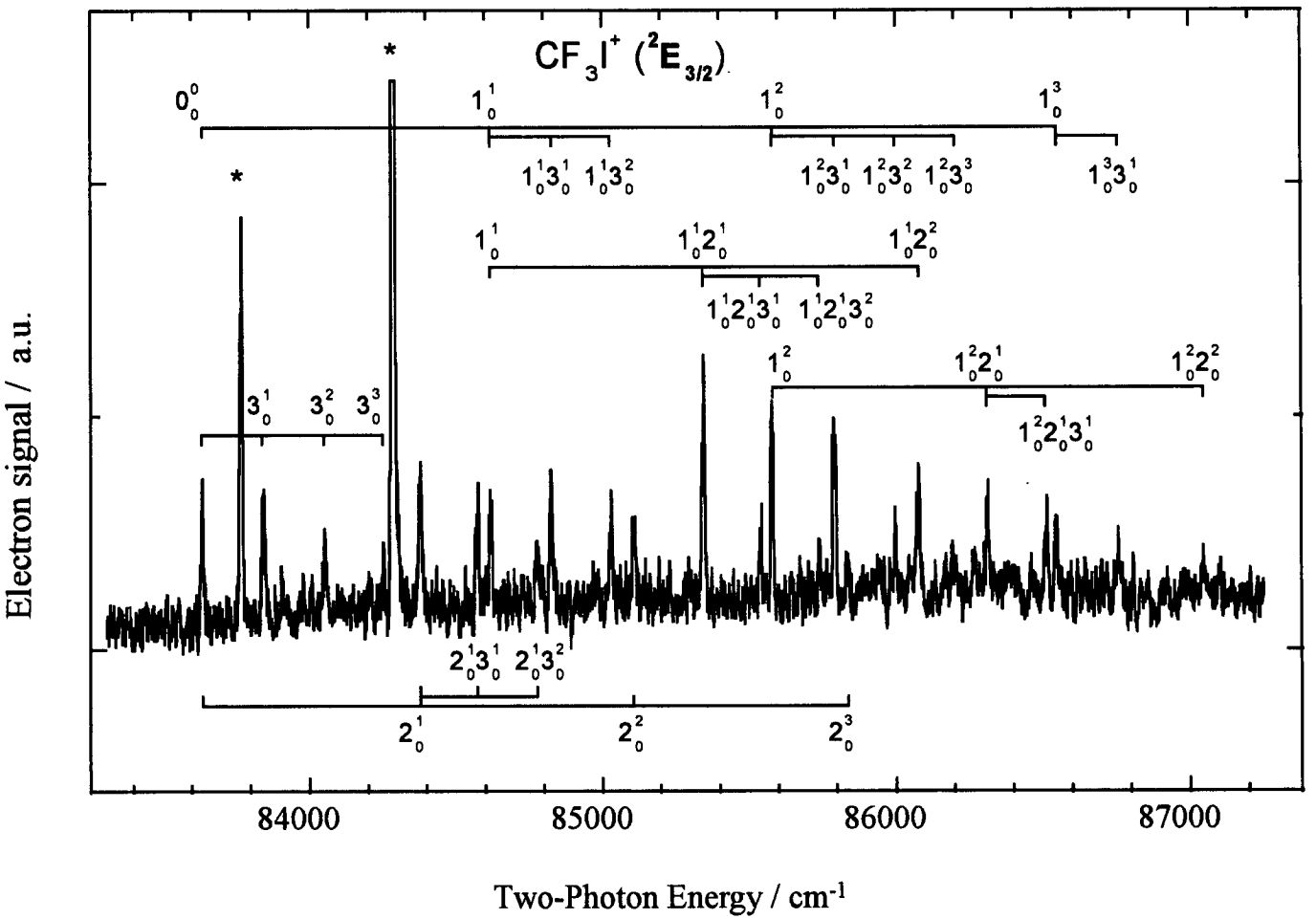

Figure 5-1: The coherent two-photon one-colour ZEKE-PFI spectrum of CF_3I^+ ($^2E_{3/2}$). (* indicates an atomic iodine line).

Table 5-1: Peak positions for the $\tilde{X}\,^2E_{3/2}$ state of CF_3I^+ obtained by ZEKE-PFI.

Peak Position / cm^{-1}	Assignment
83652[a, b]	0^0
83857[a, b]	3^1
83873[b]	6^1
84062[a, b]	3^2
84078[b]	$6^1 3^1$
84199[b]	5^1
84263[a, b]	3^3
84280[b]	$6^1 3^2$
84320[b]	6^3
84386[a, b]	2^1
84404[b]	$5^1 3^1$
84461[b]	3^4
84575[a]	$2^1 3^1$
84625[a, b]	1^1
84787[a]	$2^1 3^2$
84826[a]	$1^1 3^1$
85026[a]	$1^1 3^2$
85110[a]	2^2
85352[a]	$1^1 2^1$
85546[a]	$1^1 2^1 3^1$
85585[a]	1^2
85745[a]	$1^1 2^1 3^2$
85797[a]	$1^2 3^1$
85840[a]	2^3
86003[a]	$1^2 3^2$
86081[a]	$1^1 2^2$
86319[a]	$1^2 2^1$
86518[a]	$1^2 2^1 3^1$
86551[a]	1^3
86761[a]	$1^3 3^1$
87050[a]	$1^2 2^2$

[a]Peak seen in (1+1) ZEKE-PFI. [b]Peak seen in (2+1′) ZEKE-PFI. All values have been corrected for the field shift.

identification of these modes is an important factor in the assignment of the $[^2E_{3/2}]6p$ Rydberg states as described later. Peak positions with assignments, are shown in table 5-1. Values are corrected for the field shift (~ 5 cm^{-1}). No sign of the upper spin-orbit component ($\tilde{X}\,^2E_{1/2}$) could be found at higher energy. The coherent two-photon ZEKE-PFI photoelectron spectrum of CF_3I is thus very different to that of CH_3I, where greatly extended vibrational progressions in both spin-orbit states were observed[14-16].

Two intense peaks (denoted * in figure 5-1) can be assigned to atomic iodine transitions[21]. These have been observed in similar studies of other iodine containing molecules[14-16] and result from one-photon dissociation of CF_3I through the repulsive Ã state, followed by two-photon ionisation of the atomic fragment. However, no transitions were found which could be assigned to the other photodissociation fragment, the CF_3 radical.

5.3.2 Resonance-Enhanced Multiphoton Ionisation Spectra of CF_3I

Figure 5-2 shows the (2+1) REMPI spectrum of CF_3I in the region 65300-68100 cm^{-1} encompassing the *6p* Rydberg states based on the $\tilde{X}\,^2E_{3/2}$ state of the ionic core. Vibronic assignments were made using polarisation measurements and information obtained from photoelectron spectroscopy (see below): the assignments are presented in table 5-2.

Rotational line strengths for two-photon transitions have been derived by Bray and Hochstrasser[22] for systems in which Ω remains a good quantum number. They showed that, with one exception, the intensities of all lines of all branches of transitions from an Ω=0 state should be 1.5 times greater under circular polarisation compared with linear polarisation. The exception is the Q branch of an Ω=0→0 transition, where line intensities can decrease on going from linear to circular polarisation. Thus any lines which display this behaviour must be due to transitions to an Ω=0 state.

Only the bands in the higher energy region (above 66800 cm^{-1}) of the two-photon excitation spectrum of CF_3I show any decrease in intensity under circularly polarised light, as illustrated in figure 5-3. Hence these bands are assigned as being

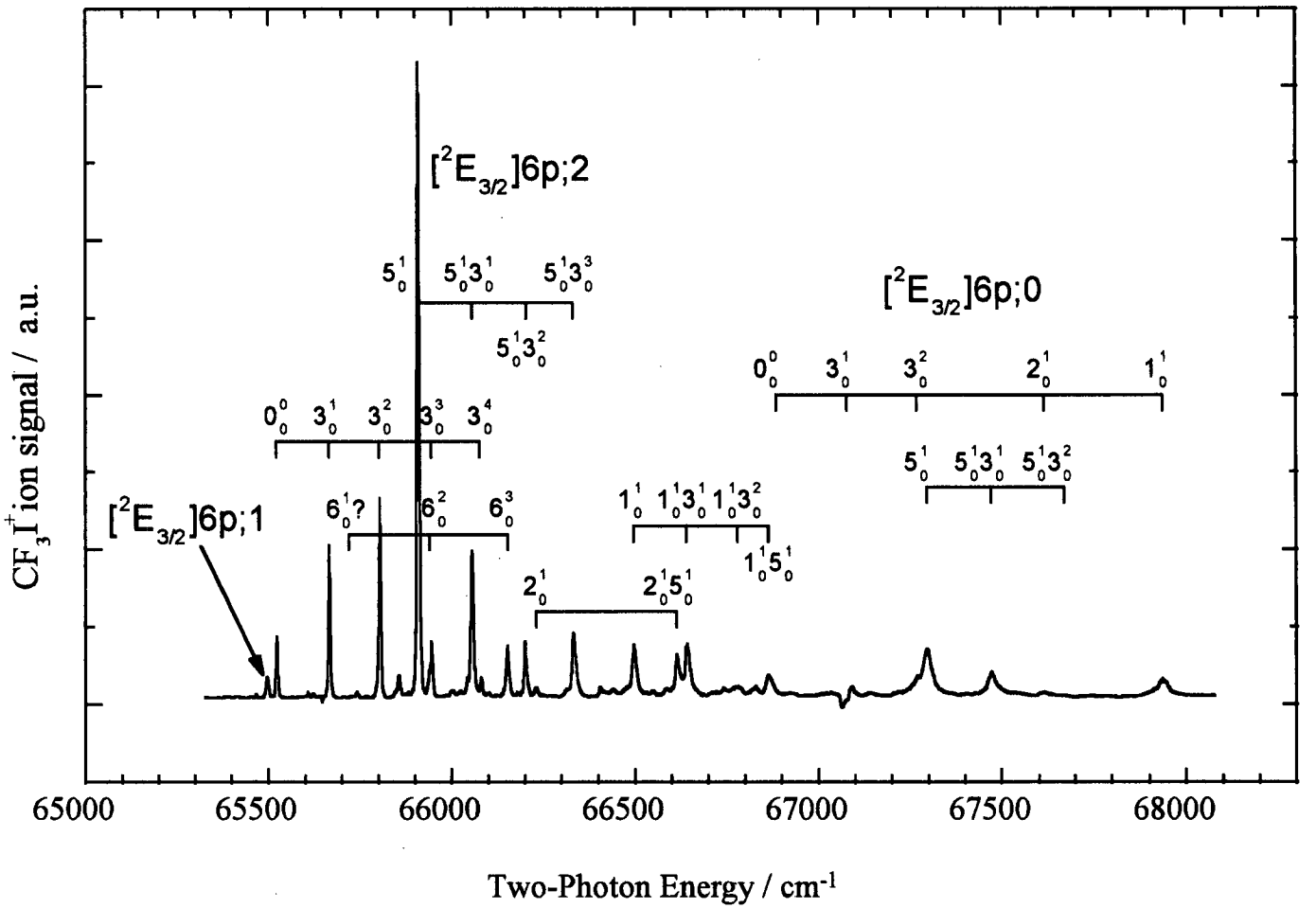

Figure 5-2: The (2+1) REMPI spectrum of CF_3I in the region 65300-68100 cm^{-1}. The assignments shown are for three states with Ω=0, 1 & 2.

Table 5-2: Peak positions and assignments for the [$^2E_{3/2}$] 6p Rydberg states of CF_3I.

Peak Position / cm^{-1}	**Assignment** [Ω] ν
65496	[1]
65522	[2] 0_0^0
65666	[2] 3_0^1
65804	[2] 3_0^2
65908	[2] 5_0^1
65940 (shoulder)	[2] 6_0^2
65946	[2] 3_0^3
66056	[2] $5_0^1 3_0^1$
66080	[2] 3_0^4
66153	[2] 6_0^3
66201	[2] $5_0^1 3_0^2$
66231	[2] 2_0^1
66331	[2] $5_0^1 3_0^3$
66497	[2] 1_0^1
66613	[2] $2_0^1 5_0^1$
66641	[2] $1_0^1 3_0^1$
66779	[2] $1_0^1 3_0^2$
66864	[2] $1_0^1 5_0^1$
66885 (not seen)	[0] 0_0^0
67077	[0] 3_0^1
67268 (shoulder)	[0] 3_0^2
67295	[0] 5_0^1
67471	[0] $5_0^1 3_0^1$
67614	[0] 2_0^1
67668	[0] $5_0^1 3_0^2$
67938	[0] 1_0^1

those of the $[^2E_{3/2}]6p;0$ state with a possible origin around 66885 cm^{-1} (note however that the origin band is very weak or missing). Figure 5-3 illustrates two important points. First, this state exhibits consistently broader peaks than those of the other states probably due to selective predissociation. A similar broadening was observed for the $[^2E_{1/2}]6s;0$ state[3]. Second, the vibrational structure and the overall intensity pattern of the $\Omega=0$ component is essentially the same as that of the $\Omega=2$ component. More specifically, both components show a very strong 5_0^1 vibrational peak, very weak origin peak and long progression in ν_3.

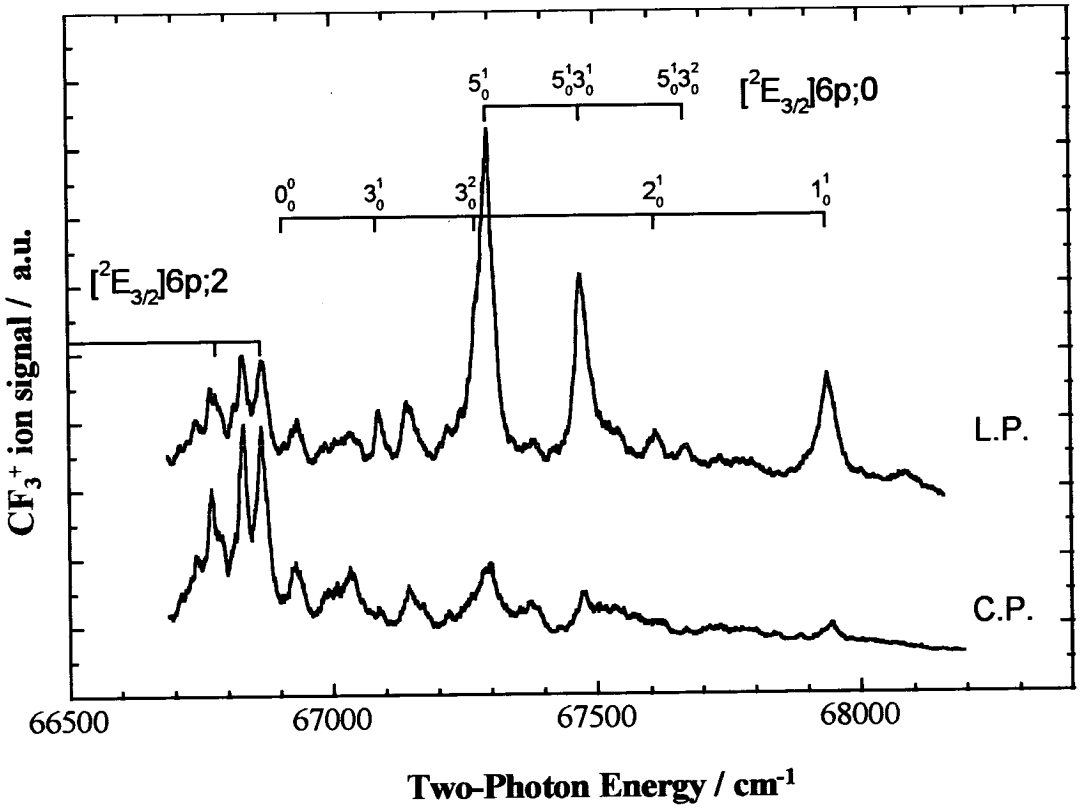

Figure 5-3: (2+1)REMPI spectra of CF_3I using linearly (LP) and circularly (CP) polarised light.

To higher energy no sign of the upper spin-orbit components was observed due to a rise in background ionisation from CF_3 and atomic iodine fragments. These fragments are formed by one-photon dissociation through the $\tilde{A}$ state of CF_3I. No signals corresponding to the molecular ion were seen in this region.

Three-photon resonant REMPI in conjunction with polarisation measurements was required to distinguish between different states in the lower energy region. This experiment was performed by J. Hennessy[26] using the REMPI apparatus. Figure 5-4 shows the (3+1) REMPI spectrum in the region 65200-65800 cm^{-1} recorded using both linear and circular polarisation. The selection rules for three-photon polarisation[23] are more complex than those for the two-photon case but they do allow Ω=1 states to be distinguished from Ω=2 states. Transitions involving all rotational branches for Ω=0→2 or 3 show an increase in intensity by a factor of 2.5 with circular polarisation while the P, Q and R branches of Ω=0→0

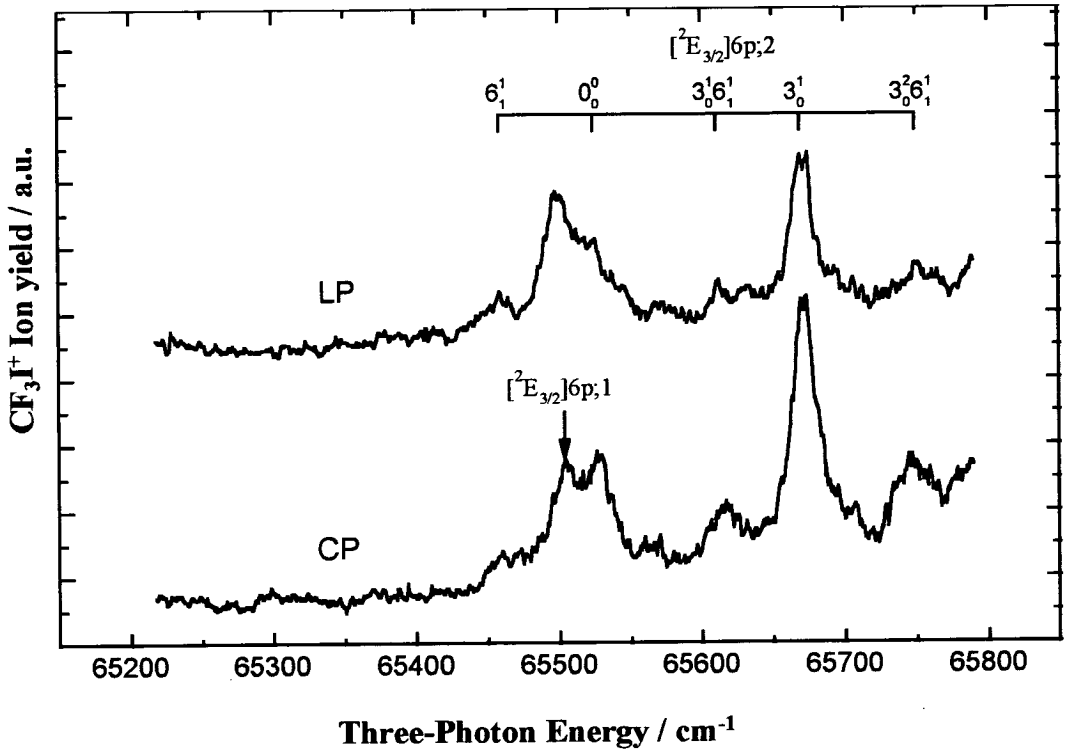

Figure 5-4: (3+1)REMPI spectra of CF_3I using linearly (LP) and circularly (CP) polarised light.

and 1 transitions show an increase of up to 2.5 but usually less than 1. It is obvious that the majority of the peaks in figure 5-4 show an increase in intensity when circular polarisation is used relative to the peak at 65496 cm^{-1} which remains unaffected by the polarisation change. Thus this transition is assigned to an Ω=1 state, although it is hard to tell whether it is an electronic origin or part of a

vibrational progression. It is noted that this peak could not be assigned as a hot band since the main hot band structure is red-shifted by around 50 cm^{-1} (corresponding to ν_6), as seen in the structure associated with the Ω=2 state. The band in question lies some 20 cm^{-1} to the red of the origin of the Ω=2 state, an energy difference which does not correspond to any possible change in vibrational frequency on going from the ground state to the Rydberg state. The remaining peaks are then assigned to an Ω=2 system. Vibrational assignments require further information and are discussed in the next section. However it is clear that the spectrum of the *6p* Rydberg states of CF_3I is very different to that of CH_3I[5], and to the *6s* states of CF_3I itself[3] where the origin band is the dominant feature.

Both two- and three-photon excitation schemes show identical vibrational structure for the *6p* states eliminating bond stretching at the one-photon level in the (2+1) REMPI spectra as a possible explanation of the unusual vibrational structure. Additionally two-colour REMPI excitation schemes with the first photon on or off resonance with the repulsive $\tilde{A}$ band also give identical spectra to those shown in figures 5-2 and 5-4.

5.3.3 (2+1′) ZEKE-PFI spectra using the 6p Rydberg states as resonant intermediates

High resolution two-colour (2+1′) ZEKE-PFI photoelectron spectra of ground state CF_3I^+ ($\tilde{X}\,^2E_{3/2}$) were recorded using various vibrational levels of the Ω=2 system as resonant intermediates. The field-free adiabatic ionisation energy was measured to be 83652±2 cm^{-1}, a considerable improvement over previous determinations[1,8]. These spectra, shown in figures 5-5 & 5-6, play a major role in the vibronic assignment of the $[^2E_{3/2}]6p;2$ system. Peak positions, corrected for field effects, with assignments are given in table 5-1. It is found that this Rydberg state has a significantly different geometry to that of the ion. This is illustrated by the non-diagonal transitions from the Rydberg state to the ion, seen in figures 5-5 & 5-6. In general, Rydberg states can be considered as an ionic core with an electron at long range which has little effect on the core. Removing such an electron causes

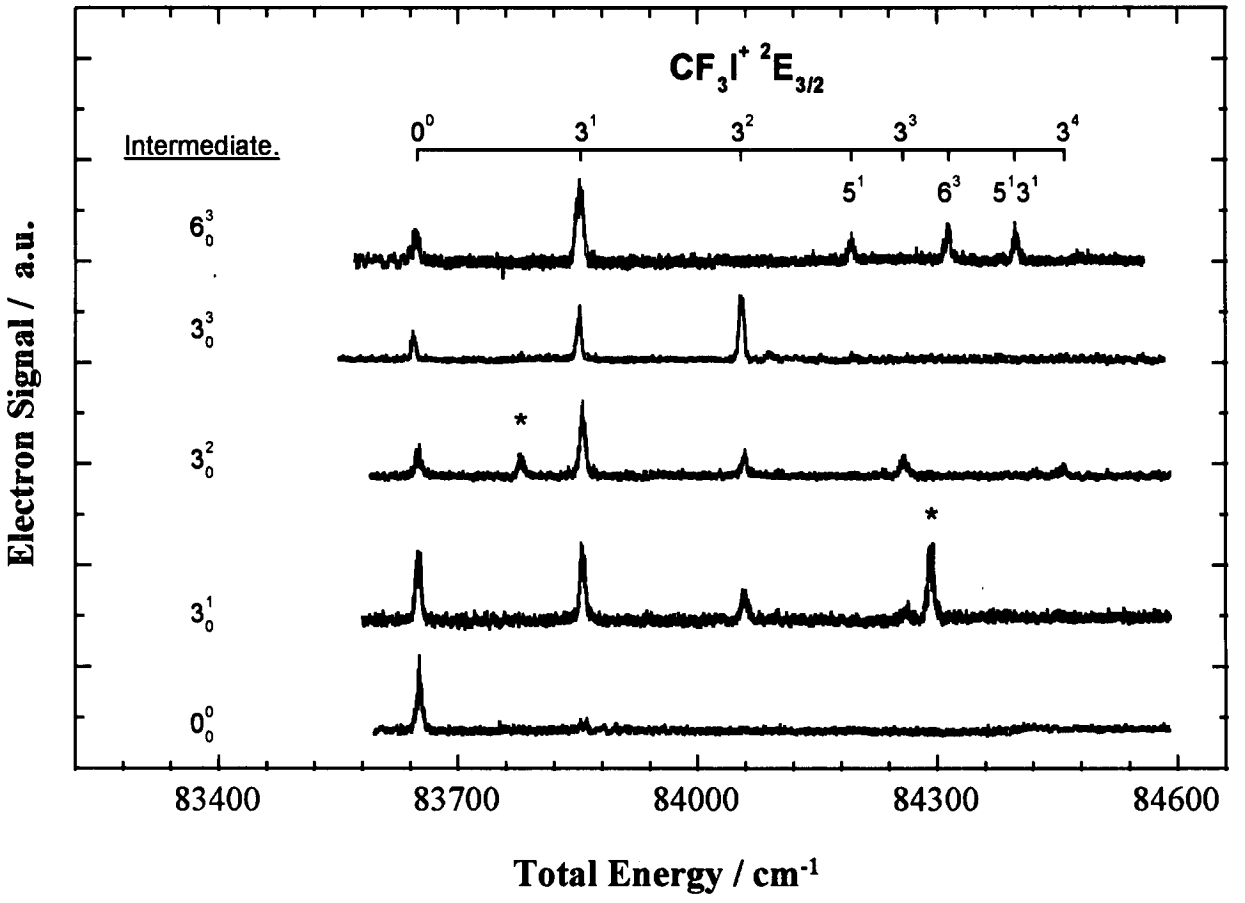

Figure 5-5: The (2+1′) ZEKE-PFI spectra of CF_3I^+ ($^2E_{3/2}$) via various members (0^0_0, 3^1_0, 3^2_0, 3^3_0 and 6^3_0) of the [$^2E_{3/2}$]6p;2 Rydberg state. (* indicates an atomic iodine line).

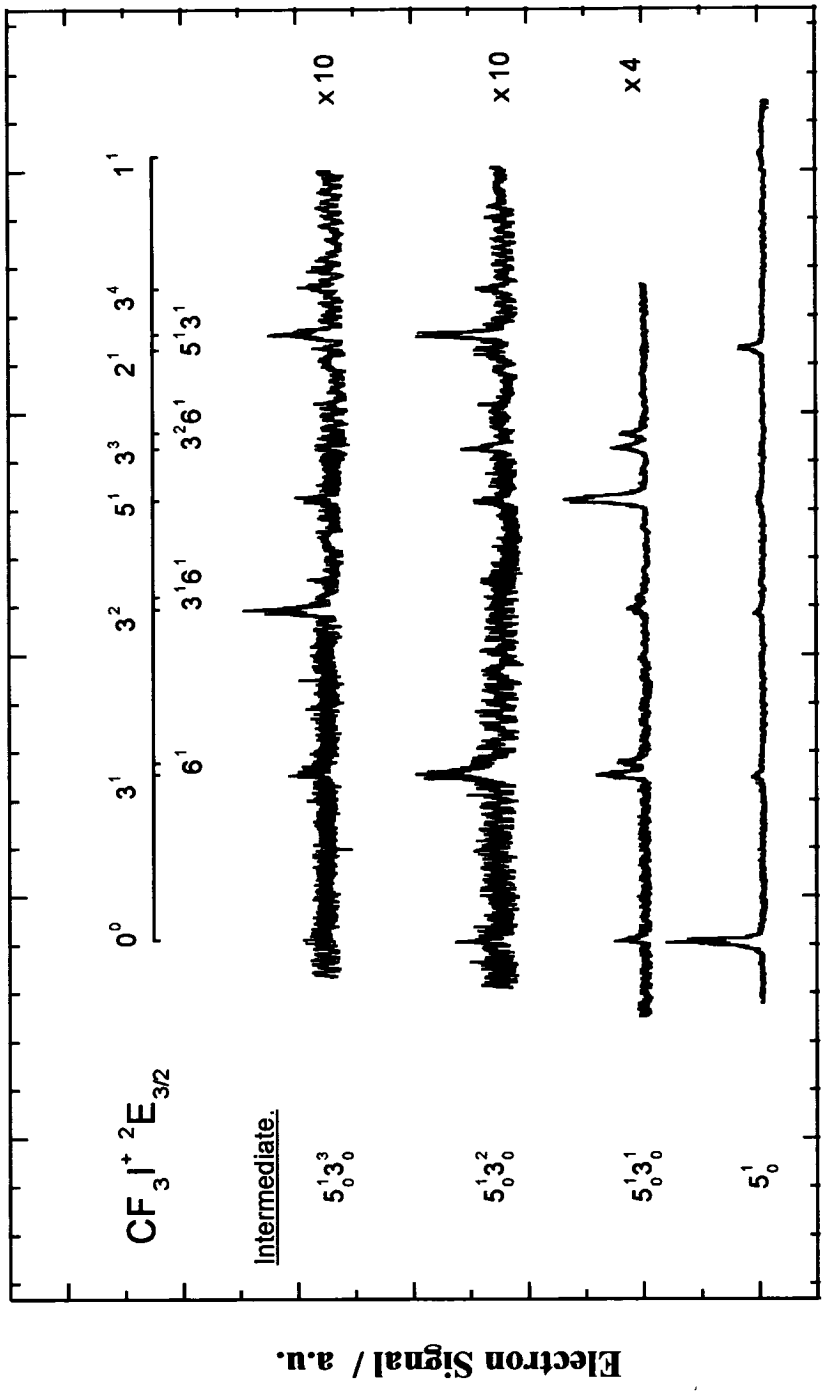

Figure 5-6: (2+1') ZEKE-PFI of CF_3I^+ ($^2E_{3/2}$) via various members (5^1_0, $5^1_0 3^1_0$, $5^1_0 3^2_0$ and $5^1_0 3^3_0$) of the [$^2E_{3/2}$]6p,2 Rydberg state.

little change in the geometry of the ionic core with the result that the most intense peaks in the photoelectron spectrum are diagonal transitions (i.e. $\Delta v=0$). However it is clear from the present work that the *6p* Rydberg states bear little resemblance to the ground ionic state of CF_3I. In particular ν_3 has values of 281 cm^{-1}, 144 cm^{-1} and 205 cm^{-1} in the neutral ground state[20], $[^2E_{3/2}]6p;2$ state and ionic ground state, respectively, indicating a substantial distortion of the Rydberg state. However the (2+1′) ZEKE-PFI data can still be used to identify which modes are excited in the resonant intermediate state. Vibrational frequencies obtained from the one-colour ZEKE-PFI experiment described above give values for all three symmetric modes (ν_1, ν_2 and ν_3) of the ion. The ZEKE-PFI photoelectron spectra obtained via the transitions at 65522, 65666, 65804 and 65946 cm^{-1} all show progressions in ν_3 alone (see figure 5-5). Hence these peaks are assigned to the electronic origin and a progression in ν_3 with a spacing of 144 cm^{-1}. A progression with similar spacing based on the transition at 65908 cm^{-1} which shows a similar intensity pattern in ν_3 in the photoelectron spectra (figure 5-6) can also be seen. This is assigned to a progression in ν_3 in combination with one quantum of ν_5 (386 cm^{-1}). The use of an asymmetric vibration in the intermediate state allows accessing similar modes in the ion such as ν_5 (547 cm^{-1}) and ν_6 (221 cm^{-1}). Also, a weak progression in ν_6 in the intermediate state can be seen. The photoelectron spectrum obtained by pumping the transition at 66153 cm^{-1} shows a peak corresponding to three quanta of ν_6 (figure 5-5); the intermediate level is thus assigned as 6_0^3. All of the mode frequencies in the $[^2E_{3/2}]6p;2$ state, and in particular ν_3 and ν_5, are reduced relative to both neutral[20] and ionic ground state values, indicating a sizeable distortion of the molecule in the $[^2E_{3/2}]6p;2$ state.

The major uncertainty which arises from the ZEKE-PFI study is the assignment of the most intense band in the (2+1)REMPI spectrum at 65908 cm^{-1}. The ZEKE-PFI spectrum obtained via this intermediate (figure 5-6) shows an intense origin band and weaker vibrational structure. In particular, The 5_0^1 band is very weak, which is usually indicative of an origin in the intermediate state. If this is the case, the strongest band at 65908 cm^{-1} in figure 5-2 would be a second $\Omega=2$

origin. Adopting this second assignment would change the assignment of the progression in figure 5-2 labelled $5_0^1 3_0^n$ to $5_0^1 3_0^{n-1}$, but still based on the first origin, with no progressions in ν_3 of ν_5 based on the second Ω=2 origin at 65908 cm^{-1}. Consequently, ν_5 in the first Ω=2 state would increase to 534 cm^{-1}, close to that of the ground state[20] and of the ion and hence would not be expected to show as much vibrational activity as observed. However, as will be discussed in the next section, based on simple theoretical considerations and the similarity of the vibrational structure between Ω=0 and Ω=2, the alternative assignment described above is very unlikely.

In addition, a reduced value of ν_3 in the Ω=0 state (ν_3~190 cm^{-1}) can be seen, indicating that a distortion also occurs in this Ω=0 system. Table 5-3 gives a summary of the vibrational frequencies for all of the states studied as well as those of the *6s* states[3] and the neutral ground state[20] for comparison.

Table 5-3: Vibrational frequencies (in cm^{-1}) for several states of CF_3I and CF_3I^+.

Mode	$\tilde{X}\ ^1A_1$ [a]	$[^2E_{3/2}]6s;1$ [b]	$[^2E_{3/2}]6p;2$	$[^2E_{3/2}]6p;0$	$CF_3I^+(\tilde{X}\ ^2E_{3/2})$
ν_1	1075	970	974	1053	973
ν_2	743	681	709	730	734
ν_3	286	232	144	192	205
ν_4	1187	1282	-	-	-
ν_5	540	525	386	410	547
ν_6	262	223	210	-	221

[a]Ref.20. [b]Ref.3.

5.4 Discussion

5.4.1 The Electronic Structure of the 6p cluster of Rydberg States

The Rydberg states are based on the two spin-orbit states of the core ($^2E_{3/2}$ and $^2E_{1/2}$). The microconfigurations of the π^3 lone pair electrons on the I atom are:

$$^2E_{3/2} = |1^+1^- - 1^+|$$

$$^2E_{1/2} = |1^+1^- - 1^-|$$

Combining these two core states with a Rydberg electron in a *6p* orbital, which may have $\lambda = 0(p\sigma)$ or $\lambda = \pm 1(p\pi)$, gives the following Ω states, Ω=3, 2(2), 1(2) and $0^{\pm}$ on the [3/2] core and Ω=2, 1(3) and $0^{\pm}(2)$ on the [1/2] core. One of the two [3/2]Ω=2 states, one of the two [3/2]Ω=1 states and the [3/2] 0^+ state exhibit mixed singlet-triplet character. The rest are pure triplets. It has generally been observed in the REMPI spectroscopy of the diatomic halogens[24,25] that strong two-photon $Ry \leftarrow\leftarrow X$ transitions are only observed if the upper state has strong singlet character, and thus it is expected that three electronic origins would be accessible in each [3/2]np cluster, having Ω=2, 1 and 0. The second [3/2] Ω=2 state would have the dominant configuration $|1^+1^-1^+|p\sigma^+$ and thus be a pure triplet.

There is a new factor in the electronic structure of CF_3I and CH_3I that does not appear in the diatomic halogens. In the latter, there is only one unoccupied valence orbital, the σ^* (σ_u in the homonuclear diatomic case) anti-bonding orbital; all the higher virtual orbitals are Rydberg in character. But in CF_3X and CH_3X there are unoccupied valence orbitals of e and a_1 symmetry formed from the antibonding combinations of the three F($p\sigma$) (directed along the three C-F vectors) with the C($p\sigma$) and $p\pi$ orbitals. Although high in energy, the virtual e orbitals will combine to some small extent with the lone pair e atomic orbitals on the halogen atom making the latter slightly bonding in the C-X co-ordinate.

5.4.2 Interpretation of the spectra

The coherent two-photon (one-colour) ZEKE-PFI spectrum in figure 5-1 is very similar to the He(I) PES[8]. In both, up to three quanta of excitation in ν_1, ν_2 and ν_3 are observed, reflecting the direct $< X^+|X >$ Franck-Condon factors. Like the positive ions of other alkyl halides[15], the frequency of modes involving the C-I stretch is appreciably reduced in the ion compared with the ground state of the neutral species. In CF_3I^+, this is particularly apparent indicating a larger amount of mixing between the valence orbitals of the CF_3 fragment and the iodine lone pairs. The main difference between the ZEKE-PFI and He(I) PES spectra is that the spin-orbit excited state of the ion is not detected. This might be due to (i) rapid spin-orbit autoionisation of the high *n* low *l* precursor ZEKE states or (ii) further up-pumping of these states to a repulsive continuum that detaches the ZEKE electron.

Two possible assignments of the REMPI spectrum were put forward in the results section. The first interpretation was that there is only one Ω=2 origin, which has an anomalously strong 5_0^1 band with a progression in ν_3 ($5_0^1 3_0^n$) built on it. Weaker Ω=0 and 1 origins are also observed. The alternative interpretation invoked two Ω=2 origins of comparable intensity. The (2+1′) ZEKE-PFI spectra on balance favour the second interpretation. The similarity between the (2+1)REMPI spectra of Ω=0 and Ω=2 systems, on the other hand, indicates that there is no reason to involve a second Ω=2 origin (without any vibrational progression based on that) to interpret the spectra. The simple theoretical arguments, based on the dominant spin multiplicity of the Rydberg components, favour only one readily accessible Ω=2 state. It is thus concluded that only one Ω=2 component (having 1:1 singlet-triplet mixture) was observed. The appearance of anomalously strong 5_0^1 bands and very weak origins in both Ω=2 and Ω=0 components suggests that the $[^2\Pi_{3/2}]6p$ Rydberg state of CF_3I is heavily distorted.

Both Ω=2 and Ω=0 components especially the former exhibit an anomalously low frequency in ν_3 that is not observed in CH_3I. One explanation might be the accidental mixing of the Rydberg configuration with an adjacent state having a configuration $\sigma^2\pi^2\sigma^{*2}$ ($^1\Delta_2$). The σ^* orbital is mainly centred on the C

atom, so this configuration is characteristic of an ion-pair state correlating with $CF_3^- + I^+$. A small admixture of this configuration would weaken the C-I bond and hence lower ν_3, but other modes involving the CF_3 bend and stretch (including ν_5) might not be much affected.

5.5 Conclusion

The CF_3I molecule has been studied by a combination of threshold (ZEKE-PFI) photoelectron spectroscopy and polarisation dependent multiphoton ionisation spectroscopy. The ionisation energy of CF_3I was accurately determined and the ground ionic state vibrational frequencies (ν_1, ν_2, ν_3, ν_5, & ν_6) have been obtained. With these aids most of the electronic and vibrational structure of the $[^2E_{3/2}]6p$ Rydberg states observed in the REMPI spectra have been assigned unambiguously. Ω=2, 1, & 0 electronic components are present, the Ω=2 bands being by far the most prominent. Both the Ω=2 and Ω=0 components show an anomalously low frequency in the C-I stretch mode that is not seen in CH_3I, pointing to a severe distortion of the potential surface in this co-ordinate. Some admixture of ion-pair character into the electronic wave function is suggested as the cause. ZEKE-PFI photoelectron spectra obtained by using several different vibronic components of the *6p* cluster support the conclusion that the $[^2\Pi_{3/2}]6p$ Rydberg state of CF_3I is heavily perturbed.

5.6 References

1. L.H. Sutcliffe and A.D. Walsh. *Trans. Faraday Soc.* 1961, **57**, 873.
2. G. Herzberg. *Disc. Faraday Soc.* 1963, **35**, 7.
3. C.A. Taatjes, J.W.G. Mastenbroek, G. van den Hoek, J.G. Snijders and S. Stolte. *J. Chem. Phys.* 1993, **98**, 4355.
4. L.D. Waits, R.J. Horowitz, R.G. Daniel, J.A. Guest and J.R. Appling. *J. Chem. Phys.* 1992, **97**, 7263.

5. M.R. Dobber, W.J. Buma and C.A. de Lange. *J. Chem. Phys.* 1989, **132**, 257.

6. R.L. Asher and B. Ruscic. *J. Chem. Phys.* 1997, **106**, 210.

7. R. Bombach, J. Damacher, J.P. Stadelmann, J. Vogt, L.R. Thorne and J.L. Beauchamp. *Chem. Phys.* 1982, **66**, 403.

8. T. Cvitas, H. Gusten, L. Klasinc, I. Novadj and H. Vancik. *Z. Naturforsch.* 1978, **33a**, 1528.

9. J.D. Bozek, G.M. Bancroft, J.N. Cutler, K.H. Tan, B.W. Yates and J.S. Tse. *Chem. Phys.* 1989, **132**, 257.

10. L. Karlsson, R. Jadrny, L. Mattsson, F.T. Chau and K. Siegbahn. *Phys. Scr.* 1977, **16**, 225.

11. A.Gedanken, M.B. Robin and Y. Yafet. *J. Chem. Phys.* 1982, **76**, 4798.

12. M. Kawasaki, H. Sato, T. Kikuchi, S. Kobayashi and T. Arikawa. *J. Chem. Phys.* 1987, **87**, 5739.

13. Z. Min, T. Ridley, K.P. Lawley and R.J. Donovan. *J. Photochem. Photobiol. Part A: Chem.* 1996, **100**, 9.

14. A. Strobel, A. Lochschmidt, I. Fischer, G. Niedner-Schatteburg and V.E. Bondybey. *J. Chem. Phys.* 1993, **99**, 733.

15. A. Strobel, I. Fischer, A. Lochschimdt, K. Muller-Dethlefs and V.E. Bondybey. *J. Phys. Chem.* 1994, **98**, 2024.

16. Y.F. Zhu and E.R. Grant.*J. Phys. Chem.* 1993, **97**, 9582.

17. T. Schultz and I. Fischer. *J. Phys. Chem. A.* 1997, **101**, 5031.

18. K. Muller-Dethlefs and E.W. Schlag. *Annu. Rev. Phys .Chem.*1991, **42**, 109.

19. M.C.R. Cockett, R.J. Donovan and K.P. Lawley. *J. Chem. Phys.* 1996, **105**, 3347.

20. H. Burger, K. Burczyk, H. Hollenstein and M. Quack. *Mol. Phys.* 1989, **55**, 255.

21. C.E. Moore, Atomic Energy Levels, Nat. Stand. Ref. Data. Ser. (US, Nat. Bur. Stand.), **35**, 1971.

22. R.G. Bray and R.M. Hochstrasser. *Mol. Phys.* 1976, **31**, 1199.

23. J.P. Berger, J. Baker and S. Couris. *J. Chem. Phys.* 1996, **105**, 6147.

24. R.J. Donovan, A.C. Flexen, K.P. Lawley and T. Ridley. *Chem. Phys.* 1998, **226**, 217.

25. R.J. Donovan, R.V. Flood, K.P. Lawley, A.J. Yencha and T. Ridley. *Chem. Phys.* 1992, **164**, 439.

26. J. Hennessy, PhD thesis, the Edinburgh University, 1999.

Chapter 6

The Spectroscopy of Near-Dissociation Ion-Pair States of ICl

6.1 Introduction

Photodissociative ion-pair formation, $AB + h\nu \rightarrow A^+ + B^-$, was first studied in the gas phase in the 1930s[1]. This dissociation channel is available to all molecules if the anion B^- is stable to autodetachment and about 50 examples of photoion production have been found[2]. Part of the difficulty in studying this type of heterolytic bond breaking is that the threshold energy, $D_0(X) + IE(A) - EA(B)$, is considerably higher than that for homolytic fission, $D_0(X)$, and frequently lies above the first ionization potential of the molecule. In these circumstances, dissociation on the ion-pair surface must compete with electronic autoionisation.

Earlier studies of photoion-pair formation using single photon excitation probed the region just above the dissociation threshold. Dibeler et al.[3], and later Berkowitz et al.[4] recorded the F^- signal in the threshold region of HF and F_2. The latter group showed the anion production spectrum to be structured in the energy range between the first molecular IE ($F_2 \rightarrow F_2^+ + e$) and the threshold for $F_2 \rightarrow F^+ + F^-$, some 0.1 eV lower.

In order to penetrate below the ionic dissociation threshold, field extraction of the bound ion-pair states must be used. An applied DC field in effect lowers the IE releasing pairs of ions trapped in very high vibrational levels of the Coulomb well binding the ions. This effect was demonstrated by Pratt et al[5] for H_2, who determined the field dependence of the free ion threshold characteristic of a Coulomb potential. Martin and Hepburn[6] found that these sub-threshold ion-pair states in O_2 could be converted into long-lived states, analogous to "ZEKE states" (i.e., high Rydberg electronic states)[7], and designated the technique threshold ion-

pair production spectroscopy as TIPPS. Pulsed field extraction (PFI) also showed that stabilised states were created in HCl[8]. The process is one of converting the initially prepared high υ low J ion-pair states into lower υ high J states in which the anion and cation are kept apart by the high centrifugal barrier and are protected from radiative decay. This conversion probably occurs through perturbation by stray fields or distant collisions with ions in the plasma created at the laser focus and it is remarkable that it can occur for heavy ions on a timescale that is presumably shorter than either the radiative lifetime or the lifetime for predissociation to all the neutral product channels. The exact analogy between these stabilised ion-pair states and ZEKE states suggests calling them ZIKE (zero ion kinetic energy) states.

In this work, the ZIKE-PFI technique is extended to the multiphoton ion-pair spectroscopy of ICl. Compared to the single photon excitation used by Martin and Hepburn[6,8], multiphoton excitation offers the opportunity of (i) widening the Franck-Condon window, (ii) accessing a wider range of electronic states that can act as doorway states to the final ion-pair states and (iii) avoiding the need to generate VUV photons. In contrast to previous experiments, in the present work we monitor the negative ion as well as the positive ion. Using the anion channel eliminates the need for a discrimination field to remove prompt positive ions, formed through the REMPI processes, that might linger in the collection region and contribute to the delayed-field extraction signal. A further difference from the previous work is that in ICl (and all the halogens and interhalogens except Cl_2)[2], the free-ion threshold is below the molecular IE, thus removing autoionisation as a process competing with the creation of ZIKE states. We will show that in the presence of a large constant DC field, where field ionisation is instantaneous and ZIKE states are not created, direct dissociation to ions is the dominant dissociation channel of electronic states coupled to the ion-pair continuum. After a survey of such doorway states down to energies 200 cm^{-1} below the field-free dissociation threshold, we investigate their lifetimes by pulsed field ionization.

6.2 Experimental

The experiments to be described were performed using the REMPI apparatus (see chapter 2). The jet system was of conventional design and employed a commercial pulsed valve (General Valve, nozzle diameter 250 μm). Helium at a pressure of 200-400 torr was passed over solid ICl_3 and the resulting mixture of ICl and Cl_2 expanded through the nozzle. The laser system consisted of two pulsed and independently tuneable dye lasers (Lambda Physik FL3002 and Lambda Physik FL2002) pumped by a XeCl excimer laser (Lambda Physik EMG 201 MSC). For one laser, two-colour experiments, Coumarin 153 dye was used in the FL3002 dye laser to produce visible photons which were then frequency doubled. No beam separator was used and thus both the visible light and the frequency doubled beam could be overlapped and introduced into the chamber. For two-laser, two-colour experiments, Coumarin 47 and PTP dyes were used for the pump and probe steps, respectively. For three-colour experiments, the fundamental and frequency doubled output of Coumarin 153 provided the two pump photons and the fundamental of Coumarin 307 provided the probe photon. In the three-colour experiments, calibration was made by simultaneously recording the REMPI or the ZIKE-PFD spectrum and the laser induced fluorescence (LIF) spectrum of I_2 in a static cell. At ion-pair formation threshold region of ICl, the calibration was accurate to ±0.5 cm^{-1}.

The two counter-propagating dye laser beams were overlapped and intersected the molecular beam at 90° between two electrodes separated by a distance of 1.6 cm using lenses of a focal length of 6 cm. A high positive or negative potential was applied to the upper electrode, while the lower electrode at the entrance to the time-of-fight tube was grounded.

For the three-colour experiments, the visible beam from the pump dye laser was slightly focused while the frequency doubled beam was defocused. In addition, the doubling crystal was detuned to further reduce the UV laser power density in

the ionisation region. A 2016 V pulse with a 20 ns rise time and a duration of 2μs, at a variable time delay after the laser pulse, was used to complete the dissociation of any long-lived ion-pair states just below dissociation. This field, according to its direction, also served to accelerate positive or negative ions into the flight tube.

6.3 Results

The first ion-pair dissociation threshold for ICl is at 72,523 cm^{-1}, calculated using the literature values of the ionisation energy[18] of I, 84,295 cm^{-1}, the electron affinity[19] of Cl, 29138.3 cm^{-1} and the dissociation energy[20] of the ground state of ICl, D_0 = 17,366 cm^{-1}. With the range of wavelengths available from the dye lasers described above, three photons are required for dissociation. The first resonant intermediate state must be the B state, and two variations were used and are compared in figure 6-1.

The first scheme involves the continuum of the shallow bound B state as the first resonant intermediate, which does not permit J state selection, and a second photon of the same wavelength excites υ = 24 of the $E(0^+)$ ion-pair state. The involvement of the $E(0^+)$ ion-pair state was determined in a separate experiment in which the REMPI spectrum of ICl was recorded (see figure 6-2). With careful wavelength calibration, the J state assignment can be made from the known spectroscopic constants of the E state and the two-photon energy. The third photon then accesses the ion-pair dissociation threshold. In the second scheme, the first resonant step is to a bound level of the B state (υ = 2, J = 20), which permits J-state selection. The frequency doubled pump photon then excites an accidental resonance with υ = 12, J = 21 of the f′ ion-pair state (which correlates with $I^+(^1D_2) + Cl^-(^1S_0)$. The probe photon then accesses the dissociation threshold as before. The important difference between the two routes is that different ion-pair states are accessed at the two-photon level but only one of them (i.e. in the first scheme) correlates with the ground state of I^+. As a preliminary to the delayed field experiments, the prompt ion-production spectra obtained by these two routes are now discussed.

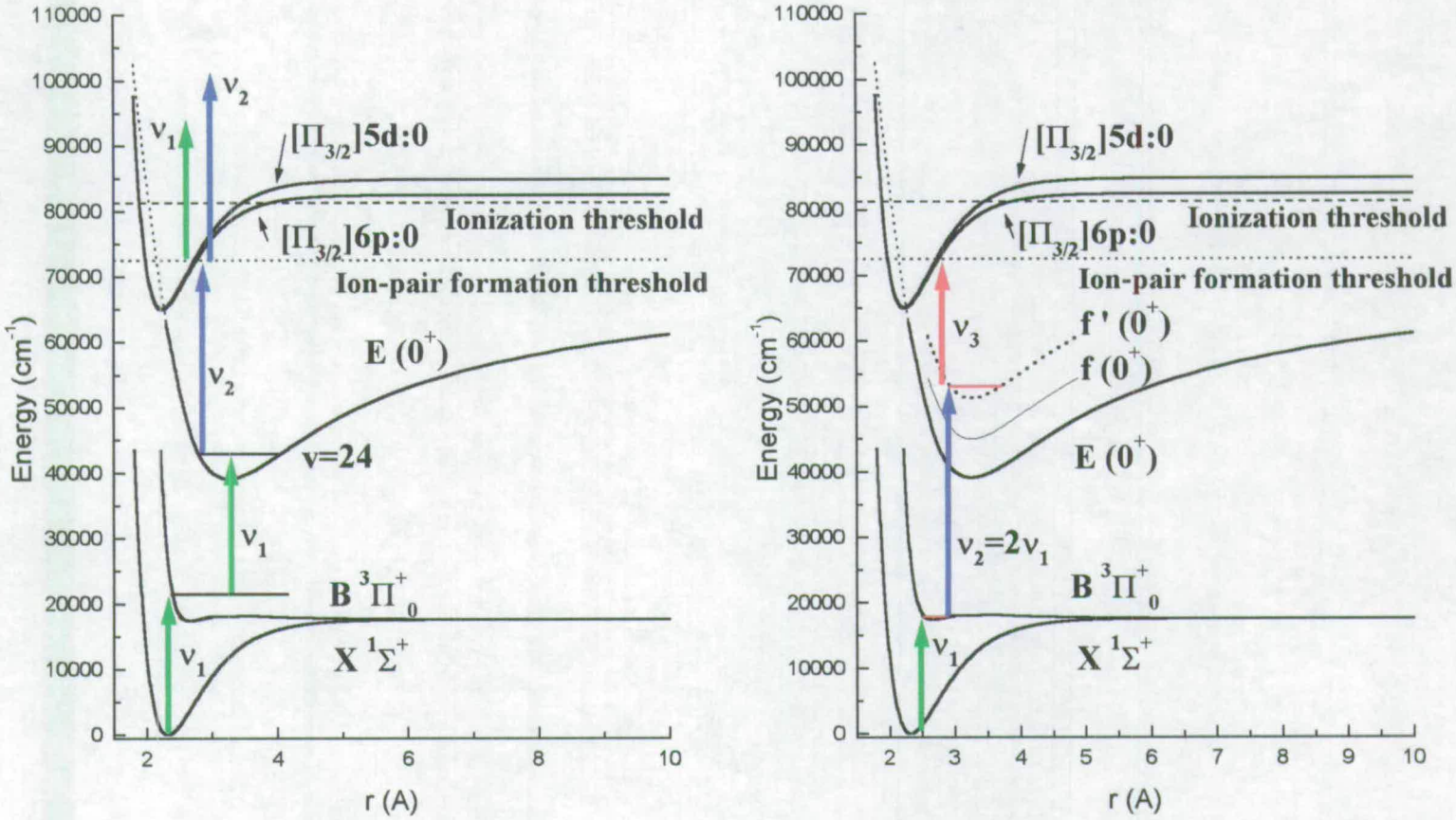

Figure 6-1: Potential curves of $I^{35}Cl$ and the excitation schemes used in this work. The potential for the B state is constructed by the same method described in ref.10. The E and f states are constructed using the turning points from ref.15 and ref.17. The f' state was obtained by simply shifting the f potential up by the difference in their term energies. The Rydberg states were constructed using Morse potentials. Excitation schemes: (a) *via* the continum of B state; (b) *via* bound level υ=2 of B state.

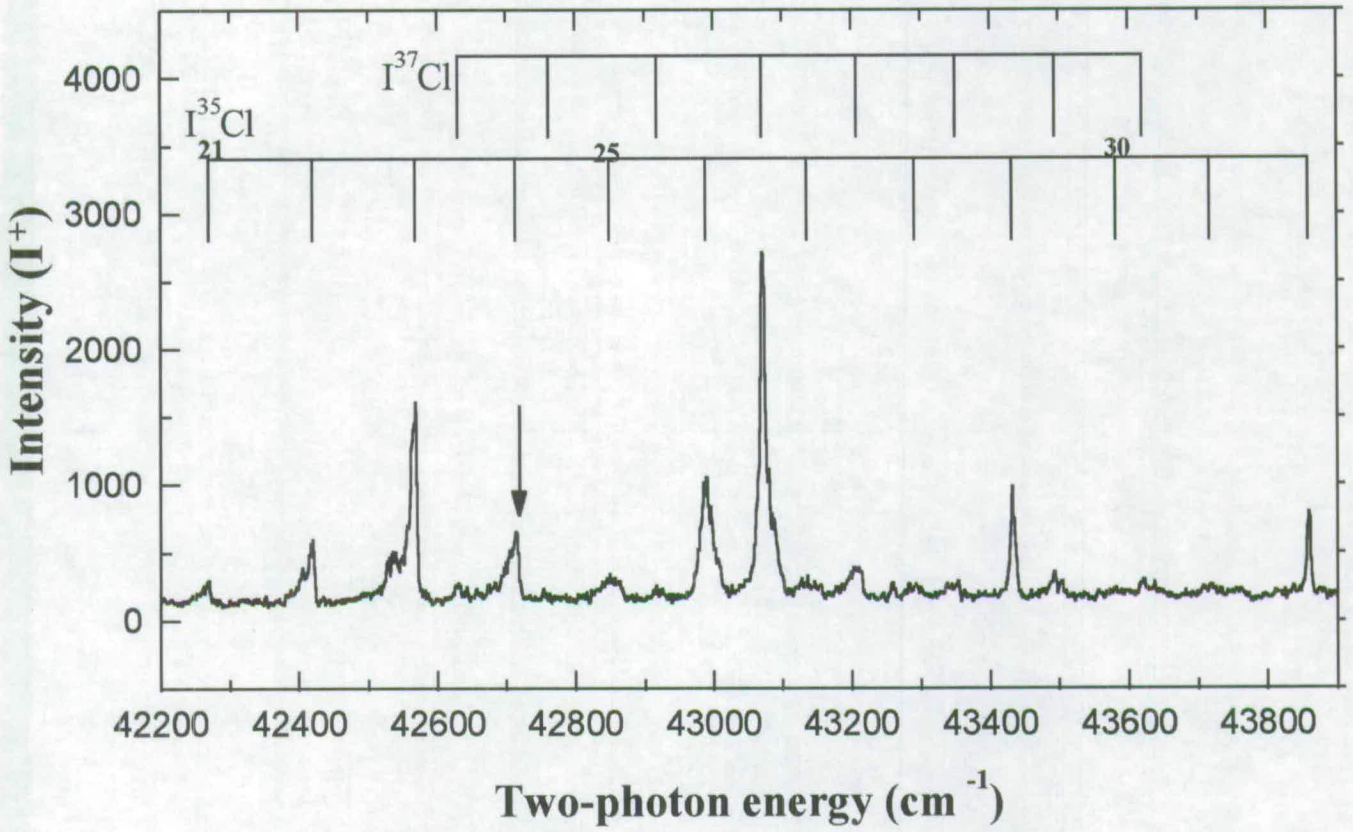

Figure 6-2: Double-resonance (bound-free-bound) REMPI spectrum of ICl. The E state is excited *via* the continuum of the B state. The $E0^+$ vibrational progressions of $I^{35}Cl$ and $I^{37}Cl$ are marked by ladders.

6.3.1 Three-photon, two-colour dissociative ion-pair formation via the $E0^+(\upsilon = 24)$ intermediate state.

Using a constant extraction field of 1260 V/cm, the prompt I^+ and Cl^- production spectra are shown in figure 6-3. The wavelength of the probe laser was scanned near the zero-field ion-pair threshold at 72,523 cm^{-1}.

The Cl^- signal shows an onset at 72,338 cm^{-1}, 180 cm^{-1} below the zero-field threshold, which is the lowering expected from a field dependence of the form $\Delta E \approx 5\sqrt{F}$. The I^+ signal continues in the energy region below the ion-pair field ionisation threshold, where it becomes a simple REMPI spectrum with I^+ ions being formed by the absorption of more than three photons to give dissociative states of ICl^+. This process must continue to higher probe frequencies when the field ionization energy region is reached, where it competes with the newly opened ion-pair formation channel. However, in this region the I^+ and Cl^- signals are of roughly equal intensity (and show the same ν_3 dependence), indicating that the ion-pair dissociation channel is a faster process than the up-pumping to $I^+ + Cl + e$. No significant continuum background signal was observed between individual peaks in the $^{35}Cl^-$ spectrum, indicating that the direct excitation from the low υ (υ=24) ion-pair states (the intermediate state) to the high υ (near-dissociation) states is not important. It is expected that this kind of cross-section would be very small.

The structured features in both ion channels indicate that ion-pair production is via initially populated doorway states that are coupled to the very high vibrational levels of the first tier ion-pair states which correlate to the $I^+(^3P_2) + Cl^-(^1S)$, which are then dissociated by the electric field. However, the structure in both ion channels does not show any obvious progressions.

In order to investigate the nature of the doorway states involved, the wavelength of the third photon was scanned to lower energy, with total energy between 69600-71600 cm^{-1}. The spectrum recorded in the I^+ channel is shown in figure 6-4. A progression with a spacing of about 360 cm^{-1} appears clearly in this energy region. The measured spacing suggests that the progression is possibly due to a Rydberg state, with vibrational quantum numbers between 10-20 (Recall the

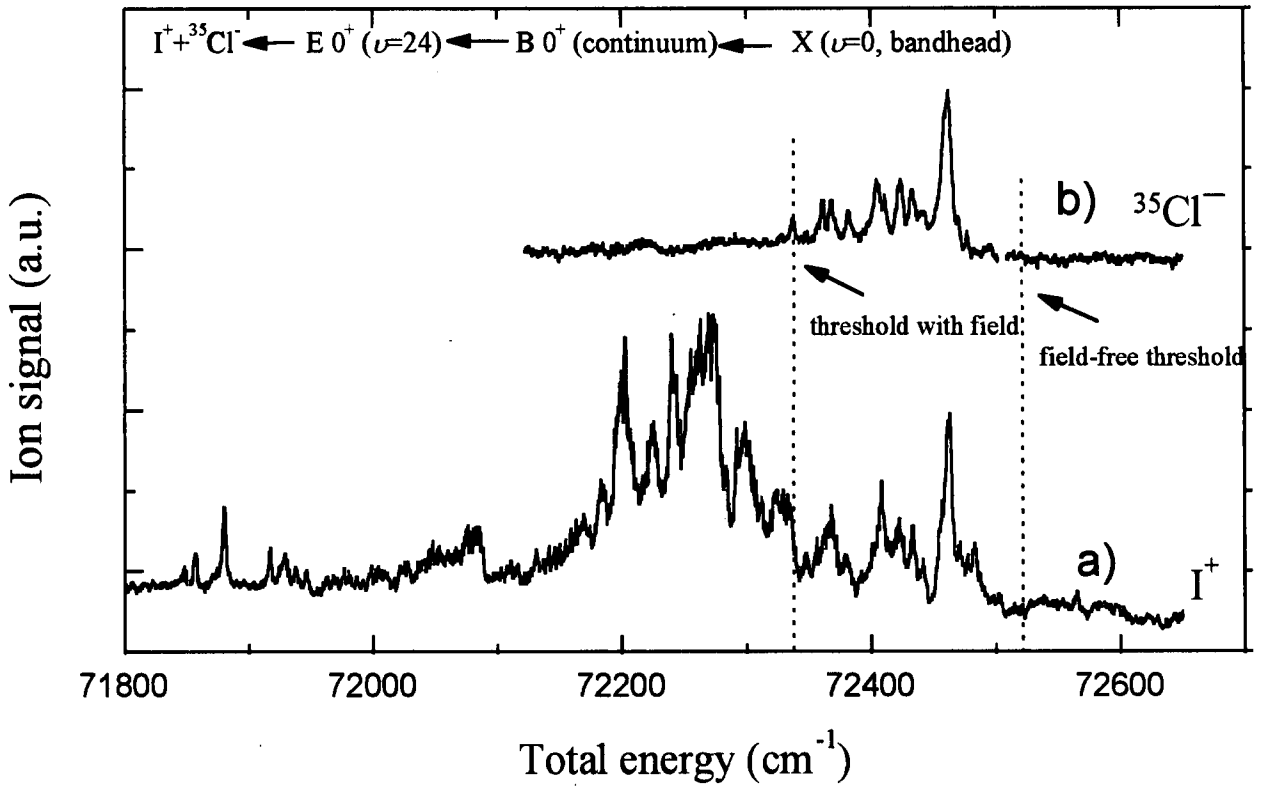

Figure 6-3: Ion-pair formation spectra from $I^{35}Cl$ following multiphoton excitation under DC field conditions. The molecule was excited from the ground state $X(0^+)$ to $E(0^+)$ (υ=24, low J) *via* the continuum of the B state by two-photon bound-free-bound transitions. Another tuneable photon from the second laser was scanned around the ion-pair formation threshold. The field-free and field-induced thresholds are marked on the spectra. a) I^+ : the signal above the field-induced threshold mainly comes from an ion-pair formation process at the three photon level, while the signal below the field-induced threshold is due to dissociative ionisation of ICl at the four-photon level; b) $^{35}Cl^-$: shows onset at the field-induced ion-pair threshold.

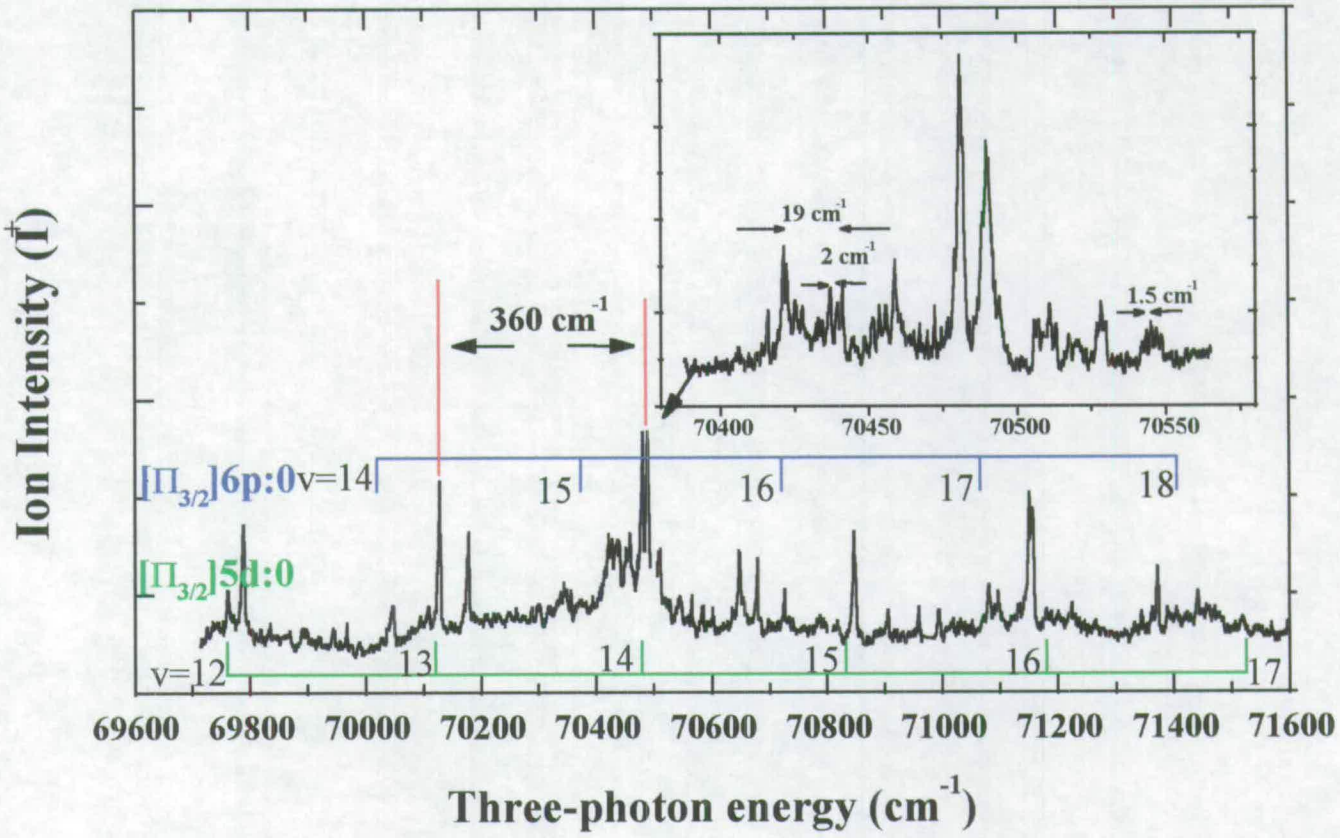

Figure 6-4: (1+1+1')+1 or 1' REMPI spectra of $I^{35}Cl$ recorded in the region 69600-71600 cm^{-1} (I^+ channel). The calculated vibrational levels of the [$\Pi_{3/2}$]5d:0 and [$\Pi_{3/2}$]6p:0 Rydberg states are marked in the spectrum by ladders. The insert is a higher resolution scan around 70500 cm^{-1}.

typical ω_e value of the Rydberg states of ICl is about 420 cm^{-1}). Indeed, as shown in figure 6-1a, the Franck-Condon window for $E0^+(\upsilon=24)$ favours higher vibrational levels rather than low levels around the origin. Although transitions from the intermediate state to *ns*, *np*, *nd* and *nf* Rydberg states are all allowed, parallel transitions (i.e. transitions to upper states which also have $\Omega=0$) are more favourable. The possible candidates which are located in the above energy region are $[^2\Pi_{3/2}]6p$:0, two $[^2\Pi_{3/2}]5d$:0, $[^2\Pi_{1/2}]6s$:0, $[^2\Pi_{1/2}]6p$:0 and one $[^2\Pi_{1/2}]5d$:0. The origins of these Rydberg states observed in the absorption spectrum are 64609, 65068, 68520, 57561, 69393 and 69913 cm^{-1}. Of all these Rydberg states, only the $[^2\Pi_{3/2}]6p$:0 state having its origin at 64609 cm^{-1} and one of the $[^2\Pi_{3/2}]5d$:0 state having its origin at 65908 cm^{-1}, could have vibrational levels lying in the energy region (figure 6-4) with the observed spacing (360 cm^{-1}). The vibrational energy levels of these two Rydberg states were generated from a Morse potential and are marked by the ladder in figure 6-4. It can be seen that agreement of the positions of the vibrational levels of $[^2\Pi_{3/2}]5d$:0 with the experimental result (strong peaks) is quite good. In contrast, features corresponding to $[^2\Pi_{3/2}]6p$:0 seems weak and sparse. It can not be ruled out, however, that some weak features appearing in the spectrum might correspond to higher vibrational levels of the $[^2\Pi_{1/2}]6s$:0 Rydberg state, though presumably they should be very weak. Another possibility is coupling of these Rydberg states with ion-pair states. Thus, the latter gains intensity from the former, as will be described below.

The insert in figure 6-4 shows a higher resolution scan around 70500 cm^{-1}. This spectrum is composed of two strong peaks followed by a series of weaker peaks with a spacing of 16-19 cm^{-1} which are superimposed on a long continuous progression of sharp peaks with a spacing of 1.5-3 cm^{-1}. The two strongest peaks appear to be Rydberg transitions. The spacing (16-19 cm^{-1}) of the weaker peaks indicates that they might correspond to high vibrational levels of an ion-pair state. Ion-pair state potentials belonging to different tiers should run parallel at large internuclear distance and thus the spacing of high vibrational levels at the same binding energy below threshold should be similar. Recall that the spacing of vibrational levels of the E state is about 18 cm^{-1} at 8500 cm^{-1} below the dissociation

threshold[13]. Thus the progression with a spacing of 16-19 cm^{-1} in figure 6-4 could belong to an ion-pair state which has a dissociation limit at ~79000 cm. The only possible candidate is the $f0^+$ state which lies in the second tier of ion-pair states. Upon closer examination of the $^{35}Cl^-$ spectrum (figure.6-3), structure with a spacing of about 10-13 cm^{-1} can be seen. This could therefore be a continuation of the $f0^+$ state.

More importantly, the appearance of a progression with a spacing of 1.5-3 cm^{-1} provides evidence for coupling of the doorway state with high vibrational levels of an ion-pair state at energies 2000 cm^{-1} below the threshold.

Higher energy regions, around the field-free threshold and above (i.e. the continuum) have also been investigated by using higher vibrational levels, υ=25, 27 and 29, of the E state and scanning the probe laser. A similar pattern of features appears.

6.3.2 Ion-pair formation using three-colour multiphoton excitation via $\upsilon = 2$ of the B state.

The spectrum in figure 6-5 was recorded by exciting ICl using a visible photon and its frequency doubled output, in a one-laser two-colour experiment, collecting I^+. The spectrum shows the rotational contour of an accidental double resonance involving both the B and f′ states of ICl. More specifically, the (2,0) band of the $I^{35}Cl$ (B←X) transition is involved and a simulation of this band is included in figure 6-5. The P and R branch lines indicated are taken from the results of Gordon and Innes[14]. The irregular intensities are caused by accidental resonances with rotational lines of $\upsilon = 12$ of the f′ ion-pair state following absorption of a UV photon. The band head for the transition to υ=12 was observed at 52 983.8 cm^{-1} in the double resonance experiments of Donovan et al.[11]

There appear to be two very strong accidental resonances corresponding to absorption via the R(19) and R(23) lines of the B ← X (2,0) band and these will be considered first. The energy of these transitions are 17 655.6 and 17 650.9 cm^{-1},

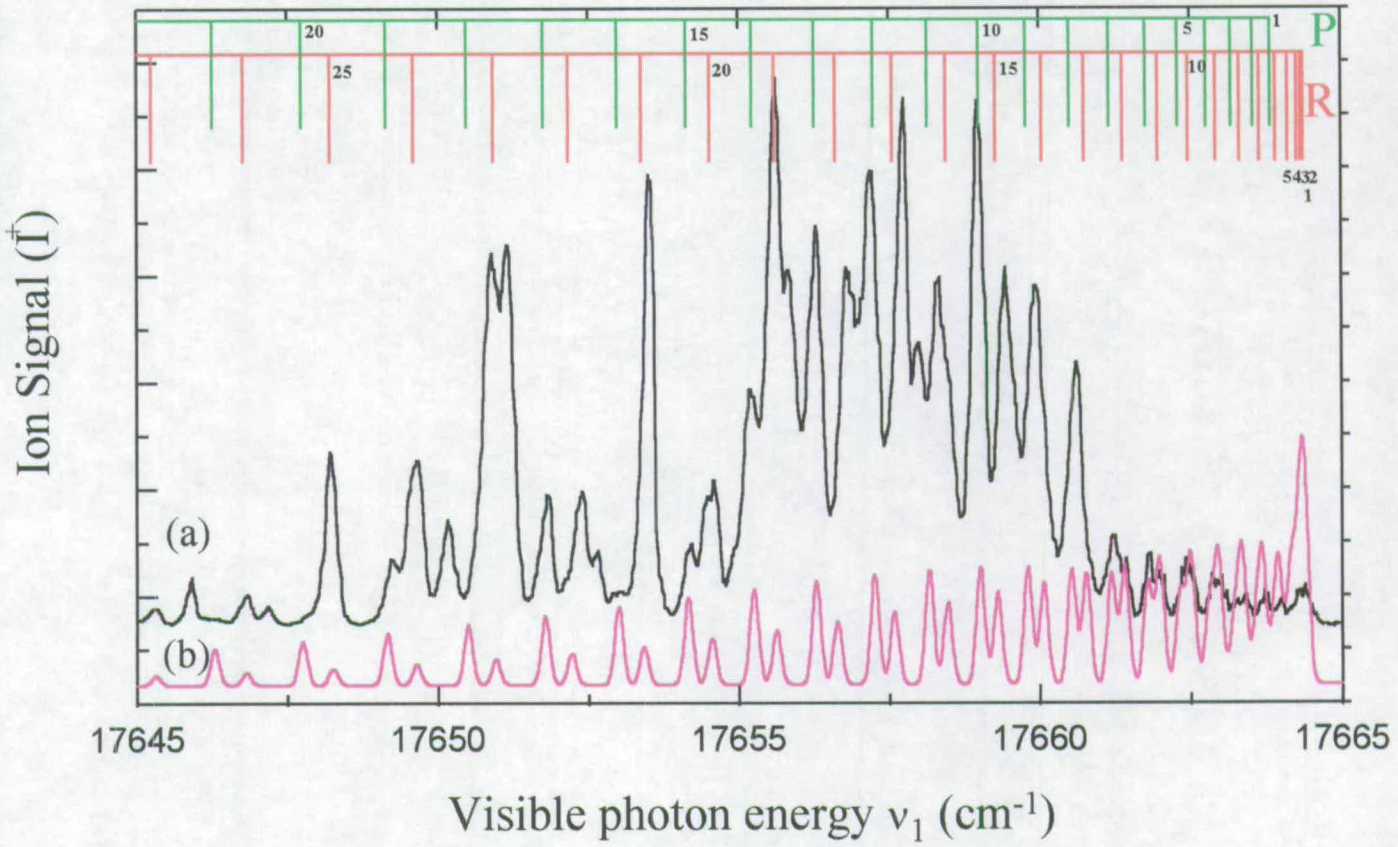

Figure 6-5: (a) (1+1')+1' REMPI spectrum enhanced by accidental resonance recorded by exciting $I^{35}Cl$ using a visible photon (ν_1) and a frequency doubled photon($\nu_2=2\nu_1$) in a one-laser experiment, collecting I^+. This spectrum is identical to that recorded in the $I^{35}Cl^+$ mass channel. The spectrum is plotted against the one-photon energy. (b) Simulation of the band contour of for the B←X (2,0) transition of $I^{35}Cl$.

respectively. If a true accidental resonance occurs, i.e. the energy of the second step is exactly twice that of the first, then the two-photon energies are 52 966.8 and 52 952.7 cm^{-1}. The initial rotational energies in the ground state of J = 19 and 23 are calculated as 43.3 and 62.8 cm^{-1} using the known B value[16] of 0.1139 cm^{-1} for the ground electronic state. Hence, the total energies above υ = 0, J =0 of the ground state, after a two-photon transition, are 53 010.1 and 53 015.5 cm^{-1}, corresponding to 26.3 and 31.7 cm^{-1} of rotational energy in the υ=12 vibrational level of the f′ state. Because of the rotational selection rules two-photon transitions using the R(19) and R (23) pump lines must terminate in J = 19 or 21 or J = 23 or 25, respectively. The four possible assignments give B values for the upper state of 0.069, 0.057, 0.057 and 0.049 cm^{-1}. The value of 0.057 cm^{-1} is comparable with the reported B value[17] for the υ = 12 level of the E state, of 0.055 cm^{-1}. Thus, these two strong accidental resonances involve the transitions: f′ (υ = 12, J = 21) ← B(υ = 2, J = 20) ← X(υ = 0, J = 19) and f′ (υ = 12, J = 23) ← B(υ = 2, J = 24) ← X(υ =0, J = 23).

The energy region around the first threshold for ion-pair formation was scanned using two-laser, three-photon excitation. The first two photons were used to access υ=12, J=21 of the f′ ion-pair state, as described above. A third, independently tuneable photon was then scanned from 495 to 520 nm to cover the threshold region. Spectra recorded in the I^+ and $^{35}Cl^-$ channels with a constant extraction field of 1250 V/cm, are shown in figure 6-6.

The signal sizes of I^+ and $^{35}Cl^-$ recorded here are not comparable because different boxcar sensitivities were used for these two mass channels. Although the frequency-doubled UV beam was defocused there was still a background signal of I^+ produced by one visible photon and two frequency-doubled UV photons, from the first laser only. No significant background signal in the $^{35}Cl^-$ channel was observed between individual peaks.

The abrupt disappearance of the Cl^- signal at 180 cm^{-1} below the zero-field threshold is again clear, although this time the I^+ signal also disappears at the same energy due to lack of structure at lower energy region. The excitation spectrum also

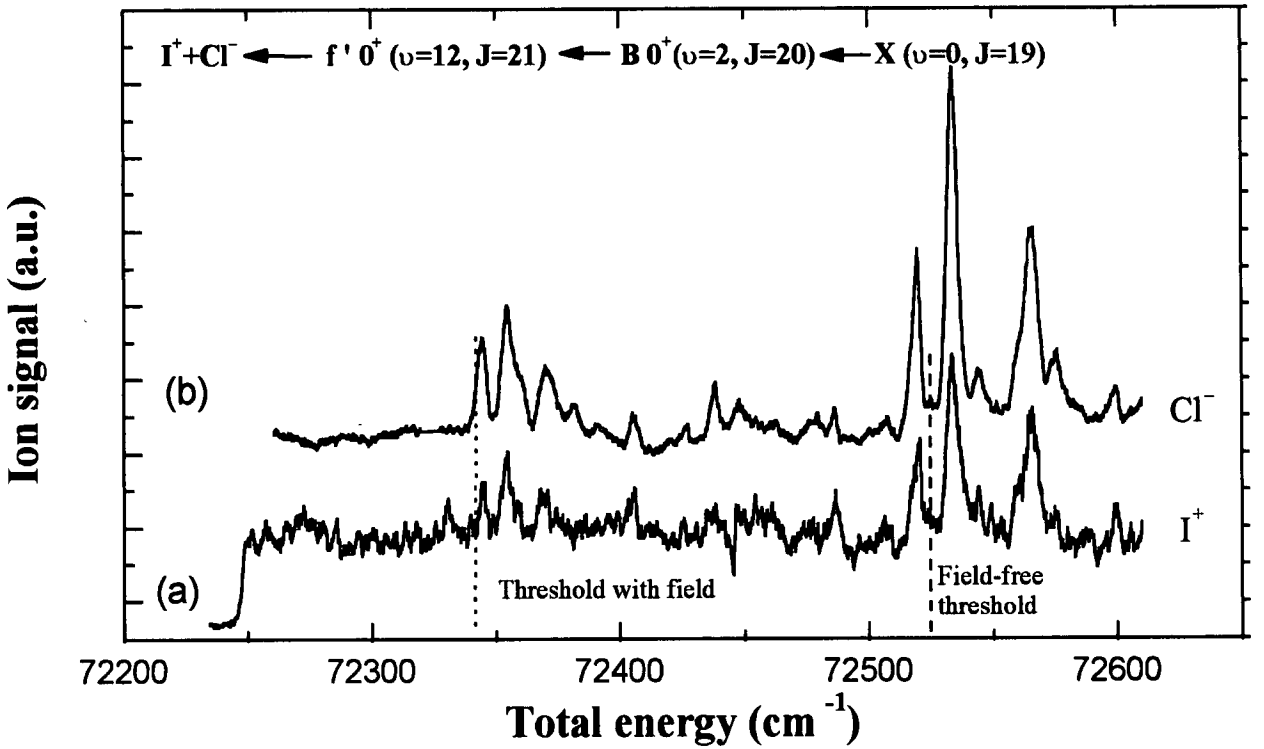

Figure 6-6: Ion-pair formation spectra of $I^{35}Cl$ following multiphoton excitation under DC field conditions. The molecule was excited from the ground state $X0^+$ to $f'0^+$ (υ=12, J=21), via B(υ=2, J=20), by one visible photon and one frequency-doubled UV photon from the first laser. Another tuneable photon from the second laser was then scanned around the ion-pair formation threshold. The field-free and field-induced threshold are marked on the spectra. (a) I^+: the signal above the field-lowered threshold comes from an ion-pair formation process at the three photon level while that below the field-lowered threshold comes from dissociative ionisation of $I^{35}Cl$ at the four-photon level. The background signal comes from two colour excitation from the first laser only. (b) $^{35}Cl^-$: onset of the field-lowered ion-pair threshold. The total energy is $\nu_1 + \nu_2 + \nu_3$ plus the rotational energy of the ground state.

clearly shows features with spacings of 10-13 cm^{-1}, the same as observed in figure 6-3 using the first pumping scheme, corresponding to high vibrational levels of the second tier $f0^+$ ion-pair state which gains intensity by coupling with the 5d Rydberg state. However, the overall structure seems quite different from the spectra shown in figure 6-3. On this excitation ladder, there do not appear to be any resonant intermediate states just below 72,350 cm^{-1} that give a strong REMPI signal. On the other hand, immediately above the zero-field free-ion threshold, where no structure was visible using the first pumping scheme, there is now strong but irregular structure in the Cl^- channel extending at least up to 73,200 cm^{-1}. One possible reason for this is due to the different Franck-Condon overlaps from different intermediate states used in the two excitation schemes.

6.3.3 The ZIKE-PFD spectrum of ICl

Pulsed field dissociation experiments were carried out using the second of the excitation schemes described above. This was chosen because there are strong resonances very close to the field-free dissociation threshold (see figure 6-6). In the first experiments, the probe laser was scanned around the calculated field-free ionisation energy of 72,523 cm^{-1} and an extraction field of 1250 V/cm applied after a fixed time delay of 1.2 μs. The TOF spectra recorded with different probe energies are shown in figure 6-7. At the highest probe frequencies (72939 cm^{-1}), the time-of-flight spectrum is twin-peaked (figure 6-7d), the fast and slow arrivals being characteristic of free ions, created by photolysis, that are initially moving either towards (slow) the entrance to the flight tube, or away (fast). The two peaks converge rapidly to a value of 7.6 μs as the probe frequency decreases. Then, within one wavenumber of 72,519 cm^{-1} (figure 6-7b), a new fast arrival peak appears . It has no slow counterpart and, on reducing the probe frequency further, the now converged peaks that were present for higher frequencies disappears, leaving only the single new peak.

In the second series of time delay experiments, the 1.26 kV/cm extraction field was applied after a variable time delay τ_d. The pump wavelength was 566.206

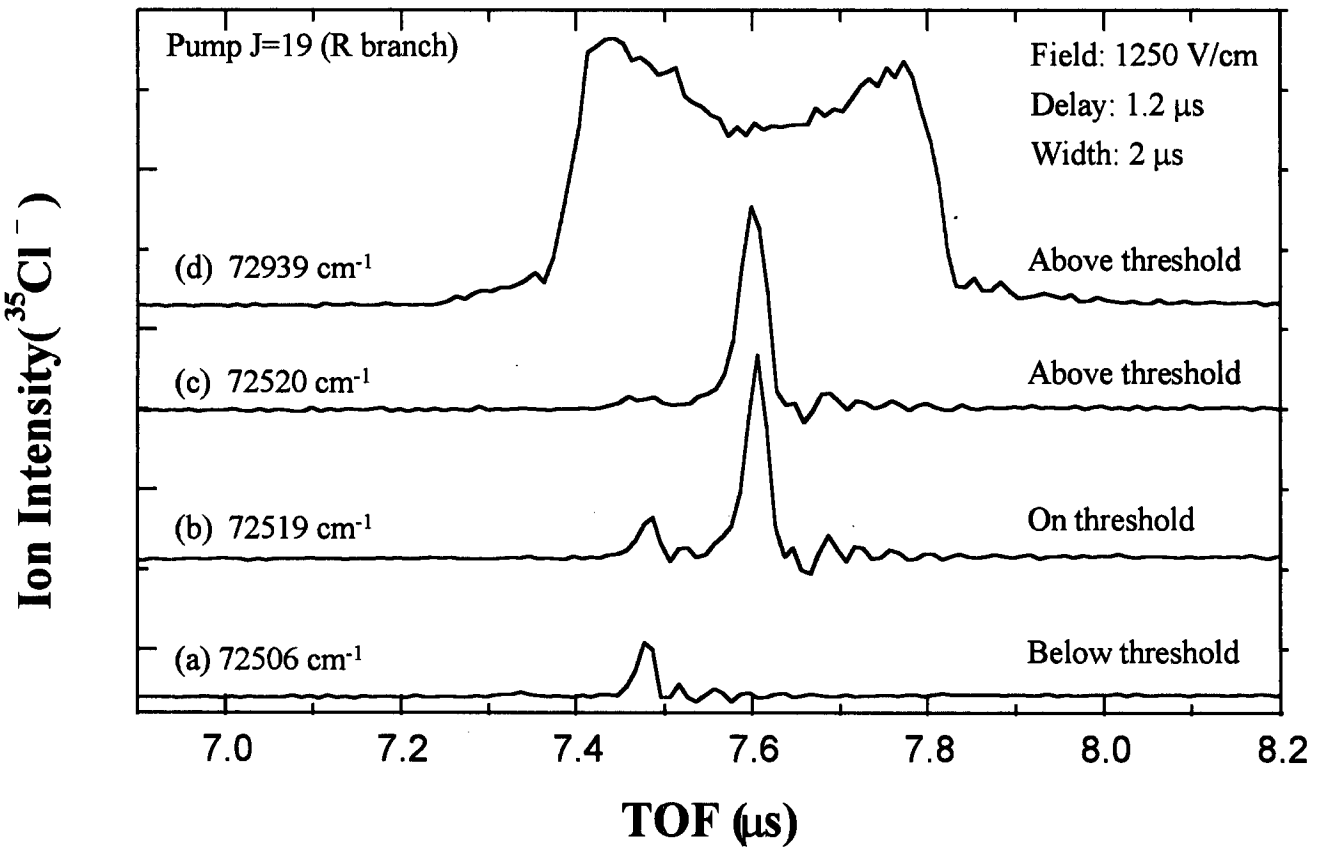

Figure 6-7 Time-of-flight mass spectrum of $^{35}Cl^-$ at four different excitation energies using a delayed pulsed-field (Delay time 1.4 μs, pulse field strength 1250 V/cm). a) Excitation energy 72506 cm^{-1}; b) Excitation energy 72519 cm^{-1}; c) Excitation energy 72520 cm^{-1}; (d) Excitation energy 72939 cm^{-1}. All excitation energies are relative to υ=0, J=0 of ground state of ICl. The excitation scheme is the same as in figure 6-6.

nm and the probe fixed as 512.39 nm, giving an energy $\nu_1 + 2\nu_1 + \nu_3 = 72519 \pm 1$ cm^{-1} (calibrated) at which the new feature in the TOF spectra identified in the above series of experiments first appeared. Two arrival peaks can be seen in the TOF spectra at each time delay in figure 6-8. One peak is essentially invariant with τ_d, both in arrival time and amplitude while the other moves to progressively longer arrival times with increasing τ_d and rapidly diminishes in amplitude. The invariant peak we attribute to the formation of ZIKE states via the band at 72519 cm^{-1} and the moving peak to free Cl^- ions with an initial energy no more than 1 cm^{-1} above threshold. Both are created within the bandwidth of the probe laser. The increase in arrival time of the slow peak is quadratically dependent on τ_d, and the expected arrival times based on $t_{arr}(\tau_d) = t_{arr}(0) + c\tau_d^2$ ($t_{arr}(0) = 7.49$ μs) are marked by arrows in figure 6-8. This behaviour is that expected from the quadratic time dependence of the distance z moved by the ion packet in the presence of a uniform stray field, F: i.e. $z = \upsilon_0\tau_d + 1/2a\tau_d^2$, where the acceleration $a = F_s/m_{Cl}$ and the ions are created with an initial velocity υ_0. A plot of the time of arrival t_{arr} of the free ion packet *vs* τ_d^2 is linear, and so υ_0 is essentially zero. From the gradient of the plot we deduce the stray field to be 1.3 ± 0.2 V/cm.

Using the value of the stray field estimated from the behaviour of free ions just above dissociation, we can apply the correction $5\sqrt{F}$ to the appearance energy of the ZIKE sub-threshold ions at 72,519 cm^{-1} to give a zero-field threshold of $72{,}525 \pm 4$ cm^{-1}. This value is in good agreement with the computed value of 72,523 cm^{-1} and supports our interpretation of the TOF spectra.

In a final time-delay experiment, we followed the long-lived ZIKE peak to lower excitation energies. τ_d was held constant at 1.4 μs and the probe frequency scanned through the free ion threshold with the boxcar gated on the ZIKE peak in the TOF spectrum (its time of arrival is invariant with ν_{probe}). The results are shown in figure 6-9. The extraction field, 1.25 kV/cm, is sufficient to ionise any long-lived ion-pair states up to ~180 cm^{-1} below the zero-field threshold, but the ZIKE signal is seen to disappear at ~50 cm^{-1} below threshold. Referring to figure 6-6, there are doorway states that generate free ion pairs right down to the lowered threshold

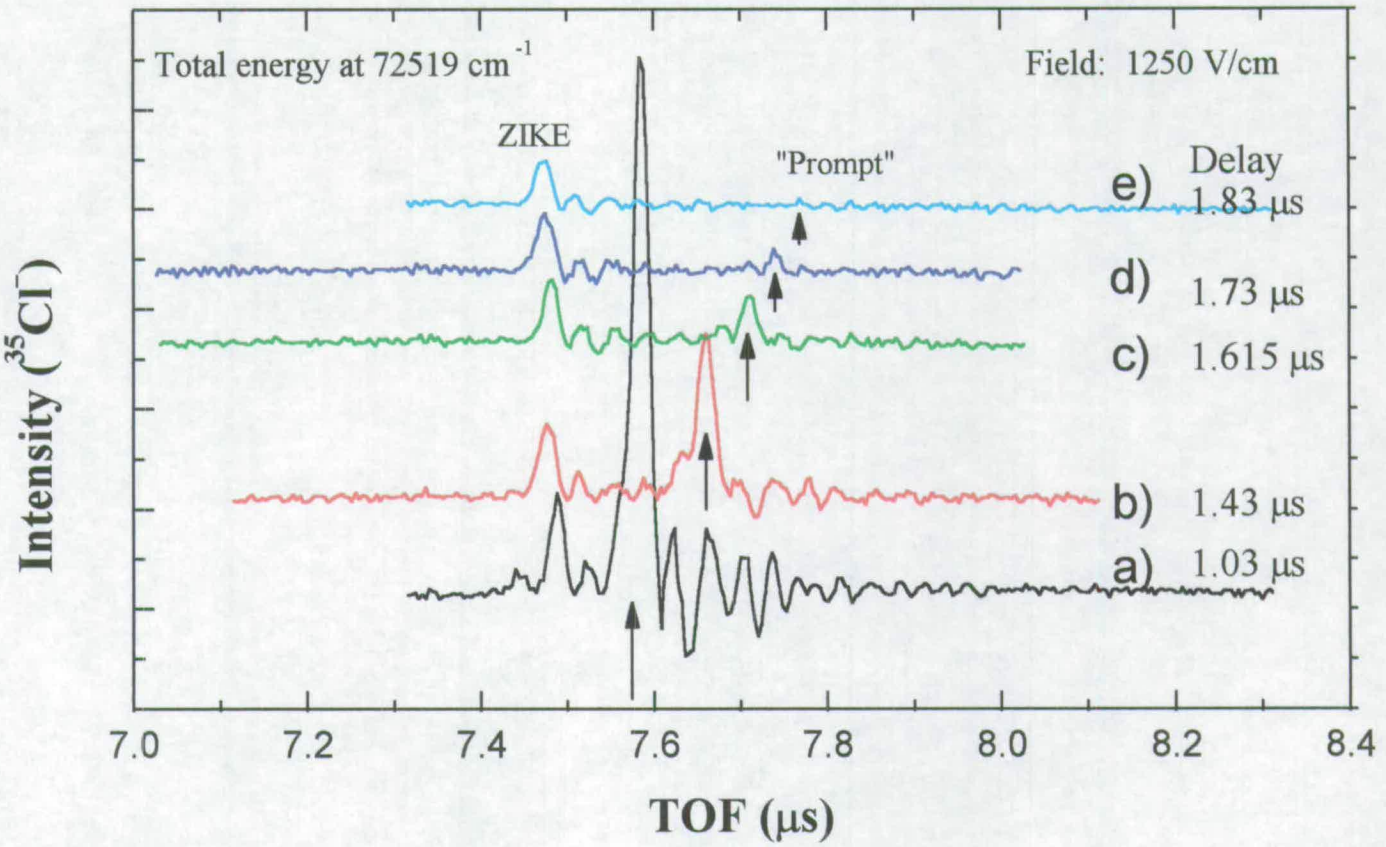

Figure 6-8: Time-of-flight spectra of $^{35}Cl^-$ at an excitation energy of 72519 cm^{-1} with different time delay of the pulsed field (pulsed field strength 1250 V/cm). Delay times: (a) 1.03 μs , (b) 1.43 μs , (c) 1.615 μs , (d) 1.73 μs and (e) 1.83 μs. The excitation scheme is the same as in figure 6-6.

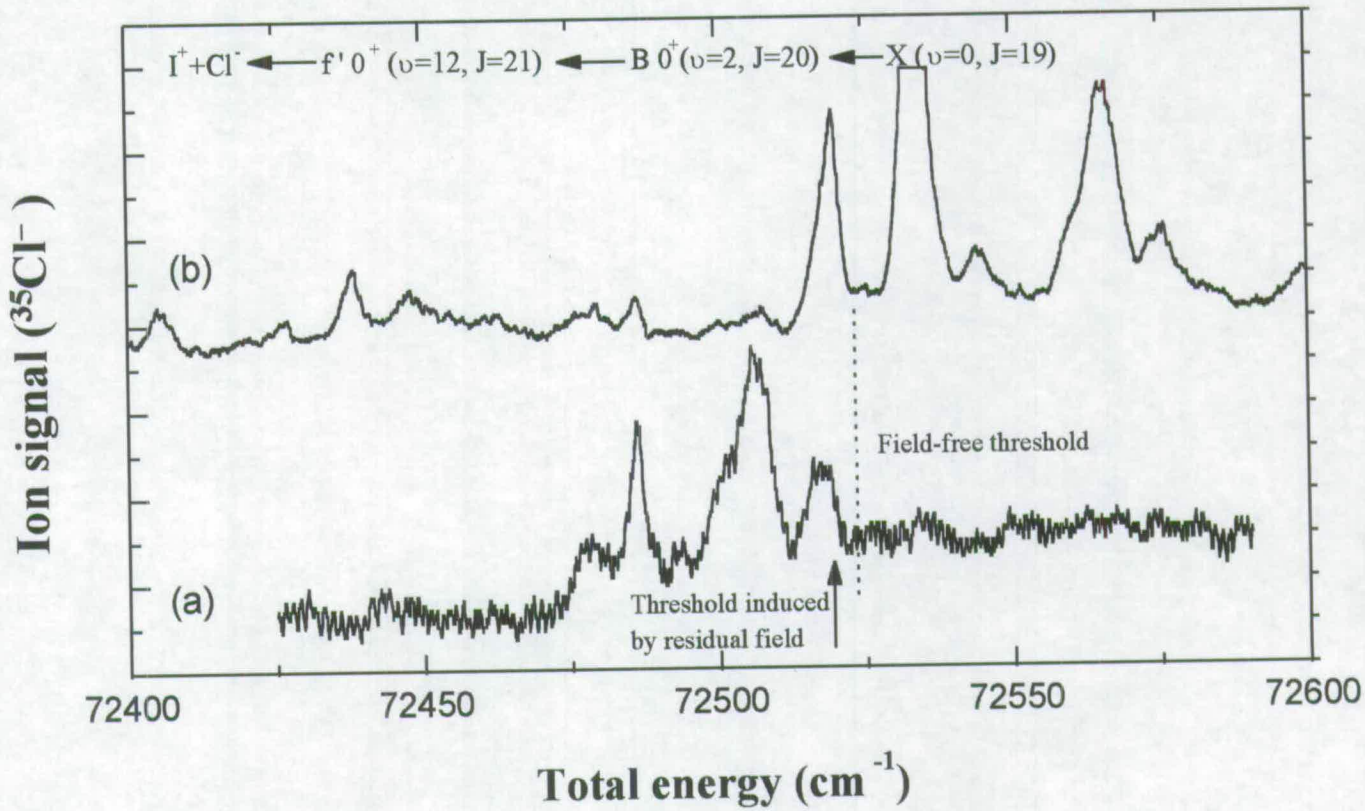

Figure 6-9: (a) ZIKE-PFD spectrum of I^{35}Cl recorded in the $^{35}Cl^-$ channel with the boxcar gated on the fast arrival peak as shown in figure 6-7b (pulsed field 1250 V/cm at a delay time of 1.4 μs). The excitation scheme is the same as in figure 6-6. (b) Replot of the spectrum in figure 6-6b for comparison.

with instant field ionisation. The disappearance of the ZIKE signal indicates that only ion-pair states down to 50 cm^{-1} below threshold can be converted to ZIKE states sufficiently quickly to survive the time delay.

6.4 Discussion

The highly structured REMPI signal recorded via the Cl^- channel (figures 6-3 and 6-6) shows the presence of doorway states that are coupled to the dense manifold of near-dissociation ion-pair vibrational levels converging on the first dissociation limit for $I^+(^3P_2) + Cl^-$. Doorway states are clearly important in accessing near-dissociation ion-pair vibrational levels in our pumping scheme, which involves low vibrational levels of intermediate ion-pair states. This is because the Franck-Condon factors for the direct transition $E(\upsilon > 10^4) \leftarrow f'(\upsilon = 12)$ are negligibly small. Classically, the momentum of the heavy ions cannot be conserved in such transitions. The doorway states are probably quite high vibrational levels of the *5d* or *6p* Rydberg states, whose outer potential walls are in the right position for a vertical (momentum conserving) transition from the inner turning point of the $E(\upsilon = 24)$ or $f'(\upsilon = 12)$ levels (see figure 6-1). The varying peak widths evident in figure 6-9 reflect different strengths of coupling to the underlying ion-pair vibrational manifold which is a near continuum ($\upsilon > 10^4$) and the coupling has the effect of broadening the transition when the resonance is detected in the ion-pair channel.

It is also possible that some doorway states are lower vibrational levels of upper tier ion-pair states such as the $f0^+$ state converging on a higher ionic dissociation limit (i.e. $I^+(^3P_0)+Cl^-$ in the case of the f state), though the Franck-Condon factors for the transition from the resonant intermediate state $f'(\upsilon = 12)$ to $f(\upsilon = \sim 400)$ would still be extremely small. The REMPI spectrum in the I^+ channel (figure 6-4 insert) at slightly lower energy shows evidence for coupling between the $f0^+$ and $E0^+$ ion-pair states and the $[^2\Pi_{3/2}]5d_\pi:0^+$ Rydberg state, i.e., three interacting states could be involved. Extensive interaction between different tiers of ion-pair states has been observed for Br_2[12]. Presumably this kind of interaction should be

stronger in the present case(ICl) because it involves one perpendicular electron shift between [1432] $f0^+$ and [1441] $E0^+$ for ICl, whereas two such shifts between [1441] $D0_u^+$ and [2332] $F0_u^+$ are required for Br_2. However, as shown in figure 1-1b, the inner walls of the potential curves of the f and E states might cross (diabatic) or avoid crossing (adiabatic) each other at energies close to $V(R)\approx D_e$. This could possibly explain the interaction strength. Direct evidence for the coupling of Rydberg and ion-pair states in ICl, albeit at a somewhat lower energy in the region of the 6s Rydberg states, comes from dips observed in the fluorescence excitation[9] and REMPI spectra of the E ion-pair state[13]. These dips form a regular progression characteristic of the vibrational levels of a Rydberg state, which is predissociated and thus shortens the lifetime of the coupled levels in the dense ion-pair manifold.

The similar ion yield spectra for both I^+ and $^{35}Cl^-$ channels, and their equally intensities, demonstrate that all states initially accessed from the intermediate states, υ=24 of E state or υ=12 of f ′ state are coupled to the highly vibrational excited levels of the E state or its continuum. Thus the dominant dissociation channel around the threshold leads to the formation of pairs of ions. This suggests that any repulsive valence states correlating with neutral atoms lie below this energy region and do not cross the outer branch of the ion-pair potential. This is consistent with the previously observed fluorescence excitation spectra[9]. Thus it appears that predissociation of the initially excited Rydberg states into neutrals does not compete with ion-pair formation process in this region. It should be noted that autoionisation is impossible as the ion-pair dissociation threshold is well below the first ionisation threshold.

The TOF experiments, with either a fixed or varying time delay before extraction of the ions, show the existence of long-lived ion-pair states just below the dissociation limit. This implies that the originally pumped states are converted to high J states within perhaps 10^{-9} s in order to be competitive with radiative decay of the doorway state from which they must become decoupled in order to survive. However, the rate of conversion must drop rapidly as the density of ion-pair state vibrational levels falls because no long-lived states more than 50 cm^{-1} below threshold are observed. This is similar to the long-lived high Rydberg (ZEKE) states

as a result of interaction with stray fields or distant collisions with free ions in the plasma.

Using triple resonance, when access to the near-dissociation ion pair states via a doorway state, as here, greatly enhances the Franck-Condon factor at the probe stage. A difference from ZEKE spectroscopy is that these initially prepared states, in order to be stabilised, have to undergo both an electronic transition as well as the large angular momentum change. In the halogens, to convert a Rydberg state energetically close to the ion-pair dissociation limit into an ion-pair state with a configuration such as $\sigma^1\pi^4\pi^{*4}\sigma^{*1}$, the Rydberg electron has to be returned to the core, and an electron promoted from the σ bonding valence orbital.

6.5 Conclusions

We have demonstrated that electronic states close in energy to the first ion-pair dissociation threshold of ICl can be efficiently converted into long-lived ($\tau_d \geq 2$ μs) sub-threshold ion-pair states which are analogous to the high Rydberg states encountered in the ZEKE-PFI spectroscopy. The doorway states are probably of mixed electronic character, but this does not inhibit the conversion process, which operates down to ~50 cm^{-1} below threshold.

The experiments reported here were designed to test whether the multiphoton, resonantly enhanced paths could be found to access the ion-pair dissociation threshold. A large extraction field F was used to probe deep into the field induced dissociation region. Using the known ionic dissociation energy of ICl, the $5\sqrt{F}$ dependence for the field-induced shift in the dissociation energy was confirmed under the tightly focused laser conditions used. We conclude that, once a suitable doorway state has been identified, it is feasible to use the versatile multiphoton technique coupled with delayed field dissociation, to obtain ion-pair dissociation energies.

6.6 References

1. A. Terenin and B. Popov, *Phys. Z. Sowjetunion* 1932, **2**,299.
2. J. Berkowitz, in *VUV and Soft X-ray Photoionization*, Edited by U. Becker and D.A. Shirley. Plenum Press, New York, 1996.
3. V.H. Dibeler, J.A. Walker and K.E. McCulloh, *J.Chem.Phys.* 1970, **53**, 4414.
4. J. Berkowitz, W.A. Chupka, P.M. Guyon, J.H. Holloway and R. Spohr, *J. Chem. Phys.* 1971, **54,** 5165.
5. S.T. Pratt, E.F. McCormack, J.L. Dehmer and P.M. Dehmer, *Phys. Rev. Lett.*, 1992, **68** 584.
6. J.D.D. Martin and J.W. Hepburn, *Phys. Rev. Lett.*, 1997, **79**, 3154.
7. E.W. Schlag, *ZEKE Spectroscopy.* Cambridge University Press, 1998.
8. J.D.D. Martin and J.W. Hepburn, *J. Chem. Phys.*, 1998, **109**, 8139.
9. K.P. Lawley, E.A. Kerr, R.J. Donovan, A. Hopkirk, D. Shaw and A.J. Yencha, *J. Phys. Chem.*, 1990, **94**, 6201.
10. R.D. Gordon and K.K. Innes, J. Chem. Phys., 1979, **71**, 2824.
11. R.J. Donovan, T. Ridley, K.P. Lawley and P. Wilson, *Chem. Phys. Lett.*, 1992, **196**, 173.
12. R.H. Lipson and A.R. Hoy, *J. Mol. Spectrosc.*, 1989, **134**, 183.
13. R.J. Donovan, J.G. Goode, K.P. Lawley , T. Ridley and A.J. Yencha, *J. Phys. Chem.*, 1994, **98** 2236.
14. R.D. Gordon and K.K. Innes, *J. Mol. Spectrosc.* 1979, **78**, 350.
15. D.I. Austin, PhD thesis, The Edinburgh University, 1988.
16. J.A. Coxon, R.M. Gordon and M.A. Wickramaaratchi, *J. Mol. Spectrosc.* 1979, **79**, 363.
17. D. Bussieres and A.R. Hoy, *Can. J. Phys.* 1984, **62**, 1941.
18. V.N. Sarma and Y.N. Joshi, *Can. J. Phys.* 1983, **61**, 1434.
19. R. Trainham, G.D. Fletcher and D.J. Larson, *J. Phys. B: At. Mol. Phys.* 1987, **20**, L777.
20. J.C.D. Brand and A.R. Hoy, *J. Mol. Spectrosc.* 1985, **114**, 197.

Chapter 7

The Spectroscopy of Near-Dissociation Ion-Pair States of I_2

7.1 Introduction

Ion-pair formation from I_2 was first observed by Morrison et al[1]., although only a low resolution excitation spectrum for I^+ was obtained. Further low resolution data on the ion-pair threshold region were reported by Myer and Samson[2]. Akopyan et al[3] observed both I^+ and I^- formation above the first ionisation limit of I_2, but again this was at low resolution and excitation functions showed no evidence of vibrational structure. In a more recent study by Kvaran et al[4], clearly resolved vibrational structure was observed in the excitation functions for ion-pair production (I^+ and I^-) in the region from the threshold to just above the first ionisation limit of I_2, using synchrotron radiation. Surprisingly, the excitation functions were found, as for Br_2, to be remarkably simple in structure considering the very high density of Rydberg states (np, nf, Ω=0,1) present in the region just below the first ionisation limit which can be accessed by one-photon absorption. The main structure was assigned to homogeneous coupling between just one component of three Rydberg states ($[3/2]_c 9p\pi$, $10p\pi$ and $11p\pi$) and the ion-pair continuum.

In the most recent study by Donovan et al[5]., ion-pair formation from jet-cooled I_2 was observed in both the I^+ and I^- channels using VUV laser radiation, with much higher resolution than any other previous measurements. It showed that the one-photon ion-pair yield spectra of I_2 which appeared quite simple under low resolution conditions were in fact much more complicated when recorded at high resolution and, to a first approximation, reproduced the one photon absorption spectra. More importantly, the field lowering effect of the ion-pair threshold was first observed for I_2 in their study. Consequently, recalling that there is a very large

number of Rydberg states in the region of the first ion-pair threshold of I_2, this molecule seems like a natural candidate for ZIKE studies using multiphoton excitation.

7.2 Experimental

The experiments were performed using a REMPI apparatus (see Chapter 2). Helium or argon at a pressure of 200-400 torr was passed over solid I_2 and the resulting mixture of I_2 and carrier gas expanded through the nozzle. The laser system consisted of two pulsed and independently tunable dye lasers (Lambda Physik FL3002 and Lambda Physik FL2002) pumped by a XeCl excimer laser (Lambda Physik EMG 201 MSC). For one-laser, two-colour experiments, Coumarin 153 dye was used in the FL3002 dye laser to produce visible photons which were then frequency doubled. No beam splitter was used so that the overlapped visible light and the frequency doubled beams could be introduced into the chamber. For three-colour experiments, the fundamental (visible) output of Coumarin 153, used in the FL2002 dye laser, provided the probe photon. The two counter-propagating dye laser beams were overlapped and intersected the molecular beam at 90°, between two electrodes which were separated by a distance of 1.6 cm. Both laser beams were focused by lenses of 6 cm focal length. For three-colour experiments, the visible beam from the pump dye laser was slightly focused while the frequency doubled beam was defocused. In addition, the doubling crystal was detuned to further reduce the UV laser power density in the ionisation region to minimize the ion signal due to pump laser only. Calibration was made by simultaneously recording the REMPI or the ZIKE-PFD spectrum and the laser induced fluorescence (LIF) spectrum of I_2 in a static cell. At ion-pair formation threshold region of ICl, the calibration was accurate to ± 0.5 cm^{-1}.

A high voltage, positive or negative, was applied to the upper electrode, while the lower electrode at the entrance to the time-of-fight tube was grounded. For the ZIKE-PFI experiments, a ±2016 V pulse, with a 20 ns rise time and

duration of 4 μs at a variable time delay after the laser pulse, was used to complete the dissociation of any long-lived ion-pair states just below dissociation. This field, according to its direction, also served to accelerate positive or negative ions into the flight tube.

7.3 Results

7.3.1 Ion-pair formation using two-colour three-photon excitation

The first ion-pair threshold for I_2 is at 72062 cm^{-1}, calculated using the literature values for the ionisation energy[10] of I, 84295 cm^{-1}, the electron affinity[11] of I, 24673 cm^{-1}, and the dissociation energy of the ground state of I_2, D_0= 12440.2 cm^{-1}.

Ion-pair formation from I_2 using multiphoton excitation was most simply investigated by a one-laser, two-colour, experiment employing both the fundamental (ν_1) and its frequency-doubled output ($\nu_2 = 2\nu_1$). The general excitation scheme is shown in figure 7-1. The photoion yield spectra of both I^+ and I^- were recorded with ν_1 scanned from 540 to 560 nm and are shown in figure 7-2. The I^- signal completely disappeared and I^+ signal dropped almost to zero (< 5%) when either the visible light or the frequency doubled UV was blocked. This indicates that all I^- ions and the majority of I^+ ions are formed by two-colour excitation.

The I^- signal shows a clear onset at $\nu_1 \approx 17950$ cm^{-1}. Energetically, three photons are required and I^- must be formed by the absorption of two visible photons and one frequency-doubled photon (i.e., $\nu_1+\nu_2+\nu_1$). Above the threshold the spectra of I^+ and I^- are almost exactly the same, but the I^+ signal continues in the energy region below the threshold where the absorption of another photon, to a dissociative state of I_2^+, is required on energetic grounds.

The overall spectra of I^+ and I^- both give rise to a quite regularly spaced progression with a spacing of ~50 – 60 cm^{-1} at the one-photon level (ν_1) and an equivalent of 150 – 180 cm^{-1} at the two-photon level ($\nu_1 + \nu_2$). The known spacing

of 90 cm^{-1} for the B ← X transition[6] in this energy region implies that other electronic states must also be involved.

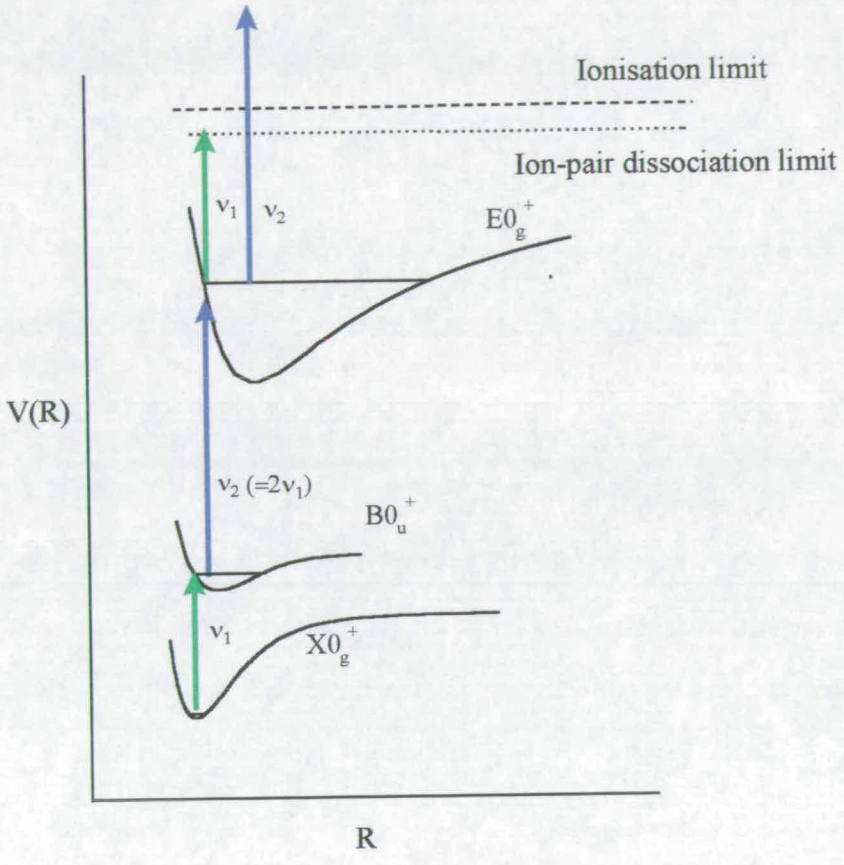

Figure 7-1 The one-laser two-colour excitation scheme.

7.3.2 Effect of jet-cooling

Figure 7-3 shows the spectra (I^+ signal) recorded with different backing pressures of helium and argon. It can be seen that with a higher backing pressure of helium, and thus better cooling, the spectra (figure 7-3a and b) become dramatically simpler. This effect is more obvious when argon is used as carrier gas (figure 7-3c). The cooling effect suggests that structures which lose their intensity correspond to hot bands or to transition from high J levels, while those that retain their intensity or get stronger, originate from cold bands or low rovibrational levels.

Two ion-pair states, the E 0_g^+ and f 0_g^+, can be accessed in the energy region of $\nu_1 + \nu_2 \approx 54000$ cm^{-1}. Table 7-1 shows some possible double resonance

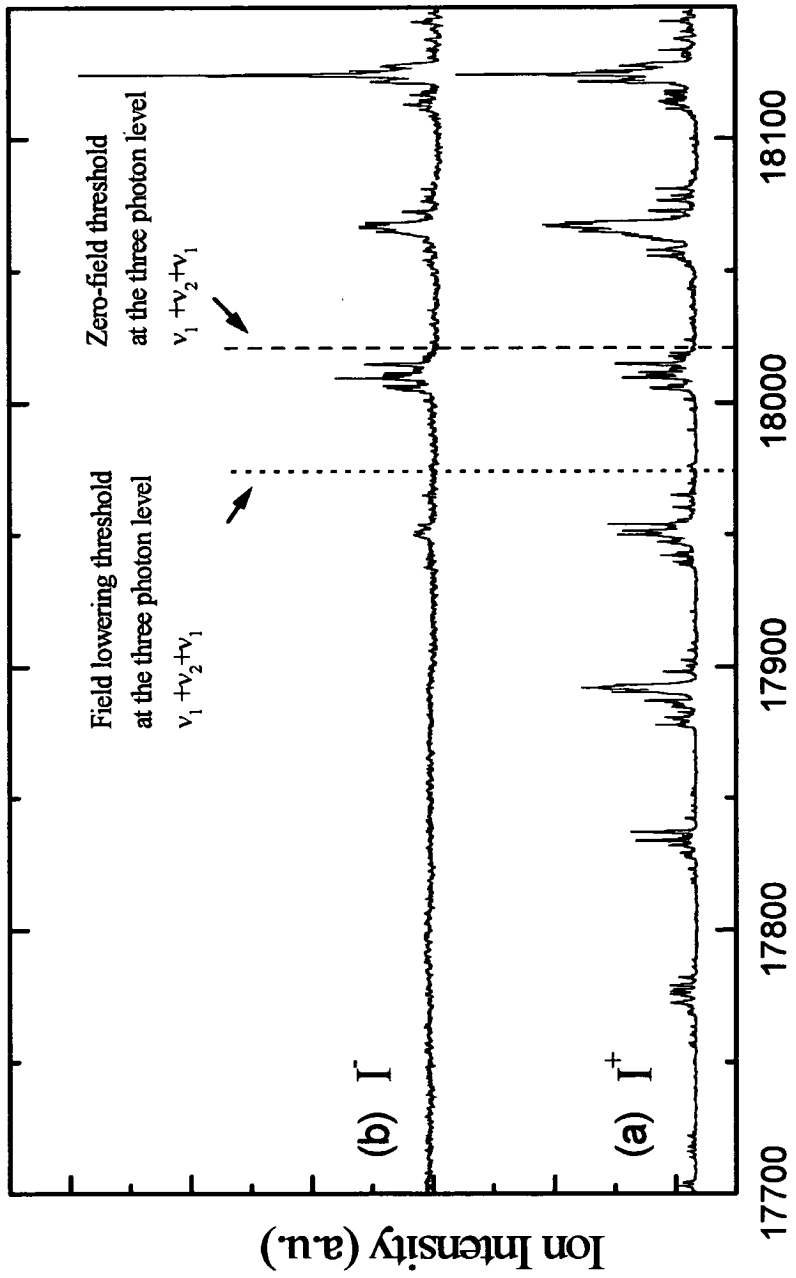

Figure 7-2: Ion-pair formation spectra using multiphoton excitation ($v_1+v_2+v_1$: with $v_2=2\ v_1$) enhanced by accidental resonance (a) I^+, (b)I^-.

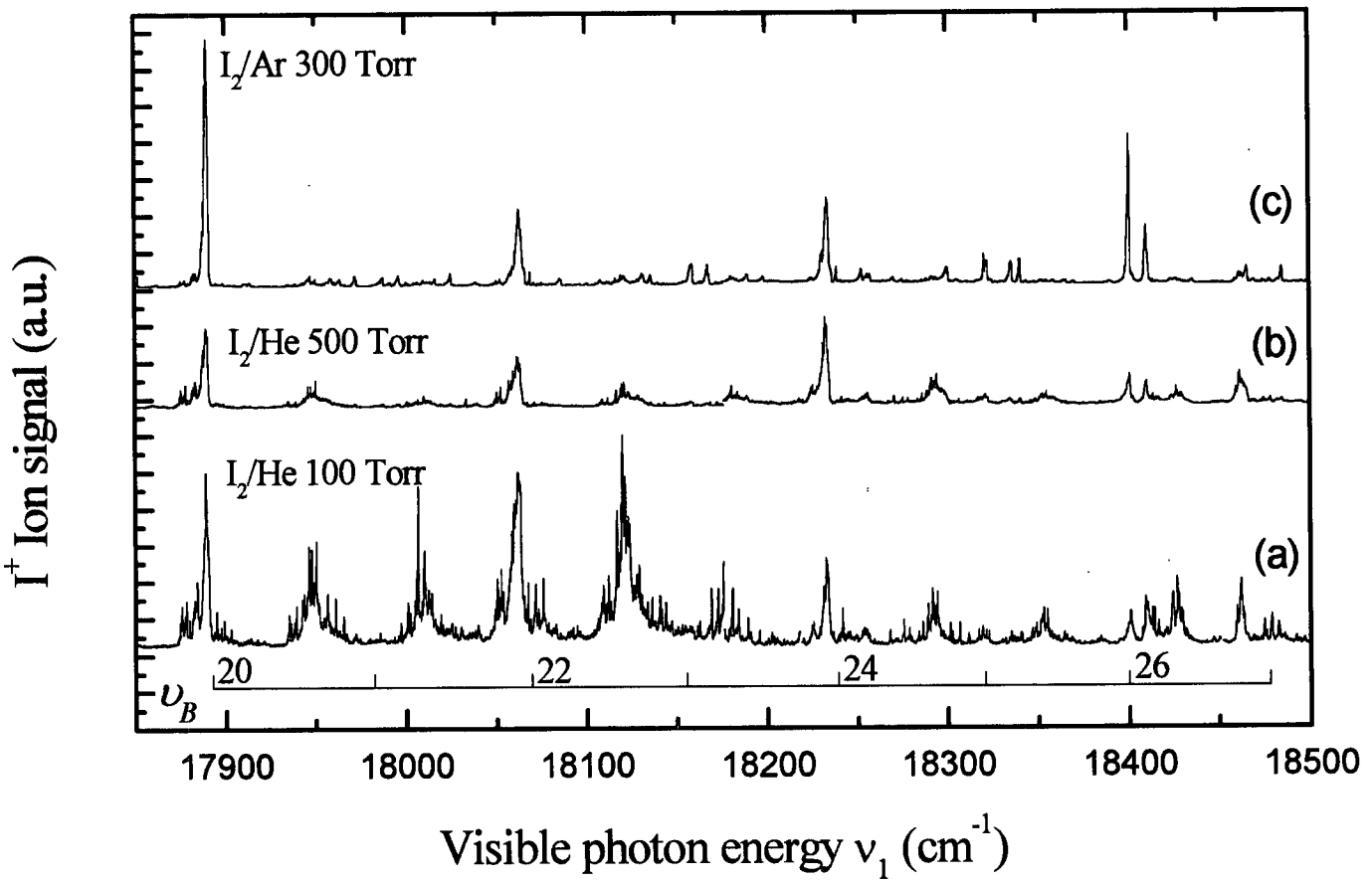

Figure 7-3: Cooling effect of carrier gases (He and Ar) on the REMPI spectra of I_2 recorded in the I^+ mass channel, (a)Total pressure I_2/He 100 torr; (b) total pressure I_2/He 500 torr; (c)total pressure I_2/Ar 300 torr.

E←B←X excitation paths. It can be seen that the strong peaks in figure 7-3b at 17890.0, 18063.1, 18233.7 and 18400.8 cm^{-1}, agree well with the predicted accidental resonances in table 7-1.

Table 7-1: The frequencies of B←X[a], E←X[b], and f←X[b] transitions. The values in green colour indicate when the B state and E state come into accidental resonance.

ν_1/cm^{-1}	υ_B	E_B/cm^{-1}	$3\times E_B$	υ_E	E_E/cm^{-1}	υ_f	E_f/cm^{-1}
	19	17801.4	53404.2	163	53425.1	71	?
17890.0	**20**	**17892.9**	**53678.7**	**168**	**53675.7**	73	53628.1
	21	17982.4	53947.2	173	53921.0	77	53932.4
18063.1	**22**	**18069.9**	**54209.7**	**179**	**54208.8**	81	54157.3
	23	18155.5	54466.5	184	?	84	54453.0
18233.7	**24**	**18239.1**	**54717.3**	**190**	**54717.0**	87	54671.8
	25	18320.7	54962.1	195	54940.8	91	54958.0
18400.8	**26**	**18400.2**	**55200.6**	**201**	**55203.0**	94	55169.6
	27	18477.7	55433.2	204	55331.7	97	55379.1

[a]Ref.6. [b]Ref.7

At low temperatures only the lower rotational levels are populated, so only transitions from low J levels close to the band heads are possible. For further excitation to the E ion-pair state with ν_2, only a few rotational levels in a small energy range are available. As a result, the condition of accidental resonance between the rotational structure of vibrational levels of the B and E states has become very important.

The rotational contours of the B←X transition are strongly red degraded. At 300K, high J levels of the B state can be accessed at any energy in the range between 17800 cm^{-1} and 18500 cm^{-1}. With vibrational spacings of 50 cm^{-1} for the E state[7], and 70 cm^{-1} for the f state[7], the rovibrational levels of these states are relatively closely spaced. In this situation accidental resonance is possible. This explains the large difference between the spectra at different temperatures.

7.3.3 High resolution study of the 17890 cm^{-1} band

A higher resolution scan of the strong accidental resonance at 17890 cm^{-1}, observed by collecting I^+, is shown in figure 7-4a. It can be seen from table 7-1 that this spectrum corresponds to the accidental double resonance

$$I^+ + I \longleftarrow I_2^+ \xleftarrow{\nu_2} I_2^{**}\ E(\upsilon = 168) \xleftarrow{\nu_2} I_2^{*}\ B(\upsilon = 20) \xleftarrow{\nu_1} I_2\ X(\upsilon = 0)$$

($\nu_2=2\nu_1$)

The band head of B ← X (20,0) lies at 17892.88cm^{-1}. A simulation of B ← X (20,0) is shown in figure 7-4c. The same transition, recorded simultaneously by laser induced fluorescence in the I_2 static cell is shown in figure 7-4b. It can be seen that the maximum (marked with a short arrow) in the double resonance spectrum in figure 7-4a corresponds to P(13) or R(17).

The energy of the band maximum in figure 7-4a is 17890 cm^{-1}. If a true accidental resonance occurs, i.e. the energy of the second step is exactly twice that of the first, then the two-photon ($\nu_1+\nu_2$) energy would be 53670 cm^{-1}. The initial rotational energies in the ground state of J = 13 and 17 are calculated as 6.79 and 11.41 cm^{-1} using the known B value[8] of 0.0373 cm^{-1}, hence the total energies above $\upsilon = 0$, J =0 of the ground state after the two-photon transitions are 53 676.8 and 53 681.4 cm^{-1}. From the work of Wilson et al[7] it is known that the band head for the E←X(168,0) transition lies at 53675.7 cm^{-1} which is a little higher(1.5 cm^{-1}) than the onset of the high energy edge of the strong feature observed here at 53674.2 cm^{-1}. Using the later value it is seen that there is either 2.6 or 7.2 cm^{-1} of the rotational energy available in the E(168) level. Because of the rotational selection rules two-photon excitation using the P(13) and R (17) pump lines must terminate in J = 11 or 13 or J = 17 or 19 of the final state, respectively. The four possible assignments give B values for the upper state of 0.0197, 0.0143, 0.0235 and 0.0189 cm^{-1}. The value of 0.0143 cm^{-1} is comparable with the reported value for B, for υ = 96 of the E state of 0.0149 cm^{-1} [9]. Thus this strong accidental resonances involves the transition, E (υ = 168, J = 13) ←B (υ = 20, J = 12) ←X (υ = 0, J = 13).

It can be seen that a secondary peak at 17889.3 cm^{-1} (marked with a large arrow) corresponds to P(15) or R(19). It is found by a three-colour experiment,

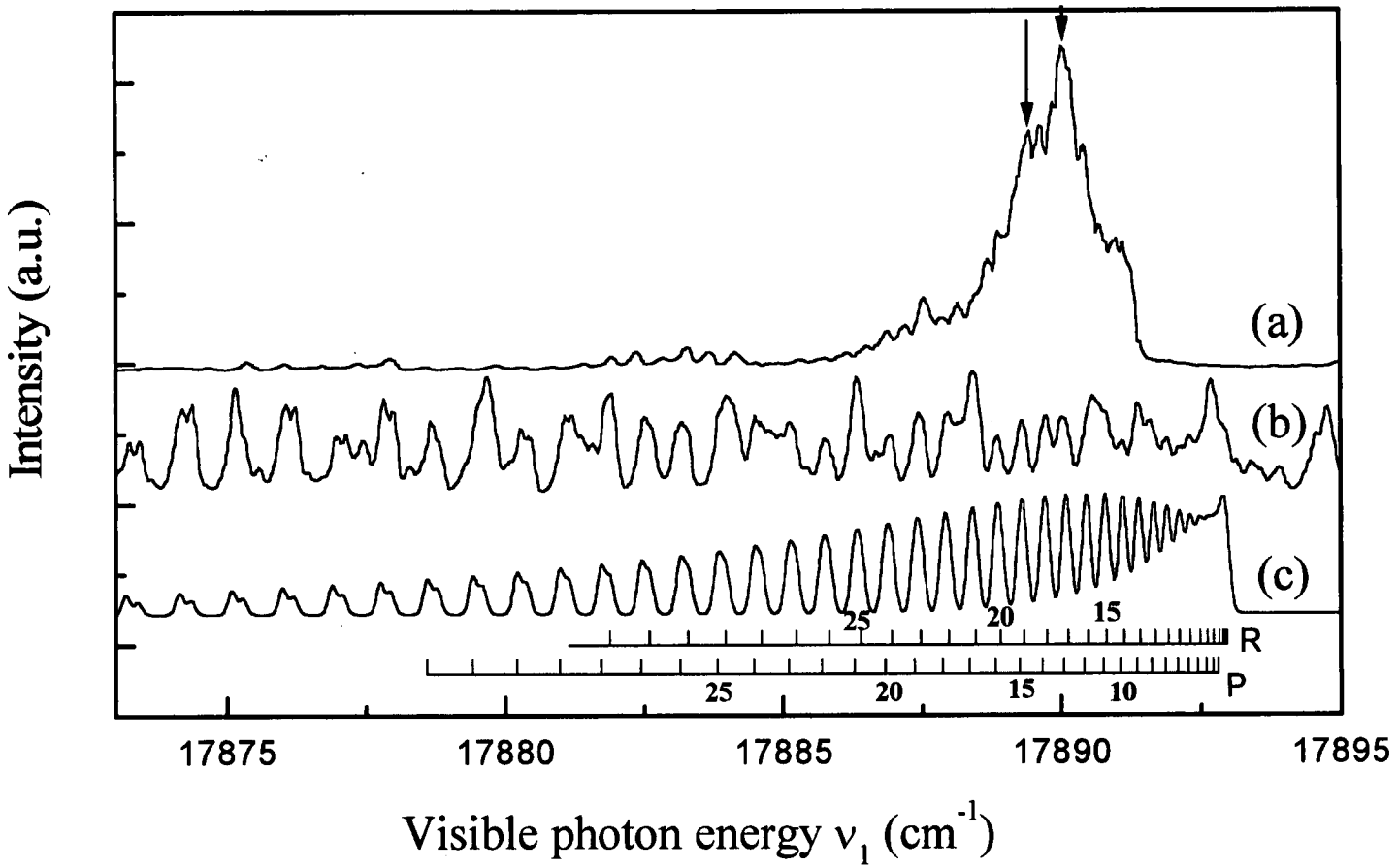

Figure 7-4: (a) Higher resolution scan of the 17890 cm^{-1} band in figure 7-2a; (b) LIF spectrum recorded simultaneously with (a) but in a static cell; (c) simulation of the band contour of (20,0) band of I_2 (B←X).

similar to those described in the next section, that transitions via P(15) terminate at exactly the same upper state, i.e. same υ and same J, at the two-photon level (one visible photon and one frequency-doubled photon), as that described above. The two-photon energy (one visible photon plus one frequency-doubled photon) of this transition is 53667.9 cm^{-1} in comparison with 53670 cm^{-1} for the above transition. The energy difference between these two transitions is 2.1 cm^{-1}. Again, according to the selection rules, two-photon transitions using the P(15) and R (19) pump lines must terminate in J = 13 or 15 or J = 19 or 21 respectively. Using the known ground state B value[8] of 0.0373 cm^{-1}, one can obtain the energy level difference of $\Delta E(J=15 - J=13) = 2.16$ cm^{-1} and $\Delta E(J=19 - J=17) = 2.76$ cm^{-1}. The value of 2.16 cm^{-1} is close to 2.1 cm^{-1} and the excitation path is assigned as:

$E (\upsilon = 168, J = 13) \leftarrow B (\upsilon = 20, J = 14) \leftarrow X (\upsilon = 0, J = 15)$

7.3.4 Ion-pair formation using three-color multiphoton excitation

The energy region around the first threshold for the ion-pair formation was scanned using two-laser, three-color, three-photon excitation, the pump laser exciting the molecule into υ=20 of the B state, via the P(13) line as described above, with the subsequent excitation to J = 13 of υ=168 of the E state. A third, independently tunable photon(ν_3) was then scanned from 535 to 553 nm to cover the threshold region. Using a constant extraction field (equivalent to zero time delay) of 1250V/cm, the prompt I^+ and I^- production spectra were obtained and are shown in figure 7-5. The strong accidental resonance at 17890 cm^{-1} in the two colour spectrum was chosen as pump resonance because the total three photon energy of $\nu_1 + \nu_2 + \nu_1$ lies below the ion-pair formation threshold, as can be seen in the spectra in figure 7-2. In this situation competition between ion-pair formation pathways by absorption of a ν_1 photon and a ν_3 photon at the third step can be avoided. This could otherwise result in a large background signal.

The I^- spectrum (figure 7-5b) shows a clear onset at 71864 cm^{-1}, 198 cm^{-1} below the field-free value of the lowest ion-pair formation threshold, which is the field lowering value expected from the field dependence observed for ICl. The I^+ ion signal disappearing at the same energy suggests that no resonant intermediate states

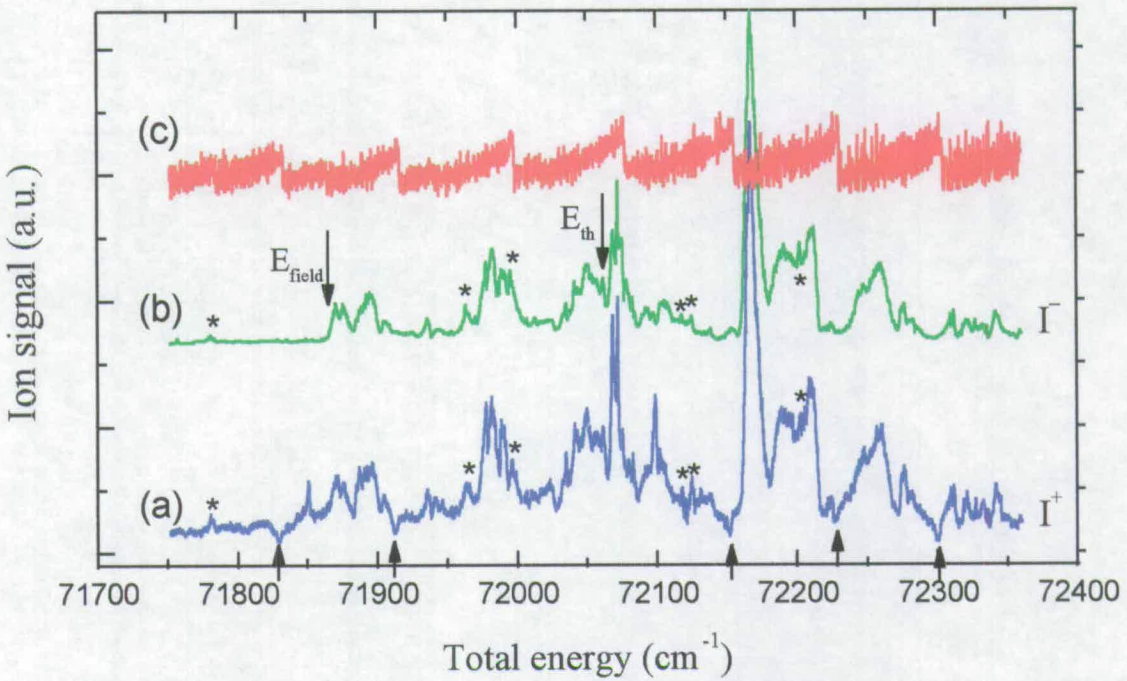

Figure 7-5: (a) and (b) Ion-pair formation spectra of I_2 using three-colour multiphoton excitation ($\nu_1+\nu_2+\nu_3$: with $\nu_2=2\nu_1$). One visible photon ν_1 pumps the molecule from the ground state X(υ =0, J=13) to the B state (υ =20, J=12). A frequency doubled photon ν_2 (=2 ν_1) subsequently excites the molecule to the E (υ =168, J=13) state by accidental resonance. Then another tunable photon ν_3 (from the second laser) is scanned through the ion-pair threshold region. The field-free and field-induced thresholds are marked with downward arrows on the spectra. The features marked by * and upwards arrows are explained in the text. Total energy is relative to υ =0, J=0 in the ground state. (a) I^+ and (b) I^-. (c) LIF spectrum of B←X transitions of I_2 by absorption of ν_3 in a static cell recorded simultaneously with (a) when scanning ν_3. The LIF spectrum is plotted on the same total energy scale as in (a) and (b) for direct visual comparison of the band head positions and for the dips in the I^+ spectrum in (a).

are present just below 71850 cm^{-1}, that can assist the REMPI photoionisation process. I^+ and I^- signals are of roughly equal intensity, indicating that the ionic dissociation channel is the dominant process in this region. Above the threshold, the highly structured spectrum, with little or no intensity between individual peaks, indicates the crucial role of doorway states in the ion-pair formation process. The 6f Rydberg state based on the ground state ($[3/2]_{c,g}$) of the molecular ion core and the 7p Rydberg state based on the excited state ($[1/2]_{c,g}$) of the molecular ion core were shown to be responsible for most of the observed structure in the VUV laser excited ion-pair formation spectra[5]. Clear strong progressions of 4f Rydberg state based on the $[^2\Pi_{1/2}]$ core were also observed at higher energy above 72500 cm^{-1}. Although the one-photon spectrum is very different in appearance with the multiphoton spectra presented here, the same Rydberg states could still be acting as doorway states.

The features marked with an asterisk (*) in figure 7-5 are caused by a two-colour (ν_3 and ν_2 only) signal due to the ion-pair process

$$I^+ + I^- \longleftarrow I_2^{***} \xleftarrow{\nu_3} I_2^{**}\ E \xleftarrow{\nu_2} I_2^{*}\ B \xleftarrow{\nu_3} I_2\ X(\upsilon = 0)$$

This is confirmed by the spectrum recorded in the I^- channel when the fundamental (ν_1) was removed from the pump laser output using a UG5 filter. It should be emphasized that the transition energies of the bands asterisked in figure 7-5 are different from the wavenumber scale shown.

The I^+ signal (figure 7-5a) shows essentially the same structure (same ν_3 dependence) as I^-, except for a small two-color background (~5-10% of its total ion signal) due to the pump laser only (i.e. ν_1 and ν_2) and a clear progression of dips superimposed on this background. From a comparison of the I^+ spectrum to the LIF spectrum from B←X transitions recorded simultaneously in a static cell (figure 7-5c), when ν_3 is scanned, it appears that the positions of these dips correspond to the band heads of B←X transitions. What is happening here is that the scanned ν_3 photon replaces ν_1 in the first step. Absorption of a ν_3 photon will compete with absorption of a ν_1 photon to pump molecules to different vibrational states other than $\upsilon = 20$. Those I_2 molecules excited by ν_3 will no longer be pumped to υ=168

of the E state and thus are depleted. This will reduce the yield of I^+ and cause dips, at certain wavelengths of ν_3 corresponding to strong absorption around the band heads of B←X system, in the photoionisation yield background, unless a ν_2 photon can pump the molecules from these B states by accidental resonance, such as those features marked with * in figure 7-5.

7.3.5 The ZIKE-PFD spectrum of I_2

Pulsed field dissociation experiments were carried out using a ±2016V high voltage pulse superimposed on a small dc voltage (0 to ±30V). The excitation scheme is exactly the same as in the previous section. When argon gas was used as carrier instead of helium in the molecular beam, it was found that ZIKE ions can be observed with considerable intensity at delays longer than 3.5 μs, in comparison with about 2 μs with helium. The most plausible explanation for this is that with heavier argon, which moves with a lower post-expansion velocity than helium, the I_2 molecules (which have the same velocity as the carrier gas) have longer residence in the collection region.

The first experiment was to determine the residual dc electric field in the interaction region of the apparatus. It is known from the experiments with ICl that the time-of-flight of the ZIKE peak is invariant to the time delay of the high voltage pulse, while the prompt ions are shifted to a different position by the small residual field, thus have a different time-of-flight. The two traces in figure 7-6a show the TOF spectra of I^+ which correspond to prompt ions at energy of 72068 cm^{-1} (above threshold) and ZIKE signal at energy of 72048 cm^{-1} (below threshold) at a time delay of 3.485 μs. In this experiment, the -HV end of the input of the high voltage switch was attached to the ground of the apparatus (see section 2.4.2 in chapter 2). It can be seen that there is no observable difference in the TOF between these two peaks, although there is a slight difference in the peak shape. Figure 7-6b shows an observable shift of about 25 ns in the TOF of I^+ prompt ions (at 72068 cm^{-1}) when the output of the high voltage pulser is held at 0.2V. Thus the residual dc field in the interaction region must be less than 125 mV/cm (considering the spacing between the two plates is 1.6 cm), when grounded.

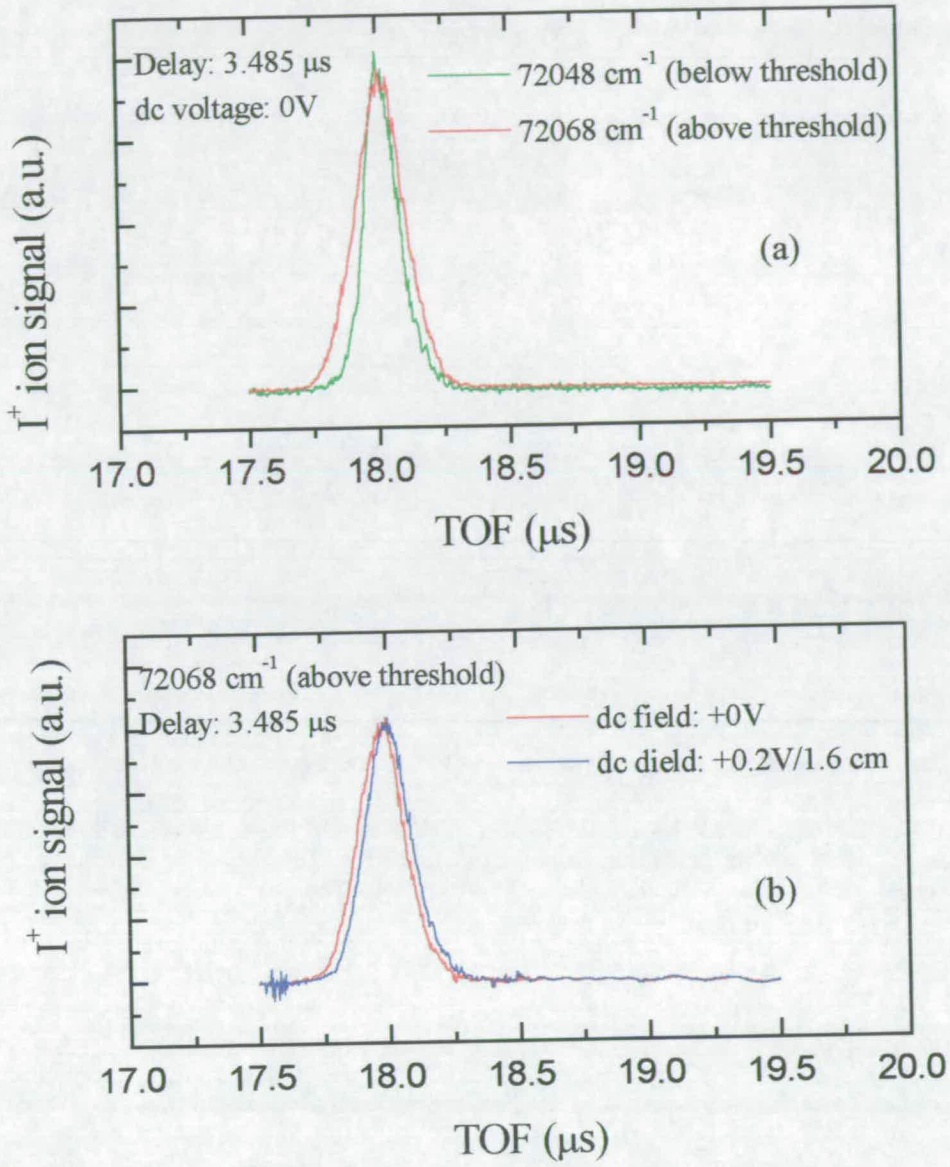

Figure 7-6: Effect of a small dc field, applied prior to the high voltage extraction pulse, on the time-of-flight spectra of I^+ (produced by ion-pair formation). Extraction pulse +1.25 kV/cm and time delay 3.485 μs. (a)zero external dc field: green-total energy at 72048 cm^{-1} (below threshold); red-total energy at 72068 cm^{-1} (above threshold); (b) Total energy at 72068 cm^{-1}: red-zero external dc field; blue-external dc field 125 mV/cm.

The TOF spectrum in the I^- channel was investigated systematically by varying the dc bias field. Figure 7-7a shows several time-of-flight spectra of I^- at a total energy of 72055.6 cm^{-1}, below the zero-field threshold of 72062 cm^{-1}, with different dc bias fields. At 0 V/cm, the TOF spectrum is single peaked at 18 μs which corresponds to the ZIKE ion signal. At –6.25V/cm, the field lowers the dissociation threshold to $72062-5.4\sqrt{6.25} \approx 72048$ cm^{-1}, which is now 7.6 cm^{-1} lower than the excitation energy 72055.6 cm^{-1}, which will produce prompt pairs of ions with maximum total translational energy of 7.6 cm^{-1}. This small negative dc field also serves to push all the prompt ions, whether initially moving towards or away from the entrance to the flight tube, towards the entrance of the flight tube, before the high voltage acceleration pulse applied. Thus the prompt ions appear at longer arrival times than the ZIKE ions as shown in figure7-8a. The maximum translational energy of the prompt ions, marked by the arrows in the figure, is not large enough to separate into two peaks. For +6.25 V/cm, as expected, the prompt ions are pushed away from the entrance to the flight tube and thus have a shorter arrival time than the ZIKE ions. The most plausible reason for the difference in the signal intensity for positive and negative fields is an asymmetric detection efficiency for the ion extraction system.

Considering that the molecules are excited to an energy region above the saddle point, due to the field lowering of the threshold, it is very surprising that ZIKE ions can still be observed, although the yield is reduced to 25%. On increasing the field to –9.375 V/cm, the ZIKE signal can still be seen though it is reduced even more. Equally surprising is that there is always a continuum background signal between the ZIKE and the prompt ions in the TOF spectra. In order to rule out the possibility of a spurious signal due to the electronics, the TOF spectrum of prompt ion produced at 72068 cm^{-1}, 6 cm^{-1} above the field free threshold was obtained with +6.25 V/cm as shown in figure 7-7b. As expected, the TOF peak simply shifts to a shorter arrival time at 16.7 μs and becomes broader, no continuum signal is present in this case.

The most plausible explanation for this is that the continuum background is due to the slow dissociation of long-lived ZIKE states initially excited above the

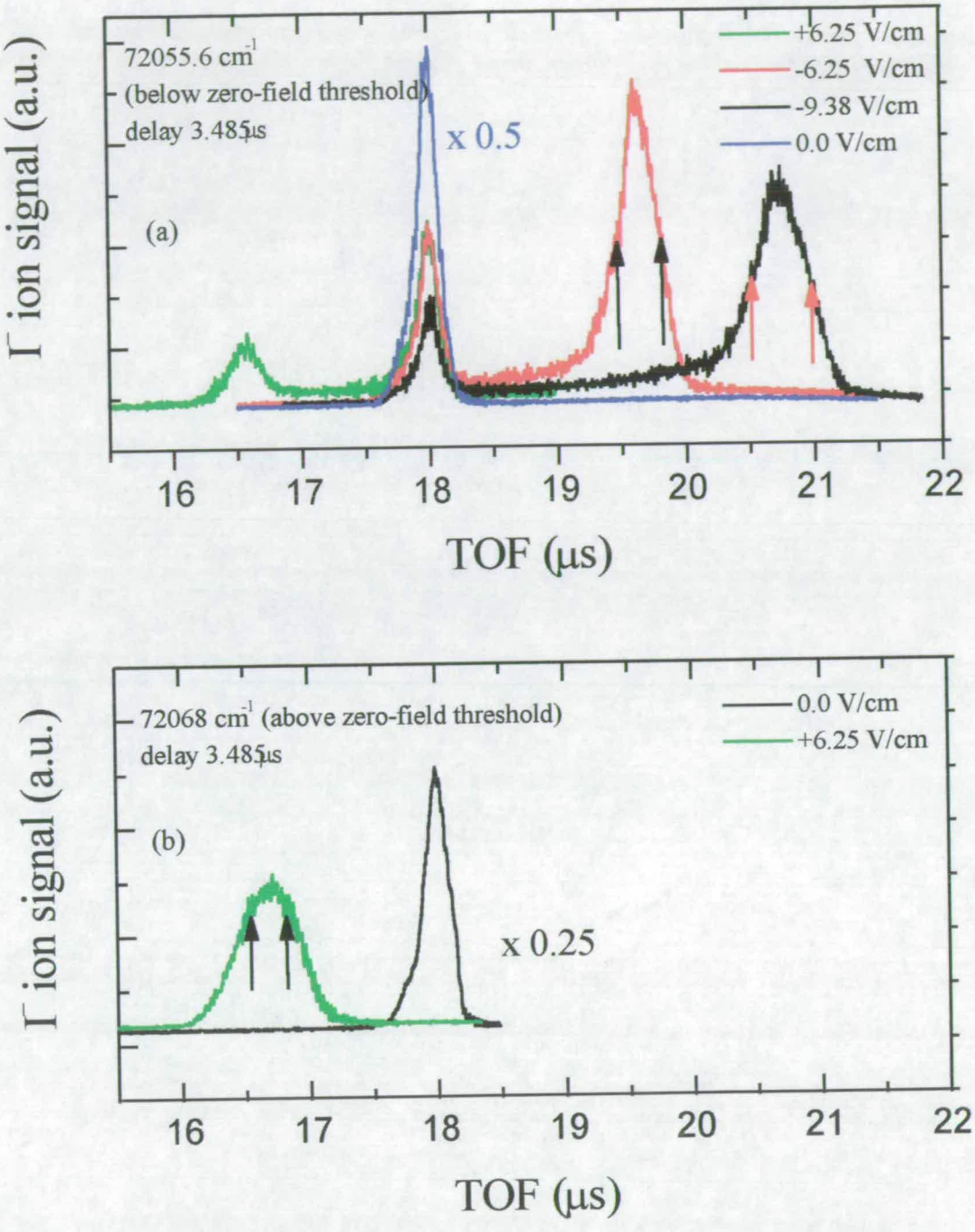

Figure 7-7: Time-of-flight spectra of I^- formation. The time delay of the extraction pulse after laser firing is 3.485 μs. (a) TOF spectra with excitation energy 72055.6 cm^{-1}, which is between the field-free threshold and the field-lowered threshold, with four different dc bias fields: 0.0, +6.25,-6.25 and -9.38 V/cm. (b)TOF spectra with excitation energy 72068 cm^{-1}, which is above field-free threshold, with dc=0.0 and +6.25V. The calculated initial kinetic energies of the ions are marked by arrows.

saddle point. Immediately after ions are formed they are then moved by the small dc field to different positions depending on the time they are produced. These ions will get a different acceleration from the extraction field depending on the time they were produced and thus have a different flight time.

The TOF spectrum in the I^+ channel was also investigated systematically by varying the dc bias fields. Similar results were observed. The total energy was fixed at 72048 cm^{-1} and the delayed high voltage pulse was set at 3.485 μs. With the dc field lower than +6.25 V/cm, only a single peak appeared at arrival 17.8 μs which corresponds to the ZIKE ion signal. On increasing the dc field higher than +6.25 V/cm, another peak which corresponds to prompt ions starts to appear at longer arrival time. The prompt positive ions are pushed towards the entrance of the flight tube, before the high voltage acceleration pulse is applied and thus have a longer arrival time than the ZIKE ions. The higher the dc field, the longer arrival time observed. As an example, a TOF spectrum of I^+ with dc bias field of 15.63 V/cm is shown in figure 7-8. The total energy is 72048 cm^{-1}, which corresponds to 7 cm^{-1}

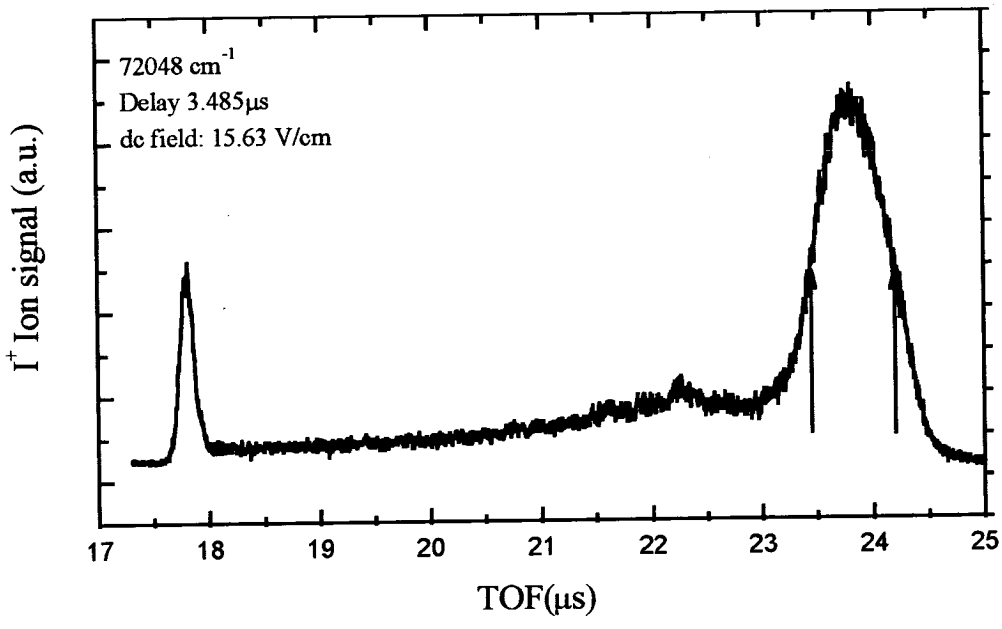

Figure 7-8: A time-of-flight spectrum of I^+ produced following ion-pair formation at a total energy of 72048 cm^{-1}, which is between the field-free and field lowered thresholds, (extraction pulse 1.25kV/cm and time delay 3.485 μs). The dc bias field is 15.63 V/cm. The calculated initial kinetic energy of the ions is marked by arrows.

above the field lowered threshold (72041 cm^{-1}). Again, a continuum signal between the ZIKE and prompt ion peaks is observed.

With the boxcar gated on the ZIKE peak and the probe laser wavelength (ν_3) scanned through the field-free ion-pair formation threshold, the ZIKE spectra observed for several different dc electric field strengths were recorded and are shown in figure 7-9. The high extraction voltage pulse, 1.25KV/cm, again delayed by 3.485 μs, is sufficient to dissociate any long-lived ion-pair states up to 190 cm^{-1} below the zero-field threshold but the ZIKE signal is seen to disappear at ~30 cm^{-1} below threshold. Referring to figure 7-5, there are doorway states that couple to high vibrational levels of the ion-pair states to generate free ion pairs right down to the lowered threshold of 71864 cm^{-1} with instant field dissociation. The disappearance of the ZIKE signal indicates that only those ion-pair states down to ~30 cm^{-1} below threshold can be converted to long-lived ZIKE states which can survive the time delay.

It is extremely surprising that in the case of I_2, unlike ICl and HCl,[17] increasing the dc field does not push the blue onset of the ZIKE spectra down in energy. It only reduces the ZIKE signal more on the blue edge with higher dc fields. The cutoff energy on the blue side of the ZIKE spectra at which the ZIKE signal disappears is invariant to the dc field, having the same value at 72061.8 cm^{-1}, which is exactly the zero-field threshold. This indicates that larger fields deplete more of the high vibrational (ion-pair) states but the process is not complete. Clearly, some of them still survive.

The I^- spectrum was also recorded as shown in figure 7-10a (lower trace) with high voltage pulse applied at 385 ns, i.e. at a very short delay after firing the laser. For comparison, the spectrum recorded under DC conditions is also plotted on the same graph (figure 7-10a., upper trace). It can be seen that at such short delay, all structure up to ~30 cm^{-1} below the threshold, except the two-colour signal due to $\nu_3 + \nu_2 + \nu_3$ (marked by *), has already disappeared. The I^- intensities at five separate energies marked by ↓ in figure 7-10a were measured, normalized to the intensity at -10.6 cm^{-1} and are plotted in figure 7-10b. It can be seen that the ratio of the intensities with delayed pulsed field to that with constant field extraction

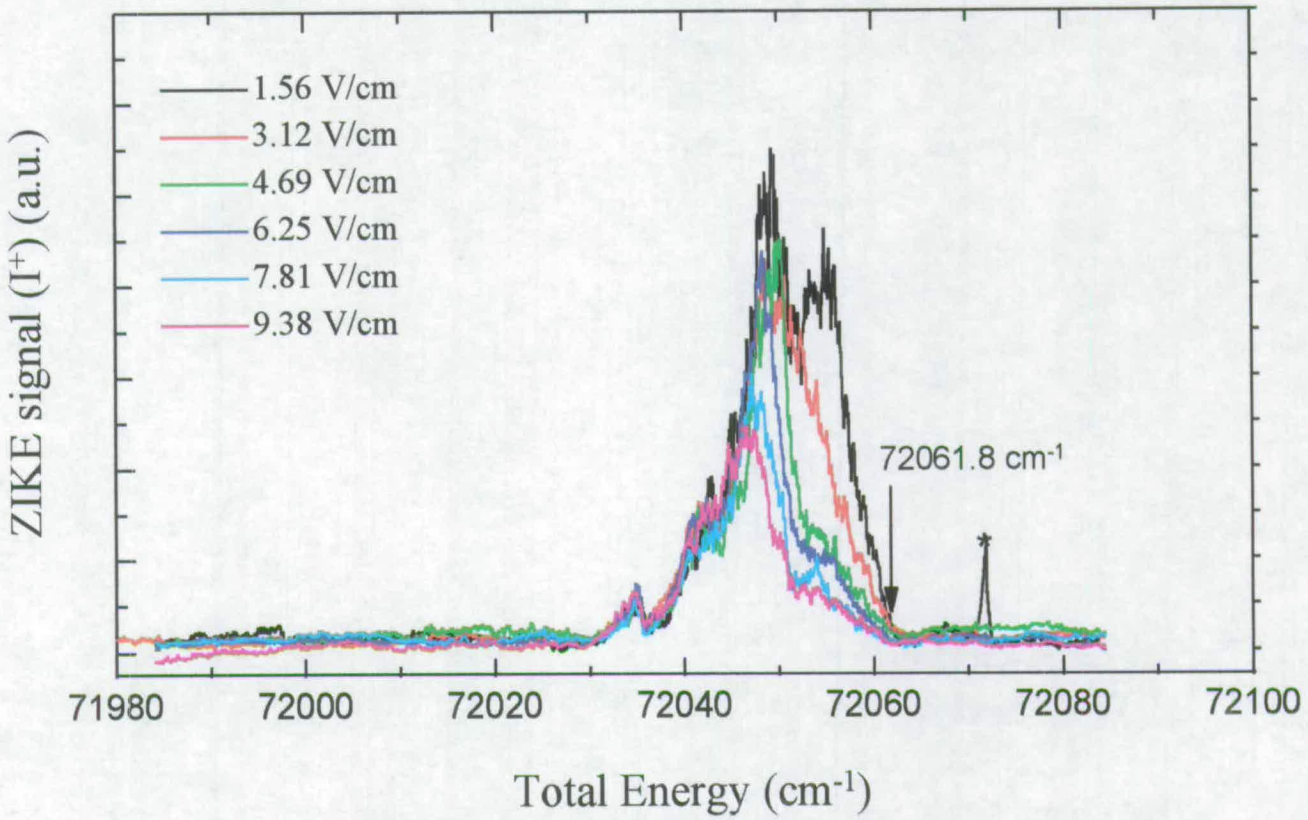

Figure7-9: ZIKE spectra observed with different dc bias fields. The excitation scheme is the same as in fig.7-5a, (extraction pulse 1.25 kV/cm and time delay 3.485 μs). The feature marked by * is due to electronic interference caused by a strong prompt ion signal at small dc field (1.56 V/cm).

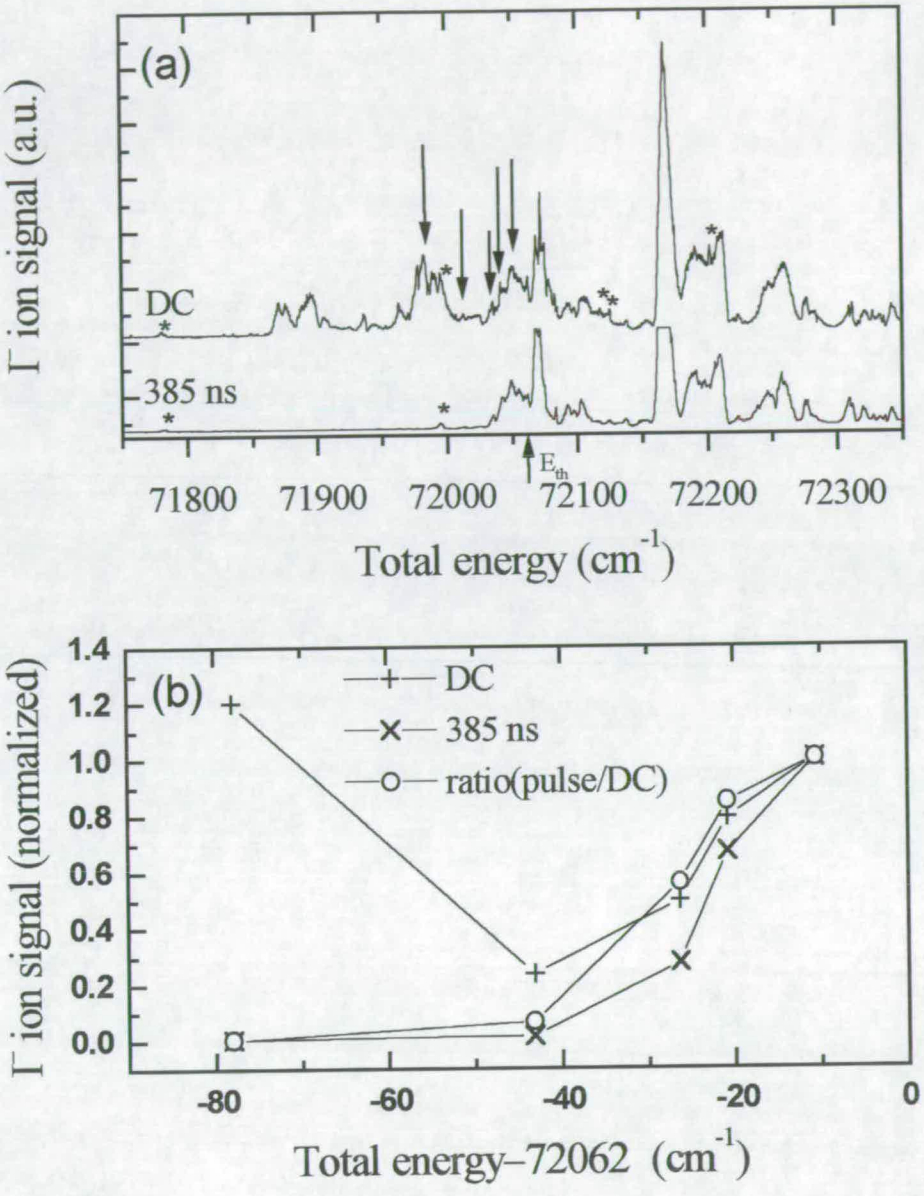

Figure 7-10: Comparison of I^+ spectra recorded using constant field extraction and pulse field extraction (385 ns delay). (a) Upper trace: constant field; lower trace: pulse field at 385 ns delay after laser firing. (b) Intensities measured at five different total energies below zero-field threshold marked by arrows in (a), normalised to the intensity at -10.6 cm^{-1}, (+) DC; (x) 385ns delay; (o) ratio of intensities with delayed pulse field to that with constant field extraction.

decreases slowly down to 30 cm^{-1} below the threshold, then drops to zero.

As expected, the prompt ion spectra obtained by recording the gated prompt I^+ ions do show a shift in the appearance energy with electric field. Figure 7-11 shows two spectra taken with two different dc fields. As can be seen the red edge is a very sharp step function. The systematic shifting of the onset with varying the dc field can be used to determine the zero-field threshold. By plotting the total energy E (cm^{-1}) vs $\sqrt{F}$ (F is the dc electric field in V/cm) and fitting a straight line to these data points (Figure 7-12), the field-free ion-pair threshold is determined as 72061.8 cm^{-1} by extrapolating to F=0. The lowering of the threshold by the dc electric field is given by the equation,

$$\Delta E\,(cm^{-1}) = 5.36\sqrt{F(V/cm)}$$

7.4 Discussion

Doorway states are seen to be crucial in accessing near-dissociation vibrational levels ($\upsilon > 10^4$) ion-pair states in ZIKE experiments. Direct transitions to the continuum from the intermediate state appear to be negligibly small. Similar to the ion-pair yield spectra observed for ICl, the highly structured ion-pair spectra of I_2 recorded in both I^+ and I^- channels (figure 7-5) reveal the presence of doorway states that are coupled to the dense manifold of near-dissociation vibrational levels of ion-pair states converging on the first dissociation limit for $I^+(^3P_2) + I^-(^1S_0)$ when below this threshold, and equally to the ion-pair continua when above. The doorway states observed near the threshold in the one-photon VUV excited ion-pair formation spectrum have been assigned predominantly to the 6f Rydberg states based on the $[^2\Pi_{3/2}]$ core and the 7p states based on the $[^2\Pi_{1/2}]$ core[5]. At higher energy, above 72500 cm^{-1}, several progressions of 4f Rydberg states based on the $[^2\Pi_{1/2}]$ core start to appear. The ion-pair states which are coupled with these doorway states are the $D(0_u^+)$ and $\gamma(1_u)$ for I_2, in comparison with ICl when the states involved are $E(0^+)$ and $\beta(1)$. As shown in figure 7-13, the inner walls of the potential curve of the D state might cross (diabatic) or anti-cross (adiabatic) with

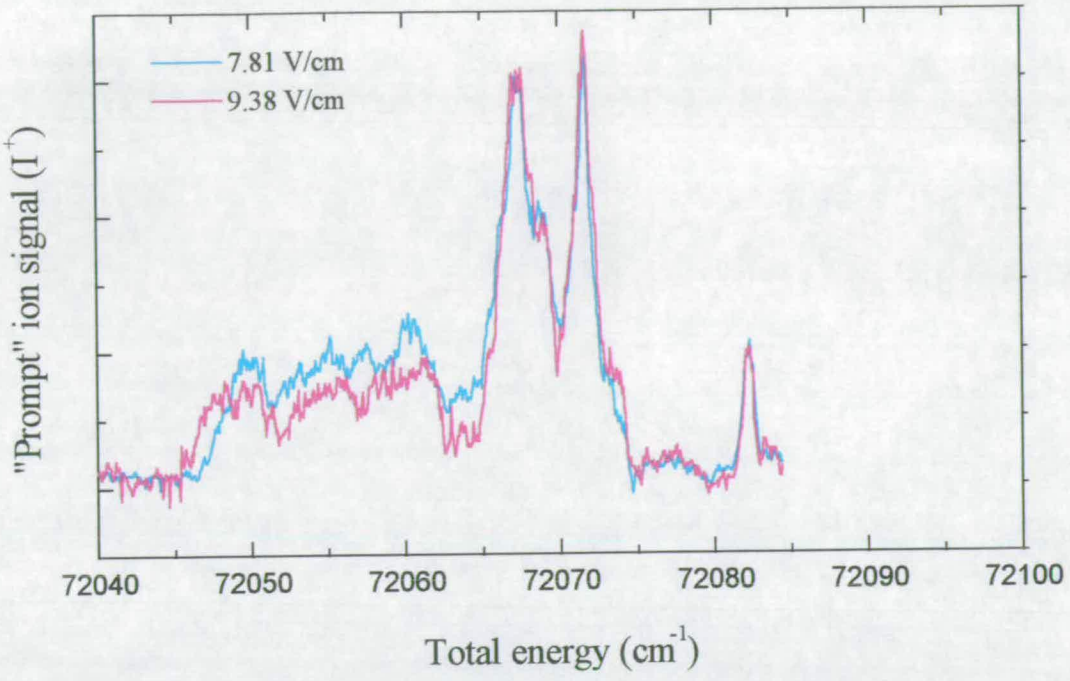

Figure 7-11: Small dc field induced "prompt" ion-pair formation spectra of I_2 recorded in I^+ channel with different dc bias fields, (extraction pulse 1.25 kV/cm and time delay 3.485 μs).

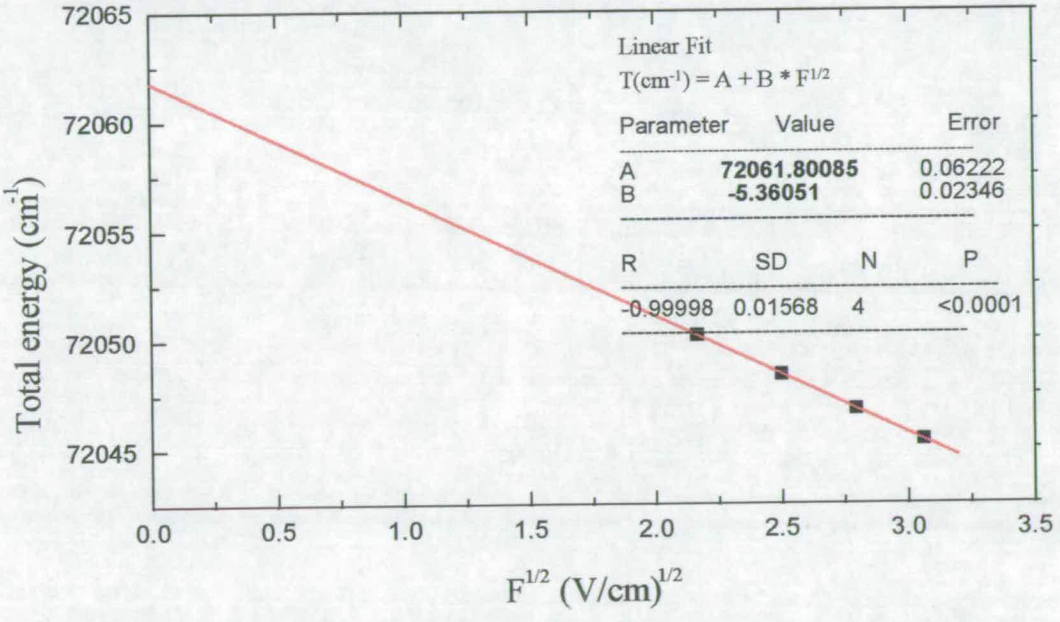

Figure 7-12: Extrapolation to determine the zero-field ion-pair formation threshold. The red edges of a series of spectra taken at different dc bias fields are plotted as a function of the square root of the dc field, (extraction pulse 1.25 kV/cm and time delay 3.485 μs).

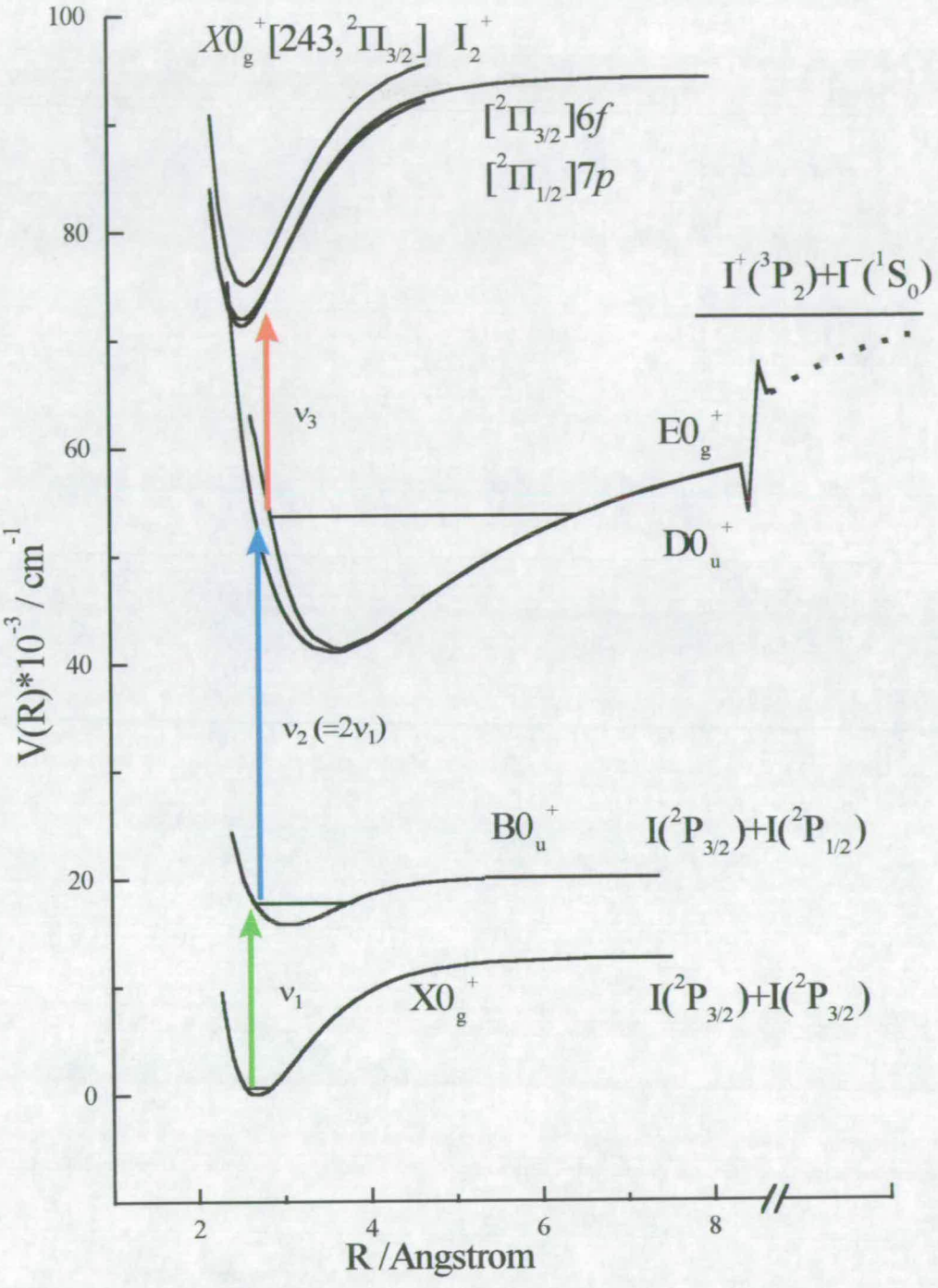

Figure 7-13: Several potential energy curves of I_2. The $D(0_u^+)$ curve is constructed using the parameters given by Tellinghuisen[13]. The $E0_g^+$ curve is made using its known turning points[12]. The potential curves of the Rydberg states are constructed assuming a Morse potential.

the inner walls of the 6f or 7p Rydberg states close to the dissociation limit. It is expected that this might result in a strong coupling between these states. It must be remembered, however, that the structure observed in the present multiphoton ion-pair formation spectra of both I_2 and ICl are completely different in appearance to their single photon equivalents[5], hence different Rydberg states may dominate the spectra.

The fact that no significant background signal, underneath the structured features in the I^- channel, was observed above the threshold shows that direct transitions to the ion-pair continua are negligibly small though a wide Franck-Condon window is present with intermediate states such as E (υ=168). Both sharp features and broad features appear in the spectra reflecting the different strengths of coupling to the underlying near continuum of the ion-pair vibrational manifold ($\upsilon>10^4$). The structured broad features suggest that it is also possible that some lower vibrational levels of upper tier ion-pair states act as doorway states.

Similar to ICl, all states initially accessed from the intermediate state, (υ=168) $E0_g^+$ state, couple to highly vibrationally excited $D(0_u^+)$ or $\gamma(1_u)$ ion-pair states or the continuum correlating with pairs of ions and thus form the dominant dissociation channel near the threshold. This suggest that repulsive valence states correlating with neutral atoms lie below this energy region or are coupled less efficiently to the doorway states. From a comparison of the absorption spectrum and the fluorescence excitation spectrum, observed by Hiraya el al[14] using synchrotron radiation, it can be seen that the relative fluorescence cross section in the energy region near the threshold is much weaker(~16%) than the lower energy region around 54000 cm^{-1}. Considering the better Franck-Condon overlap between the ground state and the excited states in the former energy region than the latter, it implies that fluorescence is a very weak channel near the threshold, indicating the opening of another channel, i.e. ion-pair formation.

The delayed pulsed field dissociation experiments show the existence of long-lived (>3.5μs) ion-pair states of I_2 just below the dissociation limit. From a comparison between spectra with delayed pulsed field extraction and with constant field extraction (figure 7-10a), it is clear that the closer to the threshold the more

efficient becomes the conversion from the originally photoexcited states to the high υ and high J states, which is consistent with the fact that the density of the ion-pair states increases closer to the threshold. This is similar to the creation of ZEKE states. However, for the same magnitude of bound energy, the vibrational levels of an ion-pair state are much denser than that of Rydberg states belonging to the series converging to the ionisation threshold. For example, at a binding energy of about 11 cm^{-1}, the density of high-υ ion-pair states is 200 times higher than that of high-n Rydberg states. Therefore the depth (the energy below dissociation limit) of ZIKE states could be larger than that of ZEKE states for similar external and surrounding interactions (~30-50 cm^{-1} for ZIKE states in comparison with ~10 cm^{-1} for ZEKE states).

When argon gas was used as carrier instead of helium in the molecule beam, it was found that ZIKE ions can be observed with considerable intensity at delays longer than 3.5 μs, in comparison with about 2 μs with helium. One possible reason for this is that argon cooling resulted in slower motion and prevented the molecules from moving out of the collection region before the extraction pulse was applied.

The onset (the minimum energy) of the spectra obtained by recording gated small field prompt ions (figure 7-11) shows a clear field-shift with varying small dc fields. By extrapolating the field dependence of the onset, the field free ion-pair threshold was determined as 72061.8 cm^{-1}. Surprisingly, however, it seems that the cutoff (the maximum energy) at which the ZIKE signal disappears does not shift with varying small dc fields though the overall blue edges do show a large reduction in intensity with increasing field. Interestingly, the cutoffs of ZIKE signal always appear at the same maximum value, ~72061.8 cm^{-1}, which is exactly the field-free threshold. At first sight this seems rather puzzling, however, when considering this phenomenon together with the observation of the continuum background ion signal in the TOF spectra (figure 7-7a and figure 7-8), the picture starts to become clear. Classically speaking, similar to the Rydberg atoms, the long-range Coulomb potential of the ion-pair states will be modified by the external electric field. It should be emphasized that the potential is only lowered in the direction of the electric field, being raised in the direction opposite to the field. A saddle point is

formed in the downhill side and the classical threshold energy is lowered compared with the field-free threshold. The molecule excited by the polarised laser will be dominantly aligned in the direction of the polarisation. In the present experiment, the probe photon is vertically polarised (parallel to the electric field). Considering the molecules being excited from the ground state ($X0_g^+$) to the $B0_g^+$ state by vertically polarised visible photons and then subsequently pumped to the intermediate $E0_g^+$ state by a horizontally polarised UV photon, there will be a considerable number of molecules in highly excited vibrational ion-pair states which have quite a large angle with respect to the field direction, assuming no change in the orientation of the molecules during conversion from the initially excited Rydberg (doorway) states. Thus, those molecules which lie close to the direction of the electric field, with I^- (still bond) pointing downhill, will dissociate to pairs of ions immediately after the excitation, while others having large angles will need time to re-orient in order to dissociate. Assuming a hydrogenic model, the radial recurrence time for the molecules excited at 5 cm^{-1} ($\upsilon \approx 50000$) below the field-free threshold is calculated to be about 0.2μs.

We note that a similar phenomenon, delayed ionisation of the highly excited atomic Rydberg states, has been observed by Noordam et al[15-16].

7.5 Conclusion

It has been demonstrated that electronic states close in energy (<30 cm^{-1}) to the first ion-pair dissociation threshold of I_2 can be efficiently converted to long-lived ($\tau_d > 3.5$ μs) sub-threshold ion-pair states which are analogous to ZEKE (high Rydberg) electronic states. The ionic dissociation limit was found by extrapolating the field-shifted onsets of the free-ion spectra to be 72062±4 cm^{-1}, which is consistent with the calculated value. The field-induced shift was found to be $5.36\sqrt{F}$.

In addition, a new phenomenon, delayed dissociation of highly excited vibrational ion-pair states, above the classical saddle point, has been observed for I_2.

The different behaviour exhibited by I_2 and ICl must reflect the dynamics of dissociation of the high vibrational levels of ion-pair states.

7.6 References

1. J.D. Morrison, H. Hurzeler, M.G. Inghram and H.E. Stanton, *J. Chem. Phys.* 1960, **33**, 821.
2. J.A. Myer and J.A.R. Samson, *J. Chem. Phys.* 1970, **52**, 716.
3. M.E. Akopyan, F.I. Vilesov and Yu.L. Sergeev, Opt. Spectrosc. 1973, **35**, 472.
4. A. Kvaran, A.J. Yencha, D.K. Kela, R.J. Donovan and A. Hopkirk, *Chem. Phys. Lett.* 1991, **179**, 263.
5. R.J. Donovan, A. Flexen, K.P. Lawley, R.R.J. Maier, A. Manck and T. Ridley, to be published.
6. J.M. Hutson, S.Gerstenkorn, P. Luc and J. Sinzelle, *J. Mol. Spectrosc.* 1982, **96**, 266.
7. P.J. Wilson, T. Ridley, K.P. Lawley and R.J. Donovan, *Chem. Phys.* 1994, **182**, 325.
8. R.J. LeRoy, *J. Chem. Phys.* 1970, **52**, 2683.
9. A.R. Hoy and A.W. Taylor, *J. Mol. Spectrosc.* 1987, **126**, 484.
10. V.N. Sarma and Y.N. Joshi, *Can. J. Phys.* 1983, **61**, 1434.
11. H. Hotop and W.C. Lineberger, *J. Phys. Chem. Ref. Data* 1985, **14**, 731.
12. P.J. Wilson, PhD thesis, The Edinburgh University, 1994.
13. J. Tellinghuisen, *Can. J. Phys.* 1984, **62**, 1933.
14. A. Hiraya, K. Shobatake, R.J. Donovan and A. Hopkirk, *J. Chem. Phys.* 1988, **88**, 52.
15. G.M. Lankhuijzen and L.D. Noordam, *Phys. Rev. A* 1995, **52**, 2016.
16. G.M. Lankhuijzen and L.D. Noordam, *Phys. Rev. Lett.* 1996, **76**, 1784.
17. J.D.D. Martin and J.W. Hepburn, *J. Chem. Phys.*, 1998, **109**, 8139.

Chapter 8

Photodissociation of Ozone between 335 and 352 nm to give O_2 ($b\ ^1\Sigma_g^+$) + $O(^3P_J)$

8.1 Introduction

The UV absorption and photodissociation of O_3 have been the subject of numerous experimental[1-13] and theoretical[14] investigations. It is generally accepted that the Hartley absorption band between 220 and 310 nm arises from the electronically allowed transition from the ground state ($\tilde{X}\ ^1A_1$) to the repulsive wall of the $1\ ^1B_2$ state followed by prompt dissociation *via* the two main spin-allowed channels:

$$O_3 + h\nu \rightarrow O(^1D) + O_2(a\ ^1\Delta_g), \quad \Phi = 0.85 - 0.9,\ \lambda_{threshold} = 310\ nm \qquad (1)$$

$$O_3 + h\nu \rightarrow O(^3P_J) + O_2(X\ ^3\Sigma_g^-), \quad \Phi = 0.1 - 0.15,\ \lambda_{threshold} = 1180\ nm \qquad (2)$$

Process (1), the dominant singlet channel, is a result of direct photodissociation on the $1\ ^1B_2$ surface whereas the minor "triplet" channel is due to a curve crossing in the photolysis exit channel.

In the "tail" of the Hartley band ($\lambda > 310$ nm), diffuse vibrational structure becomes apparent in a region known as the Huggins band[1]. In spite of the reduced absorption coefficient of O_3 at these wavelengths, the photolysis at $\lambda > 310$ nm has a profound effect on photochemistry in the troposphere. It was assumed, until recently, that the sole photodissociation channel operative in this region was process (2) as this is the only energetically accessible spin-allowed channel at this energy. Recently, however a number of groups have reported that the following spin-forbidden channels also participate in the Huggins band photodissociation:

$$O_3 + h\nu \rightarrow O(^3P_J) + O_2(a\ ^1\Delta_g), \qquad \lambda_{threshold} = 612\ nm \qquad (3)$$

$$O_3 + h\nu \rightarrow O(^1D) + O_2(X\ ^3\Sigma_g^-), \qquad \lambda_{threshold} = 411\ nm \qquad (4)$$

Ball *et al.*[3-5] observed $O_2(a\ ^1\Delta_g)$ photofragment production, with $\Phi[O_2(a\ ^1\Delta_g)] \sim 10\%$, for photolysis wavelengths out to 331.5 nm which was temperature independent and attributed it to the spin-forbidden channel (3). Similarly a number of groups[6-12] observed a quantum yield 'tail' of $O(^1D)$ with photolysis wavelengths out as far as 336.5 nm which was assigned to the other spin-forbidden channel, (4), with an estimated temperature independent quantum yield of ~ 6% [6].

A fifth photodissociation channel is energetically accessible in this wavelength region of the Huggins band:

$$O_3 + h\nu \rightarrow O(^3P_J) + O_2(b\ ^1\Sigma_g^+), \qquad \lambda_{threshold} = 463\ nm \qquad (5).$$

However, its contribution has been neglected, and in this chapter the first experimental evidence that channel (5) is operative in the region 335 - 352 nm will be presented.

8.2 Experimental

Experiments in this chapter were performed on the REMPI apparatus described in Chapter 2. The laser arrangement for the photolysis of O_3 and REMPI spectroscopy of the photodissociation fragments involved the use of both dye lasers (a Lambda Physik FL3002 and a Lambda Physik FL2002), one for photolysis and the other for probing the fragments. In the two-colour experiments, the counter propagating defocused pump and focused probe beams were introduced into the ionisation chamber of the mass spectrometer using lenses of focal length 6 cm and intersected, at 90°, the molecular beam formed of O_3 in He.

O_3 was prepared by passing the output of a commercial ozoniser through a silica gel trap (dry ice cooling) at ~ -77 °C. The trap was then placed on a vacuum

line and residual gases pumped away to a pressure of 1 Torr. The O_3 was desorbed into a bulb to a pressure of 10 Torr followed by mixing with He gas to a pressure of 1 atm. Gas mixtures formed in such a way were found to contain ~5 Torr O_2 and ~5 Torr O_3. The gas mixture was then introduced into the ionisation chamber via an all glass feed-line and a General Valve pulsed nozzle. In this experiment, a dry ice/isopropanol mixture was used in the cooling trap of the diffusion pump instead of liquid nitrogen.

8.3 Results and Discussion

8.3.1 Use of the O_2 ($d3s\sigma_g$ $^1\Pi_g$) state as a resonant intermediate in identifying the photolysis products

The resonant intermediate state at the two-photon level accessed in the detection of the O_2 photofragment throughout this work was the $d3s\sigma_g$ $^1\Pi_g$ Rydberg state (the first member of the Rydberg series converging on the O_2^+ ($^2\Pi_g$) ground state ion). The spectroscopy of the *d* state has attracted much attention from both experimentalists, using (2 + 1) REMPI techniques from both the $O_2(X\ ^3\Sigma_g^-)$ state[15-18] and the $O_2(a^1\Delta_g)$ state[19] and Kinetic Energy Release (KER) spectroscopy[20-22], and from theoreticians[23-24]. Nonetheless this state has eluded complete characterisation due to its unusual spectroscopic properties which arise from the interaction with nearby valence states. Sur *et al.*[15], however, succeeded in rotationally analysing the (0,0), (1,0) and (3,0) vibrational bands of the $d \leftarrow\leftarrow O_2(X\ ^3\Sigma_g^-)$ transition recorded using the (2 + 1) REMPI technique. The results of a second rotational analysis of the (3,0) vibrational band of the $d \leftarrow\leftarrow O_2(a\ ^1\Delta_g)$ transition, using the same technique[19], were in good agreement with those of Sur *et al.*[15] Transitions involving the v′ = 2 level of the *d* state have not been rotationally analysed as that level experiences a much stronger perturbation. However, here the v′ = 2 level is mainly focused on as there are severe experimental difficulties with the use of the v′ = 0, 1 and 3 levels for the present work.

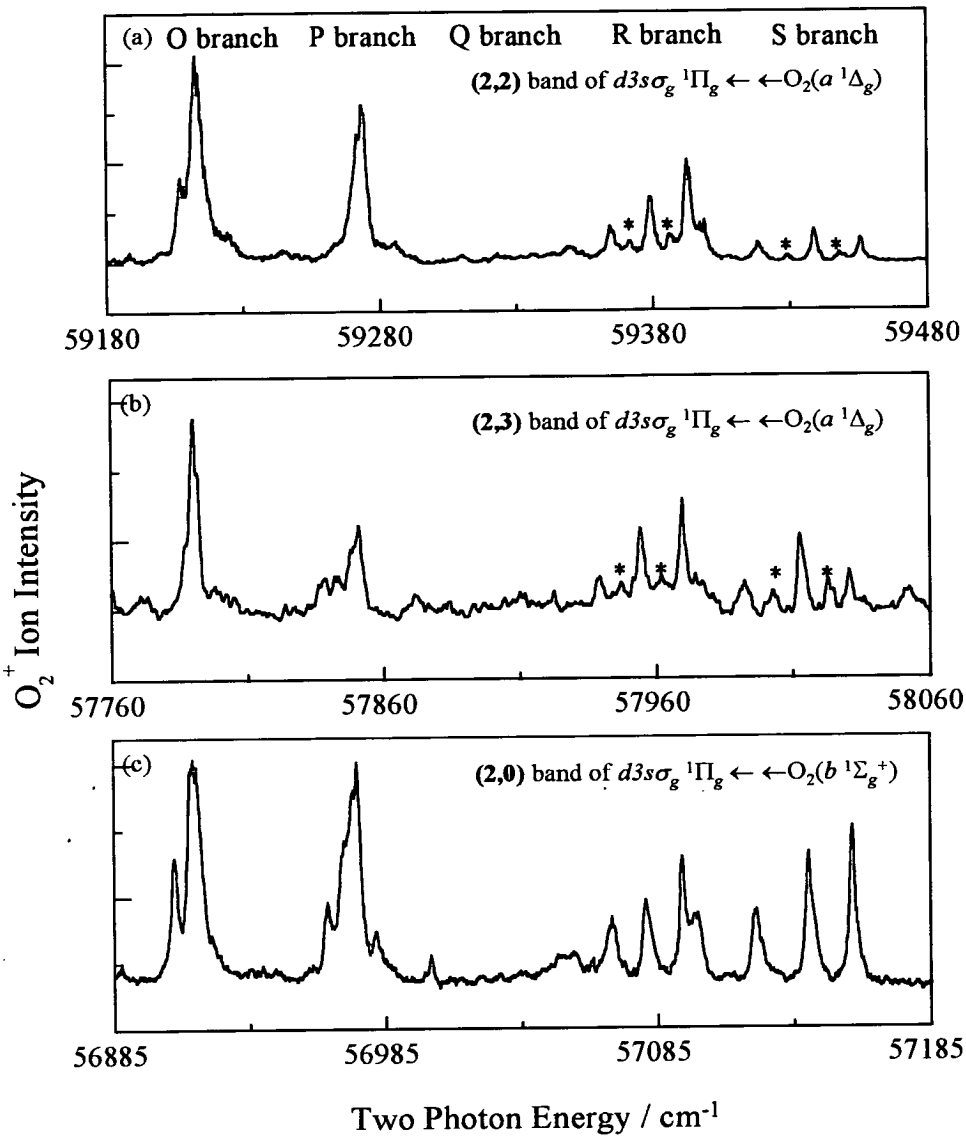

Figure 8-1: (2+1) REMPI spectra of the photofragments produced from photolysis of O_3: (a) and (b) are the (2,2) and (2,3) bands respectively of the $d3s\sigma_g\ ^1\Pi_g\leftarrow\leftarrow O_2(a\ ^1\Delta_g)$ transition recorded by probing the molecular photofragments produced in the 254 nm (Hartley band) photolysis. The spectrum in (c) is the (2,0) band of the $d3s\sigma_g\ ^1\Pi_g\leftarrow\leftarrow O_2(b\ ^1\Sigma_g^+)$ transition recorded by probing the molecular photofragment produced in the 340nm (Huggins band) photolysis. The REMPI scheme in (a) and (b) are the result of a combination of (2′+1) and (2′+1′) processes whereas the spectrum in (c) is produced *via* a combination of ((1+1′)+1) and ((1+1′)+1′) processes. The features labelled with asterisks are those due to transitions from the depleted odd J levels of $O_2(a\ ^1\Delta_g)$. These features are completely absent in the $O_2(b\ ^1\Sigma_g^+)$ band due to nuclear spin restrictions.

The spectrum in figure 8-1(a) was recorded by photolysing O_3 at 254 nm, exciting the (2,2) band of the $d \leftarrow \leftarrow O_2(a\ ^1\Delta_g)$ transition with the probe laser and ionising with a further pump photon, i.e. a (2′ + 1) process. The most obvious observation is that only a limited number of J states of the $O_2(a\ ^1\Delta_g)$ photofragment are observed. Observations made using Coherent anti-Stokes Raman scattering (CARS) spectroscopy[13], show that the rotational distribution peaks sharply at high J, with $\Delta J_{FWHM} \approx 12$, for the $O_2(a\ ^1\Delta_g, v = 2)$ photofragment. However, even with this limited number of J levels it has not proved possible to simulate the spectrum shown in figure 8-1(a) and it is clear that the upper state is too heavily perturbed to allow analysis of the nascent J distribution following Hartley band photolysis. This is further confirmed by the observation of the same J lines in the (2,3) band of the same electronic transition when photolysing at the same wavelength (see figure 8-1(b)), even though it is known that the nascent J distributions of the v = 2 and 3 levels of the $O_2(a\ ^1\Delta_g)$ state are different[13]. It is concluded that the observation of limited J lines in transitions to the v′ = 2 level of the *d* state is the result of strong Rydberg-valence interactions. However, this limited rotational contour can be considered a 'fingerprint' of transitions to this level of the *d* state and it will be used in the following section.

The other interesting point to note is the apparent intensity alternation between transitions from odd and even-J levels of the $O_2(a\ ^1\Delta_g)$ state which is evident in this spectrum (see figure 8-1(a) and (b)). A reduction in intensity of the odd-J levels (indicated by asterisks) has been shown to be a result of the selective depletion of those levels by a curve crossing in O_3 in the asymptotic region with a state correlating with the ground state products[13]. Due to spin statistics, the ground state $O_2(X\ ^3\Sigma_g^-)$ can only have odd N levels[25] and this exerts a symmetry selection rule on the crossing resulting in the depletion of only odd J levels of the $O_2(a\ ^1\Delta_g)$ state.

Having established that the $d3s\sigma_g\ ^1\Pi_g$ Rydberg state can be used to detect $O_2(a\ ^1\Delta_g)$ following photolysis of O_3 in the Hartley band, the same upper state has been used to investigate photolysis in the Huggins bands, as described below.

8.3.2 Photolysis of ozone by Huggins band excitation

To identify the peaks of the Huggins band absorption in the energy region under investigation a Photofragment Excitation (PHOFEX) spectrum was recorded by monitoring the production of $O(^3P_0)$ in the 335 - 345 nm energy region using the scheme shown in the insert of figure 8-2.

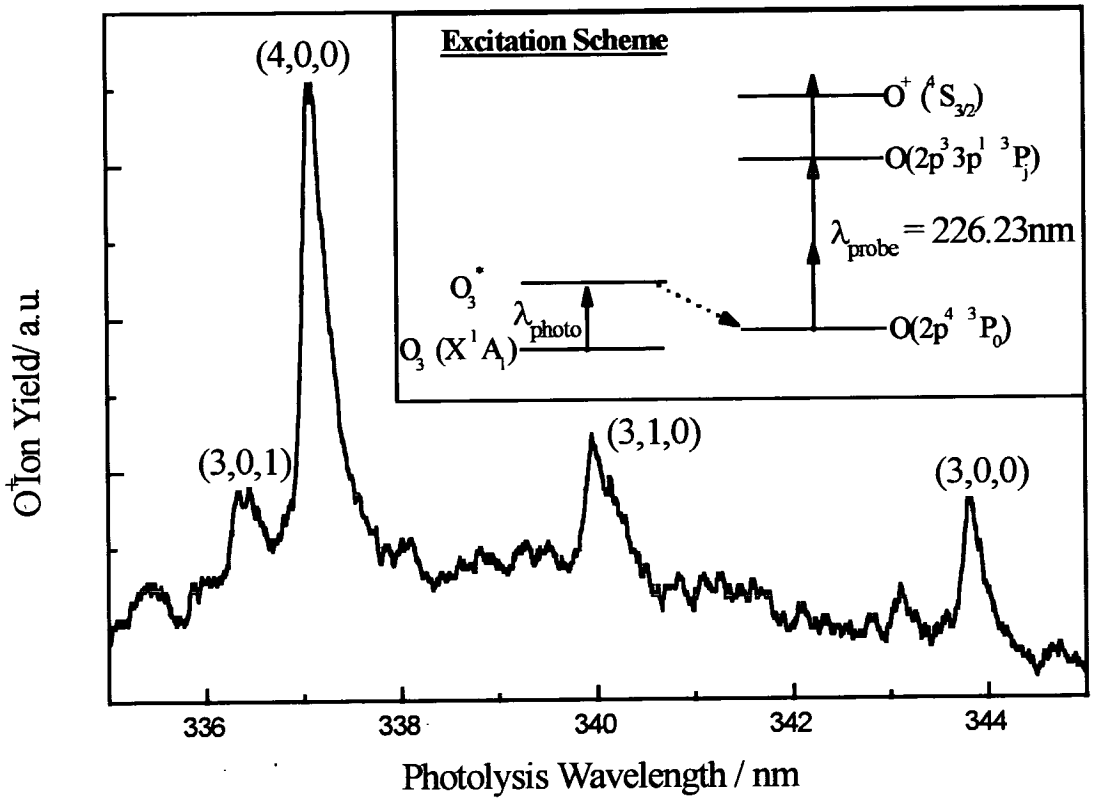

Figure 8-2: The Photofragment Excitation (PHOFEX) spectrum of O_3 recorded by probing the production of O ($^3P_0$) with λ_{probe} = 226.23 nm while scanning the photolysis laser in the 335 - 345 nm region (full scheme shown in the insert).

The resulting spectrum shows an increase in $O(^3P_0)$ production corresponding to bands in the O_3 absorption spectrum. The assignments of the bands in this spectrum in terms of (ν_1, ν_2, ν_3) where ν_1,ν_2 and ν_3 are the symmetric stretching, bending and asymmetric stretching vibrational modes in O_3, respectively,

are taken from the work of Katayama[1]. An alternative vibrational assignment has been proposed by Joens[2] but the choice of the vibrational assignment does not affect the results of this work. It is noted that the Huggins bands are readily observed, under jet cooled conditions, by monitoring the $O(^3P_0)$ photofragment. Similar results have been obtained by Takahashi *et. al.*[8] for the higher energy Huggins bands (308 - 326 nm).

Detecting the O_2 fragment following photolysis in the Huggins band is rather more challenging than detecting $O(^3P_0)$. However, using two-colour ((1 + 1′) + 1) and ((1 + 1′) + 1′) REMPI schemes a spectrum of O_2 in the region of *ca* 57,000 cm^{-1} has been observed. As will be shown below, this spectrum is attributed to $O_2(b\ ^1\Sigma_g^+, v = 0)$. The experimental approach used was to position the photolysis laser on each of the peaks in the Huggins band between 335 and 352 nm and to tune the second laser through a region where ozone absorption is negligible (i.e. 355 - 369 nm). The spectrum observed following photolysis in the (3, 1, 0) Huggins band is shown in figure 8-1 (c). At first sight the spectrum looks rather similar to those observed for $O_2(a\ ^1\Delta_g)$ (shown in figure 1(a) and (b)). However, the position of the band does not fit at all well with the transitions calculated for $O_2(a\ ^1\Delta_g)$. The origin of the nearest $O_2(a\ ^1\Delta_g)$ band, involving the v' = 2 level of the *d* state, is calculated to be some 600 cm^{-1} below the lowest energy feature in figure 8-1 (c). This, together with other evidence cited below, allows us to eliminate $O_2(a\ ^1\Delta_g)$ as the carrier of this spectrum. The possibility that the spectrum might arise from vibrationally excited $O_2(X\ ^3\Sigma_g^-)$ has also been considered. The (2,9) band of the $d \leftarrow\leftarrow O_2(X\ ^3\Sigma_g^-)$ transition is calculated to occur in this region. However, in the case of the $O_2(X\ ^3\Sigma_g^-)$ state, stronger spin-allowed transitions to the $C3s\sigma_g\ ^3\Pi_g$ Rydberg state, which lie at an energy ~ 600 cm^{-1} below that of the *d* state, should be prominent[19]. The lack of structure to lower energy of the features in figure 8-1 (c) indicates that this band is not due to the $d \leftarrow\leftarrow O_2(X\ ^3\Sigma_g^-)$ transition.

The only remaining low lying metastable state of O_2 is the $O_2(b\ ^1\Sigma_g^+)$ state and the assignment of the features shown in figure 8-1 (c) to the (2,0) band of the $d \leftarrow\leftarrow b$ transition is confirmed by the following observations. Firstly, visual inspection of the spectra illustrated in figure 8-1 (a), (b) and (c) shows that the

rotational spacings are very similar. Since the upper level is the same in each of these bands, the rotational constants of the vibrational levels of the $O_2(a\ ^1\Delta_g)$ state and the newly assigned state must be similar. This condition is satisfied by the $O_2(b\ ^1\Sigma_g^+)$, v'' = 0 level: B_v ($O_2(a\ ^1\Delta_g)$, v'' = 2) = 1.38365 cm^{-1}, $B_v(O_2(a\ ^1\Delta_g)$, v''= 3) = 1.36655 cm^{-1} and B_v ($O_2(b\ ^1\Sigma_g^+)$, v'' = 0) = 1.39126 cm^{-1} [26]. This compares with $B_v(O_2(X\ ^3\Sigma_g^-)$, v''= 9) = 1.29757 cm^{-1} [26], confirming that the lower state is not the ground state.

Secondly, the depleted odd J levels observed in the bands of the $d3s\sigma_g\ ^1\Pi_g \leftarrow\leftarrow O_2(a\ ^1\Delta_g)$ transition are now completely absent in the proposed $d3s\sigma_g\ ^1\Pi_g \leftarrow\leftarrow O_2(b\ ^1\Sigma_g^+)$ band shown. Nuclear spin statistics in $^{16}O^{16}O$ ($b\ ^1\Sigma_g^+$) dictate that only even J levels are present[25]. This is particularly convincing evidence that the lower state is indeed the $O_2(b\ ^1\Sigma_g^+)$ state.

Thirdly, as it has been shown, the rotational contours are very similar and therefore the energy spacing between equivalent rotational band heads (e.g. the O branch identified in figure 8-1) of each spectrum should reflect the known vibrational spacings of the lower levels[26]. The observed energy differences are consistent with these calculated values (G_v ($O_2(b\ ^1\Sigma_g^+)$, v'' = 0) - G_v ($O_2(a\ ^1\Delta_g)$, v''= 3) = 860.6 cm^{-1} and (G_v ($O_2(b\ ^1\Sigma_g^+)$, v'' = 0) - G_v ($O_2(a\ ^1\Delta_g)$, v''= 2) = 2291.2 cm^{-1})[26] to within the experimental limits (± 4 cm^{-1}). The (1,0) band of the same electronic transition in the expected energy region has also been observed, but unfortunately the signal-noise ratio is much lower.

The possibility that two photons are absorbed by O_3 before fragmentation takes place will be considered next. Indeed, the $O_2(b\ ^1\Sigma_g^+)$ state has been observed as a nascent product of photolysis of O_3 at 157.6 nm[27] and 193 nm[28-29]. The dependence of the $O_2(b\ ^1\Sigma_g^+)$ signal on pump power was therefore investigated. To separate the pump and probe processes, a (2' + 1') probe scheme was chosen. This experiment has the advantage that the pump photons are not involved in the detection scheme and therefore the signal power dependence of this laser can be attributed solely to ozone absorption. However, the one-colour REMPI spectrum of ozone in the region of the probe wavelengths in this scheme involves a very strong feature as a result of the coincidental overlap of the O branch of the (2,0) band of

the $d \leftarrow \leftarrow b$ transition with the 351.3 nm Huggins band in ozone (see figure 8-3 (a)). To minimise the effect of this one-colour signal it was necessary to slightly defocus the probe laser. The spectrum shown in figure 8-3 (b) was recorded by photolysing ozone at 340 nm with a pump laser which was even more defocused than the probe, and detecting the $O_2(b\ ^1\Sigma_g^+)$ with the probe laser by the (2′ + 1′) scheme described above. The resulting spectrum is essentially the same as that of the ((1 + 1′) + 1′) spectrum shown in figure 8-1 (c) with the exception that the O branch feature in figure 8-3 (b) still contains a small contribution from the one-colour probe laser signal. The pump laser power was then varied, while the two-colour signal intensity of the P branch feature was monitored having subtracted the minimal residual one-colour signals of each laser from the total signal intensity. The observed linear power dependence of the pump power (power index of n = 0.95 ± 0.09) is consistent with a one-photon photolysis scheme.

More conclusive evidence that fragmentation results from a one-photon absorption comes from kinetic energy measurements by P. O'Keeffe et al[30] on both the O (^3P_J) and $O_2(b\ ^1\Sigma_g^+)$ fragments using a delayed pulsed field extraction technique. The measured translational energy of the $O_2(b\ ^1\Sigma_g^+)$, v = 0 fragments following photolysis of O_3 at 351.4 nm confirms that these fragments are formed by a one-photon photolysis process in ozone. The translational energy distribution profile of the O ($^3P_0$) fragment following photolysis of O_3 at 322.64 nm shows three peaks, corresponding closely to the thermodynamic energy thresholds of channels (2), (3) and (5) shown in the introduction.

Valentini *et al.*[13] stated that the existence of a significant $O(^3P_J) + O_2(b\ ^1\Sigma_g^+)$ channel was necessary to reconcile their experimental observations. In fact they predicted a quantum yield for this channel of up to 0.56 for photolysis of ozone at λ_{photo} = 311 nm. The kinetic energy release profiles of the $O(^3P_J)$ fragments produced in the photolysis of O_3 ,which exhibit a sharp peak corresponding to slow $O(^3P_J)$ fragments formed in conjunction with $O_2(b\ ^1\Sigma_g^+)$, indicate a mode specific production of the $O_2(b\ ^1\Sigma_g^+)$ state with a quantum yield of ~ 30% for λ_{photo}= 337.2 nm.

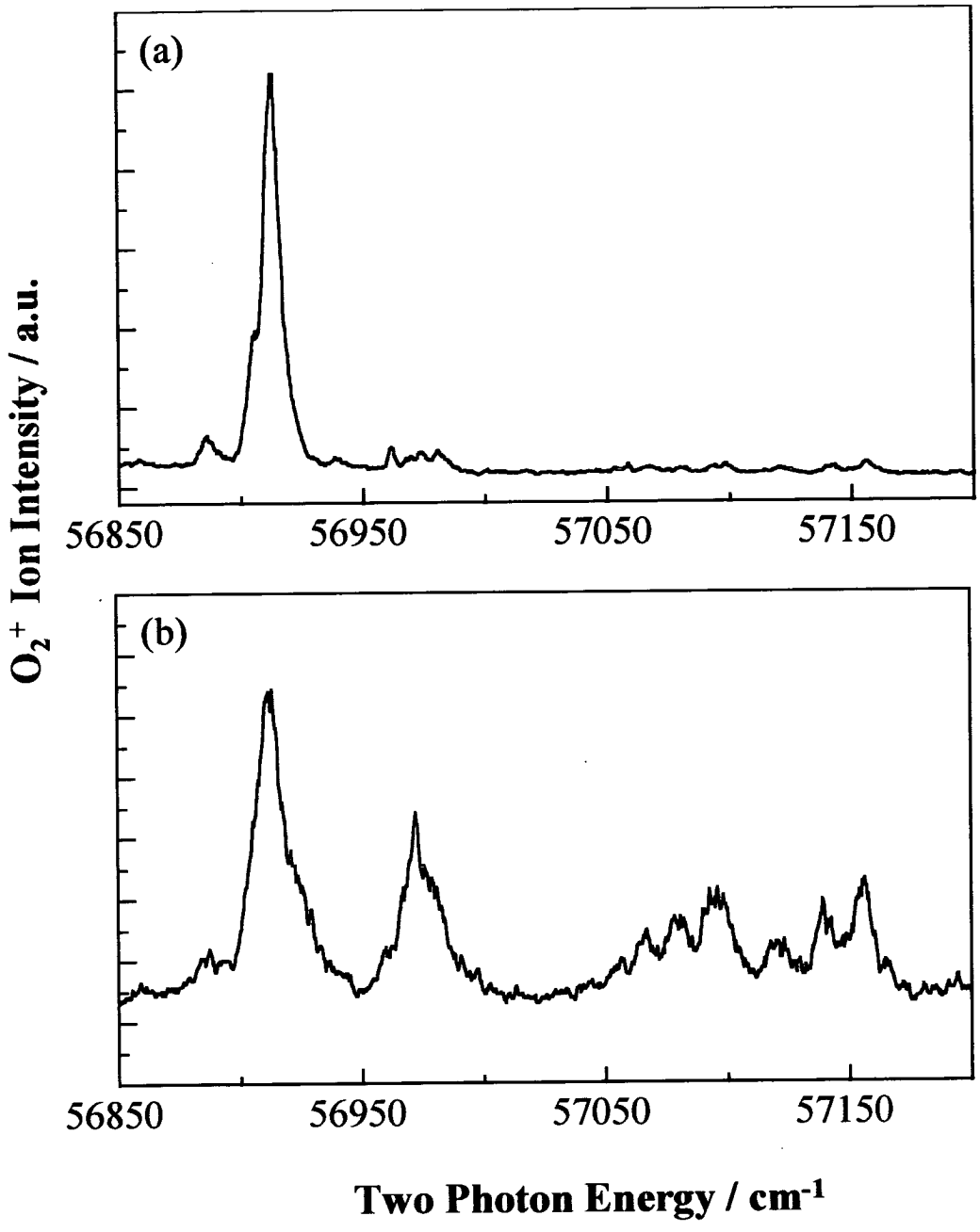

Figure 8-3: (a) The one-colour REMPI excitation spectrum of ozone recorded by photolysing ozone between 349.7 nm and 351.8 nm and detecting the O_2 fragments formed by (2 + 1) REMPI with the same laser. (b) The (2′ + 1′) spectrum of the (2,0) band of the $d3s\sigma_g\ ^1\Pi_g \leftarrow\leftarrow O_2(b\ ^1\Sigma_g^+)$ transition recorded by 340 nm photolysis of ozone followed by probing the O_2 fragments formed between 349.7 nm and 351.8 nm.

8.4 Conclusion

The formation of $O_2(b\ ^1\Sigma_g^+)$ following absorption in the Huggins band (335-352 nm) of O_3 has been observed for the first time. The $O_2(b\ ^1\Sigma_g^+)$ photofragment was detected using two-colour resonance enhanced multiphoton ionisation, with the $d3s\sigma_g\ ^1\Pi_g$ state as the resonant intermediate.

8.5. References

1. D.H. Katayama, *J. Chem. Phys.* 1979, **71**, 815.
2. J.A. Joens, *J. Chem. Phys.* 1994, **101**, 5431.
3. S.M. Ball, G. Hancock, J.C. Pinot de Moira, C.M. Sadowski and F. Winterbottom, *Chem. Phys. Lett.* 1995, **245**, 1.
4. S.M. Ball, G. Hancock and F. Winterbottom, *Faraday Discuss.* 1995, **100**, 215.
5. S.M. Ball and G. Hancock, *Geophys. Res. Lett.* 1995, **22**, 1213.
6. R.K. Talukdar, C.A. Longfellow, M.K. Gilles and A.R. Ravishankara, *Geophys. Res. Lett.* 1998, **25**, 143.
7. E. Silvente. R.C. Richter, M. Zheng, E.S. Saltzmann and A.J. Hynes. *Chem. Phys. Lett.* 1997, **264**, 309.
8. K. Takahashi, Y. Matsumi and M. Kawasaki, *J. Phys. Chem.* 1996, **100**, 4084.
9. K.Takahashi, M. Kishigami, Y. Matsumi, M. Kawasaki and A.J. Orr-Ewing, *J. Chem. Phys.* 1996,**105**, 5290.
10. K. Takahashi, M. Kishigami, N. Taniguchi, Y. Matsumi and M. Kawasaki, *J. Chem. Phys.* 1997, **106**, 6390 .
11. S.M. Ball, G. Hancock, S.E. Martin and J.C. Pinot de Moira, *Chem. Phys. Lett.* 1997, **264**, 531.
12. W. Armerding, F.J. Comes and B. Schulke, *J. Phys. Chem.* 1995, **99**, 3137.
13. J.J. Valentini, D.P. Gerrity, D.L. Phillips, J-C. Nieh and K.D.Tabor, *J. Chem. Phys.* 1987, **86**, 6745.

14. A. Banichevich and S.D. Peyerimhoff., *Chem. Phys.* 1993, **174**, 93; 1993, **178**, 155.

15. A. Sur, R.S. Friedman and P.L. Miller, *J. Chem. Phys.* 1991, **94**, 1705.

16. A. Sur, C.V. Ramana and S.D. Colson, *J. Chem. Phys.* 1985, **83**, 904.

17. A. Sur, C.V. Ramana, W.A. Chupka, and S.D. Colson, *J. Chem. Phys.* 1986, **84**, 69.

18. R.O.Loo, W.J. Marinelli, P.L. Houston, S. Arepalli, J.R. Wiesenfeld and R.W. Field, *J. Chem. Phys.* 1989, **91**, 5185.

19. R.D. Johnson III, G.R. Long and J.W. Hudgens, *J. Chem. Phys.* 1987, **87**, 1977.

20. W.J. v.d. Zande, W. Koot, J. Los and J.R. Peterson, *Chem. Phys. Lett.* 1987, **140**, 175.

21. W.J. v.d. Zande, W. Koot, J. Los and J.R. Peterson, *J. Chem. Phys.* 1988, **89**, 6758.

22. W.J. v.d. Zande, W. Koot and J. Los, *J. Chem. Phys.* 1989, **91**, 4597.

23. R.S. Friedman and A. Dalgarno, *J. Chem. Phys.* 1989, **90**, 7606.

24. Y.Li, I.D.Petsalakis, H-P.Liebermann, G.Hirsch, R.J.Buenker, *J. Chem. Phys.*1997, 106, 1123.

25. K.P.Huber and Herzberg, in *Molecular Spectra and Molecular Structure* I and II (Van Nostrand, Princeton, 1966).

26. T.G. Slanger and P.C. Cosby, *J. Phys. Chem.* 1988, **92**, 267.

27. M.R. Taherian and T.G. Slanger, *J. Chem. Phys.* 1985, **83**, 6246.

28. A.A. Turnipseed, G.L. Vaghjiani, T. Gierczak, J.E. Thompson and A.R. Ravishankava, *J. Chem. Phys.* 1991, **95**, 3244.

29. D. Stranges, X. Yang, J.D. Chesko and A.G. Suits, *J. Chem. Phys.* 1995, **102**, 6067.

30. P. O'Keeffe, T. Ridley, K.P. Lawley, R.J. Maier and R.J. Donovan, J. Chem. Phys. 1999, **110**, 10803.

Chapter 9

Photoionisation and Photoion-Pair Formation Studies using VUV Radiation Generated by Laser-Produced Plasmas and Four-Wave-Difference-Frequency Mixing

9.1 Introduction

Vacuum ultraviolet (VUV) absorption processes have been utilised for many decades[1,2] to study molecular structure, ionisation thresholds of atoms and molecules, quantum yields of photoionisation and photodissociation processes, autoionisation structure, and ion-pair production[3-4]. Different methods for producing VUV, especially synchrotron radiation, have been widely used.

It has been known for some time that continuum VUV and extreme ultraviolet (XUV) radiation can be generated by laser-produced plasmas[5]. XUV radiation has been investigated extensively and applied to processes such as inner shell photoexcitation studies of atoms and ions[6]. However, no applications for VUV radiation (around 10 eV) in the field of molecular photoabsorption and photoionisation have been reported.

A table-top, high power laser plasma x-ray source was developed at Rutherford-Appleton Laboratory using a picosecond excimer laser system[7]. This system demonstrated a very high (11%) conversion efficiency from laser energy to 1 nm (Cu L shell) x-ray radiation by using a very high laser power density (~ 10^{15} W/cm^2) on the target. This work investigates the suitability of this system, used at moderate on-target irradiance, to generate tuneable VUV radiation. Some preliminary results using this new VUV generation technique for molecular photoionisation and ion-pair production studies of CH_3Br and CH_3I in the region of

the first ionisation threshold (around 10 eV for most molecules of interest) will be presented in this chapter. For comparison, high resolution ion-pair formation study from CH_3Br is also carried out using four-wave-difference-frequency (FWDF) mixing.

9.2 Experimental

The experimental arrangements used in this chapter have been described in chapter 2. For the characterisation of VUV radiation from the laser-induced plasma, the parallel-plate ionisation chamber was pumped by a rotary pump up to $1.5x10^{-2}$ torr and then refilled with pure gaseous samples at a typical gas pressure between $1\text{-}5x10^{-1}$ torr. The voltage applied between the two parallel plates was 60V. The ion signal was measured using a LeCroy 9410 oscilloscope and averaged for 100 shots. For the photoionisation and photoion-pair formation study using higher resolution VUV output with a 1-meter spectrograph from the laser-produced plasma, the spectra were recorded using a Stanford Research Systems SRS250 boxcar integrator.

For VUV laser generation, the frequency doubled output(ν_1) of FL2002 dye laser, using Stibene 3 dye, was tuned to the two-photon resonance($2\nu_1$) of Kr used for FWDF at 94094 cm^{-1}. The other dye laser (FL3002) provided the visible or infrared photons with a tunable wavelength λ_3 by the fundamental of the dyes Rhodamine 101, Rhodamine B, Rhodamine 6G, Rhodamine 700 and Coumarin 153. A mixture of 200 torr with 400 torr of helium was introduced into the chamber of the mass spectrometer via a General Valve pulsed nozzle. The signals were always optimised by focusing the VUV at the interaction region. In this case, the UV and visible laser beams were far from focused due to wavelength-dependent refractive index. In addition, when the UV wavelength was off resonance, VUV power dropped with subsequent complete loss of CH_3^+ and Br^- intensities, confirming that the photoions were generated by the VUV.

9.3 Results and discussions

9.3.1 Characterisation of VUV radiation from laser-produced plasmas

Nitric oxide, toluene, acetone, benzene and xylene were used for the characterisation of the VUV radiation. The results are shown in figure 9-1. It can be seen that all of the spectra in figure 9-1 show a sharp high energy cutoff at the same wavelength which is caused by the transmittance of the MgF_2 window. All spectra show step functions at their corresponding ionisation thresholds and the values obtained from figure 9-1 are tabulated in table 9-1. They are in good agreement with the known values[11] in the range of experimental errors. These facts are real signatures of VUV radiation generation from the plasmas. As to our knowledge, this is the first direct evidence of VUV radiation generated by a laser-produced plasma.

Table 9-1: Ionisation energies of nitric oxide, acetone, toluene, xylene and benzene measured by single-photon ionisation using VUV radiation from laser-produced plasmas.

Molecules	Ionization[11] energy(eV)	Ionisation* energy(eV) This work
NO	9.26	9.26±0.07
CH_3COCH_3	9.70	9.70±0.08
$C_6H_5CH_3$	8.82	8.82±0.06
$C_6H_4(CH_3)_2$	8.50	8.50±0.06
C_6H_6	9.24	9.18±0.07

* Error of this work is limited by the bandwidth of the 1/4 meter spectrograph (1 nm)

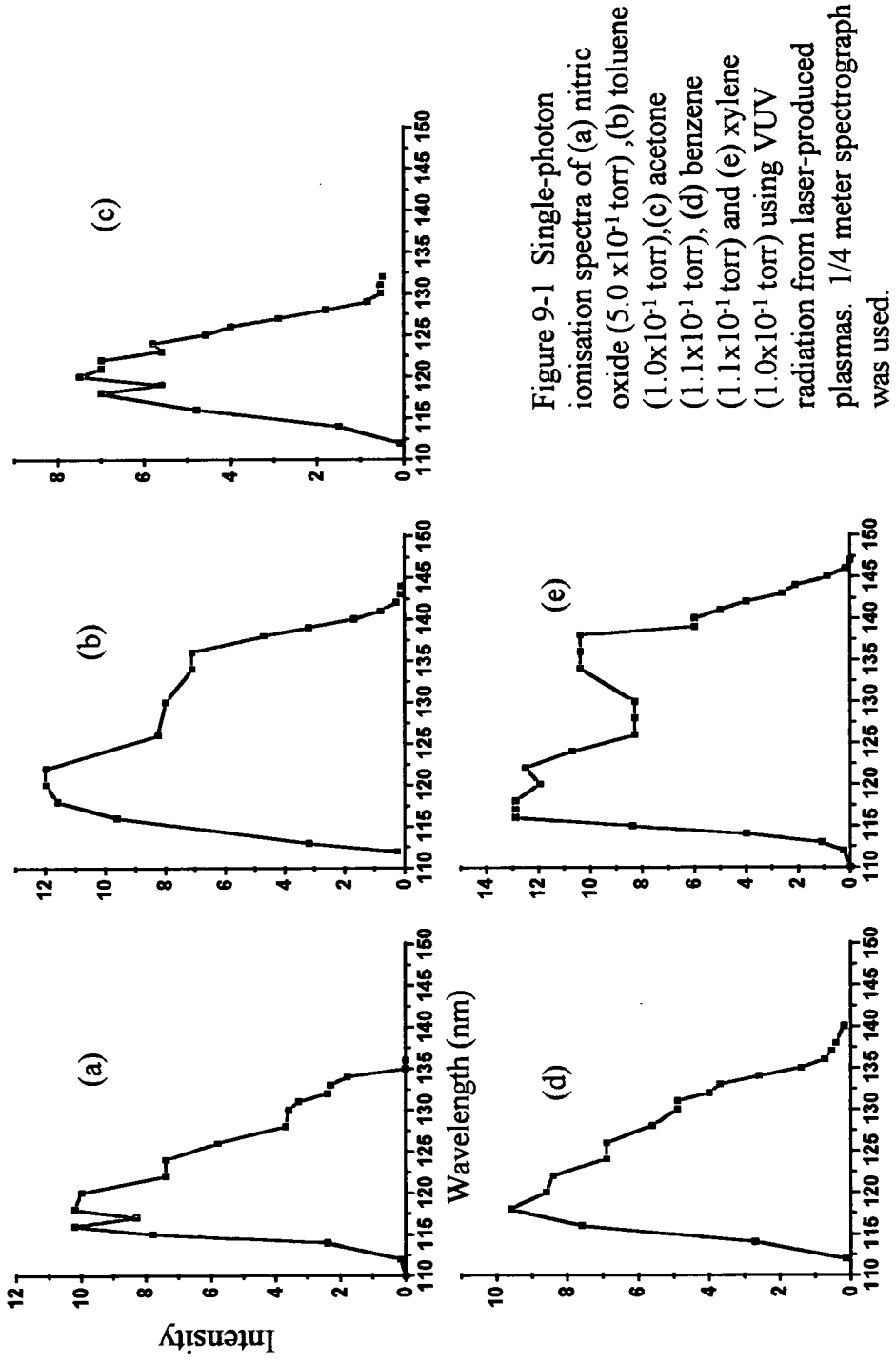

Figure 9-1 Single-photon ionisation spectra of (a) nitric oxide (5.0×10^{-1} torr) ,(b) toluene (1.0×10^{-1} torr),(c) acetone (1.1×10^{-1} torr), (d) benzene (1.1×10^{-1} torr) and (e) xylene (1.0×10^{-1} torr) using VUV radiation from laser-produced plasmas. 1/4 meter spectrograph was used.

The variation of VUV radiation intensities with wavelengths was also investigated. Two sets of experiments were performed using a photodiode and a PMT as VUV photon detectors. The photodiode was situated just behind the exit slit inside the end window of the monochromator while the PMT was behind the exit slit and a MgF_2 window. Results are shown in figure 9-2 and figure 9-3. It can be seen that the VUV radiation is fairly smooth in the range of 115-150 nm. Figure 9-2 shows again the sharp cutoff caused by the MgF_2 window.

These experiments demonstrate that VUV radiation is present in the laser-produced plasmas and could be used as a continuum VUV source for spectroscopic studies and analytical analyses. However, the spectral resolution needs to be improved for spectroscopic studies due to the limited bandwidth of 1 nm of the 1/4 meter spectrograph.

9.3.2 Improvement of spectral resolution and application to photoionisation of NO

Photoionisation of NO was investigated as an example to demonstrate the improvement of the spectral resolution of the new set-up as shown in figure 2-9 (chapter 2). The VUV photoionisation spectrum of NO obtained in the present experiment is shown in figure 9-4. The spectrum shows a sharp step function at the ionisation threshold upon which is superimposed vibrational levels of the NO^+ ground state. It is obvious that the spectral resolution is much better than that with the 1/4 meter spectrograph. The data presented here is very similar in quality to that recorded by Erman et al[8] using synchrotron radiation (figure 9-5a), who suggested that those weak peaks superimposed on the direct ionisation continuum correspond to the Rydberg series converging to the upper vibrational levels. The synchrotron radiation used by Erman et al[8] was monochromatised using a 1-meter normal incidence monochromator having a spectral resolution up to 0.02 nm. The spectral resolution in the present experiment therefore is estimated to be about 0.1-0.2 nm (70-150 cm^{-1}).

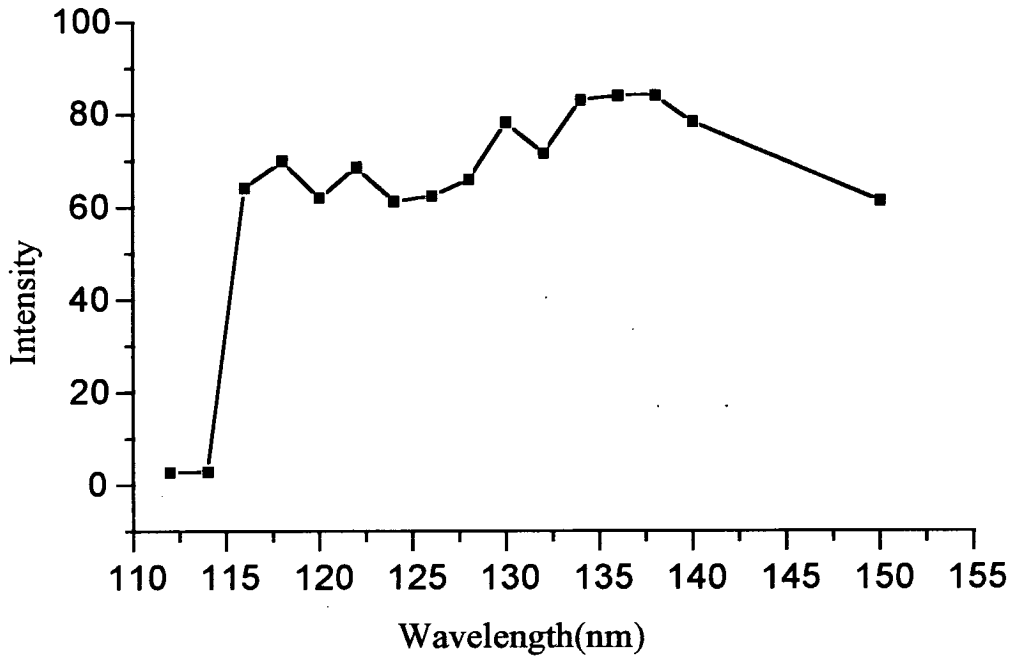

Figure 9-2: VUV radiation intensity from a laser-produced plasma measured using a PMT after a MgF_2 window.

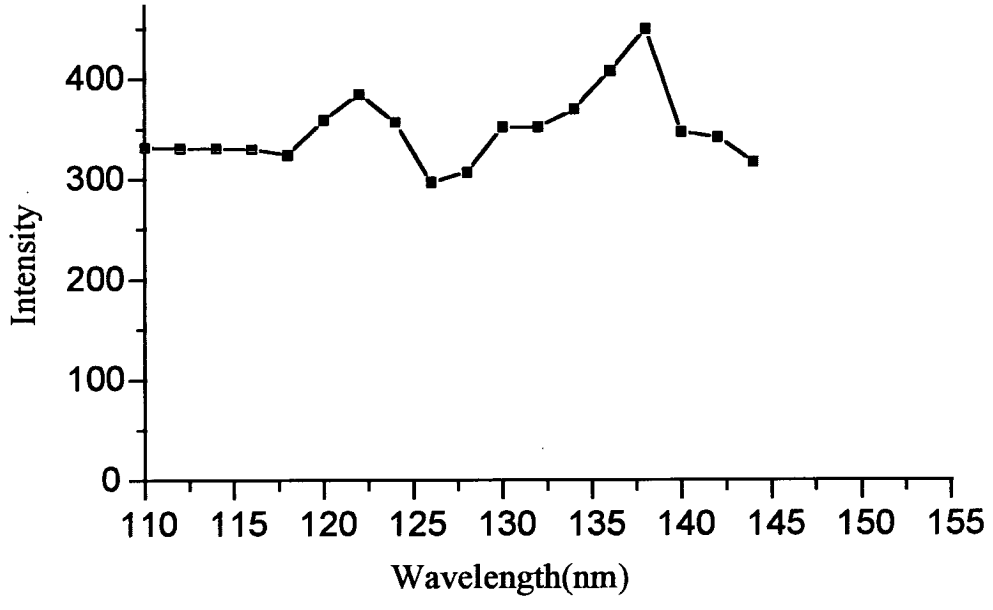

Figure 9-3: VUV radiation intensity from a laser-produced plasma measured using a photodiode without a MgF_2 window.

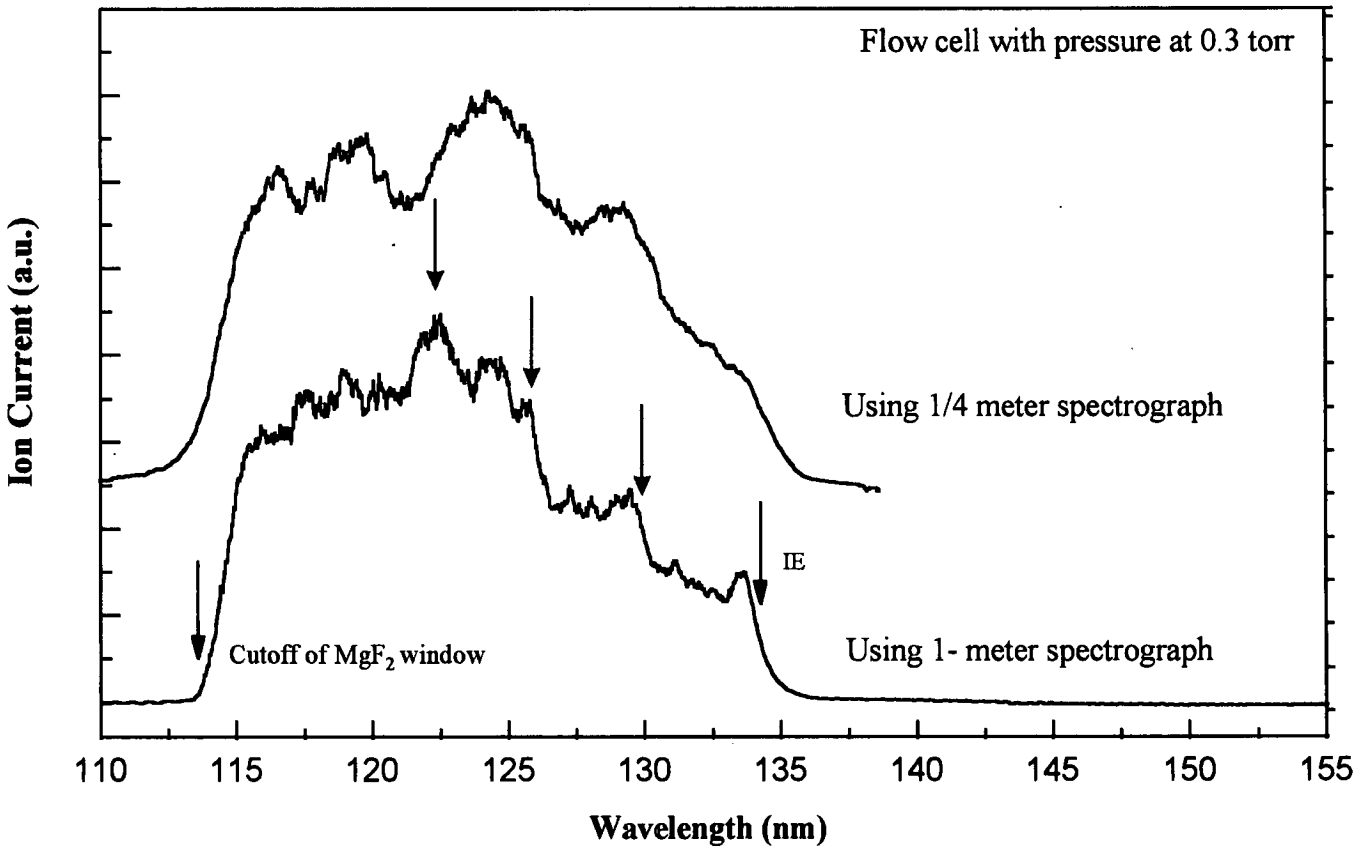

Figure 9-4: VUV single-photon ionisation spectrum of NO which shows a sharp step function at the ionisation threshold upon which is superimposed vibrational levels of the NO^+ ground state.

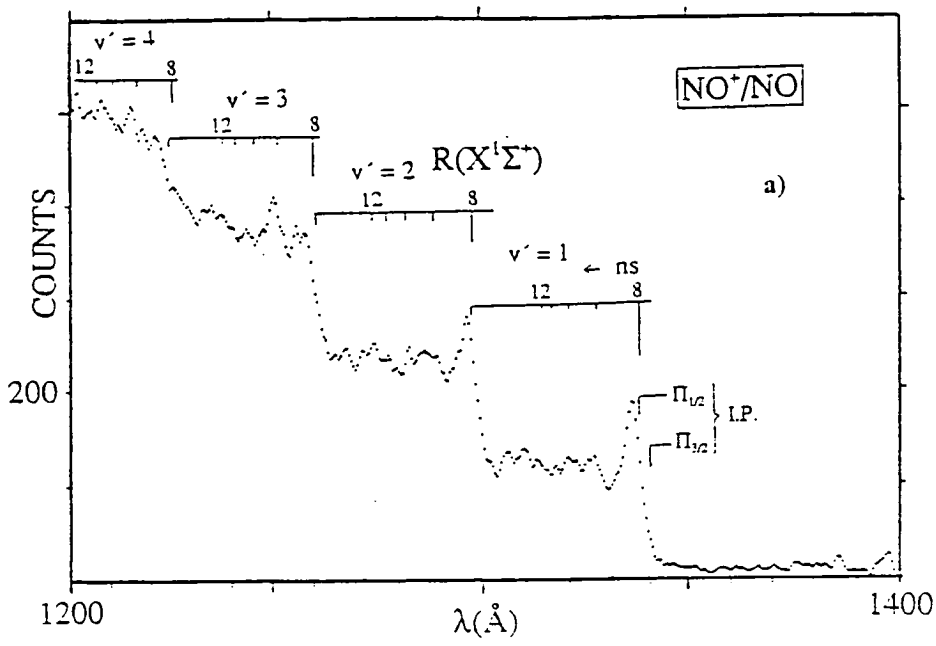

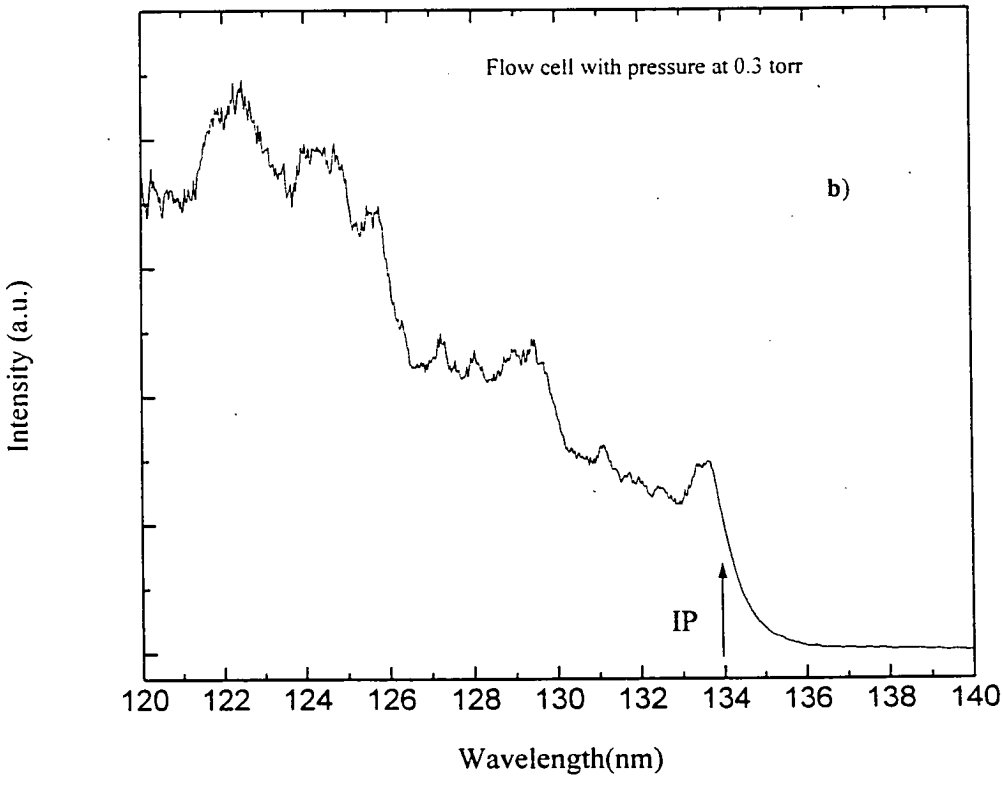

Figure 9-5: Comparison between the one-photon photoionisation spectra of nitric oxide using (a) synchrotron radiation (adapted from ref.8) and (b) VUV radiation from laser-induced plasma (reproduced from figure 9-4).

9.3.3 Application to ion-pair formation survey studies

Ion-pair formation from some halogenated methanes is known to occur upon excitation at photon energies less than the ionisation threshold of the parent molecule. The ion-pair formation from CH_3Br and CH_3I was investigated using VUV radiation from a laser-produced plasma. The ionisation threshold of CH_3Br is 10.541 eV (117.6 nm) and the calculated thermodynamic ion-pair formation threshold is 9.5 eV (130.5 nm).

Table 9-2: Comparison between Peaks observed in ion-pair production spectrum using VUV radiation from laser-produced plasma and Rydberg states of CH_3Br. The state with a prime has an excited state ionic core while the others have a ground state ionic core.

Peak	This work	Causley and Russell[10]	Hochmann et al[9]
A 128.0 nm	78125±305	77869(7s)	77985(7s)
B 125.85nm	79460±315	79542(7p)	79554(7p)
C 123.70nm	80840±457	80509(8s)	80548(8s)
D 122.19nm	81840±334	81869(9s)	81927(9s)
E 120.97nm	83008±344	82713(10s) 83264(11s)	83070(8s')

The photoexcitation function (ionisation current) obtained is shown in figure 9-6. The ionisation threshold is in good agreement with the literature value[11]. Below ionisation threshold the ionisation current is thought to correspond to the process of ion-pair formation which is very similar to the photoion-pair spectrum recorded by Berkowitz[12]. The observed threshold of 130.4 nm agrees well with the calculated value of 130.5 nm. The ion-pair excitation spectrum of CH_3Br shows several broad peaks which are tabulated in table 9-2. The first four peaks in the spectrum coincide with the four strong absorption peaks of the VUV absorption spectrum obtained by Hochmann et al[9] and Causley and Russell[10] who identified them as the 7s, 7p, 8s

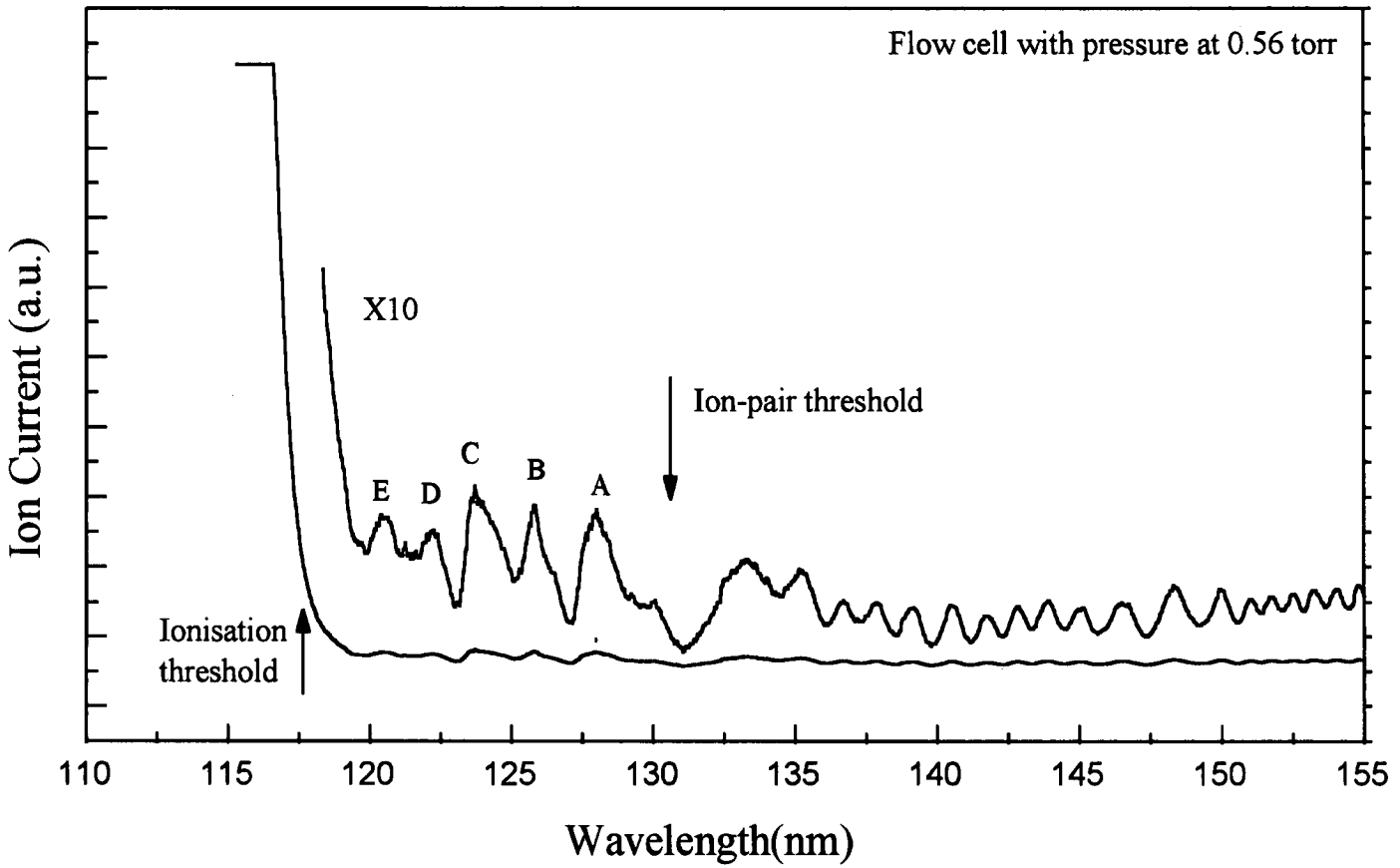

Figure 9-6: VUV single-photon excitation function of CH_3Br which shows ion-pair formation below the ionisation threshold and ionisation of the parent molecule above the ionisation threshold.

and 9s Rydberg states. In our experiment these act as doorway states to the ion-pair dissociative continuum. The intensity of ion-pair signal is about 1% of ionisation signal above the ionisation threshold.

The two peaks just below the ion-pair threshold are thought to be possibly caused by hot bands. However, it seems too low (~3000 cm^{-1}) in energy for the hot bands. At longer wavelengths the regular noise is caused by the electronic interference which could be eliminated.

The photoexcitation function (ionisation current) for CH_3I is shown in figure 9-7. The ionisation threshold of the parent molecule agrees well with the literature value[11]. Below the ionisation threshold it shows a clear stepfunction at 147.5 nm. However, the estimated thermodynamic ion-pair threshold of CH_3I is approximately 136 nm. No good explanation for this disagreement has been found yet. Even considering that some I_2 molecules might be present in the ionisation cell it still can not account for this.

9.3.4 Ion-pair formation from CH_3Br using four-wave-frequency-difference mixing (FWFD)

The one-photon ion-pair formation from CH_3Br in the regions near the peaks of A and C in figure 9-6 has been reinvestigated using VUV radiation generated by FWFD, by collecting CH_3^+ and $^{81}Br^-$. The results recorded in the CH_3^+ channel are shown in figure 9-9. As an example, the spectra recorded in both CH_3^+ and $^{81}Br^-$ channels in 127.0-128.5 nm region are shown in figure 9-8. Clearly, both CH_3^+ and $^{81}Br^-$ are formed via the same process, namely ion-pair formation, as the excitation functions are the same, within experimental limits. To higher energy around 80300 cm^{-1}, a broad peak was observed in both CH_3^+ and $^{81}Br^-$ channel. This might correspond to the doorway state, i.e. $[^2\Pi_{3/2}]$8s Rydberg state.

To lower energy, it clearly shows an onset at 130.5 nm in the CH_3^+ spectrum, which is in good agreement with the calculated value and the photoion-pair spectrum recorded by Berkowitz[12]. If this is the case, it will make CH_3Br a good example for a ZIKE experiment of polyatomic molecules. It can not be ruled

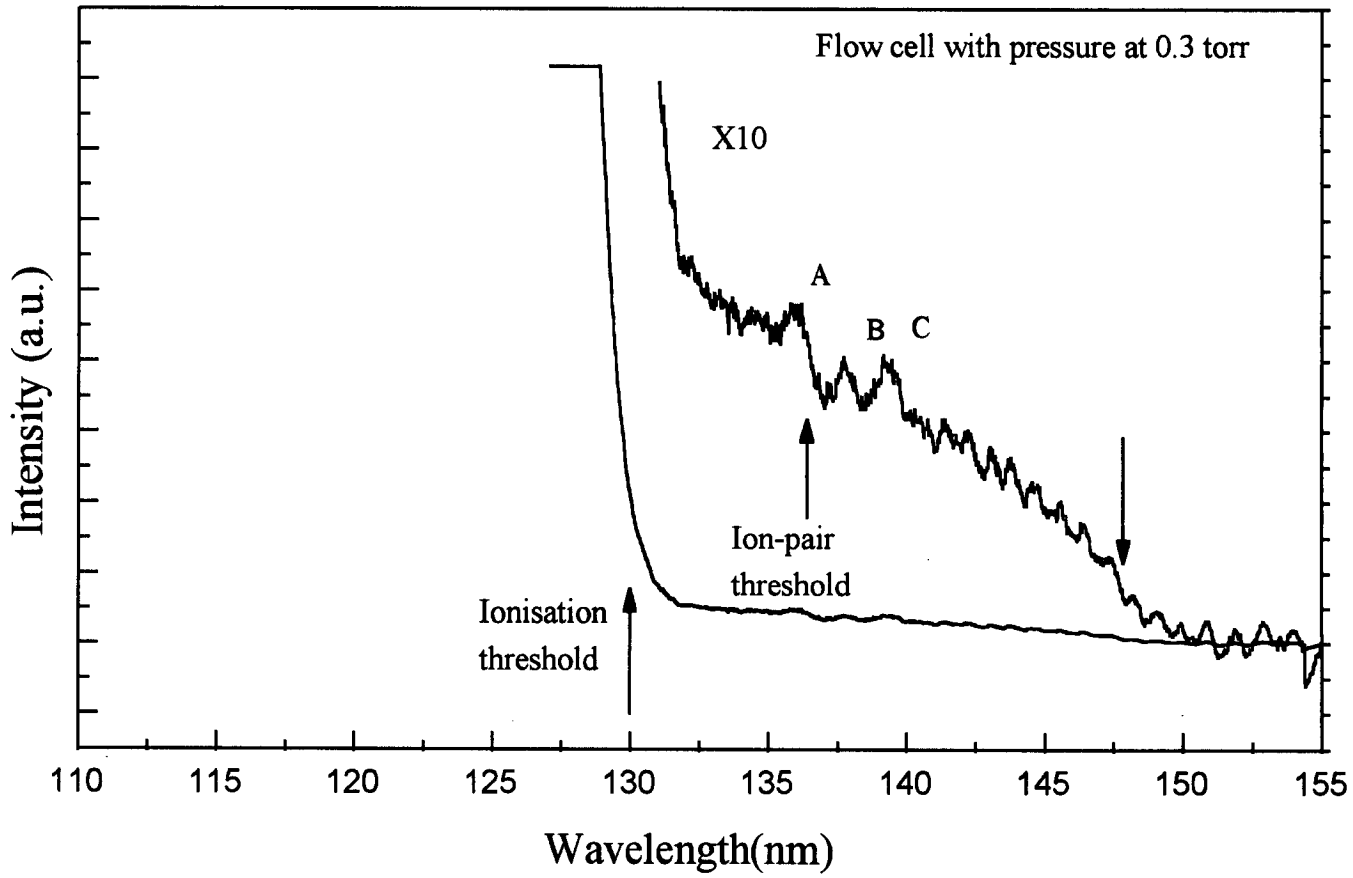

Figure 9-7: VUV single-photon excitation function of CH_3I which shows ion-pair formation below the ionisation threshold and ionisation of the parent molecule above ionisation threshold.

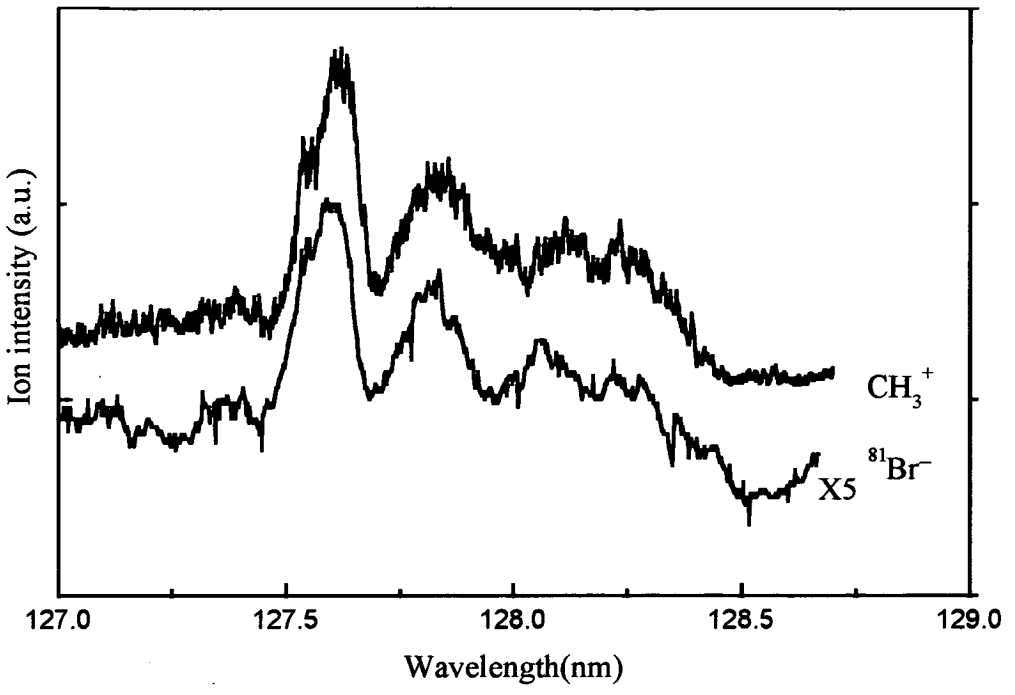

Figure 9-8: Excitation functions of ion-pair formation recorded in CH_3^+ and $^{81}Br^-$ mass channels.

out, however, that the disappearance of the CH_3^+ beyond 130.5 nm might be caused by the dying out of the VUV power. So the question if the ion-pair formation could still occur below the calculated threshold (with wavelengths longer than 130.5 nm) is still uncertain.

In order to answer this question, the dye Coumarin 153 was used to generate VUV up to 132 nm. In this region, a strong peak in the absorption spectrum was observed[9-10] and assigned as a $[^2\Pi_{3/2}]6p$ Rydberg state. However, no CH_3^+ or Br^- was observed in this region.

The peak positions appearing in the one photon absorption spectrum[9-10] in the energy range of 77800-80500 cm^{-1} (124-128.5 nm) are marked in figure 9-9, with the revised assignments made by Ridley et al based on their extensive (2+1) and (3+1) REMPI studies. All absorption peaks were assigned to the Rydberg states having Ω=0 based on the ground state ionic core or the excited ionic core. It can be seen that all absorption peaks, except that which is not covered by the laser dyes in this study, coincide with the maximum in the ion-pair formation spectrum

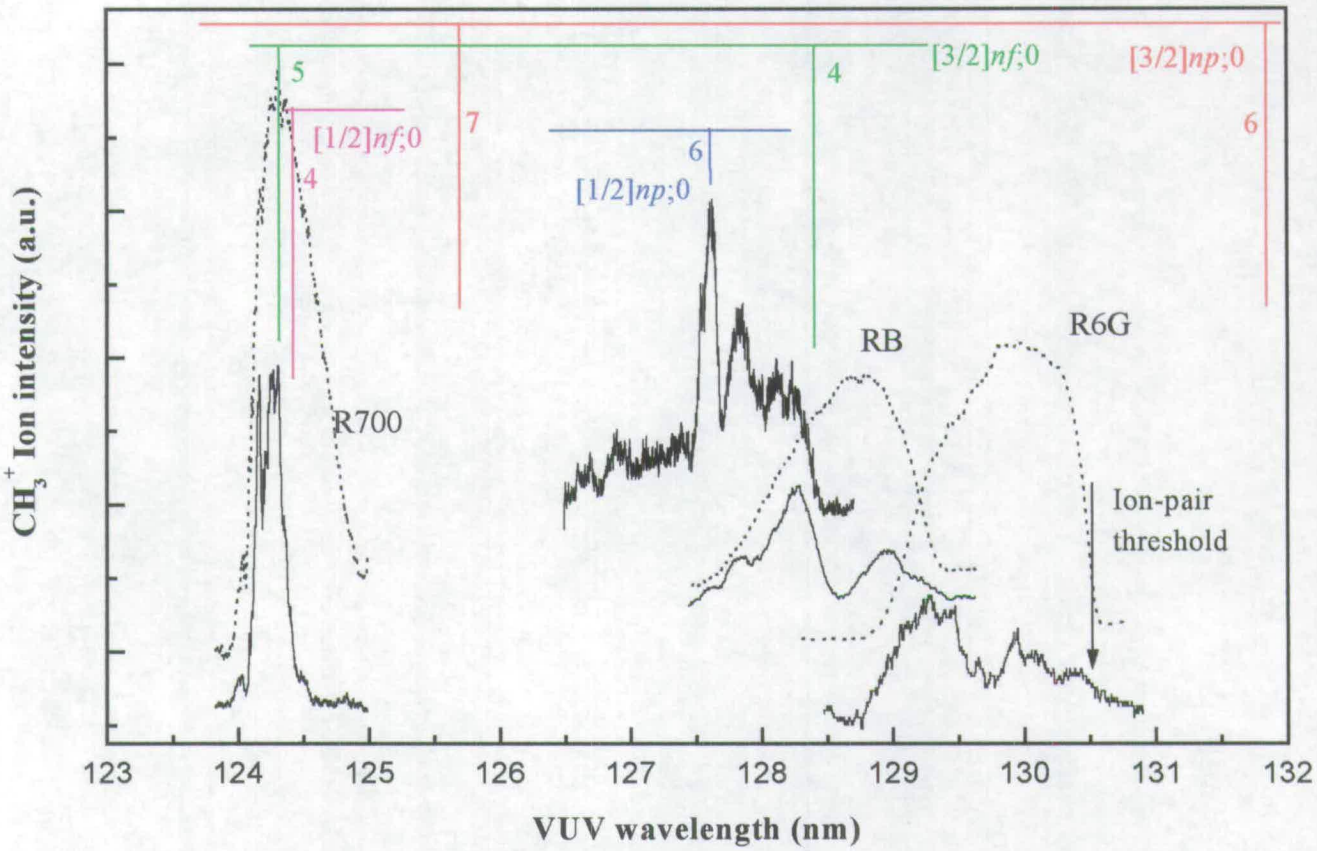

Figure 9-9: Excitation functions of ion-pair formation of CH_3Br recorded in CH_3^+ mass channel. Positions of Rydberg states observed in absorption spectroscopy (Ref. 9) are labelled in the figure. Dotted line are VUV power curves using Rhodamine 700, Rhodamine 101, Rhodamine B and Rhodamine 6G to provide the visible photons. No signal was observed in the region of 131.5-132 nm in which strong absorption was observed corresponding to [3/2]6p;0.

very well. It is known that only one ion-pair state lying in this region is a Ω=0 state and the next one lies far above in energy. The results presented here thus indicate that all initially populated Rydberg states which have an Ω=0 are coupled to the ion-pair continuum and lead to the formation of a pair of ions.

9.4 Conclusion

It has been shown that continuum VUV radiation is generated from a laser-produced plasma using the table-top picosecond laser system. By combination with a 1-meter spectrograph, this VUV radiation source can now be used for low resolution (~0.1-0.2 nm, ~70-150cm^{-1}) photoionisation and ion-pair formation survey studies of molecules. The photon number at 120 nm which reaches the ionisation chamber in the present arrangement is estimated to be about 10^6-10^8 per pulse with a pulse width of about 20-30 ns. By optimising the present experimental arrangement or using a better spectrograph, this VUV source may be used for high resolution molecular VUV spectroscopic studies especially when combined with a jet-cooled molecular beam and a time-of flight mass spectrometer.

Compared to a synchrotron VUV source, a laser-produced plasma is a table-top VUV source which is of low maintenance and construction costs, easy to operate and easy to access. For many requirements, laser-produced plasmas can provide an alternative source of VUV continuum radiation.

Compared to FWFD, laser-produced plasmas provide a continuously tunable VUV source with a large tuning range (from 150 nm to 100nm even further down to XUV) while many dyes are needed to cover a reasonable tuning range of VUV radiation for molecular spectroscopic studies by FWFD (each dye can cover about 1 nm tuning range of VUV radiation).

Both VUV generation techniques, laser-produced plasma and FWFD, have been successfully applied to CH_3Br in survey studies of the ion-pair formation. From the high resolution ion-pair formation study of CH_3Br, it is found that each peak in the absorption spectrum corresponds to a peak in the excitation spectrum of ion-pair formation. This supports the doorway state theory.

Turning to analytical applications, multiphoton processes using nanosecond laser pulses on thermally labile molecules can cause extensive fragmentation making analyses of these molecules difficult or impossible. A single VUV photon, however, can bypass completely any intermediate dissociative states. Therefore it should give large parent mass peaks which are necessary for unambiguous analytical analyses. The photoionisation of nitric oxide, benzene, acetone, toluene and xylene, demonstrated in the present experiments, indicates that the VUV radiation from laser-produced plasmas can be a new and unique source of tunable VUV photons with moderate resolution suitable for these single photon experiments.

9.5 References

1. J.A.R. Samson, *Techniques of Vacuum Ultraviolet Spectroscopy*, Wiley, New York, 1967.
2. J.Berkowitz, *Photoabsorption, Photoionization and Photoelectron Spectroscopy*, Academic Press, New York, 1979.
3. A.J. Yencha, D.K. Kela, R.J. Donovan, A. Hopkirk and A. Kvaran, *Chem.Phys.Lett.* 1990, **165**, 283.
4. A. Kvaran, A.J. Yencha, D.K. Kela, R.J. Donovan and A. Hopkirk, *Chem. Phys. Lett.* 1991, **179**, 263.
5. C. Breton and R. Papoular, *J. Opt. Soc. Am.* 1973, **63**, 1225.
6. E.T. Kennedy, J.T. Costello, J-P Mosnier, A.A. Cafolla, M. Collins, L. Kiernan, U. Koble, M.H. Sayyad, M. Shaw, B.F. Sonntag, and R. Barchewitz, *Opt. Eng.* 1994, **33**, 3984.
7. I.C.E. Turcu, I.N. Ross, P. Trenda, C.W. Wharton, R.A. Meldrum, H. Daido, M.S. Schultz, P. Fluck, A.G. Michette, A.P. Juna, J.R. Maldonado, H. Shields, G.J. Tallents, L. Dwivedi, J. Krishnan, D.L. Stevens, T.J. Jenner, D. Batani, and H. Goodson, *Proc. SPIE* 1994, **2015**, 243.
8. P. Erman, A. Karawajczyk, E. Rachlew-Kallne, and C. Stromholm, *J. Chem. Phys.* 1995, **102**, 3064.
9. P. Hochmann, P.H. Templet, H-t. Wang, and S.P. McGlynn, *J. Chem. Phys.*

1975, **62**, 2588.

10. G.C. Causley and B.R. Russell, *J. Chem. Phys.* 1975, **62**, 848.
11. *Handbook of Chemistry and Physics*, CRC Press, 1997.
12. J. Berkowitz, in *VUV and Soft X-ray Photoionisation*, Edited by U. Becker and D.A. Shirley. Plenum Press, New York, 1996, 263.

Appendix

A.1 List of acronyms

CARS	**C**oherent **a**nti-**S**tokes **R**aman scattering spectroscopy.
FWFD	**F**our-**w**ave **f**requency-**d**ifference mixing.
MATI	**M**ass-**a**nalysed **t**hreshold **i**onisation spectroscopy.
PFD	**P**ulse **f**ield **d**issociation.
PFI	**P**ulse **f**ield **i**onisation.
PES	**P**hoto**e**lectron **s**pectroscopy.
PHOFEX	**Pho**to**f**ragment **ex**citation spectroscopy.
REMPI	**R**esonance-**e**nhanced **m**ulti**p**hoton **i**onisation spectroscopy.
TOF	**T**ime-**o**f-**f**light mass spectrometry.
TPES	**T**hreshold **p**hoto**e**lectron **s**pectroscopy.
VUV	**V**acuum **U**ltra**v**iolet radiation.
ZEKE	**Z**ero **e**lectron **k**inetic **e**nergy photoelectron spectroscopy.
	or **Ze**ro **k**inetic **e**nergy photoelectron spectroscopy.
ZIKE	**Z**ero **i**on **k**inetic **e**nergy photoion-pair formation spectroscopy.

A.2 University regulations

A.2.1 Course attended:

1. Physical Section Colloquia, 1996-1997, 1997-1998, 1998-1999 academic years, Department of Chemistry.
2. Transferable Skill Program, The Faculty of Science and Engineering:
   - Word 97, Computing Services.
   - Introduction to Writing Web Pages.
   - Career Planning and Interviewing Skills.

A.2.2 Conferences attended:

1. The International Workshop on Photoionisation, Chester, UK, 16th -21st July, 1997.
2. R.S.C. Faraday Discussion No.108: Dynamics of Electronically Excited States in Gaseous, Cluster and Condensed Media, at University of Sussex, UK, 15th -17th December, 1997.
3. 9th International Symposium on Resonance Ionisation Spectroscopy and Its Applications, Manchester, UK, 21st-25th June, 1998.
4. Annual Meeting of Physical Section for the Department of Chemistry, The Edinburgh University, Firbush Point Field Centre, 1997, 1998, 1999.

A.3 List of Publications

1. "Photodissociation of ozone between 335 and 352 nm to give O_2 (b $^1\Sigma_g^+$) +O(^3P_J)", Patrick O'Keeffe, Trevor Ridley, Shiliang Wang, Kenneth P. Lawley and Robert J Donovan, *Chem. Phys. Lett.* 1998, **298**, 368-374.
2. "Ionic and Rydberg states of CF_3I studied by high resolution photoelectron (ZEKE-PFI) and resonance-enhanced multiphoton ionisation spectroscopy", N.A. Macleod, S. Wang, J. Hennessy, T. Ridley, K.P. Lawley, R.J. Donovan, *J. Chem. Soc. Faraday Trans.* 1998, **94**, 2689-2694.
3. "Higher Rydberg States of C_6H_6, C_6D_6 and C_6H_5F Studied by Two-photon Resonance Ionisation Spectroscopy", S. Wang, R.J. Donovan, T. Ridley and K.P. Lawley, *9th International Symposium on Resonance Ionisation Spectroscopy and Its Applications,* Manchester, UK, 21st-25th June, *AIP Conf. Proc.* 1998, **454**, 325-328.
4. "Formation of O_2(b $^1\Sigma_g^+$) in the Ultraviolet Photolysis of O_3", P.K. O'Keeffe, T. Ridley, S. Wang, K.P. Lawley, and R.J. Donovan, *9th International Symposium on Resonance Ionization Spectroscopy and Its Applications,* Manchester, UK, 21st-25th June, *AIP Conf. Proc.* 1998, **454**, 103-108.
5. "Continuously tuneable, high flux, VUV beamline constructed on a picosecond KrF laser plasma source", R.M. Allott, I.C.E. Turcu, N. Lisi, N. Spencer, W. Shaikh, A. Whybrew, **S.** Wang, R. Donovan, K. Lawley, K. Ledingham, M. Folkard, K. Prise, *1997 SPIE Conference on Applications of X Ray Generated From Lasers and Other Bright Sources*, San Diego, CA, USA, 31st Jul - 1st Aug 1997, *Applications of X Rays Generated from Lasers and Other Bright Sources*, 1997, **3157**, 138-147.
6. "VUV Radiation from Laser-produced Plasmas: Applications to Molecular Photoionisation and Ion-pair Production", S.L. Wang, K.P. Lawley, R.J. Donovan, K.W.D. Ledingham, T. McCanny, R.P. Singhal, R. Allott, N. Spencer, W. Shaikh and I.C.E. Turcu, *Rutherford Laboratory Annual Report*, 1997, **1996-97**, 167-168.

7. "Characterisation and Implementation of a Laser Plasma Source in the VUV", R.M. Allott, I.C.E. Turcu, N. Lisi, N. Spencer, W. Shaikh, A. Whybrew, S. Wang, R. Donovan, K. Lawley, K. Ledingham, M. Folkard, K. Prise, *Rutherford Laboratory Annual Report*, 1997, **1996-97**: 145-146.
8. "Applications of VUV radiation from laser-produced plasmas to molecular photoionisation and ion-pair production", S.L. Wang, K.P. Lawley, R.J. Donovan, K.W.D. Ledingham, T. McCanny, R.P. Singhal, R. Allott, N. Spencer, W. Shaikh and I.C.E. Turcu, at *The International Workshop on Photoionisation*, Chester, UK, 16th -21st July, 1997. Poster.
9. "Photofragment spectroscopy of ozone using resonance enhanced multiphoton ionisation", P. O'Keeffe, R. J. Donovan, K. P. Lawley, T. Ridley, S. Wang, at *Dynamics of Electronically Excited States in Gaseous, Cluster and Condensed Media, Faraday Discussion No.108*, at University of Sussex, UK, 15th -17th Dec. 1997. Poster.
10. "REMPI and ZEKE-PFI studies CF_3I", N.A. Macleod, S. Wang, J. Hennessy, T. Ridley, K.P. Lawley, R.J. Donovan, at *Dynamics of Electronically Excited States in Gaseous, Cluster and Condensed Media, Faraday Discussion No.108*, at University of Sussex, UK, 15th -17th Dec. 1997. Poster.